Detection and Effects of Volcanic Sulphur in the Stratosphere

---

Georgina Miles

Submitted for the degree of Doctor of Philosophy

Linacre Collage, University of Oxford

Michaelmas Term, 2011

"There are two kinds of truth: the truth that lights the way and the truth that warms the heart. The first of these is science, and the second is art. Neither is independent of the other or more important than the other. Without art science would be as useless as a pair of high forceps in the hands of a plumber. Without science art would become a crude mess of folklore and emotional quackery. The truth of art keeps science from becoming inhuman, and the truth of science keeps art from becoming ridiculous." -Raymond Thornton Chandler, writer (1888-1959)

Acknowledgements

I would like to acknowledge the Natural Environment Research Council for funding the initial phase of this work, and thank my Supervisors Dr Don Grainger and Prof. Ellie Highwood. Also, Dr Brian Kerridge and the Remote Sensing Group at the Rutherford Appleton Laboratory for use of their computation facilities in the latter phase. My thanks go particularly to Dr Richard Siddans (RAL) for his advice and contributions. I'd also like to thank Dr Fred Prata for a conversation in 2002 which heavily influenced the topic of this Thesis. My thanks go to the Department of Physics, University of Oxford and specifically to the Atmospheric, Oceanic and Planetary Physics Department for their patience, notably that of Prof. David Andrews and Prof. Peter Read. In no particular order I would like to thank: David Latham, Dr Paul Townsend, Dr Carly Howett, Dr Hugo Lambert, Dr Nick Faull, Sarah Harrington, Dr Anu Dudia, Dr Clive Rodgers, Dr Alison Waterfall, Dr Hugh Mortimer, Dr Sam Dean and Dr Steve Marsh. I'd like to thank the CRUSE bereavement charity (Oxford branch), without the assistance of which I may not have completed this work. Most especially I'd like to thank my parents Robin and Pamela Miles, sister Maj. Suzanna Cox (and Wednesday) for their sacrifices, understanding and moral support over the years.

Contents

Acknowledgements **i**

Abstract **v**

1 Introduction **1**

1.1 Atmospheric effects of volcanic eruptions 2

1.1.1 Volcanic emissions 3

1.1.2 Types of volcanism 8

1.2 Volcanic sulphur 10

1.3 Estimates of volcanic sulphur emissions 11

1.3.1 Volcanic signals in ice cores 12

1.3.2 Tephra analysis 13

1.3.3 Eruption frequency 14

1.4 In situ or ground remote sensing of volcanic SO_2 emissions . . . 16

1.4.1 SO_2 from the Total Ozone Mapping Spectrometer 16

1.4.2 Satellite measurements of volcanic SO_2 19

1.5 Outline of thesis 35

2 Modelling the Climatic Significance of Volcanic Eruptions **37**

2.1 Simplified model 38

2.1.1 Sulphur dioxide and aerosol evolution 40

2.1.2 Optical depth 44

2.1.3 Radiative forcing and surface temperature change 45

2.2 Validation 46

2.3 Eruption significance 49

2.4 Conclusions 52
2.5 Addendum 55

3 An introduction to infrared atmospheric profile retrieval 56
3.1 Atmospheric profile retrieval 57
3.2 Principles of retrieval theory 58
    3.2.1 Error analysis and retrieval diagnostics 60
    3.2.2 Information content 61
    3.2.3 The retrieval engine and convergence 61
3.3 Radiative transfer 62
3.4 Forward models 63
    3.4.1 Forward model error 64
3.5 Clouds 66
    3.5.1 Detection of SO_2 68

4 Retrieval of SO_2 using the HIRS/2 instrument 69
4.1 HIRS/2 instrument 69
    4.1.1 Measurements 71
4.2 Initial approach to detecting SO_2 with HIRS/2 72
4.3 Principle of SO_2 retrieval with HIRS/2 74
4.4 Forward modelling of the atmosphere 75
    4.4.1 HIRS/2 forward models 75
    4.4.2 Locating the SO_2 layer 79
    4.4.3 Initial approach 83
    4.4.4 HIRS/2 column retrieval 86
4.5 Forward model error 93
    4.5.1 *A priori* and covariance 96
4.6 Retrieval from simulated measurements 97
    4.6.1 Simulating measurements with the forward model 98
    4.6.2 Simulating measurements with the RFM 100
    4.6.3 Comparison of simulated measurements 103
    4.6.4 HIRS/2 and cloud modelling 105
    4.6.5 Sensitivity to plume profile height and shape 111

4.6.6 Summary 119

5 Case Study 122

5.1 Case study - Cerro Hudson 122
5.2 The 1991 eruption 123
5.2.1 8-9th August activity 124
5.2.2 12-14th August activity 124
5.2.3 15th August activity 125
5.3 Observations and modelling 125
5.4 Application of retrieval scheme to real measurements 127
5.4.1 Improvements to forward model error 127
5.4.2 HIRS/2 SO_2 column retrieval results 130
5.4.3 Results - 1991 Cerro Hudson eruption 132
5.4.4 Plume mass estimates 136
5.4.5 HIRS/2 comparative SO_2 151
5.4.6 Qualitative comparisons with TOMS SO_2 observations . 153
5.4.7 Errors 164

6 Discussion and Future Work 166

6.1 SO_2 column retrieval scheme for HIRS/2: Conclusions 166
6.2 Summary and discussion of thesis results 168
6.3 Optimisation of the case study - multi-satellite retrievals 169
6.4 A complete eruption emission characterisation 170
6.5 Further development of RTTOV/cloud model to include SO_2 . . 171
6.6 A HIRS/2 sulphur dioxide dataset 172
6.7 A satellite atmospheric sulphur dioxide inventory 173

A Prata Fit Method 174

A.1 Methodology 174
A.2 Implementation 177
A.3 Characteristics and sensitivity 178
A.3.1 Plume height and thickness 178

Bibliography 181

Abstract

Explosive volcanic eruptions perturb the atmosphere, and their main impact arises from the large quantities of SO_2 emitted. Within this thesis this effect is characterised from a modelling perspective and the detection and measurement of SO_2 by a satellite are improved. A stratospheric aerosol box model is developed that parameterises the aerosol evolution from an emitted mass of volcanic SO_2. Using aerosol optical depth measurements and a simple energy balance model, the SO_2 mass is directly related to a global average temperature change. Combining this model with historical eruption records yields a measure of the significance of eruptions based on frequency and magnitude. The model predicts that eruptions of 0.1-1 Mt of SO_2 are the most significant for perturbing the climate. This is consistent with recent satellite observations of stratospheric optical depth. The model establishes that the radiative forcing from a large volcanic eruption is determined by the mass of SO_2 erupted, suggesting accurate measurement of volcanic SO_2 is paramount for quantitative monitoring of its atmospheric impact. The brightness temperature difference method developed by Prata et al. (2003) demonstrated the potential for monitoring volcanic SO_2 using the High Resolution Infrared Radiation Sounder 2 (HIRS/2) instruments on the NOAA and MetOp platforms. The Prata method is fast but of limited accuracy. This thesis improves upon this by using an optimal estimation retrieval approach yielding increased accuracy for only moderate computational cost. This is principally achieved by fitting the column water vapour and accounting for its interference in the retrieval of SO_2. A cloud and aerosol model is used to evaluate the sensitivity of the scheme to the presence of ash and water/ice cloud. This identifies that the cloud or ash above 6 km limits the accuracy of the water vapour fit, increasing the error in the SO_2 estimate. Cloud top height is also retrieved and this finding quantifies a cloud screening limit that can be imposed. The scheme is applied to a case study event, the 1991 eruption of Cerro Hudson in Chile. A new total erupted mass estimate was found to be 2200 kT ± 600 kT. This fit method yields a minimum mass per unit area detection limit of 3 DU, which is comparable with that for the Total Ozone Mapping Spectrometer (TOMS), the only other instrument capable of monitoring SO_2 from 1979–1996.

Chapter 1

Introduction

Volcanic eruptions are important for climate and climate change. They perturb atmospheric chemistry and radiative transfer. Their signal in climatic records must be accurately quantified before any attribution of climate change to anthropogenic sources. Furthermore, by studying the response of the atmosphere to volcanic eruptions in terms of climate sensitivity this can test ideas relating to climate prediction. Recently, the concept of artificially emulating how volcanoes cool the planet have been explored in the context of geo-engineering. In order to do all of this, we need a good and accurate description of volcanic effects on climate. We also need an accurate record of historical volcanic eruptions, the statistics of which can also be used to help predict the likely impact of future eruptions. This thesis will attempt to improve these things by doing the following. Firstly, by developing a simplified but comprehensive model to predict the change in temperature response to past and potential future volcanic eruptions, thereby classifying which type are of greatest significance for climate. It will further develop a methodology for obtaining new long term monitoring information on sulphur dioxide (SO_2) from an instrument that has not been fully exploited. It will begin to validate this methodology using a case study of the 1991 Cerro Hudson eruption, and using other observations and measurements of the event. This introduction describes the pertinent aspects of volcanic eruptions, how they affect the atmosphere and how volcanic SO_2 may be measured.

1.1 Atmospheric effects of volcanic eruptions

The atmosphere is affected by volcanoes in a variety of ways and on different time scales depending on the nature of the volcanic activity. These broadly range from perturbation of regional tropospheric chemistry in the case of effusive eruptions lasting months or years, to transient global cooling from large explosive eruptions which release material over hours to days. Principally, explosive eruptions emit SO_2 into the stratosphere, which is oxidised into sulphate aerosols that can remain there for several years. There are the further classes of eruptions of 'super' and flood basalt, which can profoundly alter the atmospheric composition, but neither type has occurred in recent history. The main atmospheric effects of volcanic eruptions can be broadly classified, and are listed as the following:

- Aerosol direct effect (1): Stratospheric aerosols increase the stratospheric albedo decreasing the shortwave heating of the surface.
- Aerosol direct effect (2): Longwave absorption by the stratospheric aerosols, increasing the stratospheric temperature and reducing that at the surface. This property is particular to stratospheric sulphate aerosols, as they tend to be large (enough to interact with infrared radiation) and at high altitude. SO_2 itself also absorbs strongly in the infrared. Such shortwave absorption is likely to be a small and transient component of the overall radiation budget, as shown in Highwood & Stevenson (2003).
- Aerosol direct effect (3): Aerosol and ash in the troposphere may cause short-lived localised warming.
- Aerosol indirect effect: Tropospheric aerosols (or those sedimented downwards from the stratosphere above) increase the number of cloud condensation nuclei and the albedo of clouds causing a decrease in surface temperature, and possibly increase ice nucleii in the upper troposphere. They can also increase the lifetime of the cloud. These effects would be as short-lived in accordance with the the tropospheric lifetime of the aerosol.

- Acid rain.
- For continuous eruptions the build-up of greenhouse gases such as CO_2 causes an increase in surface temperature, the magnitude of which is related to the strength and length of the eruption.
- Also for long-lived effusive eruptions, a build-up of gaseous species in the region of the volcano that are hazardous to health, increasing morbidity and mortality rates among local populations.
- The emission of halogens into the stratosphere has the potential to destroy ozone, particularly at midlatitudes, principally in combination with aerosols which can act as heterogeneous catalysts for the activation of halogens.

Volcanic eruptions present a hazard to aircraft because of the ash, and to a lesser (and more speculative) extent the acidity of the sulphate aerosols that they produce. This has led to a concerted drive towards identification and tracking of volcanic plumes in near real time, discussed extensively in Carn et al. (2005) and Prata (2009). The cost of failing to accomplish this with either sufficient accuracy or timeliness can be financially damaging, but of primary concern is the threat to human life.

1.1.1 Volcanic emissions

Volcanoes have influenced the composition of the Earth's atmosphere since the lithosphere formed around the molten core of the planet. Outgassing of absorbing species such as nitrogen, CO_2 and H_2O formed the early atmosphere, which evolved closely with the geology of Earth. Erupted volcanic plumes also contain a mixture of gases including SO_2, HCl and HBr. The amount of CO_2 emitted by volcanoes is thought to range between 0.13-0.44 gigatonnes compared to 35 gigatonnes thought to have been emitted from anthropogenic origin in 2010 (Gerlach 2011). The annual emissions of the other species by volcanoes are also considerably smaller than those from anthropogenic sources (Halmer 2001). As they can be injected directly into the stratosphere they are potentially more effective at changing the atmosphere there. Ryan & Mukherjee (1975) postulated that the annual chlorine input to the stratosphere ($\sim 10^8$ kg) is roughly twice that of anthropogenic chlorine transported though the tropopause. However this was before the identification of the Antarctic ozone hole (Farman et al. 1985) caused by photolytic breakdown of anthropogenic CFCs in the stratosphere (Molina & Rowland 1974). The dual presence of water vapour and chlorine in a volcanic plume has implications for ozone loss. At midlatitudes, sulphate aerosols that form from the gases can act as sites for heterogeneous chemical reactions which liberate reactive chlorine (Solomon et al. 1996, 1998). These are similar to the reactions that occur on the surfaces of polar stratospheric clouds at high latitudes. A single chlorine atom may destroy as many as 10,000 ozone molecules before being removed from the cycle into a reservoir species (Coffey 1996). Irrespective of momentum, effusive eruption plumes appear to lose SO_2 by dry deposition, leaving it significantly depleted before it can reach the upper troposphere or stratosphere (Stevenson et al. 2003).

A useful quantity for identifying the impact on the radiative balance of the atmosphere is the 'radiative forcing'. This refers to the change in the net irradiance flux, conventionally defined at the tropopause. For example, 'greenhouse gases' (such as CO_2 and CH_4) that absorb in the infrared have a positive radiative forcing, and lead to a warming of the troposphere. A bright surface, such as snow or ice, with a high albedo reflects shortwave radiation and has a local negative radiative forcing.

Bekki (1995) proposed that very large volcanic eruptions could significantly deplete the stratosphere of H_2O and OH, although there has yet to be an eruption large enough for this to be tested by observation. The removal of water vapour could itself have a large radiative forcing. Furthermore, this mechanism is postulated to prolong the life of volcanic material in the stratosphere (Bekki et al. 1996). Lack of oxidants would mean the residence time of SO_2 would increase and the formation of sulphate aerosols slow. This is in contrast to a self-limiting mechanism (Pinto et al. 1989) in which very high local concentrations of aerosols promote their coagulation. The more massive they become the faster they fall out of the stratosphere due to gravity.

Joshi & Jones (2009) propose a further negative feedback mechanism for the cooling of the planet by stratospheric aerosols. An increase in water vapour in the stratosphere leads to stratospheric cooling, which in turn has a positive radiative forcing (Smith et al. 2001). Joshi & Jones (2009) argue that very large tropical or coastal volcanic eruptions entrain sufficient water vapour such that the longwave radiative warming effect counters the forcing from the sulphate aerosol, and further point out that the potential residency of water vapour in the stratosphere would normally exceed that of sulphate aerosol. They use the eruption of Krakatau (in 1883) to examine the observed and modelled temperature changes following the eruption with and without the addition of a significant amount of stratospheric water vapour. Their results do predict less cooling from eruptions with significant water vapour but highlight the uncertainties both in models and observations.

Localised heating effects have the potential to alter the dynamical circulation. Modelling by Stenchikov et al. (1998) suggests that the Arctic Oscillation (AO), a northern hemisphere annular pressure/temperature mode, was affected by perturbations in stratospheric aerosols and ozone by the 1991 eruption of Mt Pinatubo. They proposed that longwave heating of the aerosol in the stratosphere in the tropics or midlatitudes led to an enhancement of the poleward temperature gradient. This in turn led to a strengthening of the polar vortex and forced a positive phase of the AO. Robock & Mao (1995*a*) (and others) suggest that this is the cause of a characteristic winter warming and summer cooling (WWSC) observed in the Northern Hemisphere after large equatorial eruptions. This is however based on modeling studies after only two volcanic eruptions, El Chichón (in 1982) and Pinatubo (in 1991), thus the statistical significance of the WWSC as it is observed is low. Robock & Mao (1995*a*) maintain that effects are not observed, predicted dynamically or evident in model simulations in the Southern Hemisphere. The South Polar Vortex in winter is more coherent and long-lived than its northern counterpart due to the lack of orographic boundaries which distort the flow in the Northern Hemisphere, but its relative susceptibility remains an open question until an eruption event can test it.

Volcanic material in the tropics spreads preferentially into the winter hemisphere due to the position of the Intertropical Convergence Zone (ITCZ) and the associated stratospheric overturning Brewer-Dobson circulation (Trepte et al. 1993). Provided the eruption is sufficiently large it will eventually spread to both hemispheres, though amounts and effects will be limited if the eruption occurred further away from the equator. Circulation of volcanic material in the stratosphere is affected further by the phase of the Quasi-Biennial Oscillation (QBO), the east-west oscillation of the stratospheric equatorial winds. The dispersal of volcanic aerosols is related to the vertical structure of the QBO, which oscillates over a period of about 26 months (WMO 1998). The phase of the QBO can govern how high in the stratosphere material is lofted (Vernier et al. 2011). The regional temperature effects from volcanic aerosols in the stratosphere are sometimes masked by El Niño and La Niña events. These are characterised by warm (El Niño) or cool (La Niña) temperature differences across the equatorial Pacific, which varies temporally on a 2-7 year timescale. The strength and frequency of El Niño and La Niña events can affect atmospheric circulation as far away as the polar regions via global atmospheric teleconnection (Trenberth & Hoar 1996).

Oman et al. (2005) analyse stratospheric geopotential height (gph) anomalies, attributed to the effect of stratospheric aerosols, using an ensemble of global climate model simulations. Geopotential (or gravity adjusted) height (gph) is the equivalent altitude of a pressure surface, that can be related to geometric height by assuming hydrostatic equilibrium. The work by Oman et al. (2005) was based around reproducing the eruption Katmai (58° N) in 1912 of 5 Mt SO_2, most of which was confined poleward of 30° N. They suggest this resulted in a 9 $\mathrm{Wm^{-2}}$ top of atmosphere (TOA) forcing. Their model indicated that at high latitudes the radiative effects of the aerosols was greater than the dynamical impact (in terms of how it may have forced the phase of the Arctic oscillation). They conclude that the greatest dynamical effect was to weaken the Asian Monsoon, resulting from the cooling of Northern hemisphere land masses. An analogous affect from the presence of anthropogenic aerosols has been similarly proposed by Bollasina et al. (2011). Oman et al. (2005) also ran the model for an optical depth perturbation equivalent to three times Katmai. Their studies for different multiples of Katmai-sized eruptions comprised 20 member ensembles. When averaged the gph anomaly fields that resulted from each study showed differing spatial patterns.

To examine the relationship between climate and volcanic eruptions in the pre-instrumental past one must make use of models and proxy measurement techniques, of which there are several. Some care must taken in their interpretation, because the way in which volcanic eruptions affect the atmosphere can in turn affect the proxy. According to Robock (2000) after El Chichón the net shortwave radiation (SW) locally at the surface decreased by 35 $\mathrm{Wm^{-2}}$. However, in its components, the direct SW reduced by 175 $\mathrm{Wm^{-2}}$ and the diffuse SW increased by 140 $\mathrm{Wm^{-2}}$. The increase in diffuse radiation is caused by the attenuation and scattering by the small volcanic aerosols in the stratosphere. Evidence of this comes from the observation that trees grow preferentially in diffusely lit conditions, and must be a consideration in interpreting tree rings as an atmospheric temperature proxy. The mechanism arises because intense direct radiation can cause the stomata to contract from over-heating to prevent excess loss of moisture from the plant. This effectively depresses its respiration rate. Furthermore, there are other processes that can affect the overall increase in atmospheric carbon dioxide (which can affect tree growth rate), including changes in emission and El Niño/La Niña episodes. It has been shown that after volcanic eruptions the background trend appears to be depressed slightly in the following few seasons (CMDL 2003). Such preferential conditions for growth can be seen in tree rings. Robock (2005) suggested that tree ring width used as a proxy for net cooling after volcanic eruptions (as plants respire less under cooler conditions) may produce an underestimate of temperature change.

Between 1998–2008, the observed global temperature trend has not risen in line with model predictions. Using models, Kaufmann et al. (2011) tentatively suggest that this is due to the increase in atmospheric aerosols, predominantly due to to the increasing burning of coal in China. Vernier et al. (2011) by contrast present stratospheric optical depth measurements that appear to show that the trend in aerosol optical depth (AOD) is predominantly due to the activity of volcanoes, although they do not discount that anthropogenic aerosol emissions can contribute to the effect. It is worth noting that the temperature change (or lack thereof) in the period selected by Kaufmann et al. (2011) is still within the bounds of natural variability, particularly as the early period was marked by the end of an El Niño.

1.1.2 Types of volcanism

Figure 1.1 shows the global distribution of volcanoes which have been active in the last 10,000 years referred to as the holocene era. Their positions are zonally variable, but reflect the underlying tectonic geodesy of plate boundaries.

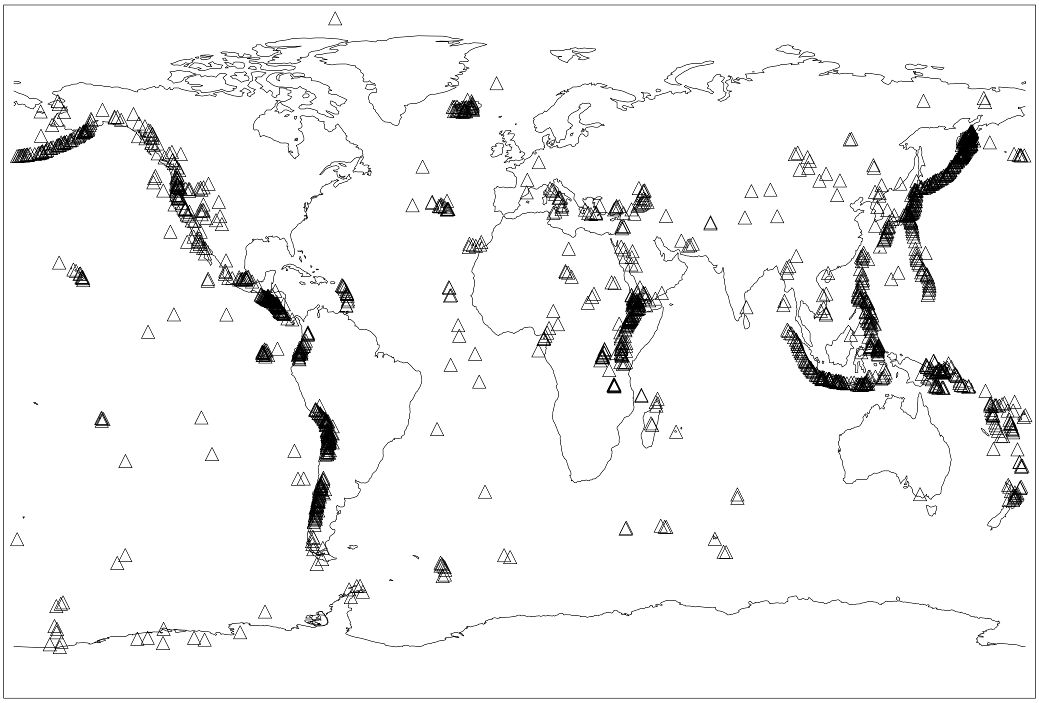

Figure 1.1: Holocene volcanoes (Smithsonian 2002).

Volcanic eruptions vary in type, strength and frequency. For the purposes of this work, only the explosive eruptions where material reaches the stratosphere are considered. This is because they occur on a geological frequency that can be observed within the satellite era, and because their frequent introduction of stratospheric aerosols perturb the climate globally to a measurable degree.

Explosive eruptions

Explosive volcanism occurs sporadically in time and is triggered by conditions deep beneath the surface. The most powerful events are associated with subduction zones at tectonic plate boundaries, where sea water brought down beneath the lithosphere seeps upwards and causes partial melting of the rock. As the melt (magmatic rock) becomes more buoyant it rises, and as vapour bubbles (water and other trace volatiles) form its density decreases further. At a critical exsolution point (in pressure and temperature) the magma will erupt upwards explosively, expanding its volume by up to hundreds of times (Sparks et al. 1997). The force of such an eruption can send the exploded material over 40 km into the atmosphere above.

During a volcanic eruption, the hot nascent plume rises turbulently entraining moist ambient air from the troposphere. Momentum and the release of latent heat from within the plume can drive it upwards. Eventually the material assumes a height of neutral buoyancy, where most of the material settles out.

This height depends on many variables, including the initial explosivity, temperature and humidity profile, ambient wind conditions, contents of the plume and temperature of the material.

The subsequent dispersion and transport of the plume is determined by the prevailing meteorology and its place in the atmosphere. In the relatively humid troposphere solid erupted rock fragments (tephra) quickly fall out due to gravity. Ash which falls more slowly and gases can condense onto water droplets that rain out over a period of weeks. Material that has made it to the drier stratosphere is generally more long-lived. Fine ash can take months to fall to the troposphere. SO_2 in the plume undergoes a microphysical transition into sulphuric acid aerosols that can remain in the stratosphere for a period of years.

The aerosols grow by further condensation and coagulation to sizes of over $\sim 0.1\,\mu$m and become too heavy to remain suspended (Grainger & Highwood 2003), but this does not mean that larger aerosols can not be present. Due to the atmospheric circulation they can be very distant from the volcano that produced them before they begin to sediment out of the atmosphere. As such, the mass of SO_2 released in explosive plumes which subsequently goes on to become sulphate aerosol fundamentally determines the subsequent atmospheric radiative forcing caused by the eruption.

1.2 Volcanic sulphur

Volcanic sulphur in species present in the atmosphere are SO_2, H_2S, sulphates and to a lesser extent COS, CS_2, S_2, SO and sulphides. Gas phase reaction rates in the stratosphere are governed by ambient temperature (for collision activation), solar radiation and atmospheric composition. In volcanic magma, the source of the volcanic gases, SO_2 is formed from the combustion or oxidation of sulphur, hydrogen sulphide and sulphur ores, such as pyrite (FeS_2) or cinnabar (HgS). H_2S is in a reduced state (-2) and oxidises in gaseous phase:

$$\mathrm{H_2S + OH \longrightarrow H_2O + HS}$$

HS will rapidly react with O_2, O_3 or NO to form SO_2.

The formation of stratospheric sulphate aerosols is thought to occur on particulate nuclei or by direct homogeneous nucleation if the reactant concentration is sufficiently high. These aerosols are typically 75 % H_2SO_4 and 25 % H_2O (Grainger & Highwood 2003). Satellite observation of erupted SO_2 often show a peak on the second day after the eruption. This is thought to be due to the oxidation of H_2S (Constantine et al. 2000). The oxidation of SO_2 is thought to be governed by the following reactions:

$$\begin{gathered}\mathrm{SO_2 + OH + M \longrightarrow H_2SO_3 + M}\\ \mathrm{H_2SO_3 + O_2 \longrightarrow HO_2 + SO_3}\\ \mathrm{SO_3 + H_2O \longrightarrow H_2SO_4}\end{gathered}$$

Where M is an inert species (N_2 or O_2) necessary for the energetics of the reaction (Sigurdsson & Laj 1992). JPL (1997) list 86 SO_x reactions which are possible with the constituents known to exist in the stratosphere. Many have improbably high activation energies or too low a constituent concentration to be of significance to the stratospheric sulphur budget, but it is likely that there are more mechanisms involved than the general case given above. These are primarily gas phase reactions, and are comparatively slow (Holloway & Wayne 2010). Therefore SO_2 may be expected to be widely distributed before complete oxidation. It would be reasonable to assume that very few photochemical reactions occur within the initial nascent plume itself due to its opacity. However, after its dispersion there is likely to be a diurnal variation in the production rate of sulphate aerosols as they are formed via photochemical reactions. Reaction kinetics suggest that the lifetime of SO_2 in the stratosphere should be about 38 days, based on the above reactions (Coffey 1996). This agrees broadly with satellite data which suggest SO_2 e-folding times (the time taken for the mass to reduce to e^{-1} of its initial value) of 30–40 days for the 1991 eruption of Pinatubo where material was placed around 20–25 km (Bluth et al. 1997). More recent analysis of both TOMS and TOVS SO_2 measurements for the Pinatubo eruption by Guo et al. (2004) provide estimates of 25 ± 5 and 23 ± 5 days respectively. In the troposphere oxidation rates of SO_2 increase due to relatively high temperature and abundance of reactants and additionally aqueous phase reactions. Typical rates range from 10 % per hour for daytime summer and 0.01 % per hour for winter (Sigurdsson & Laj 1992). More recently the combined use of satellites, chemistry transport models and trajectory anaylsis have enabled the motion of SO_2 in recent volcanic plumes to be comprehensively studied (Krotkov et al. (2010), Kristiansen et al. (2010) and others).

1.3 Estimates of volcanic sulphur emissions

One of the principal uncertainties in the understanding of how historical volcanism has affected the climate is the emission record of volcanic SO_2. If the SO_2 emission were precisely known, a simulation of the climate change following an eruption might be flawed in other ways, but it would be vastly improved and certainly less speculative. Evidence of historical volcanic activity comes from ice core samples, tephra deposition analysis and more recently, atmospheric optical depth measurements and satellite observations.

1.3.1 Volcanic signals in ice cores

If the volcanic source is local, then the presence of ash or tephra may be retained in ice cores, but for global indicators evidence of the sulphate aerosol is used. The volcanic sulphate recorded within ice cores can provide an annual to decadal record of atmospheric state from snowfall for up to thousands of years. However, the potential for pollution of the sulphate signature from other sources is substantial, particularly in the Northern Hemisphere from the intermittent effusions of Icelandic volcanism and from marine sulphate. These can distort the record of explosive eruptions that have global effects by appearing in the ice core record as very large eruptive events, when in fact they were small, regionally local and perhaps persisted for far longer timescales than an explosive eruption would. Even after efforts to correct for these, event strength requires calibration against a well known eruption for a process that may not be entirely linear. In the case of the 1883 Krakatau eruption particularly, its climatological effects do not agree well with the estimated mass of SO_2 thought to have been released (Shine & Highwood 2002), and yet it has been used as an ice core reference eruption (Hyde & Crowley 2000, Lamb 1977, Sato et al. 1993). This eruption has been recently revised down in terms of scale in a more recent historical volcanic optical depth database (Hansen et al. 2005). Air-snow transfer functions which relate the contents of the ice cores to the atmospheric state at the time of deposition are parameterisations, qualified only for intercomparision with contemporary atmospheric analysis. The spatial variability of deposition is a problem that even present day efforts are challenged by. The accumulation of snow at the poles is a complex process (Marshall et al. 1998). Dominated by the precipitation term (particularly in coastal regions where accumulation is highest), it is also affected by blowing snow events that re-distribute the accumulation (Miles et al. 2008). Also, some understanding of the local topography and prevailing winds can aid determination of the suitability of a site for taking an ice core, in deference to how well it represents the surrounding area. The concentration of some species within ice cores can vary by more than 50 % over distances of a few hundred metres. For more recent ice core samples, where there is better temporal resolution but frequently more noise, previous work by the author (unpublished) demonstrated that firn cores taken just 1.5 m apart can differ in chemistry to an extent that they are completely uncorrelated, although over time trends become more evident within an ice core. At 14 million square kilometres Antarctica presents a substantial sampling problem.

Ice core sampling can only in the first instance represent atmospheric deposition at the poles. There is therefore a problem of associating the strength of a volcanic signal with the latitude at which the eruption took place, and how representative this might be of the contemporary global distribution of sulphate aerosol. Simultaneous use of ice core samples from both poles would be an optimal way of estimating the strength of a global eruption, upon further calibration with well-characterised eruptive events. However, inter-comparison of independent ice-cores can present additional calibration problems to be overcome (Cole-Dai et al. 1997). The extent to which the measurements represent the constituent concentrations of the global atmosphere at the time of deposition is open to interpretation, although in a semi-quantitative way, ice cores are self-consistent indicators as to the periodicity of large volcanic eruptions in the past. Crowley (2004) argued that the historical frequency of eruptions emitting less than 3 Mt is indiscernible, since it is unlikely that their signal can be accurately detected in ice cores samples above noise, yet eruptions of this size are represented in ice core eruption records. A fair approximation of the eruptive frequencies for small eruptions is available by the use of satellite observations over the past 30 years. The extent to which this period may be a statistically significant representation of earlier periods of volcanism is open to question, but it is the most accurate record.

1.3.2 Tephra analysis

Tephra, or ‘fallout’ sediment analysis, can provide an estimate of the explosiveness of a known eruption event. It is however not obviously related to the amount of SO_2 emitted by the eruption. The Volcanic Explosivity Index (VEI) was derived to catalogue the explosive magnitude of historical eruptions, based on the order of magnitude of erupted mass, and gives a general indication as to the height the eruptive column reached (Newhall & Self 1982). The VEI itself is inadequate for describing the atmospheric effects of volcanic eruptions. This is clearly demonstrated by two eruptions, Agung (1963) and El Chichón (1982). Their VEI classification separates them by an order of magnitude in explosivity although the volume of SO_2 released into the stratosphere by each was measured to be broadly similar, as shown by the optical depth data for the two eruptions (Sato et al. 1993). For modern volcanism, SO_2 emission can be estimated using geological analysis including the 'petrologic method'. This involves the comparison of gas inclusions formed within the magma chamber (under pre-eruptive conditions) and erupted inclusions. It has been found that this technique can significantly underestimate the SO_2 emission when compared to satellite estimates (Self & King 1996, Westrich & Gerlach 1992). Many of the proposed mechanisms behind this disparity (such as SO_2 'bubbles' in the pre-erupted magma) rely on models of the mechanisms thought to occur within and beneath the volcano (Wallace 2001). The refinement of this technique remains an ongoing challenge for the geological community. Satellite measurements themselves, by far the most accurate of such methods, deliver mass estimates with up to 30 % uncertainty (Krueger et al. 1995), and good records only exist for the last 30 years.

1.3.3 Eruption frequency

The second data component needed for a study of the climatic effects of volcanism (in addition to strength) is information about the frequency of past volcanism. The data available have significant shortcomings and are generally incomplete (Newhall & Self 1982). The decadal rate of all eruptions recorded in ice cores has remained approximately uniform for the last 1000 years (Zielinski et al. 1994). The eruptive frequency data from other sources (for the past 500 years) show a marked increase in eruptive rate as they approach the present, especially with the advent of satellite observations which were able to catalogue smaller eruptions globally (Bluth et al. 1997, Newhall & Self 1982, Sato et al. 1993). The frequency of eruptions for the period 0–999 AD is much less than for the period 1000–2000 AD. It is unclear whether this is an actual lull in volcanism or that the record has failed to capture or preserve the events, although the latter is more likely. As such, eruptive frequency estimates can depend on the size of eruption, the period of time considered and the type of measurement technique. Extensive ice core samples reflect the occurrence of large eruptions, but fail to capture the small ones. Conversely, recent short-term observations accurately represent small, more frequent eruptions, but the repose times of the larger eruptions are beyond the length of the record.

Pyle et al. (1996) used the generally accepted premise (because the process is rare and randomly occurring), that the occurrence of large eruptions of a given magnitude follows a Poisson distribution for mid to large eruptions. They used satellite observations to model the frequency of the mid-range eruptions (over a 10 year period) and ice core and composite data sets to model larger eruptions with greater repose times. Ice-core sulphate profiles were then used to estimate the stratospheric sulphur flux per year. These and other data analysis techniques can be used to extrapolate as much information as possible from partial data.

It has been demonstrated (Sato et al. 1993, Stothers 1984), that northern and southern hemisphere optical depth perturbations diverge considerably for an eruption away from the tropics, but can be similar for equatorial eruptions. This is because erupted material, upon reaching a great enough height, can spread in the meridional circulation in the stratosphere (Roscoe 2001, WMO 1998). Small eruptions which would reach the stratosphere at high latitudes may not do so in the tropics, where the tropopause is up to 5 km higher. The classification of the explosivity of these boundary region eruptions is poorly defined, as is the degree to which a volcano's elevation may contribute to where it lies on this scale. Halmer (2003) consider the impact of latitude (relative tropopause height) and emission altitude upon the contribution of SO_2 of a particular moderate scale eruption to the stratosphere using a plume model. They found that in simulations, efficacy of stratospheric injection is aided by both altitude and lower tropopause height, concluding that eruptions had to be more powerful in the tropics (with the potential to spread to both hemispheres) to achieve longevity as a result.

1.4 In situ or ground remote sensing of volcanic SO_2 emissions

In situ or ground measurement techniques provide the means to validate measurements of volcanic plumes from space. In the past this has mainly been performed with correlation spectrometry COSPEC: (Casadevall et al. 1983, Stoiber & Jepsen 1973). COSPEC works by measuring light from a plume containing SO_2 and compares the measured spectrum to a reference spectrum. Combined with a measurement of wind speed, this can yield SO_2 flux. Ratios of gases can provide volcanologists with insights about the 'plumbing' of a particular volcano, and indicate the relative oxidation states of gases. For example, the CO_2 to SO_2 ratio can give information about the depth from which magma has arrived, based on the different exsolution temperatures of the two gases. More recently, Galle et al. (2002) introduced a miniature UV spectrometer for the remote sensing of SO_2 in volcanic plumes, called MiniDOAS. It is considered an advance/update to COSPEC, in that it is small, low cost and light weight, and they are intended to be deployed to multiple sites of volcanic interest. Compared directly it yielded comparative fluxes to COSPEC, but offers the advantage of wider sampling of the UV spectrum.

Due to the limited spatial sampling globally and confinement to measurement near the event (or one site in particular in the case of ground based lidar) groundbased SO_2 detection devices are not sufficient on their own for monitoring explosive volcanism.

1.4.1 SO_2 from the Total Ozone Mapping Spectrometer

The remote sensing of SO_2 from space has been performed by a number of instruments since their inception, and some, in the case of Total Ozone Mapping Spectrometer (TOMS), as a happy accident many years after its deployment. Anomalous measurements were observed after the 1982 eruption of El Chichón. It was subsequently realised that the observations were being contaminated by the sulphur dioxide in the erupted plume and could be exploited to calculate a column amount (Krueger 1983). TOMS is a nadir-viewing instrument that measures the radiance reflected from the sunlit Earth. The characteristics of the TOMS instruments are described in Heath et al. (1975) but may be summarised as follows. TOMS is an ultraviolet (UV) spectrophotometer which measures the sunlit earth and also a direct solar spectrum via a diffuser plate. It operates at 6 small wavelength bands (or channels) fixed between 312 and 380 nm that are used in pairs to capture the Huggins bands for ozone (O_3). It has two further channels at longer wavelengths to characterise cloud/surface albedo away from O_3 absorption features. The presence of atmospheric O_3 is derived from the sun normalised radiance (the ratio of spectral reflectivity of the atmosphere or albedo and the radiance of a sunlit diffuser plate calibrated at the associated wavelengths) (Krueger et al. 1995). This is done using carefully selected pairs of wavelengths from the six channels in the ultraviolet spectral region. SO_2 is a stronger absorber of UV light than O_3 at wavelengths less than 320 nm (the two shortest wavelength TOMS channels). The Krueger (1983) algorithm calculates the effective absorption coefficients of SO_2 and O_3, and uses this information to interpret the mass of SO_2 in volcanic plumes. The data can also be used to derive an Aerosol Index, a unitless parameter of the spectral contrast between two channels sensitive to aerosols.

The SO_2 algorithm used by Krueger (1983) was subsequently improved Krueger et al. (1995) and used to estimate the SO_2 emitted from the 1991 Pinatubo eruption. (A similar approach was followed by McPeters (1993) for a variant on the TOMS instrument type called the Solar Backscatter Ultraviolet instrument - SBUV/2 - that was been superseded by TOMS for the purposes of detecting SO_2). The Pinatubo eruption was revisited by the authors more recently (Krueger et al. 2007), following further development of the algorithm which occurs in tandem to algorithm development to more contemporary UV satellites capable of detecting SO_2. TOMS instruments have been deployed on four platforms, principally for continuity in ozone monitoring, particularly in relation to the Southern Hemisphere polar stratospheric ozone loss associated with catalytic destruction by halides. Table 1.1 details the dates for which ozone data are available, and SO_2 products were generated on an off-line basis for volcanic events.

The first SO_2 algorithm developed by Krueger (1983) was termed the

Platform	**Data Available**	**Notes**
Nimbus 7	1979-1993	-
Meteor 3	1991-1994	-
ADEOS	1996-1997	Platform failed after 10 months
Earth Probe	1996-2005	-

Table 1.1: TOMS instruments and data availability

“residual” model, that assumed that changes in the background albedo in the absorbing channels, found by interpolating values surrounding affected pixels, was solely due to the presence of SO_2. This model had limitations, not least because it could not account for the effects of variations in meteorological cloud underlying the plume. A subsequent “linear” model was developed by Kerr et al. (1980) for ground based measurements of ozone and SO_2 with a Brewer spectrophotometer. The Kerr algorithm in turn was developed for use in operational processing by Krueger et al. (1995).

TOMS has some limitations, and much use could be made of a set of observations from a contemporary infrared instrument, both for validation and for extending our understanding of recent atmospheric volcanic SO_2 flux in that period. The High Resolution Infrared Sounder 2 instrument (HIRS/2) is such an instrument, and has been in operation in one form or another in parallel to TOMS (which has been evolved into other instruments). It is discussed in depth in Chapter 4 and its potential for measuring atmospheric SO_2 has only recently been exploited (Kurbatov et al. 2006, Prata et al. 2003). As a predominantly infrared instrument it does not require daylight to make observations, and there is the facility to explore other complementary aspects of the atmosphere that a UV instrument such that TOMS was not designed to measure. The exploitation of HIRS/2 measurements to accurately quantify volcanic SO_2 becomes the predominant subject of this Thesis and as such is discussed later. Its potential usefulness is apparent when one considers that until 1995, TOMS provides the only global satellite volcanic emission detection and monitoring capability since the advent of the satellite era. After 1995, and particularly after the year 2000, many more instruments of different types have been launched with the capability of detecting SO_2. They achieve this with variable precision, sampling and viewing geometry, and are worthy of discussion here briefly to put into context the relative merits of TOMS and HIRS/2 SO_2 products.

1.4.2 Satellite measurements of volcanic SO_2

Campion et al. (2010) (their Appendix A) present a useful table of some of the instruments capable of detecting SO_2 that have been developed in the last 15 years, but it is not complete. These and other instruments that can detect SO_2 are presented and briefly discussed here, although it is worth considering that few volcanic SO_2 satellite products have been extensively validated in the way that a more well mixed or routinely monitored species (such as O_3) has been. This is partly due to the nature of volcanic plumes, in that they can occur sporadically in limited spatial or temporal scales making contemporaneous in-situ measurements very difficult, but also because of the challenges associated with the satellite viewing geometry, which arise because a satellite and a ground based instrument do not measure the same quantity.

In the infrared, there are three principal absorption bands that are used for detection of the gas by remote sensing instruments. These are located within the spectrum around $4.0\,\mu$m ($2500\,\mathrm{cm}^{-1}$), 7.3 μm ($1362\,\mathrm{cm}^{-1}$) and $8.6\,\mu$m ($1152\,\mathrm{cm}^{-1}$). They can be exploited by both broadband radiometers and spectrometers in different ways, and the higher the spectral resolution or number of independent spectral channels the more information that can be obtained. The $8.6\,\mu$m channel is affected by the presence of ash causing an occasional overestimation of SO_2, and numerous attempts have been made to account for this, as described in e.g. T. Yu & Prata (2002), Kearney & Watson (2009) and Corradini et al. (2009).

In the UV, the technique most frequently employed is Differential Optical Absorption Spectroscopy (DOAS) (Siegrist (1994) and others), but it is also used in the near infrared. DOAS is a broad term denoting the fitting of narrow absorption cross sections of a differential spectrum (for example by regression) for gaseous species using transmitted light, after removing polynomials that represent broad scale spectral variation not associated with the desired quantities. The technique is described in detail in Platt & Stutz (2008) and Rozanov & Rozanov (2010). For its application to satellite measurements, typically using measured direct and scattered sunlight, this absorption is converted into a slant column density (SCD) in accordance with the line of sight viewing geometry. The final step is to then to convert this slant column into a vertical column amount. This is most frequently achieved by way of an air mass factor (AMF), although more recently via weighting functions (Buchwitz et al. 2000). Weighting functions are discussed further in Chapters 3 and 4. The AMF or weighting function must take into account (either by explicitly modelling or parameterising) aspects of the radiative transfer (such as scattering) that are responsible for the difference in nadir and slant column observed quantities. They can range in sophistication from the very simple to the highly advanced, taking account of multiple scattering or scene inhomogeneity (Rozanov & Rozanov 2010). The principal advantage of the DOAS technique is that it can be relatively quick compared to other column amount derivation methods, but it can be hampered in terms of accuracy by the many assumptions that are required in modelling the transmission path.

MLS

The Microwave Limb Sounder (MLS) was first launched aboard the Upper Atmosphere Research Satellite (UARS) platform in September 1991, and a subsequent instrument is currently in operation aboard the NASA Aura platform, launched in 2004, with a vertical field-of-view (FOV) of 5 km. Operating in the microwave, MLS is less sensitive to the effects of ice particles and cloud than observations at other wavelengths. MLS measures thermal emission in the limb, and was originally designed to detect damaging chlorine species, ozone and stratospheric water vapour in relation to the catalytic destruction of stratospheric ozone.

Read et al. (1993) published the widely quoted estimate of the SO_2 loading in the stratosphere after the Pinatubo eruption in 1991. Their measurements were compared to observations of the evolving sulphate aerosol by the Stratospheric Aerosol and Gas Experiment (SAGE) II (McCormick & Veiga 1992). Although the instrument was launched three months after the eruption, the plume was of such a magnitude that considerable amounts of SO_2 remained above 20 km. Read et al. (1993) were able to use measurements of the subsequent decay rate of SO_2 to estimate an e-folding time (discussed in chapter 5) of the Pinatubo SO_2, and use this to estimate the original mass erupted, alongside that of TOMS and SBUV. At the time (as TOMS mass estimates have occasionally been revised with subsequent algorithm development) these were 17 Mega tonnes (Mt) (MLS), 20 Mt (TOMS, Bluth et al. (1992)) and 12-15 Mt (SBUV, McPeters (1993)). The unique observation of SO_2 profile in the stratosphere identified three distinct layers, one as high as 31 km in the tropics and two further at 26 km and 21 km. The dynamical mechanisms by which the SO_2 reached 31 km were postulated by Kinne et al. (1992) to have been aided by aerosol heating and diffusion. Below 20 km the errors associated with the SO_2 fit used in Read et al. (1993) begin to increase to the point where the error on individual profiles becomes prohibitive. For the MLS instrument aboard Aura, there is little recorded in the peer-reviewed literature to indicate that SO_2 has been quantitatively assessed by MLS. This may partly be attributed to the fact that MLS makes observations twice daily along its orbit track. This has previously been unsuitable for global monitoring of volcanic SO_2 or the hazards that may arise from volcanic eruptions, since either a high sampling frequency or large spatial sampling are required. However, Read et al. (2009) report observations of several eruptions from MLS, including Kasatochi (2008), including sensitivity to SO_2 in the UTLS region. The future next generation MLS instrument, to be part of the Global Atmospheric Composition Mission (GACM), is expected to have a scanning capability which will greatly increase its observing breadth and sampling frequency.

GOME and GOME-2

The Global Ozone Monitoring Experiment (GOME) was launched in 1995 aboard ESA's ERS-1 platform. A polar orbiting, nadir-viewing UV-Vis spectrometer, it owed much of its heritage to TOMS. Designed to continue the monitoring of the stratospheric ozone hole recovery, GOME O_3 profiles were of sufficient quality to be used in ECMWF re-analysis products, and GOME was the first to be able to demonstrate skill in directly quantifying tropospheric ozone (Munro et al. 1998). As with TOMS, the accurate fitting of O_3 and SO_2 each require the other due to their coincident spectral bands. Eisinger & Burrows (1998) reported the first SO_2 columns from GOME, with an estimated lower detection limit of 0.4 DU (10 × less than that for TOMS) under clear sky conditions and a low solar zenith angle (SZA). This equated to 150 tonnes within a GOME pixel. The conversion factor from slant column to vertical column density used in this study introduced an error of up to 20 %. Whilst GOME had a lower spatial resolution (320 km × 40 km) than TOMS, it had a significantly higher spectral resolution and spectral coverage.

Khokhar et al. (2005) presented observations of volcanic SO_2 from GOME for the period 1996–2002, detailing 20 major eruptions, and also discussed the ability of GOME to detect SO_2 of anthropogenic origin. They note that on occasion, GOME observes volcanic enhancements that TOMS does not, and that most TOMS observations are systematically larger than the GOME slant column densities. The latter is attributed to the relative pixels sizes. It is worth noting that one limitation, when examining degassing of small regional eruptive activity, is that on occasion more than one possible emission source can be located in the GOME pixel. This makes absolute emission point difficult to determine. The 'missing' TOMS eruptions cannot entirely be explained by data gaps, particularly when the global coverage by TOMS was achieved in 1 day whereas for GOME it was 3. Instead, it is attributed to the increased spectral resolution of GOME implying a higher sensitivity, particularly under some atmospheric conditions. Khokhar et al. (2005) further suggest coincident results from another instrument, AIRS (Carn et al. 2005) (to be discussed later), agree closely with GOME for an eruption by Etna in Italy in 2002.

Khokhar et al. (2005) discuss the difficulties of using DOAS in this part of the spectrum. These mainly relate to the dependence upon good estimates of O_3 in the scene because of interference of the strong Huggins bands with the weak SO_2 bands. Additionally there are the instrument effects, such as degradation, artifacts on the diffuser plate (which particularly affect UV spectrometers) and deficiencies in the slit function characterisation. These all contribute to inaccuracies in the AMF used to convert the SCD into a vertical column density, which can result in solar zenith angle and seasonally dependence in the absorption of O_3 and require the application of empirical correction factors. Khokhar et al. (2005) for example note that without such corrections, spuriously high SO_2 is detected above high or bright surfaces, which is particularly attributed to incomplete correction of the Ring effect (in-filling of Fraunhofer lines by Raman scattering in the atmosphere, which is often paramaterised rather than explicitly modelled or retrieved).

The follow-on instrument to GOME was launched in 2006 aboard ESA's MetOp-A platform. Not only is the total swath of GOME-2 twice that of GOME, but in the spectral region of interest for SO_2 (315–326 nm in Band 2), there are 24 across track pixels (40 km × 80 km) without significant sacrifice in signal to noise. The operational GOME-2 SO_2 column product is described in DLR (2010), and its application with relation to identifying emission sources is described in Rix et al. (2009). The authors routinely apply trajectory matching and use forecast models to predict the motion of volcanic SO_2 plumes. The sensitivity of GOME-2 allows detection of SO_2 in the boundary layer providing routine monitoring of strong anthropogenic emission sources. While the traditional DOAS approach has been used widely, Nowlan et al. (2011) present an optimal estimation (OE) approach for GOME-2 by applying a scheme originally developed for GOME and OMI ozone profile retrieval. An OE approach is designed to make the best use of all available information simultaneously, and therefore does not require the two step approach of DOAS. Furthermore its methodology provides an *a posteriori* estimate of uncertainty. In the case of volcanic SO_2, it also allows the height of the SO_2 to be estimated as part of the retrieval from spectral measurements. This is a significant departure from both the lower spectral resolution instruments and the traditional DOAS approach (although more advanced methodologies exist), as information external to the instrument is commonly required to accurately predict SO_2 concentration. This can include measurements made by lidar, from aircraft and use of trajectory analysis. Nowlan et al. (2011) suggest accuracies in the region of a couple of kilometers depending upon atmospheric conditions. Rix et al. (2011) also report an OE approach to detecting SO_2 with GOME-2, and compare it to that computed using AMFs defined for a plume at 3 separate heights from which the most relevant is selected. Both Nowlan et al. (2011) and Rix et al. (2011) report that for volcanic plumes the OE approach yields a higher estimate of SO_2 as compared to DOAS. Whilst the plume height retrieval has only been applied to a limited number of volcanic events, in both cases increased uncertainty is introduced to the retrieved SO_2 due to the prior error on the plume height and shape, but it does provide a method of plume height estimation internal to the instrument and consistent with the measurements. It is reasonable to conclude from this early work that a DOAS approach is faster, OE provides an opportunity to maximise the use of spectral information in the measurements and measurement error; however both methods are still subject to uncertainties in the assumed profile shape.

ASTER

The Advanced Spaceborne Thermal Emission and Reflection Radiometer (ASTER) launched aboard EOS Terra in 1999 has three channels coincident with the SO_2 feature around $8.6\,\mu$m. A full instrument description is given in Yamaguchi et al. (1998), Pugnagni et al. (2006) and others. Although the capability of ASTER to detect SO_2 was anticipated before its launch, primarily due to it having a similar channel response to the aircraft-based TIMS instrument (Realmuto et al. 1994), Pieri & Abrams (2004) introduced the value of ASTER as a tool for identifying volcanic SO_2 plumes. The principal benefit of ASTER for SO_2 is its very high spatial resolution of 90 m. Its channels are grouped into wavelength sections (visible/near IR, shortwave IR, thermal IR), each with slightly different spatial resolutions. Of the 3 bands utilised around $8.6\,\mu$m, two have a spatial resolution of 30 m and 1 of 90. Typically the pixels of the first two are co-added, to either improve signal to noise and/or combine information with the third channel appropriately.

ASTER has programmable acquisition, with a nominal repeat cycle of 16 days and a swath of 60 km. This can imply a sampling rate for a given latitude of between 4 and 7 days (Campion et al. 2010). Furthermore, the presence of cloud can reduce sensitivity to SO_2 (although the smaller footprint makes it more likely to see through cloud). As such, ASTER is not ideally suited for global monitoring of volcanic SO_2, but for encounters coincident with volcanic activity its spatial resolution is second to none at present. Having 3 bands sensitive to an SO_2 absorption feature, Campion et al. (2010) have shown that it can be exploited to use these in a way that is relatively insensitive to tropospheric water vapour, and can potentially have sensitivity to the near surface depending upon the thermal contrast in a scene. They present a method of ratioing the three channels to desensitise the SO_2 fit not only to humidity but to aspects of temperature and emissivity, relative to the discussion of outcomes of the more direct method developed by Pugnagni et al. (2006).

The method developed by Campion et al. (2010) has a relatively high detection limit of circa 20 DU (R. Campion, Pers. Comm., 2011), but this is of significantly less importance given its very high spatial resolution. Satellites such as GOME-2 or even OMI (discussed later in this chapter), effectively see a diluted picture of an SO_2 plume occurring within the pixel if its spatial scales are smaller than the pixel dimensions. ASTER is perhaps best suited to detecting small plumes such as those associated with quiescent volcanism, the spatial variability of which is significantly closer to the sensor footprint size. Indeed, the small spatial resolution can present problems for direct comparisons with other satellites, and as suggested by R. Champion (Pers. Comm., 2011) this is better undertaken in the unit of SO_2 flux, not least because this is a more pertinent measure for monitoring passive degassing volcanoes than instantaneous mass.

MODIS

The Moderate Resolution Infrared Spectrometer is currently deployed aboard the NASA platforms Terra and Aqua, first launched on the former in December 1999. It has 36 spectral bands (between 0.4 and 14.4 μm) with a spatial resolution that varies between 250 and 1000 m depending on wavelength, and a swath of 2330 km. Imaging the total Earth every 1-2 days, the instrument was designed to yield a greater understanding of global dynamic, land, sea and atmospheric processes. Watson et al. (2004) took retrieval algorithms for sulphate, ash and SO_2 that were developed for other instruments that have some measurement commonality with MODIS, including the Advanced Very High Resolution Radiometer (AVHRR), Geostationary Operational Environmental Satellite(GOES) and TIMS. This is a principal advantage, as with such a broad spectral range, MODIS allows joint monitoring of sulphate aerosol, ash and SO_2, enabling estimation of the SO_2 loss rates and aerosol evolution in the same field of view. Watson et al. (2004) compare to TOMS SO_2 some examples of MODIS SO_2 from 7.3 and 8.6 μm spectral fits (the algorithms differ slightly due to the contrasting radiative transfer requirements for the two bands). While spatially their resolutions differ by 1500 times in terms of footprint (TOMS being the poorer), for the eruption examples given they both capture the plume in a similar way. The mass estimates commonly differ. The 7.3 μm fit often predicts an underestimate, explained by the fact that the plume's altitude is either partially beneath the penetration depth at that frequency, or high water vapour masks its signal. The fit at 8.6 μm on occasion produces a (sometimes considerable) over-estimate, which Watson et al. (2004) attribute to the interference from ash. For such low-altitude plumes in the examples given, TOMS is expected to give the more realistic estimate of SO_2, but the potential for MODIS SO_2 detection is evident, particularly when the respective algorithms were developed to look at high, significant SO_2 plumes (7.3 μm) and passive degassing (8.6 μm). They do however remark that the volcanic species (SO_2, sulphate, ash, volcanic ice and water vapour) commonly interfere with each other. This suggests that a global or joint retrieval approach could be more appropriate, but that the nature of the volcanism must still be considered for an optimal scheme (passive degassing or explosive).

SCIAMACHY

Aboard the European Space Agency (ESA) platform Envisat (launched in 2002), SCIAMACHY is a UV/visible instrument that measures sunlight reflected and scattered through the Earth's atmosphere (Bovensmann et al.

(1999), Gottwald et al. (2006)), and continued to provide data until 2011. The nadir footprint size is 30 × 30 km at its minimum, but varies with wavelength and solar elevation. The instrument has many similarities to GOME in terms of its spectral coverage, allowing previously tested SO_2 derivation from its measurements, such as the DOAS approach described in Eisinger & Burrows (1998) and others.

Lee et al. (2008) presented a weighting function DOAS (WF-DOAS) methodology applied to SCIAMACHY SO_2 retrievals. WF-DOAS is able to account for the sensitivity of the DOAS fit dependent variables upon scene specific variables. This means, for example, that the ring fitting component is calculated as a function of SZA, total column ozone, albedo and surface pressure. This effectively reduces the potential for spurious bias discussed earlier that the conventional approach can yield, and attempts to correct for it in a physical way.

SCIAMACHY has both limb and nadir viewing capability, designed for the sampling of the same 'air' at only slightly temporally removed instances along the orbital track. This combined view yields tropospheric column abundances by differencing the columns derived from each viewing mode, since the limb view cannot view down into the troposphere fully because of cloud. The principal disadvantage of this geometry is that the alternating function causes frequent periodic interruptions in the along track nadir sampling. A consequence of this for large volcanic plumes is that the likelihood of under-sampling the plume is increased. For anthropogenic or continuously degassing sources, temporal averaging combined with the high spectral sensitivity is sufficient to characterise highly localised sources.

AIRS

The Atmospheric Infrared Sounder (AIRS) instrument was launched in 2002 aboard the NASA Aqua platform. AIRS has a ground footprint ranging from 15 × 15 km at nadir to 18 × 40 km at the edge of the 1690 km swath. A grating spectrometer, AIRS has a high spectral resolution of 2378 channels between 650 and 2700 cm^{-1} (15.4 – 3.7 μm) (Chahine et al. 2006). Spectral data used for trace gas retrieval are sub-selected by removal of noisy channels and optimising channel selection for desired species. Carn et al. (2005) presented an SO_2 and ash retrieval scheme for AIRS applied to measurements during an eruptive phase of Mt Etna in 2002, detecting tropospheric SO_2. Their model used the radiative transfer scheme SARTA (Stand-alone AIRS Radiative Transfer Algorithm) by Strow et al. (2003). Prior knowledge of plume height is in the form of an ash/SO_2 altitude from the Toulouse Volcanic Ash Advisory Centre (VAAC). This information was used to simulate a 2 km thick profile shape in simulations that was scaled iteratively to achieve a fit with the measurements. Carn et al. (2005) "tentatively estimate" the minimum detection limit to be 3 DU in cloud free scenes, with a retrieval error of 20 % (not related to assumptions about the altitude of the plume). Using mid infrared information about SO_2, this spectral region has limited sensitivity to the lowest altitudes and depending upon the height or vertical distribution of an SO_2 plume this may result in an underestimate in column amount by AIRS. Also, like many other infrared instruments it cannot 'see' through ash. Carn et al. (2005) note that AIRS compares "favorably" with COSPEC measurements, but describe how further assumptions are required to directly compare COSPEC flux measurements with a nadir plume mass estimate. Furthermore the nature of the COSPEC measurement cannot account for variability due to local loss mechanisms or inhomogeneous dispersion.

Prata & Bernado (2007) present an alternative AIRS SO_2/ash algorithm comprising two parts. The first pre-selects pixels which are likely to contain SO_2, before using a least squares fit to retrieve a forward modelled spectral match to the measurements. The amount of spectral information that AIRS provides can also potentially yield some indication of SO_2 altitude. The results presented by Prata & Bernado (2007) are compared with some other instrument observations (TOMS and GOME) for a sample of volcanic eruption plumes. Despite differing observation times and spatial sampling, the agreement shown is relatively good, but day/event specific agreement is variable due to the changeable states of measurement (overpass time, plume and spatial sampling, vertical sensitivity). Prata & Bernado (2007) offer a quantified accuracy of 3 - 6 DU, depending upon atmospheric factors. They usefully note that the perceived disadvantage of IR sensors (such as AIRS, MODIS and HIRS) an inability to discern SO_2 in the boundary layer, can be useful in distinguishing SO_2 that might play a significant role in climatically perturbing the atmosphere.

Prata et al. (2010) add an AIRS SO_2 fit at $4.0\,\mu$m, in a study of the SO_2 and ash from the 2008 eruptions of Kasatochi and Okmok. They note that with less interference from water vapour and sensitivity at a lower altitude the detection of SO_2 in the lower atmosphere is favourable despite this being a weaker SO_2 band. The fit is achieved using the correlation of a synthetic (line-by-line generated) spectrum and the measurement, accepting that in this spectral region particularly accurate representations of the line features are necessary to limit errors, and that the contributions of a solar term in the radiative transfer may have to be considered. Analysis of the signal to noise for SO_2 at a range of altitudes indicates that above 500 hPa (in the atmospheric example given) there is little sensitivity to SO_2 in this spectral region, but notably this band does not saturate at as low a limit as the $7.3\,\mu$m band for AIRS. Principally, Prata et al. (2010) demonstrate that the two bands give information about SO_2 at two different altitudes. Adding to this the capability of the instrument to detect ash properties, AIRS can be considered very useful for understanding the evolution of a volcanic plume. An Algorithm Theoretical Basis Document (ATBD) for SO_2 detection with AIRS and other instruments is given in Prata & Corradini (2009).

TES

The Tropospheric Emission Spectrometer (TES) was launched in 2004 aboard the NASA Aura platform. TES is a Fourier transform spectrometer (FTS) designed to monitor tropospheric ozone and CO, with both limb and nadir viewing capability. It has a high spectral resolution of $0.1\,\mathrm{cm}^{-1}$ (apodised) in four bands in the infrared. Its detector is a 1 by 16 array, which translates to an array consisting of footprints of 0.5 km along track and 5 km across track in nadir view, and in the limb 2.3 km in the vertical by 23 km in the horizontal at the tangent point around 3100 km away. Operationally it provides temperature, H_2O, CO, O_3 profiles optimised for the troposphere and lower stratosphere, although for some species there is little sensitivity to the boundary layer, and in the limb the lower troposphere can be obscured by cloud. TES has a relatively low spatial sampling rate due to its small footprint. For species with small column concentrations it may be necessary to use an average of the 16 pixels to improve signal to noise. Corradini et al. (2006) conducted a feasibility study to discern whether or not there would be sufficient information content for detecting SO_2 with TES. They found that for a modelled column of 100 DU, there was just 0.3 degrees of freedom for signal (DFS) for SO_2 (see Chapter 3). They suggested that a singular vector decomposition of the spectra could be used to effectively remove extraneous instrument noise, and for the case given this increased the DFS to 3. Clerbaux et al. (2008) provided the first retrievals of SO_2 using TES measurements, using a line by line radiative transfer model called Atmosphit (Coheur et al. (2005), Clerbaux et al. (2005)) and optimal estimation. On comparison with OMI (to be discussed later in this chapter), they found good agreement for eruptions where the SO_2 reaches the UTLS or lower stratosphere. Poorer agreement is found when part of the SO_2 column lies lower in the atmosphere where TES has little or no sensitivity. A further reason cited is the 'dilution' effect of OMI due to its greater footprint compared to TES. High altitude plumes produce "narrower and stronger lines" (Clerbaux et al. 2008), but line widths can be used to discriminate between high and low altitude SO_2, resulting in an approximate 4–6 km height resolution in the nadir. Due to its low rate of sampling and small pixel size, TES is less well suited for monitoring volcanic SO_2 plumes, although the high spectral resolution is an advantage.

SEVIRI

The Spinning Enhanced Visible and Infrared Imager (SEVIRI) is a scanning radiometer with 12 channels ranging through the visible, NIR to IR. Aboard Meteosat Second Generation (MSG), a geostationary platform launched in 2005, SEVIRI offers near complete view of the Earth's disk (centred at 0°N,0°W) every 15 minutes, at a ground resolution of 1–3 km at nadir. This is of principal value for continuous monitoring of a volcanic plume (in the hemisphere) above polar orbiters. Prata & Kerkmann (2007) and Thomas & Prata (2011) show examples of simultaneous detection and monitoring of ash and SO_2, another advantageous capability of SEVIRI. Prata & Kerkmann (2007) describe the methodology used, and estimate column errors of $\pm$ 10 DU, which they equate to a mass loading error of $\pm$ 0.01 Tg. Both the 6.8 and 7.3 μm channels can be used to obtain information from slightly different altitudes in deference to their relative sensitivities.

IASI

The Infrared Atmospheric Sounding Interferometer (IASI) is a relatively new class of instrument (although similar in some ways to AIRS), with sufficient spectral width and resolution, measurement rate and coverage, that even 5 years after its launch applications are being found for the data being produced. Launched aboard MetOp-A in late 2006, it is further set to fly on future MetOp platforms in its current form and even in an advanced form still under development, ensuring continuity of measurements for at least the next 15 years. The spectral resolution varies between 0.35 and 0.5 cm^{-1} depending upon wavelength. The approach followed by Karagulian et al. (2010) allows the opportunity for a single instrument to be used to characterise a volcanic plume in terms of ash, sulphate aerosol and SO_2. They used the broad band feature at 1072-1215 cm^{-1} associated with aerosol, where extinction can be used to match the spectrum to either ash or sulphate aerosol in the more mature plume, and Karagulian et al. (2010) credit themselves with "the first spectral detection of H_2SO_4 from nadir radiance measurements". The multispectral data and optimal estimation approach allows for retrieving SO_2 height or profile to an accuracy of $\pm$ 4 km. It also allows the use of multiple SO_2 bands, some of which are preferable above others in certain atmospheric conditions or SO_2 loading amounts. For the volcanic eruptions used in their examples, Karagulian et al. (2010) used the 7.3 μm and for the first time with IASI the ν_1+ν_3 band at around 4 μm (2500 cm^{-1}).

OMI

The Ozone Monitoring Instrument (OMI) is a nadir viewing imaging spectrometer, launched aboard NASA's Aura platform in 2006 (Levelt et al. 2006). The instrument comprises two grating spectrometers with CCD detectors that provide comparatively enhanced spatial sampling. It was designed to provide continuity to the TOMS total ozone record, and can distinguish between aerosol types and meteorological cloud. OMI has significantly more spectral information than TOMS and a smaller ground footprint (13×25 km at nadir) than both GOME and GOME-2.

Krotkov et al. (2010) and Yang et al. (2007) both suggest an SO_2 noise for OMI in the UTLS of $\sim$0.3 DU, which is 1 standard deviation (SD) of the background retrieved SO_2 where none is expected, but Krotkov et al. (2008) states that this is only achieved after an amount of spatial averaging. On a pixel by pixel basis the value is stated as circa 1.5 DU for SO_2 located in the planetary boundary layer. For the lower limit, Krotkov et al. (2010) defines a detection limit based on 5 neighbouring pixels with SO_2 concentrations greater than 5 SD, that equates to 30–50 tonnes. This is quoted to be 200 times smaller than the TOMS equivalent, 20-30 times smaller than GOME-2 and 10 times smaller than SCIAMACHY.

OMI represents a significant advance on previous UV satellites able to measure SO_2, principally because of its small ground footprint and wide swath. This, combined with the low altitude sensitivity of OMI, allows for the first time the passive degassing of volcanoes to be globally monitored. This provides an opportunity to examine the emission inventories assembled for use in tropospheric modelling, such as Stoiber et al. (1986) or Andres & Kasgnoc (1998).

Yang et al. (2007) developed a linear fit (LF) algorithm and a residual removing system that are both general and can be applied to previous UV instruments. Although the spectral resolution of OMI is significantly higher than TOMS, the LF algorithm uses specific and discrete wavelengths and as such is compatible. Yang et al. (2007) compare the LF algorithm to the OMI SO_2 derived using the Band Residual Difference algorithm (Bhartia & Wellemeyer

2002, Krotkov et al. 2006, 2008). They demonstrate significant improvement for high SO_2 atmospheric loadings. They do state however that for very high volcanic eruption SO_2 concentrations, off-line iterative techniques are required to obtain accurate estimates from measurements.

OMI SO_2 estimates have been partially validated with in situ measurements by Spinei et al. (2010) and Krotkov et al. (2008), which found good agreement. OMI has also been used extensively in satellite SO_2 inter-comparisons.

Future instruments for volcanic SO_2

In addition to the continued deployment of both an IASI-type instrument and that of HIRS in the MetOp series, future instruments that will contribute to the monitoring of global SO_2 in the atmosphere are NPP-OMPS, an ozone mapper and profiler suite launched in October 2011 and TROPOMI, aboard the Sentinel 5 Precursor platform scheduled for launch in 2014. In particular, TROPOMI will offer increased spectral and spatial resolution compared to previous UV instruments.

Use of trajectory models

For some eruption satellite case studies where the SO_2 detection method benefits from some knowledge about the plume height, trajectory or chemistry transport models (CTM) are used to provide an estimate in the absence of any in situ or prior information (eg. Doiron et al. (1991), Kristiansen et al. (2010), Krotkov et al. (2010), Thomas et al. (2005)). Both forward and backwards trajectory models, driven by forecast/re-analysis winds can be used, where air parcels are initialiased at a particular location (at vent or downstream) at a variety of height levels. Once the trajectory model has been run, the parcel or tracer location is compared with the plume location observed by the satellite. The height region that results in the best agreement is an indication of the emission height. This can be particularly useful for establishing whether or not a given plume has penetrated the stratosphere, an important distinction in terms of establishing the potential climate impact of a volcanic eruption.

Combined or compared instrument approaches to remote sensing of volcanic SO_2

In the last decade the number of instruments capable of detecting volcanic SO_2 has increased considerably, and it is apparent that each offers measurements that have both advantages and disadvantages when compared amongst each other. For example, UV instruments commonly offer increased sensitivity to the boundary layer when compared to most infrared instruments, but IR sensors do not require sunlight to make observations and so can sample more frequently. Spectrometers such as TES provide very high resolution data but the satellite footprint in the nadir is so small it cannot be used for routine monitoring of volcanic SO_2. Limb sounders such as MLS can provide measurements with very good height resolution in the stratosphere but in the microwave the errors below about 20km can become prohibitively large for SO_2 (Read et al. 1993), and in the infrared (e.g. TES) measurements in the troposphere become increasingly hampered by the presence of cloud. These relative attributes are the case for most trace gases, and for full monitoring of variability it is increasingly the trend to take a synergistic approach, to combine measurements from different sensors in a way as to optimally exploit their collective information. This can be attempted by a direct combination of the measurements, especially useful if the instruments happen to be on the same platform, with appropriate forward modelling (discussed in Chapter 3) and provided the measurements are spectrally consistent. Alternatively, the measurements from a limb sounder may be used as a prior for a retrieval with a nadir viewing instrument that is less sensitive to the stratosphere. Finally, measurements from diverse sensors can be looked at comparatively in order to observe an eruption from all possible angles of observation, with consideration for the different characteristics and accuracies of the instruments involved, which has been the approach traditionally followed.

Thomas et al. (2009) present a multi-sensor comparison of the 2005 eruption of Sierra Negra (Galapagos Islands) in 2005, using concomitant observations by TOMS, OMI and MODIS. Due to the differing spatial sampling, the MODIS data are re-sampled at the resolution of the UV instruments. They found a wide estimate of total mass tonnage from the three instruments, ranging from 60 kT to 1800 kT. They cite contributing error sources to be plume altitude estimate and relative over-pass times, but were also contributed to by how each sensor is affected by other volcanic species and individual instrument error.

The principle of combining measurements from multiple sensors becomes increasingly relevant for detecting ash and SO_2 for the purposes of mitigating hazard to aviation (Carn et al. 2009, Prata 2009). In addition to making use of atmospheric chemistry transport or trajectory models to improve their estimate of plume height, in the case of aviation hazard mitigation forecast and assimilation models may also become involved. The work presented in Thomas et al. (2009) and elsewhere highlights the range of difficulties that arise from attempts to directly compare SO_2 measurements from different satellites. There remains no suitable comparative basis that can be applied to all eruptions, atmospheric conditions or instrument types, and thus far only side-by-side comparisons have generally been performed for a given event in order to establish the relevant merits or short-comings of an individual instrument.

1.5 Outline of thesis

This work is intended to demonstrate the importance of accurate measurements of volcanically emitted SO_2, in terms of a stratospheric aerosol precursor. Stratospheric aerosols that evolve after large volcanic eruptions affect the atmosphere in many ways, but from a climatological perspective their potential radiative forcing is of principal interest. Chapter 2 discusses how to determine whether or not a volcanically erupted SO_2 event can be considered climatically significant, by means of developing a box model that relates erupted SO_2 mass to a change in global average surface temperature, by way of stratospheric aerosol evolution and radiative forcing as a function of time. It uses a selection of the largest volcanic eruptions that occurred at the end of the 20^{th} century for comparison to the model results. It concludes that there is a strong dependence upon an accurate knowledge of the amount of SO_2 that reaches the stratosphere for assessing its atmospheric impact. Chapter 3 introduces the theory required to develop a method by which a new stratospheric SO_2

emission dataset can be derived by applying ‘inverse methods’ to the HIRS/2 satellite measurements. This will demonstrate that not only can volcanic SO_2 be retrieved from these measurements, and discusses the particular attributes relevant to the instrument and trace gas species, but also explains how an estimate of their accuracy can be obtained by applying such methods. Chapter 4 details how this method was developed and specifically applied, and the practical steps that were required in order to produce optimal results, including results from retrieval simulations. Chapter 5 presents a case study for a particular volcanic eruption, that of Cerro Hudson located in Southern Chile, which erupted explosively in August 1991. The eruption is described in detail, followed by some of the further development of the retrieval scheme that was required when applied to real data. The results for the eruption are presented, and compared quantitatively to a more simplistic measurement ‘fit’ method developed by Prata et al. (2003) and others, that has shown promise for estimating SO_2 with HIRS/2 but has some limitations. It is compared qualitatively to retrievals of the erupted SO_2 previously reported for the TOMS instrument. This work will conclude that quantitative retrievals of SO_2 using the HIRS/2 instrument may indeed provide an accurate, long-term dataset that could have use in terms of an accurate measure of stratospheric aerosol precursor, and the radiative forcing record which that implies, spanning many decades.

Chapter 2

Modelling the Climatic Significance of Volcanic Eruptions

Increasingly GCMs are being used to model the effects of eruptions. However with the large shortcomings in the available data of the frequency and magnitude of historical volcanism already discussed, models of these events are limited to the extent to which they can be validated with observations of the real atmosphere. Particularly, attribution of global temperature change to one event is problematic and the climate response variable. It is therefore reasonable to question whether thorough and complex models can be any more accurate at representing historical volcanism than a simple physical model designed to capture gross characteristics of past global atmospheric eruptive effects, with a consistent level of sophistication throughout each stage. The first section of this chapter describes the development of such a model, and its validation then discussed. Then the model is used together with a frequency distribution for eruptions to determine which size is most climatically important. This is followed by a discussion of the results. This work has been published in the Quarterly Journal of the Royal Meteorological Society (Miles et al. 2004).

2.1 Simplified model

Simple models have been used to model parts of the volcanic atmosphere interactions before. Stothers (1984) modelled northern hemisphere visual extinction observations after the 1815 eruption of Tambora to obtain an empirical relationship describing the evolution of the aerosol optical properties. It was of the form, $\Delta m = 3.0t^{0.4}\exp(-1.1t)$, where Δm is a measure of optical depth and t is the time since the eruption in years. In the study by Stothers (1984), only eruption statistics for equatorial events, which are most likely to have global consequences, are considered. This also affords greater simplicity for the model being developed here. This model fit to a few data points allowed the peak stratospheric loading and time evolution of the aerosol to be estimated; however it was eruption specific, with too many degrees of freedom to make it adaptable to other eruptions.

Bluth et al. (1997) used TOMS data to create a potential aerosol loading model, and attempted to reproduce the optical depth time series from Sato et al. (1993). They created a simple box model governed by two rate equations. The first described the rate of formation of H_2SO_4 from the oxidation of SO_2, and the second the rate of aerosol removal. It was found that this model achieved a peak aerosol loading approximately four times faster than the observed aerosol optical depth peaks, and was attributed to a rate-limiting reaction missing from the chemistry of the model. Here, the concept of a simple box model is extended to link an initial eruption of SO_2 to a change in surface temperature. This process can be thought of as comprising five steps. Conceptually, this model would ideally describe the evolution of the atmospheric constituents and their physical properties at uniform points in time and space.

- A mixing ratio of sulphur dioxide is injected into the stratosphere and distributed over time, formally described by $\mathrm{M}_{\mathrm{SO_2}}(t, z, \phi, \theta)$, where t and z represent time and altitude, ϕ and θ horizontal coordinates.
- A mixing ratio of aerosol evolves over time due to the oxidation, condensation and coagulation of SO_2 characterised by $\mathrm{M}_{\mathrm{Aerosol}}(t, z, \theta, \phi, n(r))$, where $n(r)$ is the aerosol size distribution.

- An optical depth perturbation results from the optical properties of aerosol present $\tau(t, \theta,\phi)$.
- A radiative forcing results from the change in optical depth, $\Delta\mathrm{F}(\tau, t, \theta, \phi)$.
- The surface temperature changes as a response to the radiative forcing, $\Delta\mathrm{T}_s(\Delta\mathrm{F},t, \theta, \phi)$. It is important to note that whilst $\Delta\mathrm{F}$ and $\Delta\mathrm{T}_s$ are both functions of θ and ϕ, $\Delta\mathrm{F}$ does not necessarily map to $\Delta\mathrm{T}_s$ geographically.

At present, the available measurements and observations can only validate some of these steps. It is also important that the relative sophistication of each step be limited by the mechanism modelled or validated with the most uncertainty. With regards to the relatively simple parameterisations used here, it is the surface temperature response to a radiative forcing, $\Delta\mathrm{T}_s$, (global by definition) that is most uncertain. Over-sophistication of the physical mechanisms can hide varying degrees of speculation. Furthermore, with this model the gross global effects are captured at a resolution that can be reasonably validated with available optical depth data. As such, a range of assumptions and approximations are required. Firstly, the aerosol precursors are taken to be spread homogeneously in a stratospheric box from the moment of eruption. Such an assumption limits the applications of this model to simulating equatorial eruptions, since their material is most efficiently distributed to both hemispheres (Roscoe 2001, Stothers 1984, Trepte et al. 1993). The total amount of SO_2 injected into the stratosphere is assumed to be directly related to the amount erupted, although this relationship is beyond the scope of the model developed here.

Sulphur evolution is prescribed by steady rate constants in an optimally oxidising stratosphere. The long-wave effects of sulphate aerosols are neglected here as they are thought only to account for 10 % (after Pinatubo) of the magnitude of total volcanic radiative forcing (but opposite sign to short-wave) (Stenchikov et al. 1998). Possible dynamical changes due to long-wave heating in the stratosphere are also neglected here, since the climate model used is based solely on the concept of global energy balance. Optical depth is considered to be independent of the aerosol vertical profile. It is also assumed that the background stratosphere is ‘clean’, i.e. that material integral to the model forms the only aerosol present.

2.1.1 Sulphur dioxide and aerosol evolution

It is proposed that a linear average of the spatial properties of the atmospheric products is a reasonable concept. This means that taking the global mean erupted SO_2 which initially would be concentrated at the source and non-existent elsewhere, is equivalent to modelling the mass spread homogeneously from the moment of eruption. The formation and evolution of sulphate aerosol will be modelled here by three equations. Firstly erupted SO_2 will be oxidised, the gaseous product will then condense into aerosols, and these aerosols will gradually fall out of the stratospheric box. For a given mass of SO_2 released from an explosive volcanic event, spread homogeneously, an appropriate column mass is evolved subject to the following differential equations. For the decay of SO_2 gas in moles, s

$$\frac{ds}{dt} = -as \tag{2.1}$$

with the boundary condition $s(0) = M$, the total mass injected into the stratosphere. a is the rate constant which describes the decay of SO_2 as it is oxidised. The amount of gaseous H_2SO_4, g and liquid $H_2SO_{4(aq)}$, l, is determined from

$$\frac{dg}{dt} = as - bg \tag{2.2}$$

$$\frac{dl}{dt} = bg - cl \tag{2.3}$$

The rate of change of the concentration of gaseous H_2SO_4 (2.2) is controlled by a gain term from the oxidation of SO_2 (as) and a loss as aerosol particles are formed (bg). This formation is taken to occur at a constant rate, b. This intermediate rate constant grossly describes a number of processes that occur for sulphate aerosols to be produced, including nucleation, condensation, and coagulation (Pruppacher & Klett 1997). Equation 2.3 describes the evolution of aerosols as they are formed, and are subsequently lost from the stratosphere by gravitational sedimentation, governed by rate constant c. The solutions are

$$s(t) = Me^{-at} \tag{2.4}$$

$$g(t) = \frac{1.53aM}{b-a}\left(e^{-at} - e^{-bt}\right) \tag{2.5}$$

$$\begin{aligned} l(t) = {} & \frac{2aM}{c-a}\left(e^{-at} - e^{-ct}\right) \pm \frac{a^2 2M}{(c-a)(b-c)}\left(e^{-at} - e^{-ct}\right) \\ & - \frac{2abM}{(b-a)(c-b)}\left(e^{-bt} - e^{-ct}\right) \end{aligned} \tag{2.6}$$

There is a mass factor introduced upon the oxidation of SO_2 to account for the molecular mass increase from 64 to 98(H_2SO_4). The liquid aerosol formed in the model are taken to be composed of 75% H_2SO_4 and 25% H_2O (Hofmann et al. 1992), so the total mass increases by $\frac{4}{3}$ upon the introduction of water to the mass of $H_2SO_{4(l)}$. The initial mass of SO_2 is doubled upon development to mature aerosol, a factor included in the above equations. Thus rate constants a and c have been inferred from satellite measurements. For the eruption of Mt Pinatubo, a was of the order of $\frac{1}{35}$ per day, i.e. it had an e-folding time of 35 days (Rose et al. 2000). The loss of mature aerosol from the stratosphere for this eruption had an e-folding time of 365 days (Lambert et al. 1997). A best fit for Pinatubo was obtained where b took a value of $\frac{1}{100}$. This rate constant is not measured directly in the real atmosphere. The extension of using these rates universally for the size range of eruptions considered here is supported by validation against a number of eruptions of varying strength, including Agung [1963] and El Chichón [1982], as will be presented here.

The individual solutions to these equations are shown in Fig. 2.1 for a 17 Mt Pinatubo-like initial injection of SO_2. When the model aerosol (2.6) is eventually converted to an appropriate optical depth it is found to underestimate the satellite retrieved global average optical depth for all eruptions. The effect is more pronounced with smaller column concentrations. Rather than a deficiency in the optical depth calculation, this is attributed to insufficient aerosol mass being created by the model. It is thought that this may be due in part, to poor representation of the sedimentation process. As shown in

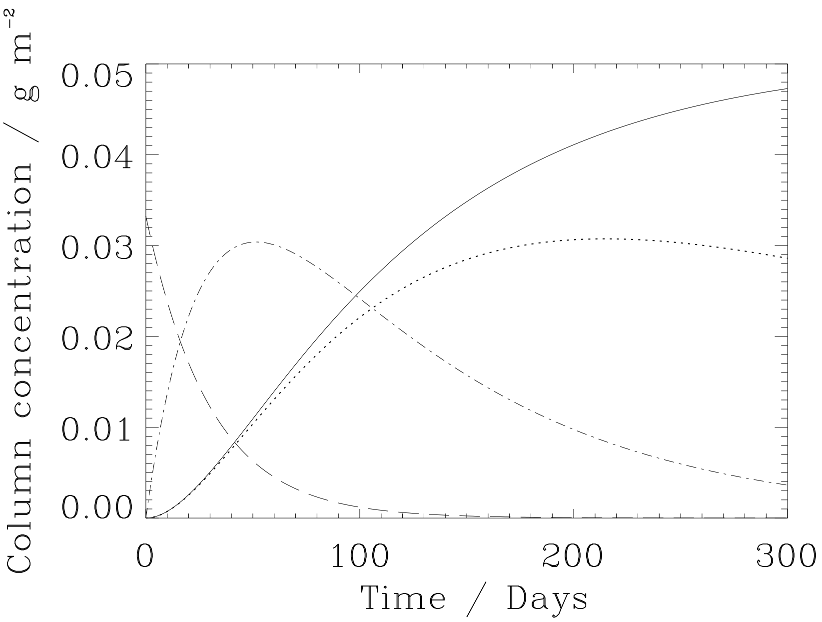

Figure 2.1: The solutions of the differential equations (2.4, 2.5 and 2.6). The lines show the relative concentrations of SO_2 (dashed), H_2SO_4 (dot-dashed) and aerosol (solid) for the first 300 days after a Pinatubo-like eruption. The SO_2 depletes exponentially, with a characteristic e-folding time of 35 days. The 'gaseous' H_2SO_4 is created at this rate, but is gradually evolved into liquid aerosol and so decreases. The aerosol increases at this rate, but is lost as it sediments out of the box with an e-folding time of $\approx$ 1 year. Also shown is the lower concentration of aerosol predicted by eq. 2.8 (dotted). See text for an explanation as to why this is too low.

Fig. 2.1, the material ‘sediments’ from t=0, when in reality the aerosol would be too immature to do so (Bluth et al. 1997, Pruppacher & Klett 1997). In the atmosphere, the rate of growth of aerosol is related to the ambient concentration of the reagents, but here this is compounded by immediate fall out. Furthermore, sedimentation velocity is a function of aerosol size and height (Pruppacher & Klett 1997). None of these factors are implicitly included in the model. In order to characterise a more realistic representation of the sedimentation process, a delay is imposed upon its initialisation (Eq. 2.7-2.8). This delay allows aerosol in the model to ‘grow’ to generate a more realistic optical depth than if they sedimented from the start of the eruption at a uniform rate. It is worth noting here that the mass distribution of aerosols would show that the action of the heavier particles dominates the mass transport, as 10^6 particles with a radius of $0.1\,\mu$m have the equivalent mass of one $10\,\mu$m particle, although the smaller ones may be more optically important at short wavelengths.

After a finite time of p days, an upper bound to the rate of change of the aerosol concentration is prescribed, and represents the latest time that sedimentation can reasonably be considered to have begun.

$$\frac{dl}{dt} = \begin{cases} bg & t \le p \\ bg - cl & t > p \end{cases} \tag{2.7}$$

This has solution:

$$l(t) = \begin{cases} \frac{2baM}{b-a}\left[\frac{1}{a}\left(1-e^{-at}\right) - \frac{1}{b}\left(1-e^{-bt}\right)\right] & t \le p \\ \frac{2baM}{b-a}\left[\frac{e^{-at}}{c-a} - \frac{e^{-bt}}{c-b} + \left(\frac{1-e^{-ap}}{a} - \frac{1-e^{-bp}}{b} - \frac{e^{-ap}}{c-a} + \frac{e^{-bp}}{c-b}\right)e^{cp}e^{-ct}\right] & t > p \end{cases} \tag{2.8}$$

A good fit to the optical depth data after Pinatubo is achieved for p=300 days. This is close to the peak aerosol loading time of mid to large eruptions (Sato et al. 1993). Using this method in combination with the previous (Eq. 2.6), where sedimentation begins at t=0, the model can represent a range of sedimentation scenarios. This delay factor is an indication that in order to accurately describe the evolution of the aerosols, more rate-determining steps would be required than the three in this model. It is found that the same value of p adequately parameterises these processes for the size range of eruptions considered here, and the model remains computationally inexpensive.

2.1.2 Optical depth

The model is then required to calculate a visible optical depth from the calculated column of H_2SO_4 aerosol. A conversion relationship was derived using balloon-borne optical particle counter data (Deshler et al. 2003). Vertical profiles of size-resolved aerosol concentrations in the wake of the Pinatubo eruption were measured above Laramie, Wyoming (41° N). A sample of these vertical profiles was integrated over their size distribution to find their mass concentration with height, and then summed through the stratospheric column to find the total mass of aerosol. The results are shown in Fig.2.2, and compared against the column optical depth measured from the ground. The measurements made at this one site are taken to be analogous to aerosol optical properties globally. This may introduce some uncertainty, as will a possible difference in the optical properties of nascent and mature aerosol (although this is likely to be small). The effects of the height distribution of the aerosol are considered to be minimal, as the height dispersion of an erupted plume (of the type considered here) in the stratosphere is of the order of a few kilometres at most. Note that Fig.2.2 contains volcanic and non-volcanic measurements and so includes the variability of effective radius. The figure shows that optical depth can be parameterised in terms of stratospheric column liquid sulphuric acid. The global average optical depth conversion from a column mass of aerosol (g m^2) found by this method is:

$$\tau = (3.56 \pm 0.11)l \tag{2.9}$$

The uncertainty specified here results only from the linear fit to data and is small (3 %). For comparison, Zielinski (1995) used an value of $\tau = 3.4\ l$ based on a theoretical study by Stothers (1984).

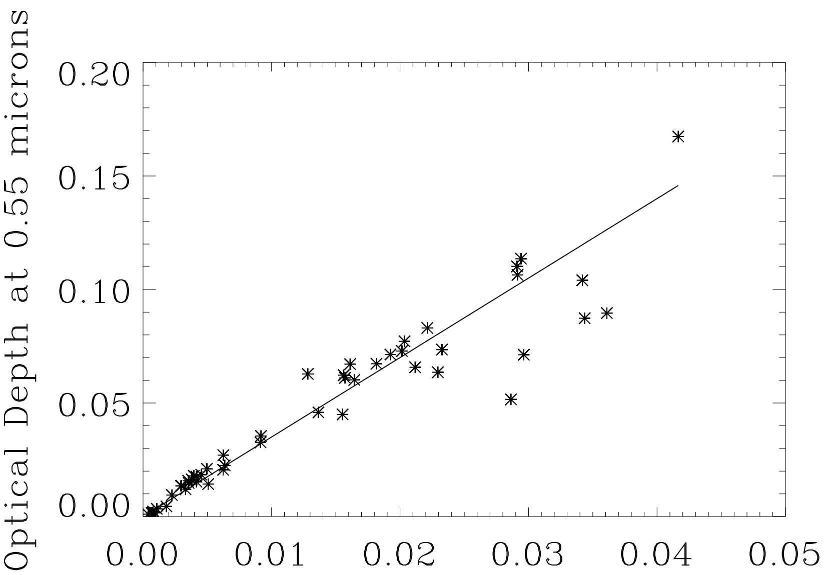

Figure 2.2: The optical depth, corresponding to a measured column mass of H_2SO_4. A linear trend line to data provides a linear conversion factor from modelled column H_2SO_4 and an associated optical depth perturbation.

2.1.3 Radiative forcing and surface temperature change

A radiative forcing resulting from the optical depth perturbation is then required (in accordance with this chain of processes) to estimate a theoretical surface temperature response. This model uses the standard relationship for net radiative forcing of

$$\Delta F \approx (-30 \mp 7.5)\tau \qquad (2.10)$$

after IPCC (1996) and Lacis et al. (1992), although this is likely to be an over-estimate of the radiative forcing due to aerosols (Andronova et al. 1999, Hansen et al. 1992, Trentmann et al. 2002). The climate response to forcing is calculated using a one-dimensional Energy Balance Model (EBM)(Shine & Highwood 2002). The time varying temperature response of the atmosphere is represented by Eq. 2.11.

$$C\frac{d\Delta T_s}{dt} = \Delta F(t) - \frac{\Delta T_s}{\lambda} + \text{noise} \qquad (2.11)$$

C represents an effective heat capacity of the ocean-atmosphere system, ΔF the time-varying radiative forcing and λ the climate sensitivity. The EBM calculates a change in the global mean effective surface temperature. Shine & Highwood (2002) evaluated an 0.3 K agreement of the EBM with a GCM for a doubled CO_2 forcing. This results in an error on an equilibrium calculation of 12.5 %. This error is particularly sensitive to the value of λ used. EBMs are widely used by the IPCC and in the literature, and yield good simulations of the evolution of historical global mean surface temperature deviations when compared to observations (Kinfe 2003). The nature of this EBM means that it will calculate a linear response to forcing. The degree of non-linearity in the actual climate response is an open question at present.

2.2 Validation

The model was tested by reproducing the global average optical depth for initial stratospheric injections of sulphur dioxide according to the magnitudes in the literature for Mt Pinatubo [1991], El Chichón [1982] and Agung [1963]. These were all near-equatorial eruptions (less than ± 30° latitude) for which the model was designed. However, these eruptions produced aerosol plumes which spread initially to different hemispheres. In the lower stratosphere the material is spread preferentially to the winter hemisphere, but if the aerosol is resident for more than one season material will eventually spread to both hemispheres and the atmospheric effects are global. These represent the three largest recent eruption cases for which observations were available for both the eruptive material and the atmospheric effects. The principal uncertainty affecting the model arises from the estimate of initial SO_2 released from an eruption, but it is a pivotal variable in the model. The mass estimate of erupted SO_2 from Pinatubo is taken from Bluth et al. (1992) (2.2). An SO_2 mass of 9 Mt was used to model El Chichón. This value lies at the upper end of the range of uncertainty for the value estimated by Bluth et al. (1997). A best fit was achieved for Agung using a SO_2 mass of 7 Mt, which is in good agreement with estimates of Self & King (1996). The results of the model were compared with measurements of global average optical depth following the eruptions

(Sato et al. 1993), shown in Fig. 2.3. Optical depth measurements were offset to eliminate the background level before comparison with the model results. The good agreement between observations and the model suggests that the model is of adequate complexity to represent the global average time-varying optical depth properties of volcanic aerosol, based on an initial injection of SO_2.

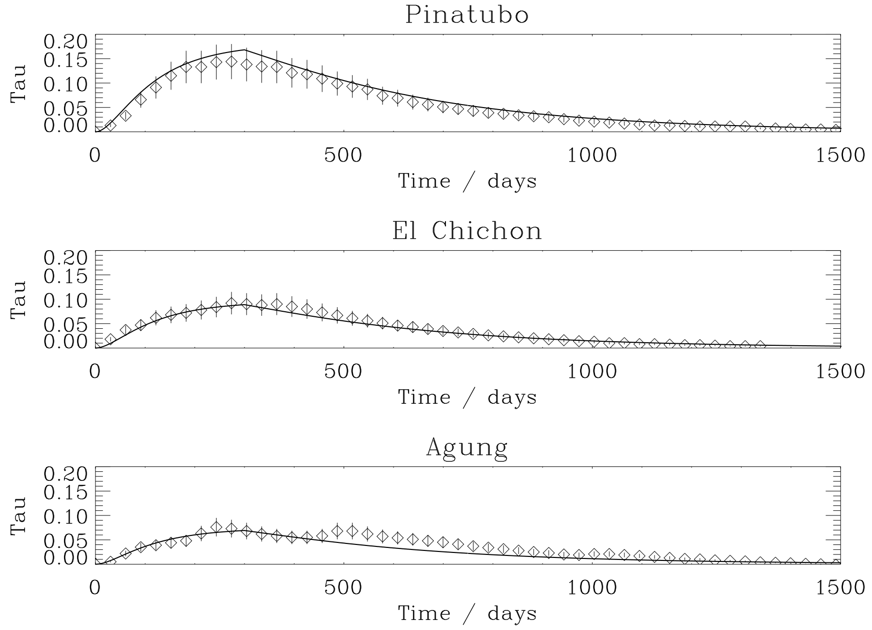

Figure 2.3: The 0.55 μm optical depth reconstruction of three equatorial explosive volcanic eruptions. The solid line represents modelled optical depth evolution from initial SO_2 mass injections (see text for discussion). Also plotted are month and global mean observed stratospheric optical depth, associated with a 25 % uncertainty estimate, according to Sato et al. (1993). The second peak in the Agung plot is possibly spurious due to poor contemporary sampling (Dyer & Hicks 1968). Despite its simplicity, this model achieves a good fit to these observations.

Figure 2.4(a) shows the peak change in temperature predicted by the model in its delayed sedimentation regime for a range of initial SO_2 mass injections. In response to an estimated SO_2 loading, the model predicts maximum global average optical depths and temperature perturbations for three eruptions, as shown in Table 1. These results are compared with observed maximum optical depths and temperature changes calculated using more complex models or observations.

		Optical Depth		Max. Global Δ T/°C	
Eruption	SO_2/Mt	Observed[1]	Model	Observed	Model[2]
Pinatubo	17	0.14 ± 0.04	0.17 ± 0.05	0.5^3 ± ?	0.54 ± 0.15
El Chichón	9	0.09 ± 0.02	0.089 ±0.025	0.4^4 ± ?	0.29 ± 0.08
Agung	7	0.088 ± 0.02	0.069 ± 0.02	0.3^5 ± ?	0.22 ± 0.06

Table 2.1: [1] Sato et al. (1993), [2]Based on model error of 28 %, [3]Hansen et al. (1992), [4]Predicted, but observations coincided with an El Niño event (Robock & Mao 1995*a*), [5]Sadler & Grattan (1999), Uncertainty on these measurements not given, and denoted '?'

For comparison, also plotted is a best fit line to 5 eruptions, from Sigurdsson & Laj (1992), attributing a change in Northern Hemisphere surface temperature to the sulphur yield of an explosive eruption. Four of these were equatorial and the remainder Northern Hemisphere, so the comparison with this tropical eruption model is not entirely a fair one. As mentioned, associating a change in global temperature with an eruption is difficult, and heavily reliant on computer models. The Northern Hemisphere eruptions used in the data within Sigurdsson & Laj (1992) include Laki [1783] and Mt St. Helens [1980]. These are not the types of eruptions the model seeks to represent. The former was an effusive event, with eruptive episodes occurring intermittently over a period of many months in the higher Northern mid-latitudes, and there is some debate over whether any SO_2 could have made it to the stratosphere (Highwood & Stevenson 2003). The latter was again in the mid-latitudes, and whilst powerful its blast was predominantly sideways of the volcano, and the proportion of SO_2 which reached the stratosphere was significantly reduced. Mt St Helens does not show a signature in polar ice core samples, and was associated with only a large, local (and very temporary) temperature change. Furthermore, the temperature changes attributed to these eruptions have uncertainty associated with them. Pollack et al. (1976) give a modelled relationship between optical depth and global average temperature perturbation of

$$\Delta T = 0.35 - 6.8\tau \qquad (2.12)$$

By evaluating the gradient of the line produced from calculating the maximum change in temperature for a given optical depth, this study has produced an alternative relationship of

$$\Delta T = (-4.5 \mp 1.3)\tau \qquad (2.13)$$

Also by gradient method, this results in the final relationship between total SO_2 loading (in grams) and maximum temperature response of

$$\Delta T = (-3.2) \mp 0.9 \times 10^{-14}[SO_{2(g)}] \qquad (2.14)$$

We have calculated a conservative estimate of model error to be 28 % formulated from errors in each step of the model. The model error is less than the measurement error of SO_2 loading, which at best is 30 % and at worst an order of magnitude.

This relationship is valid for amounts of SO_2 up to 25×10^{13}g. Above this, non-linear effects in aerosol formation, and possibly climate response, would suggest caution is needed. It has been proposed that self-limiting effects from stratospheric dehydration may prolong the lifetime of the aerosols (Bekki 1995), or higher concentrations may promote increased aerosol coagulation and shorten their lifetime in the stratosphere (Pinto et al. 1989). Future chemical modelling and GCM experiments would be needed to determine the validity of this relationship for larger eruptions.

2.3 Eruption significance

A measure of the climatic significance of a particular size of eruption can be understood as a product of the magnitude of an explosive volcanic eruption and its frequency. Small eruptions are frequent, very high magnitude ones which may discernibly affect global temperature are rare, and a spectrum exists in

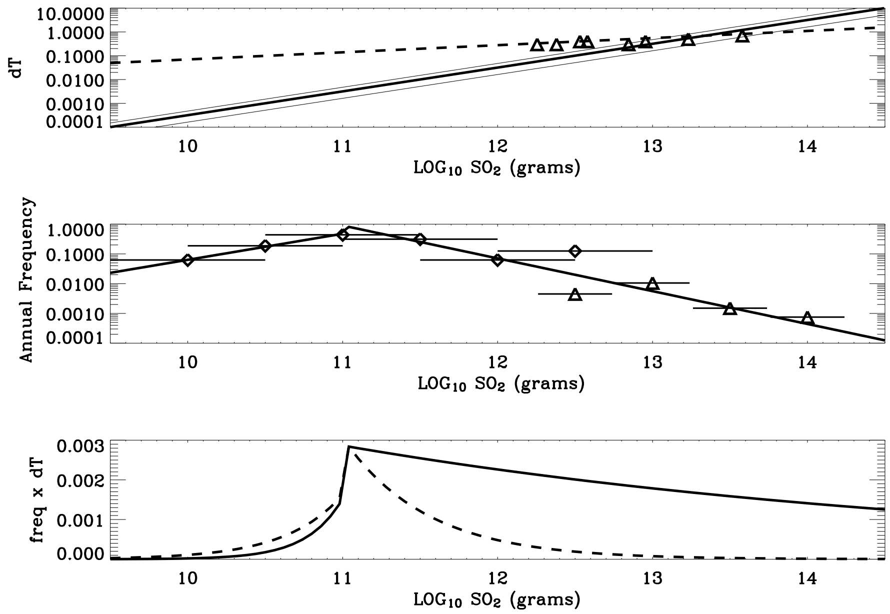

Figure 2.4: (a) Temperature change predicted by the model for a given initial volcanic SO_2 injection into the stratosphere from an explosive equatorial eruption with model error bounds (solid lines - solution thick, errors narrow) and modelled/observed data (dashed line) for northern hemisphere temperature response (Sigurdsson & Laj (1992) unless otherwise stated). Data points from left to right are Fuego, Agung(1),St. Maria, Krakatau, Agung (2, Sadler & Grattan (1999)), El Chichòn (Robock & Mao 1995*b*), Pinatubo (Hansen et al. 1992), Tambora. (b) Frequency distribution from ice core (triangles) and satellite data (diamond symbols - see text). The points are mean annual frequency estimates with large SO_2 mass uncertainty estimates. The line is a fitted distribution to the two parts of the trend. (c) The product of the annual rate of eruption from the combined data sets and change in global average surface temperature modelled for an emission of SO_2 (solid line) and northern hemisphere observations (dashed line).

between. It is therefore asked, which magnitude of eruption is climatically more significant, when its frequency is also taken into account?

With the data presently available, an effort at describing the frequency distribution of large equatorial eruptions is attempted. An important consideration in any frequency analysis of this sort is that various data sets from different sources over different periods of time will yield dissimilar frequency estimates. Hyde & Crowley (2000) produced a volcanic radiative perturbation PDF, based on 600 years of composite ice core data, to predict the chance of future climatically significant global eruptions. Efforts have been made to combine what frequency data are available to categorise the properties of eruptions. These include the Volcanic Sulphur Dioxide Index, VSI (Schnetzler et al. 1997) and Volcanic Gases Into the Stratosphere, VGIS (Halmer 2001) (both tied to the VEI), but there are many statistical ways of analysing such data, and it is not clear whether one particular method is more valid than another.

Here, two data sets are considered in order to describe different regions of the frequency and strength spectra. These measures have been chosen to be directly related to actual aerosol mass loading amounts. Firstly, it has been demonstrated that data from the TOMS can be used to retrieve column SO_2 amount (Bluth et al. 1997). The satellite data set used here spans 16 years. This period includes the eruptions of El Chichón [1982] and Pinatubo [1991]. This is the most accurate record of large SO_2 emissions into the atmosphere. Secondly, GISP2 (Greenland Ice Sheet Project 2) data, as presented in Zielinski (1995), are used to describe historical volcanism over the last 1360 years (dated from the first eruption after a break in the data in which no eruptions could be retrieved). This length of time is more likely to include more larger eruptions, which have repose times greater than that of the shorter satellite record. Zielinski (1995) parameterises a maximum total atmospheric mass loading of H_2SO_4 to eruption SO_4^{2-} signatures in the ice core. Intermediate estimates of half this predicted atmospheric loading (as calculated in Zielinski (1995) are used here to account for uncertainties in the conversion and so that the effects of sampling are adequately represented.

Figure 2.4(b) shows the annual frequencies calculated for a range of SO_2 emissions from the two data sets. These may be considered Poisson coefficients for each size range (Pyle et al. 1996). Two linear relationships have been fitted to different parts of the distribution: before and after the maximum. This fit is likely to change upon the introduction of other data sets, particularly the peak value and the shape of the turning point.

Figure 2.4(c) shows the product of the change in temperature predicted from a mass of SO_2, and the annual frequency of eruptions of each mass range. The curve peaks sharply where the frequency data indicate the largest annual flux of SO_2 occurs. It demonstrates that the most climatically significant eruptions are those that occur most often, but which just reach the stratosphere: eruptions emitting on average 0.1 Mt. The dashed line shows the product of the Sigurdsson & Laj (1992) ΔT fit multiplied by the frequency distribution, and shows that the quantification of the significance of larger eruptions appears to be strongly dependent upon how the temperature response of the atmosphere is modelled or measured.

2.4 Conclusions

A simple model has been developed to estimate the global average surface temperature response to the change in radiance resulting from an injection of sulphur dioxide into the stratosphere from a large explosive volcanic eruption. The model is built upon the parameterisation of five steps whereby this process is understood to occur. The concentration of SO_2 within a stratospheric box, representative of the global average, is evolved into a mass of sulphate aerosol. A relationship between aerosol mass and an optical depth perturbation is parameterised from balloon data of the Pinatubo aerosol. This in turn is converted to a radiative forcing, all of which is adjoined to a simple energy balance model to predict an idealised global average surface temperature response.

There are little data to directly connect an SO_2 perturbation with a change in surface temperature resulting from the optical properties of aerosol that follows. The temperature change predicted by the model compares adequately with other more sophisticated climate model results for two eruptions, but it should be stressed that the energy balance model is one-dimensional, and predicts a linear response to direct forcing. Sedimentation in the real atmosphere is a complex and spatially varying process after an eruption, but a good parameterisation of its global average properties has been achieved with some relatively simple mechanisms. The use of delayed sedimentation allows the progressive sedimentation due to the different rates of aerosol growth and location in the stratosphere after an idealised eruption to be expressed. The primary strength of the model lies in its ability to accurately re-create the global average optical depth perturbation from some significant eruptions, using only simple physical relationships, from a single input variable (SO_2). Consistent levels of (un)sophistication are maintained throughout the model and yet it does fairly well. There are some direct applications of this part of the model, including putting mid to large volcanic eruptions into more sophisticated climate models in an accurate but computationally inexpensive way. Working backwards to retrieve an initial mass estimate from global average optical depth measurements could prove illuminating for historical eruption recreation, but would be complicated by multiple events. There are obvious limitations to the model. There is no account of the background aerosol layer, or of other nuclei or aerosols that could already be present in the atmosphere. The model is only an appropriate analogue for eruptions of a size that can be validated with observational optical depth data, and that are not so large that non-linearities become important. This has clear applications for estimating the gross effects of the proposed geoengineering concepts relating to deliberately placing SO_2 into the stratosphere to off-set tropospheric warming by greenhouse gases. For this use it would suit modification to include a source term.

By linking volcanic SO_2 to global average temperature change in a physical way, an attempt to characterise historical volcanism in terms of strength and climatic significance is made. This required a frequency distribution be modelled, and two combined sets of volcanic eruption records were used to form its basis. In principle, satellite data for a recent period of 16 years provide accurate information about mid-range frequent eruptions, but cannot capture the frequency distribution of eruptions larger than any that have occurred within the satellite's operation. Ice cores represent a different problem, in that they may describe well the frequencies of large eruptions, but large uncertainties are associated with values of SO_2 erupted, and these are crucial for climate studies. It is likely that some kind of response function which varies with both time and eruption strength must be applied to ice core signals, but the shape of this function is undetermined. Ice cores do however provide the best information available about historical explosive volcanism.

The size significance maximum (Fig.2.4(c)) is very sensitive to the frequency distribution (especially for larger eruptions), but possibly more so to the rate at which the atmospheric response changes with eruption size. For eruptions in the range of 0.1 Mt – 20 Mt, this model achieves a good representation of the global average properties it seeks to reproduce. Below this range it is probable that eruptions are not powerful enough to significantly perturb the stratosphere, and are less significant for global climate change for timescales of more than one year. Furthermore, the global average temperature perturbation from an eruption emitting less would be undetectable above natural variability. It is likely that eruptions of 0.1 Mt, where figure 2.4(c) peaks, affect the atmosphere in more subtle ways than direct radiative forcing, or result in temperature changes comparable with natural variability. Such mechanisms cannot be diagnosed with this model, but their sheer frequency suggests their importance.

Above this range the stratospheric response to such a sulphur loading is uncertain, but may be complicated by non-linearities not included in this model. Eruptions of this size are rare in the period of modern measurements, and may not be climatically significant on decadal to century timescales by themselves. Better observations of climate response and transport are required to validate any model output. The biggest uncertainties for future work lie in not knowing precisely how much SO_2 was released by individual historical eruptions, and in inferring the ways in which the atmosphere was affected by these and modern eruptions.

Any attempt to provide a comprehensive estimate of the historical frequency of the various size ranges of volcanic eruptions will be subject to large uncertainties. Equally (in importance, and possibly more so in magnitude), efforts to calculate a generic temperature response from the climate will be uncertain due to the complexity of the system. The process developed here is considered to be of a sophistication appropriate to these high levels of uncertainty. This method of calculating a temperature response that is directly related to the initial volcanic SO_2 perturbation (for the range considered) begins to show how two different eruptions can be compared for their potential climatic impact, based on their stratospheric SO_2 emission alone.

2.5 Addendum

Vernier et al. (2011) present stratospheric optical depth measurements from a range of satellites in the post-Pinatubo era. They show that the background layer optical depth has increased since around the year 2000, particularly in the tropics. This general trend was also found by Hofmann et al. (2009) using ground-based lidar, and they tentatively attribute this to an increase in coal burning in South East Asia penetrating the tropopause and being lofted upwards into the stratosphere. Kaufmann et al. (2011) use model experiments to demonstrate that this hypothesis is consistent in reconciling the observed lack in global average surface temperature warming predicted in global warming scenarios based on the increase in concentration of greenhouse gases of anthropogenic origin. Contrary to this, Vernier et al. (2011) are able to show with profile optical depth with time measurement analysis that the dominant measureable contribution of aerosols came from a series of tropical mid-sized eruptions. They show that these eruptions have replenished and increased the stratospheric aerosol loading in the last decade, and propose the significance for climate of medium sized explosive volcanic eruptions, particularly in the tropics, which agrees well with the predictions of Miles et al. (2004) and presented here.

Chapter 3

An introduction to infrared atmospheric profile retrieval

The previous chapter established that a main shortcoming in quantifying the atmospheric effects of volcanic eruptions is uncertainty in SO_2 amount emitted to that atmosphere. This thesis will subsequently aim to provide the potential for a further dataset of SO_2 emitted from explosive eruptions in the 32 operational years of HIRS (High resolution Infrared Radiation Sounder 2) satellite instruments. Additionally, the methodology will provide a quantitative estimate of error in the emitted SO_2. HIRS/2 has desirable advantages for volcanic SO_2 detection, including comprehensive spatial coverage at high latitudes, and observations both day and night. To this end, an understanding of the methods of satellite retrieval is required.

A 'retrieval' is a mathematical (and computational) method to extract a set of variables of a state from measurements of their related attributes. In the case of atmospheric profile retrieval, discrete points of temperature or atmospheric gas concentration are derived from measurements of radiance. The radiance and temperature or concentration of gaseous species in that profile are related by a forward model that defines our understanding of the physics of the atmosphere. In the case of nadir atmospheric profile retrieval we define the 'Forward Problem' as the calculation required to relate what a satellite would detect given an atmospheric state, and the 'Inverse Problem' as inferring properties of the ground and atmosphere given a satellite measurement. Both are required in the retrieval process. The forward problem requires knowledge of the physics of the system - in this case how temperature and gaseous constituents interact with radiation to result in observed radiances. It also requires a representation of how the instrument makes measurements. The inverse problem is a mathematical technique necessary because the state and the measurement are not necessarily linearly related. The principal reference that details much of the method discussed and employed here is found in Inverse Methods for Atmospheric Sounding - Theory and Practice by Dr C. Rodgers (Rodgers 2000).

3.1 Atmospheric profile retrieval

The object of a retrieval is to turn a finite set of radiances as measured by an instrument at multiple wavelengths into an atmospheric profile. A nadir sounding radiometer incorporates a set of m “filters”, “bands” or “channels” centred on a range of frequencies ν_i. They are chosen to be close together such that B_ν, the Planck function, is similar yet between which atmospheric transmittance varies substantially. They may also be chosen to exploit a particular emission peak of an atmospheric constituent, such as the $667.4\,\mathrm{cm}^{-1}$ ($14.98\,\mu$m) CO_2 vibrational mode. Carbon dioxide is a well mixed gas, and since its density profile is known much can be inferred about the temperature structure of the atmosphere from its radiative modes.

Atmospheric emission at a given frequency range (such as within a channel) will principally originate from a localised region in the atmosphere, where its transmittance ($\tau_{\nu i}$) changes with height. This is because such emission lower in the atmosphere will be re-absorbed and higher in the atmosphere air will not absorb or re-emit at this frequency range. The sensitivity (or derivative) of the measurement to changes in the atmospheric state is deemed the weighting function $\mathbf{K}$. The weighting function is an m by n matrix, where n is the number of pieces of information sought from the measurements.

The region where $\tau_{\nu i}$ changes rapidly with height is exhibited by a peak in the weighting function. Its shape is affected by the density of the air and the concentration of its constituent species. The atmosphere has a continuous profile of temperature, which conceptually has a unique value at an infinite number of points. Viewing in the nadir, a satellite takes measurements with a finite number of spectral channels and will effectively record one piece of information per channel (often with some overlap leading to information redundancy). Some of the channels will be sensitive to broad regions of the atmosphere and as a result the associated weighting functions are often broad. Furthermore these weighting functions typically overlap spatially (although they are chosen to minimise this origin of redundancy). Fundamentally there can be no unique solution obtained from these measurements, only one evaluated to be most likely, generally termed "optimal estimation". If all other pertinent information about the atmosphere is known, or if the variable sought is not affected by other unknown variables, and information about its properties arise solely and directly from the measurements, a variable may be independently retrieved. As is more often the case with multiple wavelength satellite observations, many variables contribute to the measurements and may be sought simultaneously. This is what constitutes a joint retrieval.

3.2 Principles of retrieval theory

As outlined above, the calculation of an atmospheric profile from radiance measurements requires knowledge of the underlying physics of the atmosphere, and also of the measurement itself. The measurement $\mathbf{y}$ is an m element vector representing one 'scan' (also referred to as "pixel" or "footprint"). This is related to the atmospheric state $\mathbf{x}$, a discretised n element vector representing the continuous profile, by the forward model $\mathbf{F(x)}$, with some account of measurement error ϵ:

$$\mathbf{y} = \mathbf{F}(\mathbf{x}) + \epsilon \tag{3.1}$$

For small departures from a defined state $\mathbf{x}_0$, we make a linearised approximation of finite difference in order to examine the quality of the relationship:

$$(\mathbf{y} - \mathbf{y_0}) = \mathbf{K}(\mathbf{x} - \mathbf{x_0}) + \epsilon \tag{3.2}$$

$$\mathbf{y} - \mathbf{F}(\mathbf{x_0}) = \frac{\mathbf{dF}(\mathbf{x})}{\mathbf{dx}}(\mathbf{x} - \mathbf{x_0}) + \epsilon = \mathbf{K}(\mathbf{x} - \mathbf{x_0}) + \epsilon \tag{3.3}$$

All measurements are subject to error, and this forms an inherent and useful part in the retrieval of $\mathbf{x}$. For an under-constrained problem, where the number of unknowns is greater than the number of measurements (an unavoidable aspect of nadir sounding of a continuous state), errors define how well the solution can be known. The measurement error for each channel may not be entirely uncorrelated (as described in section 3.4.1). As such it is necessary to construct a m by m covariance matrix of the measurement error $\mathbf{S}_{\mathrm{y}}$, where

$$\mathbf{S_y} = E\{\epsilon_i \epsilon_j\} \neq 0 \tag{3.4}$$

and E is the expected value and $_i$ and $_j$ denote the elements of each dimension of $\mathbf{S}_{\mathrm{y}}$. Diagonal elements of $\mathbf{S}_{\mathrm{y}}$ are the channel noise, which is a function of scene temperature and must be evaluated for each scan. Off-diagonal elements represent the channel error covariance. The terms of Eq. 3.2 may be gathered for practicality such that the forward model error is incorporated into $\mathbf{S}_{\mathrm{y}}$ and usually dominates the term, so it is important to quantify it accurately.

The method of optimal estimation benefits from the use of some prior information about the state, which can help to guide the retrieval. It often makes use of departures from a predefined state or *a priori*, usually derived from a climatology. This also requires some estimate of the quality of the climatology and the degree to which it may vary. This forms the *a priori* error covariance, a n by n matrix $\mathbf{S}_{\mathrm{a}}$. The use of *a priori* information helps to constrain such ill-posed, under-constrained problems. The elements of $\mathbf{S}_{\mathrm{a}}$ act to limit the freedom of the retrieval to depart from the climatology, driven by the measurements and their error, so they must be appropriately derived. Given the nature of the problem outlined above an exact or unique solution for a given set of measurements cannot be found. In practical terms, the most probable solution is the optimal one (Rodgers 2000).

It can be shown that (assuming Gaussian statistics for the probable and expected state) the expected solution x̂ may be derived as:

$$\mathbf{\hat{x}} = (\mathbf{K^T S_y^{-1} K} + \mathbf{S_a^{-1}})^{-1}(\mathbf{K^T S_y^{-1} y} + \mathbf{S_a^{-1} x_a}) \tag{3.5}$$

with associated error covariance

$$\mathbf{\hat{S}} = (\mathbf{K^T S_y^{-1} K} + \mathbf{S_a^{-1}})^{-1} \tag{3.6}$$

where $\mathbf{x}_\mathrm{a}$ and $\mathbf{S}_\mathrm{a}$ are the *a priori* and *a priori* error covariance respectively.

This solution is found iteratively by minimising the cost function (χ^2), with constituents of both the measurement information and *a priori* in an 'optimal estimation' retrieval:

$$\chi^{\mathbf{2}} = (\mathbf{y} - \mathbf{F}(\mathbf{\hat{x}}))^{\mathbf{T}}\mathbf{S_y^{-1}}(\mathbf{y} - \mathbf{F}(\mathbf{\hat{x}})) + (\mathbf{x_a} - \mathbf{\hat{x}})^{\mathbf{T}}\mathbf{S_a^{-1}}(\mathbf{x_a} - \mathbf{\hat{x}}) \tag{3.7}$$

3.2.1 Error analysis and retrieval diagnostics

To ascertain the quality of the retrievals it is necessary to know how they are affected by the various contributions of error from non-retrieved or assumed elements that contribute to the simulation of the state. The gain matrix (or contribution function), a m by n matrix is defined as follows:

$$\mathbf{x} = \mathbf{Gy} \tag{3.8}$$

For a retrieval involving *a priori* information,

$$\mathbf{G} = (\mathbf{K^T S_y^{-1} K} + \mathbf{S_a^{-1}})^{-1}\mathbf{K^T S_y^{-1}} \tag{3.9}$$

It is useful to recognise the contribution to **G** of the error covariance of the expected solution as shown in equation 3.6. **G** encapsulates how the retrieval is affected by a change in the measurement, where the expected solution can be re-expressed as:

$$\mathbf{\hat{x}} = \mathbf{x_a} + \mathbf{G}(\mathbf{y} - \mathbf{Kx_a}) \tag{3.10}$$

G is required in determining where in the atmosphere the information reaching the satellite is coming from, which comprise the rows of the averaging kernel **A**, an n by n matrix. **A** can also be understood as the weighting functions mapped onto state space by **G**, and indicates the sensitivity of the retrieved state to changes in the actual state.

$$\mathbf{A} = \mathbf{G}\mathbf{K} \tag{3.11}$$

3.2.2 Information content

For an atmospheric profile retrieval, it is necessary to ascertain where the information from the measurement is coming from in the atmosphere and therefore where best to place retrieval levels. It may be sufficient to use the averaging kernel, **A**. Not only does **A** tell us where the information is coming from, but the sum of its diagonal elements indicates a measure of the Degrees of Freedom for Signal (DFS). Nominally for a well constrained problem, one DFS is required for each piece of information sought, or element of the state vector. There are other methods of assessing information content that are used in a diagnostic sense within the retrieval. These involve calculating the entropy of the error covariance matrices, which can be a measure of the quality of the retrieval. It should be noted that the information content and averaging kernels can be influenced by both the prior covariance and the state. In the case of the former, it is therefore important to have an *a priori* covariance that is representative of the real atmosphere in order to gain an accurate estimate of the DFS.

3.2.3 The retrieval engine and convergence

The retrieval engine implemented in the following chapters uses equations 3.5 and 3.6 to iteratively converge upon a solution by alternately calling the forward model and re-evaluating the state, cost and convergence criteria. Equation 3.12 is the Levenburg-Marquardt method and is a “hybrid of steepest descent and Newtonian iteration” (Marks & Rodgers 1993). Both are numerical methods of finding minima of functions.

$$\mathbf{x_{i+1}} = \mathbf{x_i} + [(\mathbf{y} - \mathbf{F})\mathbf{S_y^{-1}}\mathbf{K^T} + (\mathbf{x_a} - \mathbf{x})\mathbf{S_a^{-1}}][(\mathbf{1} - \gamma)\mathbf{S_a^{-1}} + \mathbf{K}\mathbf{S_y^{-1}}\mathbf{K^T}]^{-1} \tag{3.12}$$

This method was chosen because in some situations this can aid convergence if the solution is far from the initial guess (Rodgers 2000). The iteration step size is given by γ^{-1}, and as γ approaches zero this tends towards the Newtonian iteration method. As γ tends to infinity it becomes more like the steepest descent method. Values of γ are chosen to give steepest descent far from the solution and Newtonian iteration nearer (Jay 2000), which can significantly improve time taken for convergence. Far from the solution the retrieval takes bigger steps. Closer, it takes smaller ones. This is accomplished by monitoring the cost, χ^2. If the cost increases γ should be increased and $\mathbf{x}$ unchanged. If the cost decreases γ should be decreased and $\mathbf{x}$ updated.

3.3 Radiative transfer

Infrared radiative transitions in the atmosphere occur when a photon encounters a molecule with a permanent dipole moment. Thus, molecules such as N_2 and O_2 are difficult to observe in the infrared. Well-mixed chemical species, including CO_2, that do have a dipole moment can be used to infer the temperature profile of the atmosphere. When a photon interacts with such a molecule, it is either absorbed or scattered, depending upon the energy of the photon and the characteristics of the molecule. Upon infrared absorption the molecule is excited to either a higher energetic rotation or vibration state. A vibrating or rotating electric dipole emits radiation at a characteristic frequency, and can be detected remotely. These excited states can be predicted for a given temperature and molecule, and so for a given concentration pressure and temperature the spectral radiance of a gas can be modelled. The temperature and pressure are important for calculating the effects of remotely observing the line shape of atmospheric emission. Random collisions at high pressures, and Doppler broadening at high altitudes cause an emission line to be smeared over a finite wavenumber range, which has to be accounted for when inferring measurements of total radiance (Haken & Wolf (1987), Goody & Yung (1995)).

The radiative transfer equation in the infrared, neglecting reflectance and scattering, is given by:

$$R = (I_0)_\nu \tau_\nu + \int_{z_0}^{\infty} B_\nu[T(z)] \frac{d\tau_\nu(z)}{dz} dz. \tag{3.13}$$

where $\frac{d\tau_\nu(z)}{dz}$ is recognised as the weighting function. $B_\nu[T(z)]$ is the profile of the Planck function. $(I_0)_\nu$ is the surface emission. The first term is the Planck function emission (in radiance units) from the hot surface. The Planck function is given by:

$$\begin{aligned} B_\nu(T) &= \frac{2hc^2\nu^3}{\{\exp[\frac{hc\nu}{kT}] - 1\}} \\ &\approx \frac{1.19 \times 10^{-5}\nu^3}{\exp[\frac{1.439\nu}{T}] - 1} \end{aligned} \tag{3.14}$$

The monochromatic transmittance τ_ν at an angle θ from the nadir is given by:

$$\tau_\nu(z, \theta) = \exp\left\{-sec(\theta) \int_{z0}^{\infty} k_\nu(z)c(z)\rho(z)dz\right\} \tag{3.15}$$

where $c(z)$ is the mass mixing ratio of the absorbing gas, $\rho(z)$ is the air density at height z. It is often more convenient to express this in pressure coordinates. Assuming hydrostatic balance:

$$\tau_\nu(p, \theta) = \exp\left\{-sec(\theta) \int_0^p k_\nu(p)c(p)\frac{dp}{g}\right\} \tag{3.16}$$

The above equations provide the basis for forward modelling of the atmosphere when observed in the nadir.

3.4 Forward models

The two functions of the forward model are to synthesise an expected radiance measured by a channel for a given state of the atmosphere, and to calculate weighting functions. The forward model is then used in conjunction with a retrieval algorithm to interpret the profile of an atmospheric property, based on satellite measurements. An estimate of this profile is used by the forward model to calculate what the satellite should measure and the sensitivity of the measurements to changes in the profile (weighting functions). The retrieval algorithm uses these sensitivity relationships to calculate the most likely atmospheric profile, and this is then put back into the forward model to calculate a new set of probable synthetic measurements. As previously suggested, this process iterates until a condition of maximum likelihood is obtained (as outlined in section 3.2.3), and the predicted profile results in calculated measurements in close agreement with the actual measurements. Forward models generally exist in three types. Line by line (LBL), broad band (BB) and narrow band (NB). LBL models calculate the contribution of each absorbing line and are computationally expensive but accurate. In BB models, the integrated channel response is simulated directly with parameterisations of transmittance, commonly generated by LBL calculations. An intermediate class of models are narrow band, with the spectrum divided into wavenumber intervals of $\sim$ 1–20 cm^{-1} wide (Garand et al. 2001). The conception of NB models is more 'flux' oriented, made to include variations in the surface and cloud properties with wavelength. BB models are often 'tuned' to the LBL model used to create them, so whilst NB models can potentially have greater resolution, without tuning their relative accuracies often differ little. The forward model to be used in this work is a BB model, and a LBL model will be used for some aspects of validation. Both will be introduced in chapter 4.

3.4.1 Forward model error

The deficiencies in the forward model to represent the real atmosphere are expressed in the forward model error, which must be quantified to achieve an accurate uncertainty estimate from the retrieval. In the retrieval process, forward model error is combined with measurement error and is 'mapped' on to measurement space. It has three main sources. To run a forward model using all of the known species in the atmosphere would be computationally expensive and unnecessary. Typically the instrument measurements being simulated only use selective regions of the infrared spectrum, and there is some knowledge of the relevant radiatively active species that they are sensitive to. Those gases, the climatological concentration of which leads to absorption above the measurement noise level, may be included in the model. Some small error will result from those gases that are excluded altogether, particularly non-well mixed gases. Secondly, there will be a component of error from estimating the climatological concentration for background gases that are not retrieved. If it is assumed that their expected concentration will vary within one standard deviation ($1\,\sigma$) of the climatological value, the model can be used to calculate what change this may bring to simulated measurements. There are a number of methods of quantifying such uncertainties, of which this is one example as it is used in the methodology in chapter 4. Thirdly, there is the error brought about by using a discrete height grid upon which the state vector is defined and weighting functions evaluated. The real atmosphere is a continually varying field. An attempt may be made to model this error by simulating measurements using a very high resolution grid (that is computationally very expensive) and comparing it to a more efficient but sparser grid. Not only is a reduced grid more desirable for speed, but frequently this is an ill-posed problem and the information content held within the measurements is finite. The instrument is not capable of ‘seeing’ the atmosphere at high resolution, therefore the benefits of modelling it so are limited.

There is also some introduction of error depending on the spectral resolution at which the forward model is run. The magnitude of this can be evaluated again by comparing a fine (computationally expensive) resolution run with a standard resolution run, or comparing a BB model to a LBL simulation. Since the spectral radiance is effectively averaged across the channel bandwidths (weighted by the instrument response as a function of wavelength) the benefits of very high resolution modelling are automatically limited for a radiometer such as HIRS/2.

3.5 Clouds

At any given moment, a high percentage (thought to be between 50 and 70%) of the Earth is covered in cloud and this presents a challenge for remote sensing of atmospheric gases, particularly in the infrared. Both the type of cloud and its height determine the way in which they affect the local radiation budget. Low, shallow cloud (such as marine stratus/stratocumulus) is composed primarily of water droplets and typically exist from 500 m to 3 km. As such, they are relatively warm and radiate at warmer temperatures. At some wavelengths very low cloud can be difficult to distinguish from the surface for this reason. High, thin cloud (cirrus, cirrostratus) are optically thin but very cold. Deep, convective cloud that spans the troposphere (for example cumulonimbus calvus/incus) are optically thick and also have very cold tops composed of ice crystals when they mature and become glaciated. Thus their emitting temperature is significantly colder than the surface. As a result, in terms of radiative forcing, these cold-topped clouds tend to warm the planet from a climatological perspective. The visible albedo of glaciated clouds is higher than that of the surface reflecting more of the incoming solar short wave radiation. Often more than one cloud type will exist on top of each other, and mid-layer or thick clouds are often mixed phase. Multiple cloud decks are exceedingly difficult to diagnose with passive nadir techniques, primarily because the majority of the information reaching them comes from the upper-most optically-thick surface. To complicate matters, the field of view of an instrument is often larger than the expanse of a single cloud feature. Therefore, any one pixel may ‘view’ the surface, some low cloud and some high cloud simultaneously. A complex algorithm is then required to determine whether or not a pixel is to be considered cloudy or cloud free, although in reality the majority will be somewhere in between. If it is the cloud that is the object of the observation, there are multiple techniques designed to retrieve cloud properties such as cloud height, optical thickness and even liquid water path. Observations may be made around 11.1 μm, coincident with a so-called atmospheric window. That is, there is very little absorption by CO_2 and other trace gases (and consequently the vertical profile of temperature) in that region of the spectrum, and as such it is predominantly sensitive to the temperature of the emitting surface (with some dependence on the surface emissivity at that wavelength). This may be the surface of the Earth, or the surface of a meteorological cloud that is sufficiently optically thick. This channel can be used to retrieve some information about the presence of cloud, including its height. This still requires a forward model, but it can potentially negate the need to comprehensively or exhaustively screen out cloud contaminated measurements for the purposes of retrieving other gaseous species in the atmosphere.

More precise estimates of cloud height can be obtained using a technique called CO_2 slicing, which iteratively retrieves down to an atmospheric layer until the modelled atmospheric radiance suggests the presence of cloud to determine the cloud top pressure, and then compares the radiance in various channels that are related to the properties of the cloud (e.g. Wylie et al. (2005)). This also requires forward modelling of the clouds themselves. Given the variability of cloud properties, this is not a trivial exercise, and even the most advanced numerical weather prediction models employ a considerable degree of parameterisation. The degree of modelling also has implications for the time required for their computation. The task of atmospheric profile retrievals is therefore greatly simplified by initially only considering cloud-free profiles.

For the HIRS/2 instrument (to be introduced in full in the following chapter), there are two main ways of cloud clearing. The first requires the utilisation of the IR window channel at 11.1 μm. In the absence of cloud, this is very close to the emitting temperature of the surface (or bulk surface temperature in the oceans), although is dependant upon the surface emissivity at that wavelength. It is however potentially subject to contamination by atmospheric moisture. In the CO_2 slicing method this is corrected using nearby channel information: 11.1-8.3 μm (for the National Oceanic and Atmospheric Administration satellite platforms NOAA 10 and 12) and 11.1-12 μm (NOAA 11). This correction can alter the interpreted brightness temperature of the channel by ≈ 0 K at dry polar latitudes, to 7 K in the tropics (Wylie et al. 1994). If the moisture corrected 11.1 μm brightness temperature deviates more than 2.5 K from the 'known' surface temperature, the FOV is interpreted as cloudy. Operationally, the surface temperature is obtained from ocean and land meteorology forecast models. A second way of detecting cloud is to use the visible channel, however this is only applicable during daytime. The disparate albedo of cloud from that of the surface allows its distinction, although there are some considerations required in the use of this method. It cannot be used above ice or at night, and as with the use of the IR window channel the distinction from clear to cloudy is not a discrete one.

In a simplistic representation, it may be possible to estimate the (optically thick) cloud top height using the 11.1 μm channel alone, iteratively using a fast forward model. This may be used to guide a joint retrieval (as a first guess), where water vapour is also retrieved, for a more accurate cloud top height.

3.5.1 Detection of SO_2

For detection of a trace gas in the atmosphere the sensitivity of the retrieval will depend heavily upon its concentration in the atmosphere, as it is related to the signal in the measurements. The contribution from the measurements is weighted by the confidence in the *a priori*. For a good retrieval the retrieved error $\mathbf{S}$ must be less than the *a priori* error, but this depends upon the information present. SO_2 for example, has a very small climatological concentration but after a volcanic eruption it can exist in very much higher concentrations in the atmosphere over a range of spatial scales. As such, the variance $\mathbf{S}_a$ must be carefully characterised, so as not to make the contribution from the measurements insignificant.

The next Chapter will apply the attributes of retrieval theory and radiative transfer described in this chapter to the HIRS/2 instrument to retrieve volcanic SO_2 in the upper troposphere and stratosphere, and test whether it is a viable pursuit for exploitation in deriving a further data set of volcanic emissions.

Chapter 4

Retrieval of SO_2 using the HIRS/2 instrument

This chapter will introduce the High Resolution Infrared Radiation Sounder 2 (HIRS/2) instrument, and describe its potential for detecting SO_2 from large volcanic eruptions. A forward model will be developed, using extensive simulations and retrievals from simulated data to optimise and assess its performance, in anticipation of applying the retrieval algorithm to real HIRS/2 measurements for a volcanic eruption case study in Chapter 5.

4.1 HIRS/2 instrument

HIRS/2 is one of three instruments that originally constituted Television Infrared Observation Satellite (TIrOS) Operational Vertical Sounder (TOVS), designed to provide atmospheric profile measurements of temperature and water vapour structure. The other TOVS instruments were the Stratospheric Sounding Unit (a radiometer) and the Microwave Sounding Unit (a scanning microwave spectrometer). The TOVS instrument was first launched in 1979 aboard the new NOAA satellites based on the TIROS-N design, and evolved in to the Advanced TOVS (ATOVS) system. Subsequent replacements have been deployed for the last 30 years aboard NOAA satellites (NOAA 6-17) (JPL 2003), and more recently European platforms including most recently

MetOp-A as HIRS/4. Throughout its deployment there have been at least 2 instruments and occasionally three orbiting simultaneously. HIRS/2 has 19 detector channels in the infrared and 1 in the visible part of the spectrum for cloud detection during the day. These channels are relatively broad, spanning between 0.1 and 0.5 μm depending upon wavelength. Table 4.1 shows the HIRS/2 channel wavenumber information and the principal atmospheric constituents that absorb therein.

Channel Number	**Central Wavenumber (cm^{-1})**	**Central Wavelength (μm)**	**Principal Absorbers**	**Peak Energy Contribution**
1	668	15.00	CO_2	30 hPa
2	679	14.70	CO_2	60 hPa
3	691	14.50	CO_2	100 hPa
4	704	14.20	CO_2	400 hPa
5	716	14.00	CO_2	600 hPa
6	732	13.70	CO_2 / H_2O	800 hPa
7	748	13.40	CO_2 / H_2O	900 hPa
8	898	11.10	Window	Surface
9	1028	9.70	O_3	25 hPa
10	1217	8.30	H_2O	900 hPa
11	1364	7.30	H_2O	700 hPa
12	1484	6.70	H_2O	500 hPa
13	2190	4.57	N_2O	1000 hPa
14	2213	4.52	N_2O	950 hPa
15	2240	4.46	CO_2 / N_2O	700 hPa
16	2240	4.40	CO_2 / N_2O	400 hPa
17	2361	4.24	CO_2	5 hPa
18	2512	4.00	Window	Surface
19	2671	3.70	Window	Surface
20	14387	0.70	Window	Cloud

Table 4.1: HIRS/2 Channel Characteristics. Adapted from NOAA (1981). Applies for NOAA 9, 10 and 12. For all others channels 10 and 17 were centred at 800 and 2415 cm^{-1} respectively

Details of some of the instrument parameters that must be incorporated into an atmospheric profile retrieval process and forward model, as introduced

Instrument Parameter	
Cross-track scan	± 49.5° (± 1125 km) nadir
Number of steps	56
Optical Field Of View	1.25°
Step angle	1.8°
Ground resolution IFOV (nadir)	17.4 km diameter
Ground resolution IFOV (end of scan)	58.5 km by 29.9 km
Distance between IFOV's	42 km along track and nadir

Table 4.2: HIRS/2 Instrument Parameters

in Chapter 3, are given in Table 4.2. HIRS/2 is not sensitive across its channels in a spectrally uniform way, but in a way that varies across each channel. These variations are described as the instrument response function (or 'filter function') and constitute an envelope function when applied to a monochromatic radiance that might be used to simulate the radiative transfer of the atmosphere.

4.1.1 Measurements

The measurements used here are all-sky brightness temperatures from NOAA 11. They are a product derived from the raw voltage measurements via a radiance and brightness temperature conversion and have been subject to calibration factors and some quality control. The data set was prepared specifically by Dr D. Jackson at NOAA, with testimony that they represented the best set that could be extracted from the raw data for these purposes. The data format contains the time in seconds from midnight of the measurement, the solar zenith angle, 19 IR channel brightness temperatures, one visible channel albedo, latitude, longitude, satellite altitude, line number for each orbit and the scan position (see Table 4.2).

The NOAA 10 and 12 instruments that were contemporaries of NOAA 11 did possess a channel that coincided more faithfully with the 8.6 μm SO_2 feature, centred at 8.3 μm, as shown in Table 4.1. However, this channel is known to also be particularly sensitive to mineral dust contamination (Corradini et al. 2009, Kearney & Watson 2009). This is especially a problem in the early days after an eruption when the gaseous and solid material may remain collocated. This situation presents scope for further development, but in deference to brevity only NOAA 11 data will be evaluated in this study. There are potential benefits from having a 12.5 μm channel in place of that at 8.3 μm, for use in diagnosing the presence of ash or aerosol in ratio to the 11.1 μm and other channels, which will be explored further in later parts of this work. Indeed, the latest HIRS instrument HIRS/4 aboard MetOp-A (launched in November 2006) has the same channel configuration as the NOAA 11 HIRS/2.

4.2 Initial approach to detecting SO_2 with HIRS/2

Preliminary methods have been designed in an attempt to identify and quantify SO_2 (in particular by Dr Prata (formerly at CSIRO, currently at the Norwegian Institute for Air Research) and Prof. William Rose and co-workers at Michigan Technical University, USA), but these have so far been eruption specific and have limited accuracy. One method is based on a synthesis of the expected clean atmosphere brightness temperature for the channel, and the observed deviation from it when contaminated by SO_2. This method, hereafter referred to as either the Prata fit method or after Prata et al. (2003), uses a linear interpolation between the brightness temperatures of adjacent channels. It also assumes a fixed height of erupted volcanic SO_2, since theoretically only one piece of information can be obtained from one channel, and column amount is not insensitive to the height of the plume. The technique requires the SO_2 to be located in the upper troposphere/stratosphere, and there is no information about the height of the plume from the instrument itself. This information may be gleaned from other types of observations, but the fit is reliant upon this independent information for the fit to be in any way accurate.

A description of how the Prata method operates is detailed in Appendix A. Its most significant shortcoming is that due to its simplicity, the model is unable to capture atmospheric variability (other than potentially that of SO_2). This particularly alludes to the variability of cloud, temperature and water vapour. Without independent height information of the SO_2 the radiance relationships are subject to profound error. Its strengths are that the operations required are computationally inexpensive and straightforward, as it is based on the principles of a band model. It has also performed well against other observational data sets, although the nature of the previously mentioned uncertainties that may contribute to error make quantifying fit uncertainty difficult. It uses a munimum offset threshold in brightness temperature for the channel affected by SO_2 in order to predict the presence of SO_2 and yet excludes the effects of atmospheric water vapour variability. As such, its sensitivity to low amounts of SO_2 is limited.

The HIRS instruments also have a channel at $4.0\,\mu$m, a window channel sensitive to the surface. It has never been used to detect SO_2 with HIRS and it is likely that the broadband nature of the channels may hide the signature in the surface temperature noise. The SO_2 $\nu_1+\nu_3$ band at this wavelength is a weak, and only a high resolution spectrometer (IASI) has been able to demonstrate its usefulness for SO_2 detection (Karagulian et al. 2010).

The Prata fit method works sufficiently well to suggest that the $7.3\,\mu$m feature is robust enough to make further exploitation more refined. Use of information arising from the observations from other HIRS channels would be a significant development, depending upon what is desired from them. Multiple wavelength information can be used to diagnose attributes of the atmospheric profile such as temperature and the presence of cloud. Given the above, an improvement to the Prata fit method would have to incorporate, use or derive information about the atmosphere for a given HIRS/2 measurement that would improve the estimate of SO_2. The forward model is required to be of sufficient complexity to incorporate these variables, if a full optimal estimation retrieval scheme is to be developed. As with the Prata fit, it will require some estimate of an SO_2 plume height. The Prata fit for HIRS/2 SO_2 can be compared to this optimal estimation scheme.

4.3 Principle of SO_2 retrieval with HIRS/2

Two HIRS/2 channels coincide with SO_2 spectral absorption features, these being 7.3 μm (a strong asymmetric stretch vibration band) and 8.6 μm. The precise central wavenumber is dependent upon instrument version, and as Table 4.1 shows not all versions of the instrument include the 8.6 μm channel. These channels were originally chosen to be sensitive to water vapour for use in sounding and applying corrections for the CO_2 and window channels. The 8.6 μm channel is also reported to be sensitive to volcanic ash and other aerosols (Kearney & Watson 2009). Prata et al. (2003) postulated that providing the SO_2 perturbation is strong enough, and located above any significant sources of water vapour, it might be detected by contamination of the expected channel radiance. A small caveat is that volcanic plumes can contain significant quantities of water vapour. Conditions are such that much of it will condense and freeze, often scavenging hydrophilic gases (halides) and falling out of the atmosphere due to gravity, depending on where in the atmosphere it is located. A plume's relative height distribution (and neutral buoyancy height) relative to ash and other hot gaseous species is convoluted but a significant degree of fractionation will occur (Graf et al. 1999). The authors surmise that in essence, the height distribution of volcanic water vapour is complicated. Figure 4.1 shows a line-by-line model calculation of two radiance spectra for a clean and volcanically perturbed atmosphere observed in the nadir. The discrepancies in this case are due solely to the presence of SO_2 distributed in a characteristic volcanic height structure in the stratosphere.

The spectra shown in figure 4.1 are coincident with two HIRS/2 channels as demonstrated in figure 4.2. The instrument response functions for each channel are shown with simulated transmission features by an SO_2 enhancement.

The previous work by Dr Prata and others, and the indications from simple radiative transfer experiments, suggest that there is ample scope for developing a retrieval algorithm that is more comprehensive, with a view to more accurate detection of SO_2 with the HIRS/2 instrument. To do this, a forward model is required to represent both the atmosphere and the instrument itself.

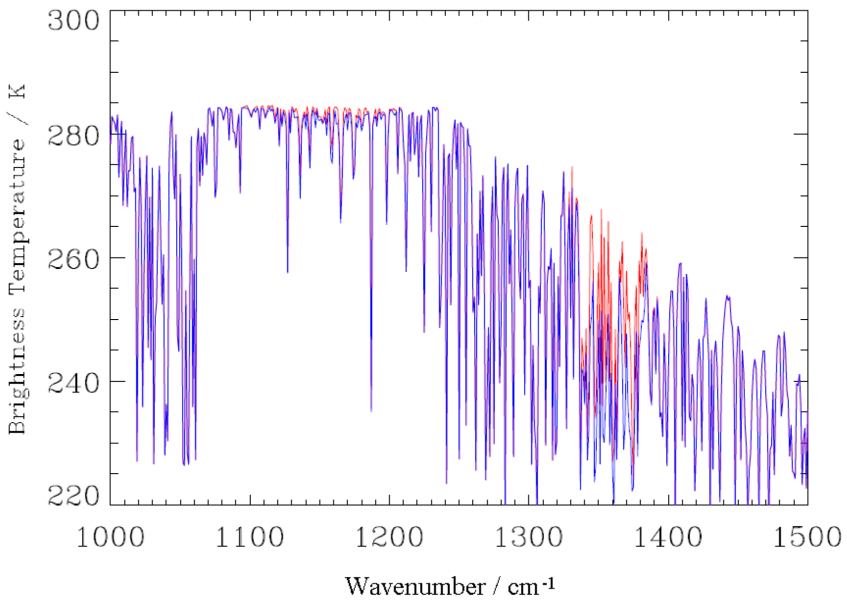

Figure 4.1: Brightness temperature spectrum for a midlatitude day climatological atmosphere (red) and the same atmosphere with a moderate amount of SO_2 between 11 and 17 km (blue). The main features are apparent between 1100 and 1250 cm^{-1}.

4.4 Forward modelling of the atmosphere

The operational forward models developed for near-realtime weather forecast and assimilation purposes (with HIRS/2) are comprehensive and could be computationally expensive. As mentioned in Chapter 3 there are many ways of forward modelling the atmosphere that should be appropriate to the desired product.

4.4.1 HIRS/2 forward models

Radiative Transfer for TOVS (RTTOV) is a radiative transfer model (developed by the UK Met Office, (ECMWF 2001, Saunders et al. 1999) designed to simulate the instruments of TOVS including HIRS/2, and is used extensively (particularly for assimilation) because of its speed. It calculates layer transmittances for a variety of trace gas species using look-up tables of parameterised

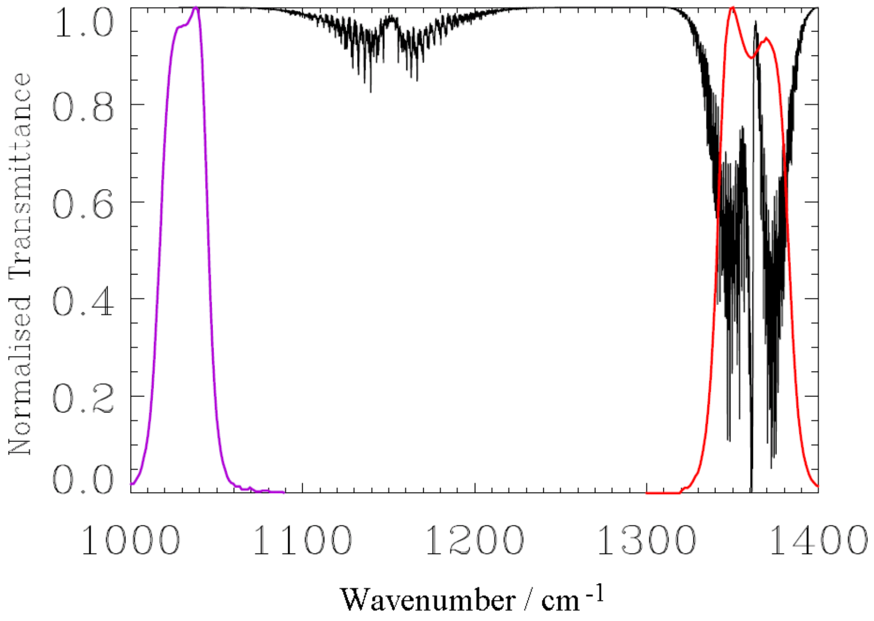

Figure 4.2: Relative positions of two NOAA 11 HIRS channel response functions centred at 9.7 μm (1028 cm^{-1}) (purple) and 7.3 μm (1364 cm^{-1})(red), and two local absorption features of SO_2.

regression coefficients for a range of temperatures and pressures. It has been further developed since the TOVS system was first deployed, and is currently at version 10. There is also a version based on principal components for use with IASI (Matricardi 2010). RTTOV also has the functionality to compute partial derivatives using the forward model.

Whilst the operational retrieval methods for HIRS/2 data are generally comprehensive, they can only infer those atmospheric attributes that are physically represented in the forward model. In illustration, it has become apparent that in particular circumstances, atmospheric phenomenon require that the forward model be extended. Weaver et al. (2003) report that for high tropospheric dust loadings, HIRS channels sensitive to surface and lower tropospheric temperature and water vapour, are subject to a $\sim$ 0.5 K decrease in observed brightness temperature. Ackerman (1996) identified negative brightness temperature differences between HIRS channels 8 (11 μm -window: surface/cloud detection) and 12 (6.7 μm - 500 hPa: H_2O) over cold scenes. Ordinarily, surface emission is expected to yield a higher brightness temperature than at 500 hPa, thus negative differences (BT_8-BT_{12}) indicate a temperature inversion. This is consistent with radiative cooling under clear skies and indicates a cloud free scene. This has been exploited for use in low level cloud detection (Wylie et al. 1994).

Desired features of a forward model are both sufficient accuracy relative to the instrument it is designed to emulate and computational speed. The radiation from the atmosphere that a satellite would see can be calculated in a variety of ways. The most accurate (with most complete physics) is a model that calculates the spectral radiance as a function of wavenumber, for a given atmospheric state. There must be some representation of atmospheric gases, temperature and pressure. One such model is the RFM (Reference Forward Model) (Dudhia 2002) discussed later in this chapter. This performs a line-by-line calculation for the emission of desired atmospheric gases, and their contribution to the top of the atmosphere spectral flux up to 120 km. Depending on the wavenumber resolution of the calculations, this may take too long to be of practical use, especially for large wavenumber ranges, but can yield high accuracy. Another method, preferred for its speed, is that of a band model, such as that which the Prata fit method is based upon. These are generally instrument specific. The spectral range of each channel and instrument response function for that channel are used to produce simulated channel measurements using low resolution look-up tables (or parameterised functions) representing atmospheric emission in that region. These models are limited in their accuracy by their construction (Goody & Yung 1995), but they are quick. As described, RTTOV estimates channel brightness temperature based on ‘predictors’ or coefficients for layer transmittances that are generated for a range of atmospheric profiles. As such, it is extremely fast, but as it stands it does not incorporate any representation of SO_2 other than a climatological value. If one were to alter the transmittance model to include SO_2 it would require substantial re-working of program code, which was considered beyond the scope of this project.

Defining the SO_2 column

Total SO_2 amounts are conventionally measured, as with O_3, in Dobson Units (or milli-atmospheric centimetres). These are defined as the height, in centimetres of a column with a cm^2 cross section of a gas if all the mass were to be brought down to room (not standard) atmospheric temperature and pressure, i.e. the surface. Alternatively, one Dobson Unit is equal to 2.69×10^{16} molecules cm^{-2}. The atmospheric SO_2 column is calculated using a finite summing of SO_2 concentration (in parts per million by volume) converted into units of number density. The partial pressure of SO_2 is equal to the molar fraction of the atmospheric pressure constituted by SO_2. Its density is calculated and is temperature dependant, whence its total mass and volume (for a Dobson Unit though strictly a height may be interpreted as a volume as its other dimensions are fixed) may be found, according to:

$$\rho = \frac{P[SO_2]M_r}{RT} \tag{4.1}$$

$$m_{SO2} = dz\rho \tag{4.2}$$

Where m_{SO2} is the total mass in a layer dz thick, $P[SO_2]$ is the partial pressure of SO_2, Mr its molecular mass, R the specific gas constant, T layer average temperature, m_{SO2} the mass of SO_2 in a given layer and density is denoted ρ. These are summed in the column section to yield M_{SO2}.

$$DU = \frac{M_{SO2}RT_0}{P_0M_r}. \tag{4.3}$$

where T_0 and P_0 the temperature and pressure at the surface. Outside the region of an explosively erupted volcanic SO_2 plume, the background level of SO_2 in the atmosphere is small, typically less than 1 DU. The uncertainty on this value that may contribute to an error in plume mass estimates error is considered to be negligible. As discussed in the introduction chapter, sources of tropospheric SO_2 (in addition to volcanic effusion or minor explosive eruption) include fossil fuel or biomass burning. The vertical transport of these emissions is limited to convective processes and SO_2 is quickly oxidised and mixed in the troposphere. Away from source regions or in the stratosphere SO_2 levels are reasonably static (Holloway & Wayne 2010). It is a large but necessary assumption that the only presence of SO_2 that will contribute to the profile radiance comes from within the bounds of the estimated region of the plume (beyond that of a suitable climatology). It can be shown that there is limited information for signal for SO_2 with HIRS/2 and lack of inherent height information, so accurately locating all of the material is challenging. It must be accepted therefore that from *a priori* information the SO_2 is expected to lie within this region, and that some degree of tailoring is required for each eruption case to which this method is applied.

4.4.2 Locating the SO_2 layer

The case study involves the 1991 eruption of the Chilean volcano Cerro Hudson (Chapter 5). Doiron et al. (1991) used an atmospheric transport model to recreate the advection of the plume as detected by the TOMS instrument. They found that the best spatial fit to TOMS observations in terms cloud position was achieved by initialisation of the material between 10 and 14 km, with a “best estimate” of 12 km. The ash and the SO_2 plume did not remain collocated for very long after the eruption as suggested by ash detection from the Advanced Very High Resolution Radiometer (AVHRR) (Constantine et al. 2000). These results supported the findings from CTM modelling experiments presented in Schoeberl et al. (1993). In addition, contemporary lidar measurements of the Hudson plume were made at the CSIRO (Commonwealth Scientific and Industrial Research Organisation) Division of Atmospheric Research, at Melbourne, Australia (38° S, 145° E) (Barton et al. 1992). The observations were made at wavelengths of 355 and 532 nm by a Nd:YAG lidar (circa 1 μm), which is considered sensitive to tropospheric cloud, mineral and aqueous aerosol. Observations at the lower wavelength did not begin until October, and dual wavelength operation still incurs a time delay of up to 75 minutes between observations as the instrument is re-calibrated. Noisier profiles can result from fewer ‘shots’ from the laser, and its contributing uncertainty may be quantified after normalisation of the backscatter profiles. Some very useful (although more qualitative) information may be gleaned from the backscatter profile alone, and constitute the results discussed below.

Figure 4.3 shows 4 backscatter profiles measured by Young et al. (1992). They tend to indicate peaks at around and above 20 km, and frequently at 10-13 km. The higher peak is attributed to aerosol from the Pinatubo eruption. Some features above the Pinatubo main feature are artifacts of low signal and poor calibration for use at that height. Young et al. (1992) interpret the majority of observations that are thought to include Hudson material as the feature at 12 km in October, with variable cirrus at 10 km. It is reported by the authors that the cloud was observed consistently from 28th August until December 1991 between 10 and 13 km, with a decreasing scattering ratio.

The confirmation of the material responsible for the lidar backscatter may be obtained by comparison to other observing methods. Retrospective SAGE II (Stratospheric Aerosol and Gas Experiment II) measurements identified the dual presence of aerosol originating from the earlier Pinatubo eruption and localised enhancements from the smaller, confined Hudson cloud (Young et al. 1992). It should be re-iterated that the lidar does not locate the presence of gaseous SO_2, but the presence of erupted small volume tephra or the fully oxidised aerosol, as does SAGE II. To some extent it may be possible, using a combination of multiple measuring techniques including lidar, satellite observations of SO_2 and satellite aerosol measurements at more than one wavelength, to diagnose the exact life-cycle of a particular erupted plume. This has been attempted for the much larger case of Pinatubo, with some degree of success (Pitts & Thomason (1993), Schoeberl et al. (1993) and others), the mechanisms of which form part of the model developed in Chapter 2.

Since the lidar observations were made from a single location at a point distant from the source of the volcanic material, there are considerations when interpreting them. Firstly, there will be a lapse in time before the material can be expected to have been advected to the location of observation. Secondly, the spatial coherence of the cloud (which can be high for smaller eruptions) may preclude it from being observed even if it crosses in the locality of the zenith of the observation point. Furthermore, since the spatial and chemical characteristics will change with time, some evolution of the plume must be

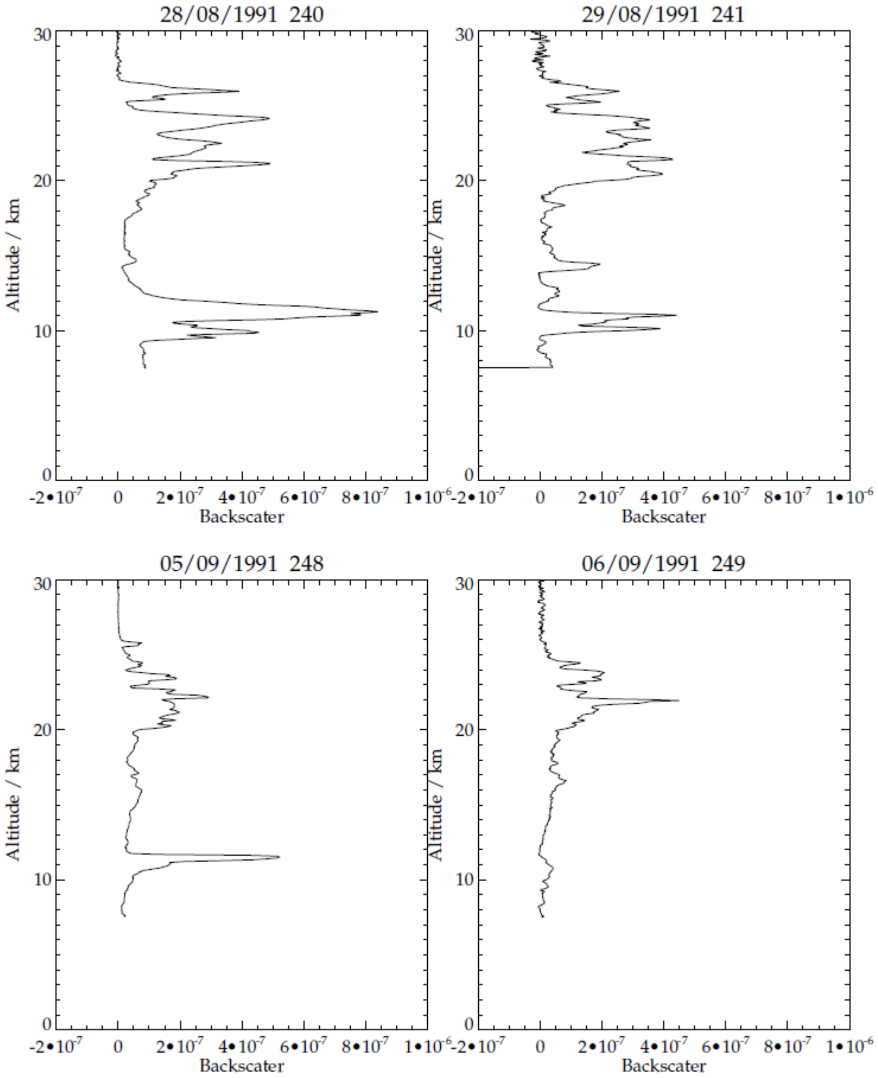

Figure 4.3: Lidar backscatter profiles measured at Melbourne, Australia. the feature around and above 20 km is associated with the residual aerosol from the Pinatubo eruption that occurred on 15th June 1991, two months before the eruption of Cerro Hudson. The features that occur intermittently at 10-14 km are thought to be associated with the material from the Hudson eruption.

allowed for. Lidar is sensitive to sulphate aerosol and ash. As mentioned, these materials may have differing heights of neutral buoyancy, and be advected at differing rates.

Whilst lidar is not sensitive to the presence of gaseous SO_2 inferences can be drawn from the height of the aerosol it eventually becomes. The backscatter cannot be trivially inverted to yield an estimate of profile amount, since it depends on both effective radius of the material and its concentration. Such avenues of pursuit are beyond the scope of this project, but are discussed in Young et al. (1992). In this case the lidar information may only be considered a starting point, and perhaps a guide for estimating the cloud height of the SO_2, to be considered in the context of other information.

Defining the lowest confine of the perturbation using lidar is challenging, as meteorological cloud is indistinguishable from an aerosol/ash cloud. Furthermore, the ash in particular will exhibit a more noticeable downward propagation owing to a higher sedimentation rate than sulphate aerosol, and certainly SO_2. The relative proportions that contribute to the backscatter measured are expected to be dominated by ash in the first few weeks after the eruption. Little ash is expected to be present after a month beyond the eruption, but by this time the vast majority of the SO_2 will have oxidised into aerosol.

In total there were six observations made in August 1991 from 13^{th} onwards. Only two in August, on 28 and 29^{th}, display a prominent feature at the height at which material from the Hudson eruption is expected. Six observations were made in September, five of which were 4–7 days apart and each showing some evidence of material at around 12 km. In October 1991 three observations were obtained, and all potentially indicate that the Hudson material is still present. A sample of observations is shown in figure 4.3.

Aircraft and ground observations of the Cerro Hudson plume are reported in Naranjo & Stern (1998) (in Spanish) and partially reproduced (in English) in Constantine et al. (2000), but in the latter it is not stated how the altitude of the plume is estimated (or inferred) or whether from the ground or from the aircraft. Plume heights are reported from 7 to 18 km, and would relate to the ash or optically thick erupted material such as condensed water vapour. The eruption on the 15^{th} August is reported to be the highest at 18 km, with plumes on previous days estimated at 12 and 15 km, however at present it cannot be determined to what extent this is a qualitative estimate.

These data from lidar, aircraft and modelling with TOMS data provide some justification for estimating the height of the material as being between 10 and 14 km, and that its most probable profile shape is triangular when considering the typical profile of volcanic intrusions into the stratosphere. Based on this the SO_2 profile will be represented in the forward model as a triangular profile based at 11 km, peaking at 12 km and returning to the climatology at 13 km. An attempt will be made in forward model simulations to estimate the potential errors that arise from incorrect supposition of both plume height and plume thickness in the forward model.

4.4.3 Initial approach

The initial approach followed to create a retrieval scheme for SO_2 with HIRS/2 was a full line-by-line profile retrieval of water vapour, temperature and SO_2. It used 17 of the 19 HIRS/2 channels. The state vector comprised a temperature profile which spanned the troposphere and lower stratosphere (to encompass any volcanic plume height), a tropospheric water vapour profile (which had some correlation with height) and a short SO_2 profile in the expected height region of the plume in question. Sulphur dioxide and H_2O profiles were retrieved in log space to promote numerical stability, better representing the relative magnitudes of H_2O and SO_2, and background SO_2 and volcanically perturbed SO_2. Initial tests revealed that depending on the state - namely the amount of SO_2 in a column - there was usually less than one degree of freedom for signal for SO_2. Accordingly, this SO_2 profile was represented by three points, one each above and beneath the plume, and one at its centre (in pressure), which formed a triangular profile. The outer points had a very small *a priori* covariance, essentially fixing them at the background value, and the centre point was free to move, to be scaled by the retrieval. As such, the retrieval was only really retrieving one element for SO_2 in accordance with the level of information available in the measurements. The core of the forward model was the RFM. The RFM has the ability to evaluate spectral radiance line-by-line at a resolution of up to 0.0001 cm^{-1}. The RFM is based on the General Line-by-line radiative transfer model (GENLN2) (Edwards 1992) and uses databases of atomic and molecular properties in its calculations. The

RFM is initialised by a driver file, which details the spectral range(s) and resolution upon which emission/absorption is calculated, the gases that make up the atmosphere modelled and the location of the files that contain the gaseous concentrations, temperature and pressure at predefined height levels. The driver table also tailors the model with more sophisticated parameters, including the invocation of particular line shape models and the atmospheric continuum depending on what aspect of the atmosphere is being modelled. The output files of the RFM for these purposes consist of the spectral radiance for the specified wavenumber range.

A considerable degree of effort was applied to making the multi-channel line-by-line approach work, but it eventually proved unsuccessful. Though the scheme worked successfully on simulated retrievals (introduced later in this chapter), it fared poorly with real measurements. It is not within the scope of this work to digress excessively into the shortcomings of this approach, but they are briefly outlined. It is considered that the forward model could not fully characterise the instrument and its measurements. Measurement noise for each channel relied solely on the noise equivalent differential radiance (NEdN) combined with a derived forward model error (FME) appropriate for the RFM. In retrospect, this FME was undoubtedly an under-estimate, and failed to represent the true variability of the atmosphere as measured by HIRS/2. Fundamentally, it lacked an estimate of the error covariance between the channels and species (i.e. the off-diagonal elements of $\mathbf{S}_y$). As such, the impacts of failure to represent variations in water vapour and temperature upon the retrieved SO_2 were neglected. Of the scheme's ability to retrieve SO_2, it would be fair to say that it was capable of predicting the presence of a large amount of SO_2, with poor accuracy, or predicting that there was none, with slightly better accuracy. The number of elements in the state vector were also too many. Despite resorting to a generous correlation length in the a priori covariance for water vapour to prevent oscillations in the profile, all retrieved profiles of water and temperature had a characteristic shape in the lower troposphere that was un-physical. Any deficiency in the retrieved water vapour had a significant impact on retrieved SO_2, because the $7.3\,\mu$m channel is sensitive to both. As it stood, achieving a global fit for all channels for the three components of the state vector was unfeasible. As the RFM was incapable of representing cloud, all test retrievals were completed on data that had to be cloud-cleared. The cloud clearing used both the IR and visible HIRS/2 channel information. The former used the departure in the 11.1 μm window channel from the skin temperature as defined by the European Centre for Medium-range Weather Forecast (ECMWF) 40 year Reanalysis (ERA40) data 1 [1]. The latter used the visible reflectance derived from channel 20. Whilst the criteria would have screened for most cloud, there are many circumstances where they may have been insufficient. The presence of any sort of cloud would have introduced significant problems in attempts to fit the measurements with the RFM/forward model.

There were also significant limitations from using a line-by-line model for multi-channel (covering relatively broad spectral regions) with a large state vector; that of computational expense. In order to obtain the optimal solution in the retrieval process, the forward model was required to call the RFM to calculate the atmospheric radiance and adjust the input profile until the modelled brightness temperature converges to the measurement. There are of the order of 700,000 scans for all channels for one day of global coverage by HIRS/2. After several iterations at an appropriate wavenumber resolution it would require the RFM to be run several million times just for one day's data. This is highly inefficient and would take too long to be useful. Part of the functionality of the RFM is the ability to pre-compute look-up tables of the transmissivity of the atmosphere at a range of heights as a function of pressure, temperature and conceivably water vapour (since it can potentially alter the transmission properties of a layer in high enough concentrations). In reality, this means calculating tables of the absorption coefficient, K_ν (Eq.3.16). K_ν is a function of these variables, and varies with the amount of absorbing material and the absorbing properties of the material at that wavenumber. Utilising these tables proved sufficiently accurate and speeded up the retrievals considerably, but it would still have taken up to a week to process 1 day of HIRS/2

---

[1] ECMWF Reanalysis product that used a consistent model and observations to produce a 40 year set of variables that best represented the atmosphere. It is discussed further later in this Chapter.

measurements, even with strict cloud screening.

There were some positive outcomes from this approach, upon which a new scheme arose. The triangular, mid-point variable representation of the SO_2 column was retained, for being a more intuitive way of representing the SO_2 mass in a volcanic plume. The principal advantage was an opportunity to understand the process of building the rest of a forward model around a line-by-line radiative transfer model. Convolution of instrument response functions with spectral radiance for channel brightness temperatures (BTs) and correct calculation of the weighting functions, in addition to generating a retrieval engine tailored to the problem, provided a grounding for the updated scheme. Furthermore, the simulation of HIRS/2 channel BTs for a given atmosphere may be used to test a future forward model, where the RFM represents the reference case, since it is spectrally most accurate. An overview of the mathematics involved with this aspect is detailed later in this chapter, in the discussion of simulation of measurements (Section 4.6.2).

4.4.4 HIRS/2 column retrieval

Given the experience yielded by the previous approach to retrieving SO_2 with HIRS/2, a new, simpler approach was proposed. The $7.3\,\mu$m channel proved to be sensitive to both water vapour and SO_2. The weighting function for water vapour of the $6.8\,\mu$m channel peaks at around 500 hPa (around 5 km), and as such would be sensitive to the region where the vast majority of the water vapour in the column resides. To represent both channels accurately, some knowledge of cloud is required, which may be gleaned from the $11.1\,\mu$m channel window channel. This channel is highly sensitive to the emitting temperature of the lowest surface it observes (be it cloud or the surface), thus with some knowledge of the surface and atmospheric temperature profile it is possible to obtain an estimate of cloud top height. This yields a condition where there are potentially three desired quantities, based on information from three measurements.

Other useful information can be obtained from the remaining HIRS/2 channels, but they are not used directly in the retrieval. Notably, channel 10

(12.5 μm) can be used in ratio with channel 8 (11.1 μm) as an indicator of ash or aerosol. Many of the other channels can be used to gain information about cloud and aerosol, including the shortwave channels 18 (4.0 μm) and 19 (3.7 μm), the results of which are shown later in this chapter and the next.

The background and meteorological information used for this column retrieval is that of the ECMWF Re-analysis (ERA) -Interim product. ERA are the output of the ECMWF operational re-analysis product run for a period of time with a consistent version of the re-analysis model and available observations. This then provides a consistent dataset for examining trends in atmospheric variables over a number of decades (Dee et al. 2011).

The forward model

As discussed in section 4.4.1, RTTOV is a fast forward model (FM) that is widely applied as a forward model for many instruments, notably those from the TOVS genus. The main reason that it was not considered feasible for use for modelling SO_2 with the HIRS/2 instrument previously is that it did not represent SO_2 as a variable within its coefficients used for calculating transmittance. It was considered that a major reworking of RTTOV was outside the scope of this project. As a consequence of extensive work with its application to other instruments, Dr Richard Siddans, at the Rutherford Appleton Laboratory, was able to offer some sets of bespoke predictors for RTTOV that did not require any modification of the mechanics of RTTOV itself. The coefficients were generated by 'training' methodology using an extensive range of atmospheric profiles, where the SO_2 was represented from very low/background levels to very large perturbations, after Matricardi (2008) and Siddans (2011). This approach retains the speed and accuracy offered by RTTOV and enables the model to be used to represent atmospheric gases for future instruments not already catered for by ECMWF (2001).

The RTTOV coefficients for SO_2 are generated using physical properties of SO_2, but in the atmospheric information that is given to RTTOV, they replace that for CO, which can be shown to be an unimportant species for the HIRS/2 channels used. The calculation of these coefficients is an involved and time consuming computational effort. Three versions of the coefficients were provided for the purposes of this work, where the third was found to be suitable. Despite being trained with column amounts up to 100 DU and 300 DU respectively, the first two versions of the coefficients did not perform well in simulations. Dr Siddans was able to ascertain that by limiting the predictors that could be selected within RTTOV to just those that had a linear relationship to the column SO_2, rather than the more complex higher order predictors that were related to the SO_2 column squared for example, then their behaviour was stabilised. It is thought that this might be a result of both the dynamic range that SO_2 can exhibit in a volcanically perturbed atmosphere, and the fact that RTTOV was not explicitly designed to model SO_2 for this instrument. These more straightforward sets of coefficients come at a cost of some degree of accuracy, which is explored further in comparisons to a line-by-line model. Some comparative simulations are shown and discussed further in 4.6.3.

From TOMS results for the case study eruption in this work (Constantine et al. 2000), it was apparent that column amounts exceeding 200 DU were present where TOMS values appear to saturate, and that HIRS/2 could potentially observe. As such the forward model would have to behave in a physical way up to at least this value, and preferably beyond.

The column retrieval uses atmospheric profiles from the ERA-Interim product to simulate the atmosphere. These contain profiles on a pressure grid of 37 levels from 1000 hPa to 1 hPa. Within RTTOV these are interpolated on to an internal height grid if required. RTTOV is capable of generating weighting functions, but they refer to the sensitivity of the simulated measurements to perturbations in the atmospheric profile, rather than directly to changes in state vector. As a result, these are calculated numerically in the forward model. RTTOV has certain physical limits for its input values, and when occasionally the predicted new state values lie outside these they are manually constrained in the FM by the physical limits that RTTOV will accept. The weighting functions are allowed to make linear extrapolations beyond these limits, allowing the retrieval more freedom, as shown in equations 4.4 and 4.5.

$$\frac{dY}{dX_i} = \frac{Y_{pert} - Y_i}{dX_i} \tag{4.4}$$

$$Y_{new} = Y_i + (\frac{dY}{dX_{i,SO2}})(X_{i,SO2} - X_{SO2,allowed}) + (\frac{dY}{dX_{i,H2O}})(X_{i,H2O} - X_{H2O,allowed}) \tag{4.5}$$

Where Y_i are the measurements simulated by RTTOV for a given element of the state vector X_i, $\frac{dY}{dX_i}$ are the weighting function evaluated at Y_i and Y_{new} are the predicted measurements, which will equal Y_i except in the case that the predicted state falls outside the stated permissible ('allowed') limits.

Weighting function perturbations were 0.1 km for cloud top height and 1.0 % for the water vapour and SO_2 column scaling factors. For the version of the RTTOV coefficients used in the retrievals, to be referred to as 'vc3', the physical limit is additionally constrained to a maximum of 800 DU, as simulations with a line-by-line model suggested that above this value the channel itself begins to saturate. This means that even for an increasing amount of SO_2, the instrument channel is no longer sensitive to it. The H_2O profile scaling factor is limited to a minimum of 0 and a maximum of 20, where 1 would suggest that the ERA-Interim profile and the HIRS/2 pixel measurement it is matched to were entirely consistent. The maximum cloud top altitude that the forward model permits is 16 km, and is a level defined by RTTOV in this instance.

Simulation tests were performed where no physical limits were placed upon the forward model except those implied by RTTOV, but under rare circumstances attributed to particular atmospheric profiles from ERA-Interim this increased the frequency of a failure to converge, and often led to longer iteration time with no improvement in performance. Limiting the application of the H_2O scaling factor to a nominal 'troposphere' depth did not improve the performance of the retrieval.

As per the initial approach, measurement noise as defined by the noise equivalent differential radiance values given by NOAA (NOAA 2000), are used to create look-up tables with the RFM of scene dependent noise estimates for HIRS/2, as described in section 4.6.2.

Figure 4.4 shows the profiles upon which the RTTOV coefficients were based, using perturbations on a range of profiles for different atmospheres, and used elsewhere in this work to generate information about the covariance between ERA-40 profiles. It is worth noting that none of these profiles explicitly resemble the volcanic plume perturbation that is used in the case study for this work. As such, it is important to test (against a line-by-line model and where relevant a cloud model) that the forward model incorporating RTTOV behaves appropriately. As further versions of the coefficients were developed, these were scaled to represent larger perturbations up to 300 DU for vc3. It is possible that inclusion of training profiles that better resemble those that are used in the retrieval, or those that typically exist in the real atmosphere, might present an avenue for development of the RTTOV coefficients. Indeed, for higher column amounts or larger eruptions that place material higher in the stratosphere, this would certainly be appropriate, but is beyond the scope of this work.

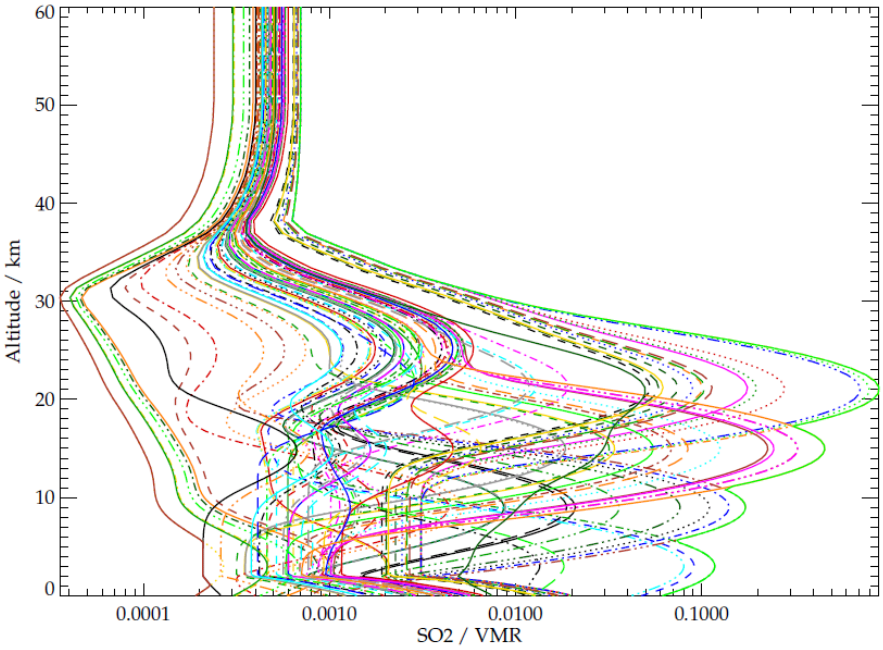

Figure 4.4: 83 SO_2 profiles used to generate the RTTOV coefficients for SO_2 in volume mixing ratio (VMR). They represent a range of SO_2 perturbations at different altitudes and magnitudes, and include maximum and minimum envelope of the function, and a mean of all of them.

Representing SO_2 in the forward model

For SO_2, the approach used during previous work (4.4.3) is largely retained. The profile was represented by a 3 point triangle where the bottom and top elements were essentially fixed by means of a very small *a priori* error. Thus the retrieval was essentially only free to move the mid point. For the present application, this approach is slightly modified. The element of the state vector concerned with SO_2 is a profile scaling factor. In the forward model, this scaling factor applies to a specified height region of the SO_2 profile, scaling all elements within and none outside this. The expected region of the volcanic plume is estimated using lidar and the reported results from modelling of the eruption, and are introduced later in this chapter. The SO_2 profile within this height region is normalised to a triangular profile with an integrated mass of 1 DU over its entirety. This was partly done to ease interpretation, since the retrieved scaling factor would be approximately equal to the total amount of SO_2 in the column. The rest of the profile is prescribed by a background SO_2 volume mixing ratio climatology 2, the total column mass of which is less than 1 DU [2]. As the ERA-Interim profiles are based on a constant pressure grid, the precise altitude grid varies from profile to profile. In the expected region of the SO_2 plume, a consequence of irregular pressure levels can be insufficient levels upon which to represent a triangular plume profile for scaling. When this occurs, the retrieval/profile height grid adds additional equally spaced levels from which it can construct the background 1 DU plume profile in that region. The additional levels are also applied to the rest of the trace gas and temperature profiles. An example of how this is achieved within the setup of the retrieval is given in Figure 4.5.

Establishing an appropriate SO_2 *a priori* error is potentially a non-trivial issue, with regard to a retrieval problem where the measurements have relatively little sensitivity. As discussed previously in this work, a volcanically perturbed SO_2 profile can contain 2 or 3 orders in magnitude more than a background profile, and at the heart of a large plume this can be even more.

---

[2] Set of climatological profiles originally developed by Prof. J. Remedios for use with the MIPAS instrument and provided as part of the RFM package (Dudhia 2002).

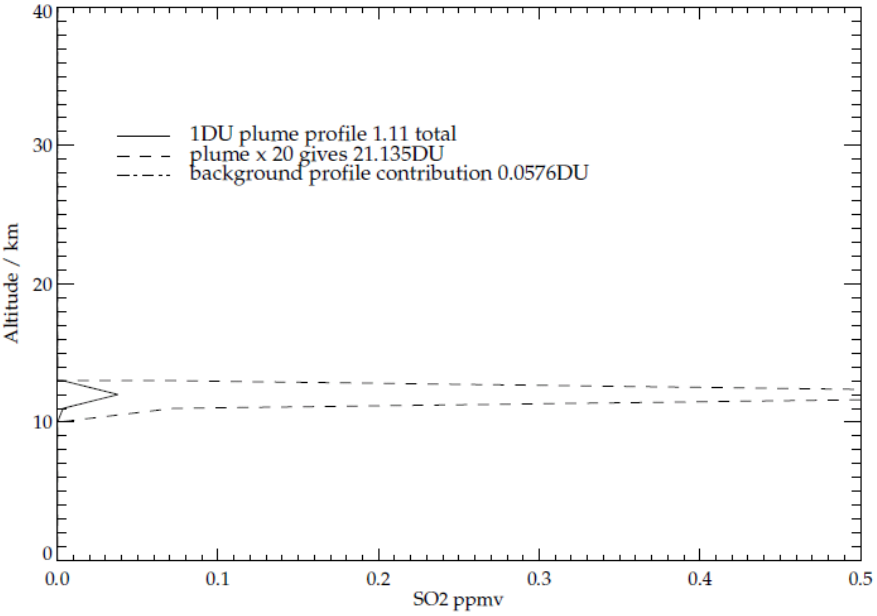

Figure 4.5: The 1 DU basis profile for the forward model is shown by the thick black solid line in parts per million by volume (ppmv). The profile is triangular in log pressure. It is generated individually for each pressure profile. An exemplar scaling factor of 20 DU has been applied to this, and indicated by the dashed line.

A good *a priori* error gives the retrieval the freedom to find a correct minimum in cost space, and can restrict it from converging on a solution that is un-physical. The variance for a background profile would be very small, as opposed to a profile where SO_2 is expected, which would be very large. If there is sufficient information contained within the measurements, one would conventionally use a $\mathbf{S}_{a(SO_2)}$ that spans both scenarios.

Representing H_2O in the forward model

In an analogous way to SO_2, H_2O is represented in the state vector by a profile scaling factor, but it applies to the entire profile rather than a localised region. The profiles used for retrieval are those from the ERA-Interim product, but any climatological profile can be used. In the case where a scaling factor is close to one, it would indicate that the H_2O profile is similar to that which produced the measurement. In the case of a simulation, this is exactly the case.

Representing cloud in the forward model

The third element of the state vector is cloud top height (CTH), or specifically the geopotential height at an equivalent pressure level. The channel primarily sensitive to cloud top height is the 11.1 μm window channel. It was found that the speed of convergence was greatly reduced when the first guess and a priori cloud top height were very close to the solution. As such, these are assigned before the retrieval using a mini retrieval fit, where the cloud top height alone is estimated using RTTOV and the ERA-Interim temperature and pressure profiles. The channel BT is simulated iteratively for a range of cloud top heights spanning the troposphere. The CTH most probable is that for which the simulated BT agrees best with the measured channel BT. There is some account for the presence of a temperature inversion, which occurs when the temperature lapse rate with height changes sign. This can occur under several meteorological circumstances. Most pertinent to the region of interest (Southern Hemisphere mid to high latitude over ocean) is the occurrence of large regions of cool air over the sea surface that arise because of sea fog formed by radiative cooling under clear skies, or from other types of cloud over a cold ocean. The test for cloud top height checks for an inversion in the temperature profile, and if present will select the cloud height above the inversion if the simulated BT is also in good agreement. The *a priori* error associated with cloud is 10 km, which implies a variance of 10^2 km^2.

4.5 Forward model error

As discussed in the previous chapter, forward model error (FME) is an important component of the retrieval. The evaluation of accurate forward model error is challenging. Ideally it can only truly be evaluated by a comparison with a real atmosphere, or alternatively a 'perfect' model, which constitutes a substantial theoretical problem. As such, other ways must be contrived to estimate the magnitude and sources of uncertainties that arise from the limitations of the forward model, or the way in which it is used. There are a number of ways of estimating FME, many of which depend on the relative sophistication of the forward model and its flexibility. For a forward model based on an accurate line-by-line radiative transfer model such as the RFM, one may break down the components of the FME and estimate them individually. They might include the following, whereby the model is tested in comparison to an appropriate ‘reference’ state:

- Spectral resolution of the forward model.
- Use of precalculated look-up tables for speed as opposed to ‘online’ line-by-line calculations.
- Including in the FM non-retrieved gases at their climatological value.
- Excluding other gases which are known to exist in the real atmosphere.
- Representing the vertical atmosphere at limited height resolution.

The prior version of the HIRS/2 retrieval scheme used the RFM for its principal radiative transfer calculations, and thus required extensive simulations in order to generate estimates of the FME. The FME components are defined in terms of the effect on the channel brightness temperatures calculated from a modelled atmosphere, as compared to some reference case. This may be arbitrarily defined. It may be as closely related to the real atmosphere as possible, or represent some extreme aspect of accuracy within the model setup. For the scheme presented here based on RTTOV, these estimates of FME are still applicable, but represent the lowest possible estimate for each channel due to the relative accuracy of these radiative transfer models. It is possible to then estimate further components of FME specific to the model based on RTTOV or the forward model in its entirety.

Error contributions deemed significant in the discussion of the RFM are those that for a channel stand out from the others in terms of magnitude, and that exceed the noise equivalent brightness temperature difference for a given scene temperature. The absolute difference between each test case and the reference case is taken as the channel contribution of FME. The simulations were performed for all 19 of the HIRS/2 channels, irrespective of the fact that only three are used in the column retrieval. Extensive simulations with the RFM were performed that tested the sensitivity of the channel brightness temperatures to variation of the elements listed above. The RFM was run with spectral resolution ranging from $0.001\,\mathrm{cm}^{-1}$ to $0.1\,\mathrm{cm}^{-1}$ to quantify the effects of a reduction in spectral resolution. The largest difference is seen in the first few channels. As well as being sensitive to the forward model resolution, channel 1 is known to be subject to considerable noise (Susskind et al. 1983).

The change in simulated channel brightness temperature for gaseous species at their climatological level and 1 SD from it were used to quantify the individual impacts of non-retrieved trace gas variability. The most prominent feature is that resulting from the representation of O_3 in channel 10. In the real atmosphere ozone concentration varies significantly, which is reflected in the variance of the climatology used in this test. The effect is so significant that without retrieving ozone the channel becomes effectively swamped by noise from ozone variability. This channel is used operationally as an indication of column ozone concentration, and not used in the SO_2 column retrieval. The RFM was also used to simulate the impact of including all of the minor species such as SF6 and F12-14 (anthropogenic halides). They showed that provided one accepted that their variability was low in the real atmosphere, there was very little sensitivity to them and they did not require inclusion in the background profile used in the forward model, but by this method their exclusion contributed quantitatively to the FME.

All elements of forward model error are combined in quadrature. The combined FME estimated is shown in Figure 4.6 as a function of channel.

The forward model error as defined by calculations with the RFM is not definitively appropriate to a forward model centred around RTTOV. It will contribute to the estimate of the total FME for the purposes of this method development in the absence of an equivalent term being evaluated for RTTOV, and broadly constitute a minimum envelope of FME for the HIRS/2 channels.

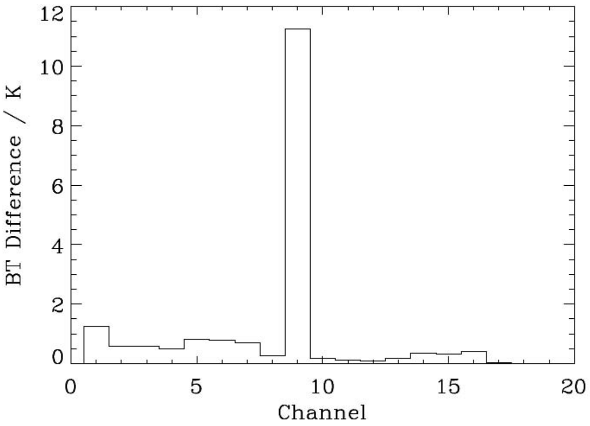

Figure 4.6: The combined elements of the forward model error components as estimated using the RFM, combined in quadrature. The 'BT Difference' is the estimate of forward model error for each channel.

4.5.1 *A priori* and covariance

The amount of SO_2 in the stratosphere and troposphere can vary enormously. It is not a well mixed gas, and readily oxidises (as does one of its precursors H_2S) into sulphate aerosol in the presence of water vapour and other oxidising species. The implication for retrieval using optimal estimation of such a sporadic and inhomogeneously localised species is that the *a priori* and *a priori* covariance must reflect this variability. For the majority of simulations, and later with real measurements, the SO_2 scaling factor *a priori* is set to 1.1 times the value of the first guess, 100 (equivalent to a column of 100 DU). The variance is assumed to be 500^2, representing the fact that the background SO_2 column can be less than 1 DU, and after a large explosive eruption it can rise to more than 500 DU, but for the eruption that comprises the case study in this work, it is not expected to. A first guess of 100 is chosen because when there is a relatively weak amount of information within the measurements, it is often possible that the retrieval can converge before it has reached the correct minimum in the cost function, but it would be very unlikely that the converse would occur. For low levels of SO_2 there can plausibly be occasion where an aberrant water vapour profile can be retrieved in place that sufficiently meets the convergence criteria of the retrieval engine. To optimise the opportunity for a good solution for SO_2, the first guess and therefore the *a priori* are set relatively high.

Water vapour varies a great deal, particularly within the low to mid-troposphere. For retrievals with real measurements, meteorological data will come from the ERA-Interim product. For testing the retrieval, the water vapour profiles typically come from the atmospheric profiles that were used to simulate the measurements (which can include ERA-Interim, but also ECMWF and MIPAS climatologies). As such, the *a priori* of the H_2O profile scaling factor is nominally set to 1. There are several ways of estimating the *a priori* covariance of a water vapour profile in the atmosphere, but this must be represented for the purposes of this scheme in one number that applies to the whole profile.

The covariance used here is based upon a variance of ECMWF profile error. This is translated to a fractional difference to a water vapour profile and used as a representative of variance in the scaling factor. It is expected to be a lower bound. There are several ways of improving upon this estimate, but they are reserved in anticipation of an evaluation of how the scheme performs on real measurements, as this will better reflect how the variance in the water vapour profile affects all aspects of the retrieval.

As mentioned in section 4.4.4, the first guess for cloud top height is obtained using a pre-fit with the 11.1μm channel only. This value is then used as both the first guess and the *a priori* to promote efficient convergence. Cloud top pressure can vary between effectively zero and the tropopause. As such, the a priori error is 10 km.

In all cases, it is required that this is tested using simulations to examine the sensitivity of the retrieval to both the *a priori* and the first guess.

4.6 Retrieval from simulated measurements

It is a requirement that the forward model used in the retrieval has the functionality to be able to simulate measurements, with which the scheme can be tested. If a retrieval scheme can retrieve properties of a state from measurements that the forward model generated, and those properties bear sufficient semblance to those that created the measurements, then one may have some confidence that the scheme is functioning in a desirable way. The retrieval scheme can be progressively tested for the appropriate ranges of the dependent variables, and some estimate of the scheme's quality and sensitivity can be established. It is also a pertinent exercise to elucidate the presence of more subtle problems and shortcomings of the scheme.

4.6.1 Simulating measurements with the forward model

The flexibility of the forward model was sufficient that a number of atmospheric scenarios could be used for tests with simulated retrievals. These included ECMWF, RTTOV and RFM sample climatologies, plus the ERA-Interim profiles for intended use with real measurements.

This retrieval scheme utilises the Levenburg-Marquardt method detailed in Chapter 3. The forward model called by the retrieval had the capability to simulate measurements from a given atmospheric state. As such, the forward model could be tested for its sensitivity to the amount of SO_2 in an atmospheric column, water vapour, cloud, the first guess, *a priori* and estimate of the measurement noise/forward model error. Dependence upon scan angle was tested but simulations did not indicate a bias with respect to scan position.

Figure 4.7 shows an idealised simulation that was one of several simulation tests of the column retrieval to qualify its behaviour, where the simulated retrieval was given the solution as a first guess and as an *a priori*. This is a basic and important test that must be performed to ensure that there are not inconsistencies between the forward model and the way that the retrieval simulates measurements, and if successful is expected to converge after one iteration to the solution. These are used to test the sensitivity of retrieval to various factors, and to compare it to other forward models in a useful way. The forward model weighting functions as described by equations 4.4 and 4.5, are given in Figure 4.8.

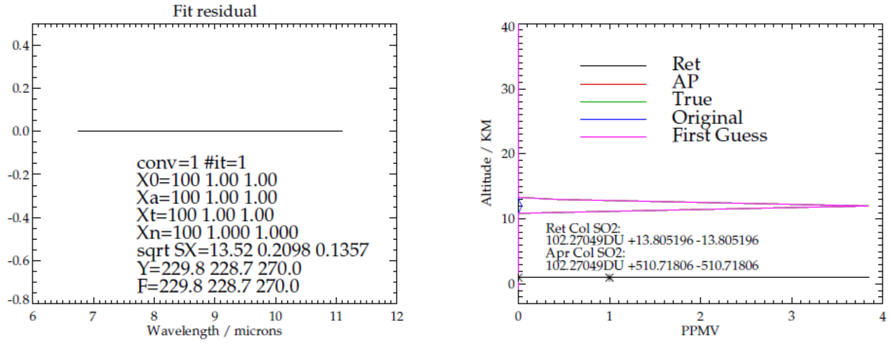

```
conv=1 #it=1
X0=100 1.00 1.00
Xa=100 1.00 1.00
Xt=100 1.00 1.00
Xn=100 1.000 1.000
sqrt SX=13.52 0.2098 0.1357
Y=229.8 228.7 270.0
F=229.8 228.7 270.0
```

```
Ret Col SO2:
102.27049DU +13.805196 -13.805196
Apr Col SO2:
102.27049DU +510.71806 -510.71806
```

Figure 4.7: The results of an idealised retrieval from measurements simulated by the forward model. In the left plot are printed some of the retrieval properties and diagnostics, where the order of the state vector X is SO_2 scaling factor, water vapour scaling factor and cloud top height. In the right plot, the retrieved profile (Ret),*a priori* (AP), True, and the First Guess profiles all overlay each other. Given the solution as the first guess equal to the *a priori* it converges after 1 iteration with no residual (given no noise), demonstrating that the simulated retrieval is consistent with the forward model. The Original unscaled profile is too small to be evident on this scale.

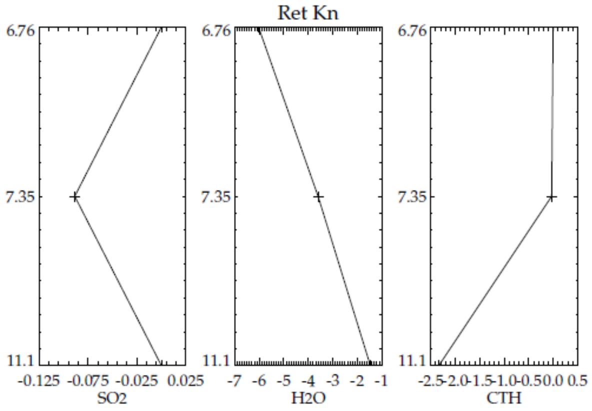

Figure 4.8: Weighting functions ('Ret Kn') for the column retrieval simulation. In the left plot, the enhanced SO_2 sensitivity in the 7.3 μm channel is apparent. For water vapour both the 6.8 μm and to a lesser extent 7.3 μm have sensitivity. The sensitivity to cloud top height comes from the 11.1 μm channel.

4.6.2 Simulating measurements with the RFM

As outlined earlier in this chapter, the RFM was used previously as the basis for a forward model for simulating HIRS/2 channel measurements. It may be used here to portray a reference model for comparison. The work presented here also demonstrates aspects of the instrument and application of previously outlined theory.

The RFM was used to calculate the spectral radiance in the region of the HIRS/2 channels for a given atmosphere, and also had provision to calculate the weighting functions, defined as:

$$K = \frac{dY}{dX(i)j} \tag{4.6}$$

That is, the partial derivative of the measurements to the state. As discussed in Chapter 3, this can be understood as the sensitivity of the measurement to a change in some element i of the state at height j. For weighting functions calculated using the RFM, the nominal change in $\mathbf{X}$ is 1 K in temperature or 1 % (ppmv) for gaseous constituents. The resulting RFM output is a difference spectrum.

$$\frac{\Delta Y}{\Delta X} = \frac{Y(X) - (Y(\Delta X) + Y(X))}{\Delta X} \tag{4.7}$$

This may subsequently be used to evaluate $\mathbf{K}$ in respect of the desired measurement units/quantities, but the RFM is used here principally to compare simulated measurements for the forward model used in this scheme. In the RFM evaluation, Y represents the change in spectral radiance (rather than channel brightness temperature in the retrieval). The desired measured quantity with regards to a nadir viewing satellite can be thermal emission from a small field-of-view of the atmosphere over a finite spectral region for which it has varying sensitivity, or an equivalent brightness temperature, as used for HIRS/2.

The RFM output as used here is in the form of spectral radiance as a function of wavenumber. However, for a given wavenumber range (or channel), the instrument response to the radiance will vary across it, as discussed in Section 4.1. This variation is termed here the instrument response function F(ν), and is predetermined at the time of the construction and calibration of the instrument. Thus, the total radiance 'seen' by the channel will be attenuated by the envelope of the filter or instrument response function. Therefore, it is necessary to integrate over the channel with regard to the variation in response from the channel as a function of frequency $F(\nu)$ for a channel i:

$$R_i = \frac{\int R_\nu F_i(\nu) d\nu}{\int F_i(\nu) d\nu} = \int_\nu R_\nu f_\nu d\nu \tag{4.8}$$

Where R_i is the channel radiance, R_ν is the radiance at wavenumber ν and f_ν is a fractional response function.

Since brightness temperature T is sought and the filter functions vary so much over a channel, it is not possible to use channel mean radiance and the central wavenumber to invert the Planck function directly. For each channel, look-up tables are required to relate T to R_i. The look-up tables were made by calculating a normalised channel radiance for a range of temperatures:

$$\int B_\nu(T).f_i(\nu) d\nu = \int R_\nu.f_i(\nu) d\nu \tag{4.9}$$

As described in Chapter 3, $B_\nu(T)$ is the Planck function at a given wavenumber as a function of temperature. Figure 4.9 shows the integrated channel radiances from the look-up table for channels 2 and 11 generated using this calculation. Also illustrated are the scene temperature dependent noise equivalent differential radiance values converted to brightness temperature, for which the RFM was used to generate look-up tables for use with the main retrieval scheme. Channels 2 and 11 represent channels with low and high noise respectively. As one would expect, the noise diminishes considerably with increasing scene temperatures.

The appropriate weighting function for modelling the state of the atmosphere, is a change in brightness temperature with respect to a change in state, each as a function of height in the atmosphere, $\frac{dT_\nu}{d\Gamma_j}$, where dT_ν is the change in brightness temperature at ν and $d\Gamma_j$ is the change in temperature at the jth level in the atmosphere. Since T$_\nu$ is a function of radiance R$_\nu$, and

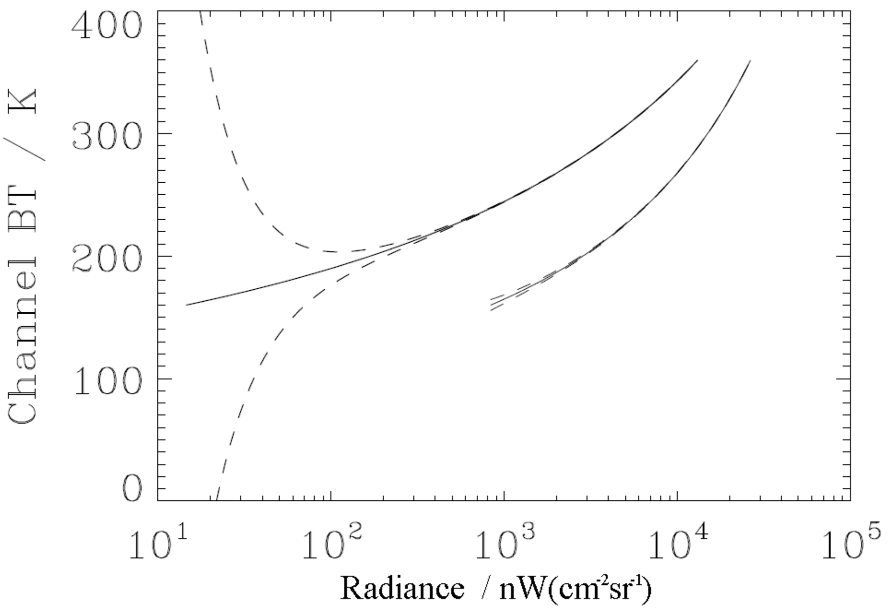

Figure 4.9: Brightness temperature conversion from channel integrated radiance, channel 2 (lower line) and channel 11 (upper line), with noise values indicated by the dashed lines. This demonstrates that channel noise increases as scene temperature decreases.

R_ν=F(T_ν), the weighting function is formulated using the chain rule of their partial derivatives:

$$\frac{dT_i}{d\Gamma_j} = \frac{dT_\nu}{dR_\nu}.\frac{dR_i}{d\Gamma_j} \tag{4.10}$$

where

$$\frac{dR_i}{d\Gamma_j} = \int_\nu f_i(\nu)\frac{dB_\nu}{d\Gamma_j}d\nu \tag{4.11}$$

$\frac{dB_\nu}{d\Gamma_i}$ can be evaluated directly with RFM and $\frac{dR_i}{d\Gamma_j}$ is then calculated with a separate integration function.

The term $\frac{dT_\nu}{dR_\nu}$ is the derivative of the inverse of the Planck function, or the rate of change of measured brightness temperature for a change in radiance:

$$\frac{dT_\nu}{dR_\nu} = \left(\frac{dR_\nu}{dT_\nu}\right)^{-1} \tag{4.12}$$

$$\frac{dR_\nu}{dT_\nu} = \int_\nu f_i(\nu)\frac{dB_\nu}{dT_\nu}d\nu \tag{4.13}$$

$$B_\nu = c_1\{exp(\frac{c_2}{T}) - 1\}^{-1} \tag{4.14}$$

$$\frac{dB_\nu}{dT_\nu} = \frac{c_1 c_2 \nu^4 exp(\frac{c_2\nu}{T})}{T^2(exp(\frac{k_2\nu}{T}) - 1)^2} \tag{4.15}$$

Where $c_2{=}\frac{hc\nu}{k}$ and $c_1{=}2hc^2\nu^3$. The weighting function (or **K** matrix from a previous algorithm) is identified as $\frac{dT_i}{d\Gamma_j}$ from Eq.4.10. As with calculating the brightness temperatures, calculation of each element of **K** requires the use of pre-calculated look-up tables. The derivative Planck function cannot be directly inverted over a finite spectral range. The total channel brightness temperature or radiance (as used for simulation comparisons with the RFM), is required to complement this, to locate the solution in derivative space on the look-up-table.

4.6.3 Comparison of simulated measurements

In Figure 4.10 are shown a comparison of brightness temperatures simulated by the RFM, and three versions of RTTOV coefficients for varying amounts of SO_2 modelled in the atmospheric column. They are for a background atmospheric profile at 60 °S and 0 °W in August 1991, which is relevant in time and space to the case study presented in the following chapter.

Figure 4.11 shows the results of column retrievals from HIRS/2 channel BTs simulated by the RFM, using a sample ERA-Interim atmosphere at 60 °S latitude and 0 °W longitude, where only the column amount of SO_2 is changed. It also shows the SO_2 fit by the Prata method, introduced at the start of this chapter and detailed in Appendix A. The Prata fit method does not fit SO_2 below 5 DU, which depending upon the atmospheric state can be equivalent to an observed brightness temperature difference of up to 4 K. For this latitude, the Prata fit overestimates the SO_2 column by up to 5 DU for much of the range below 100 DU that it does fit. Over 100 DU, it begins to underestimate the SO_2 in the column up to a maximum of 60 DU, according to the channel measurements simulated by the RFM. The column retrieval with the first ver-

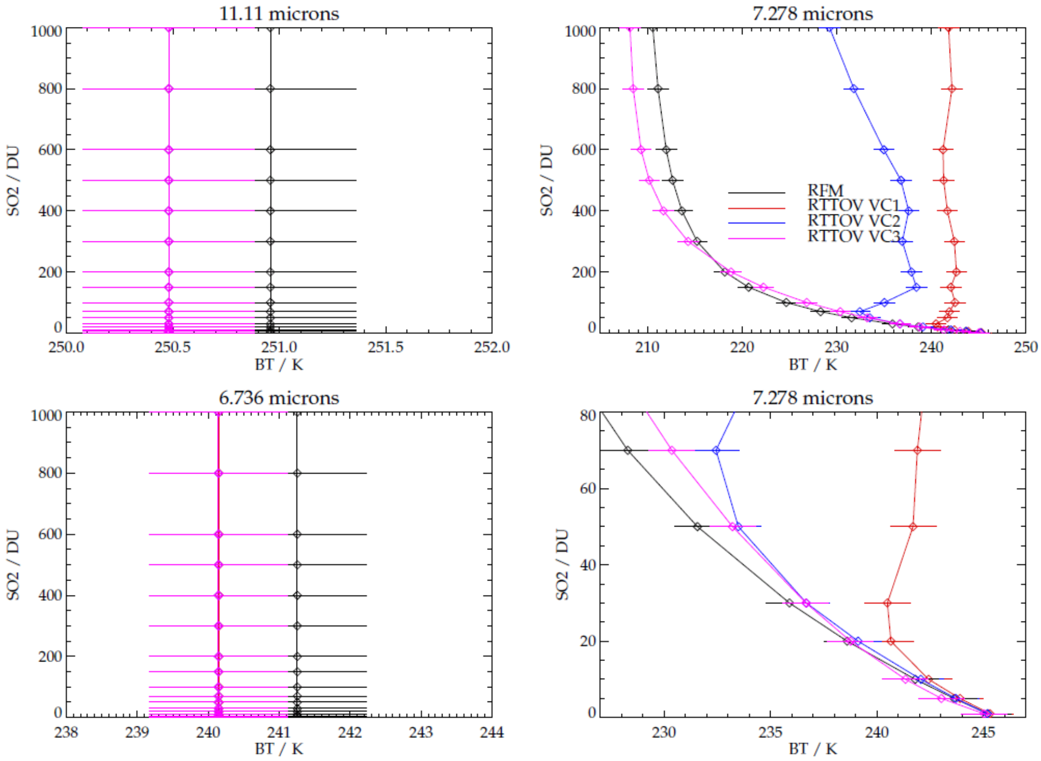

Figure 4.10: The top left panel shows the 11.1 μm channel brightness temperatures modelled for varying amounts of SO_2, using a specimen ERA-Interim atmospheric profile at -60 degrees latitude and 0 degrees longitude. The black line represents the RFM, the red line version 1 of the coefficients, and the blue version 2, and version 3 in purple. In the left hand plots the RTTOV lines all lie in the same place. The lower left panel shows the results for the 6.8 μm channel. The upper right for 7.3 μm channel, and beneath it a zoomed-in version of the same, illustrating the behaviour of RTTOV with both coefficients at the lower values.

sion of the RTTOV coefficients retrieves in an approximately linear manner to around 20 DU, and the second version fares favourably to around 50 DU, demonstrating that neither is particularly suitable for an eruption of any significant magnitude. Furthermore, this kind of unstable behaviour of the RTTOV coefficient causes a retrieval to have more than one solution for a given set of fitted channel brightness temperatures, causing spurious SO_2 columns to be retrieved. The third set of coefficients, vc3, fared significantly better and were assessed to be suitable for forward modelling SO_2 with RTTOV.

Further simulations at different latitudes (an example is shown in figure 4.12) suggested there was some sensitivity in the accuracy of the coefficients vc1 and vc2 to the atmospheric profile, compared to the RFM. The comparison in the tropics results in a more positive bias for the Prata fit SO_2 column. This is perhaps a consequence of the internal coefficients of the band model used therein that are less suitable at a tropical latitude. This effect is not observed in the behaviour of the columns fit with vc3.

It is noted that all of these simulated measurements do not have any cloud in their simulation, irrespective of whether or not cloud was actually present in the real atmosphere for that ERA-Interim profile and any effect that might have had on the model re-analysis fields.

Figure 4.13 shows the synthetic brightness temperature difference that the Prata fit uses to define the presence of SO_2 in the 7.3 μm channel. It is defined as the difference between the 7.3 μm channel BT and a point at 7.3 μm on a linearly interpolated line between the 6.8 and 11.1 μm channels. This BT difference includes the difference between what the channel BT would be if there were no SO_2 in the column, and additionally a buffer that accounts for how variability in predominantly water vapour affects the 7.3 μm channel that isn't accounted for in the other channels. The figure shows how this compares to the actual departure in BT in the channel as a function of SO_2. Whilst this is a robust offset that vastly reduces the number of false positives (although as shown in the subsequent chapter it does not eliminate them all), depending upon the atmospheric conditions it can impose a minimum detection limit of between 5 and 10 DU for the Prata fit method.

4.6.4 HIRS/2 and cloud modelling

The RFM represents the more accurate of forward models for the radiative properties of trace gases, but in its current form as applied here it can not account for or model the presence of cloud. Some understanding must be obtained of how the column retrieval forward model behaves in the presence of cloud of different type. Rose et al. (1995) showed that the 7.3 μm channel

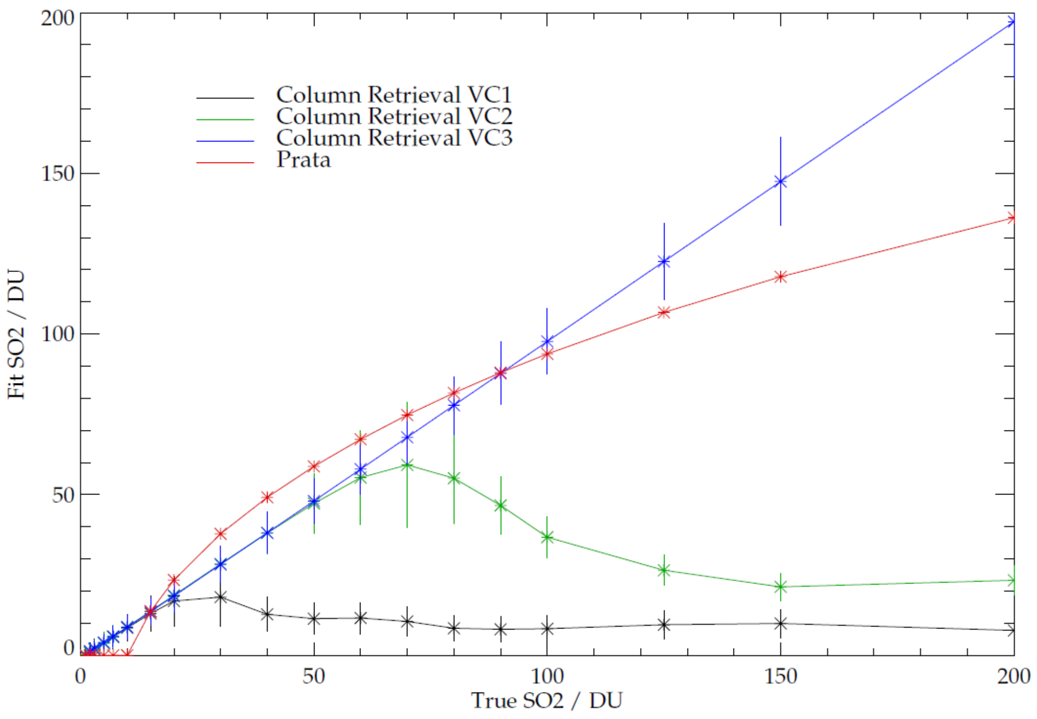

Figure 4.11: These simulations use an ECMWF atmosphere on 15^{th} August 1991, for a grid box centred at -60 °S and 0 °E. The error bars show the retrieved error for the column retrieval. The terms vc1-3 are those referred to in the text, denoting versions of the RTTOV coefficients.

can potentially be affected by the presence of ice, since transmission decreases below 8 μm. The forward model fits a cloud top pressure using the 11.1 μm channel, which is expected to work well for most tropospheric cloudy scenes. The effect of cloud on the other channels is examined here using a cloud model, the Oxford and RAL Aerosol and Cloud (ORAC) model. The model is described in detail by Poulsen et al. (2011), where it was used as part of an optimal estimation retrieval of cloud properties for the Along Track Scanning Radiometer (ATSR) by simulating radiances in a combination of visible, NIR and IR channels. The model parameterises a cloudy scene by ascribing cloud phase, effective radius of a size distribution, the 0.55 μm optical depth and a cloud top pressure. It uses the plane parallel approximation model cloud as a

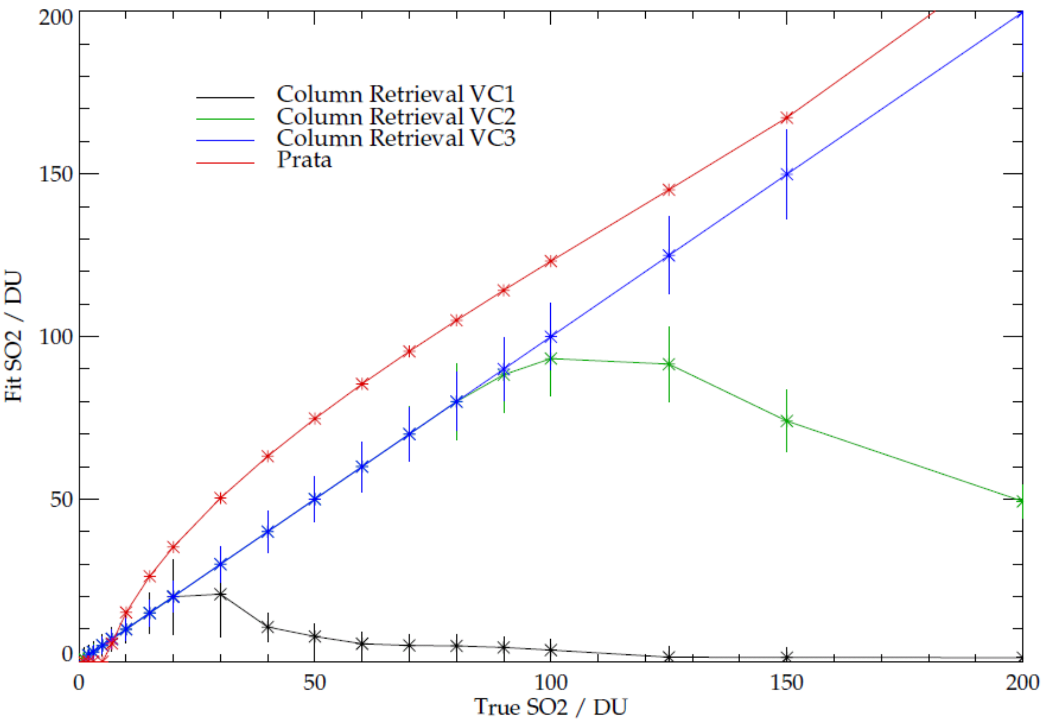

Figure 4.12: These simulations use an ECMWF atmosphere on 15th August 1991, for a grid box centred at 0 °N and 0 °E. The error bars show the retrieved error for the column retrieval. It is apparent that the Prata column fit (as used here) cannot differentiate between a change in SO_2 and changes in other particulars of the atmospheric profile to varying degrees at different latitudes. The terms vc1-3 are those referred to in the text, denoting versions of the RTTOV coefficients.

single layer, although this has experimentally been progressed to two layers (R. Siddans, 2011, Pers. Comm.). For a given cloud fraction, it uses linear weighting to the cloudy and cloud free portion of the scene to simulate the radiance. The radiative transfer is performed by two models for the IR and shortwave parts of the spectrum, but they share some common features (for example the use of DISORT look-up tables for emissivity). The thermal infrared (TIR) RTM makes use of RTTOV for clear sky radiance calculation. Four terms of the contributing radiance functions are identified as the transmission from beneath the cloud, emission from the cloud, downward reflection from above

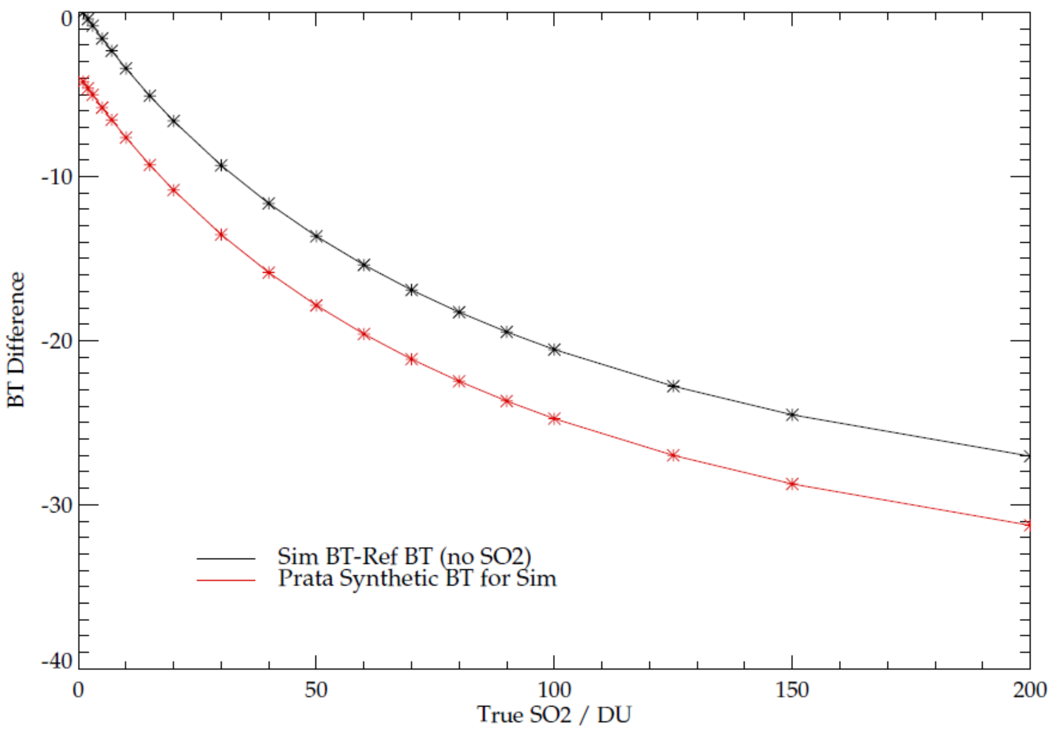

Figure 4.13: This figure shows the difference between the synthetic brightness temperature (BT) difference used as a threshold to discern the presence of SO_2 in the Prata fit method, and the simulated channel BT difference that arises solely due to the presence of SO_2 in a column.

the cloud and emission of radiance from the atmosphere above the cloud. The cloud model is also capable of modelling aerosols including volcanic ash. For most atmospheric states the BT difference between any measurements at 12.5 and 11.1 μm is positive in the presence of ash and negative in all other cases. This test is often used to identify the presence of ash. It is applied to the HIRS/2 data in the following chapter for inspection, although due to atmospheric variability it is not always effective in every case, and would require a retrieval or some combination of other infrared channels to improve this. It is possible however to use the ORAC model to investigate the effects upon the HIRS/2 SO_2 retrieval by the presence of volcanic ash in the field-of-view.

This version of the cloud model (Poulsen et al. 2011) does not implicitly model variations of most trace gases (notably SO_2) but uses a background climatological profile to establish the contribution of most of these to the atmospheric radiance.

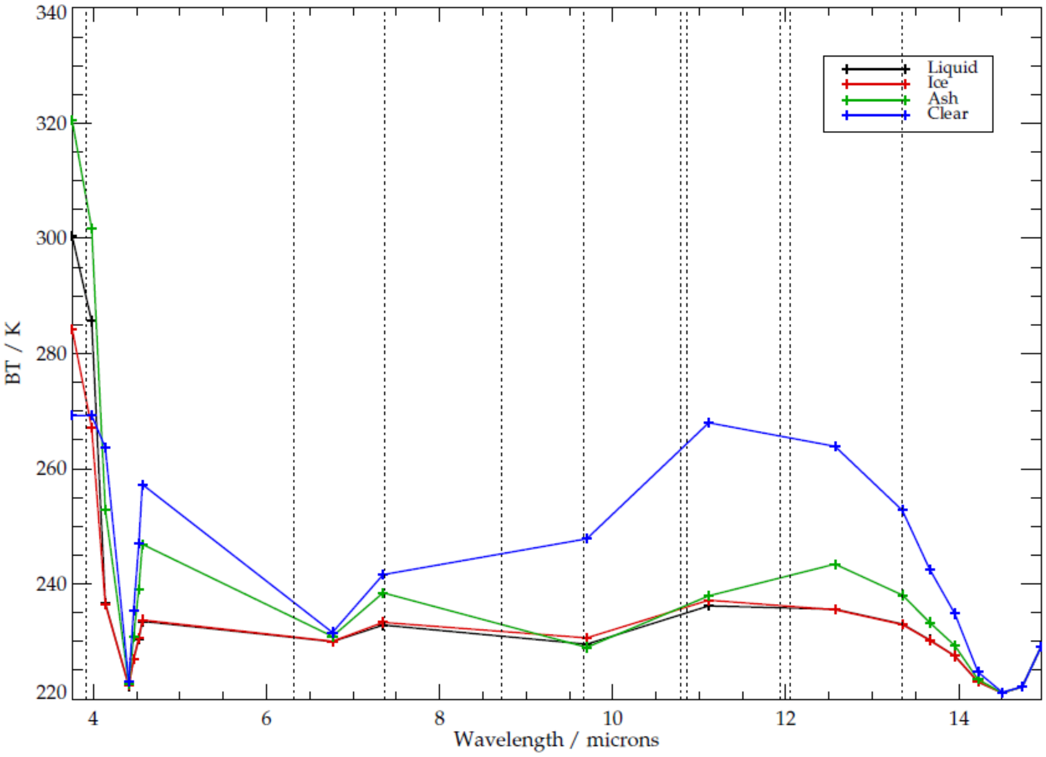

Figure 4.14: This plot shows the HIRS/2 channel brightness temperatures for an ECMWF climatological profile, and how they are affected by the presence of liquid water or water ice cloud and ash. The black vertical lines denote the channel wavelengths of another instrument. Courtesy R.Siddans (RAL).

The cloud model was used to simulate firstly clear sky HIRS/2 channel brightness temperatures, so that they could be compared to the simulated clear sky brightness temperatures in the column retrieval. Identical atmospheric gas, temperature and pressure profiles were used. The clear sky BTs were found to agree to better than 0.1 K in all three channels, and whilst effort was made to improve the agreement, the relative sophistication of the two models may lead to slight disparities. For the purposes of indicating how the presence of cloud may affect the quality of SO_2 retrieved this is deemed acceptable. The cloud model was used to simulate HIRS/2 channel BTs for a range of cloud top heights of liquid water, water ice and ash cloud, with varying optical depths and effective radii, none of which contained SO_2 in the column above a climatological background value. These BTs were then used as simulated measurements by the column retrieval. The results for liquid water cloud are shown in figure 4.15. For both liquid and ice cloud, the retrieval begins to return spurious SO_2 and water vapour for cloud situated much above 5 km, and cloud top height up to 9 km. Cloud above 9 km degrades the fit of the measurements to the point where the retrieval does not converge, and the SO_2 and water vapour scaling factors become unphysical. The cloud top height limit is similar for water ice and ash cloud (modelled with effective radii of 50 and 1 respectively, and optical depth of 1), although importantly in the case of ash the departure of the retrieved SO_2 from the nominal 1 DU is 100 DU for an ash cloud at just 10 km, with continued aberrant behaviour as ash height increases. It is also worth noting that the *a posteriori* errors for both water vapour scaling factor and for cloud above 5 km, when the values begin to depart from 1, are often smaller than their distance from the true solution, indicating that retrieval error alone (and to an extent cost) is insufficient to indicate when the retrieval has converged on an incorrect solution, and the retrieved cloud top height must also be used.

Figure 4.16 shows the affect on the retrieved variables as a function of liquid cloud optical depth. The results for SO_2 clearly indicate that a cloud top height of 6 km returns spuriously high values of around 10 DU when there should be no more than 1 DU. It also indicates that the retrieval performs even more poorly in the presence of liquid cloud with optical depth of less than 1.5, beneath which SO_2 values of over 20 DU are retrieved. In such cases, the retrieval also underestimates the cloud top height by up to 3 km. It is unsurprising that the retrieval behaves this way for optically thin cloud, but it may be a source of false positives in retrievals with real data that only occasionally might be indicated by their having a relatively large error.

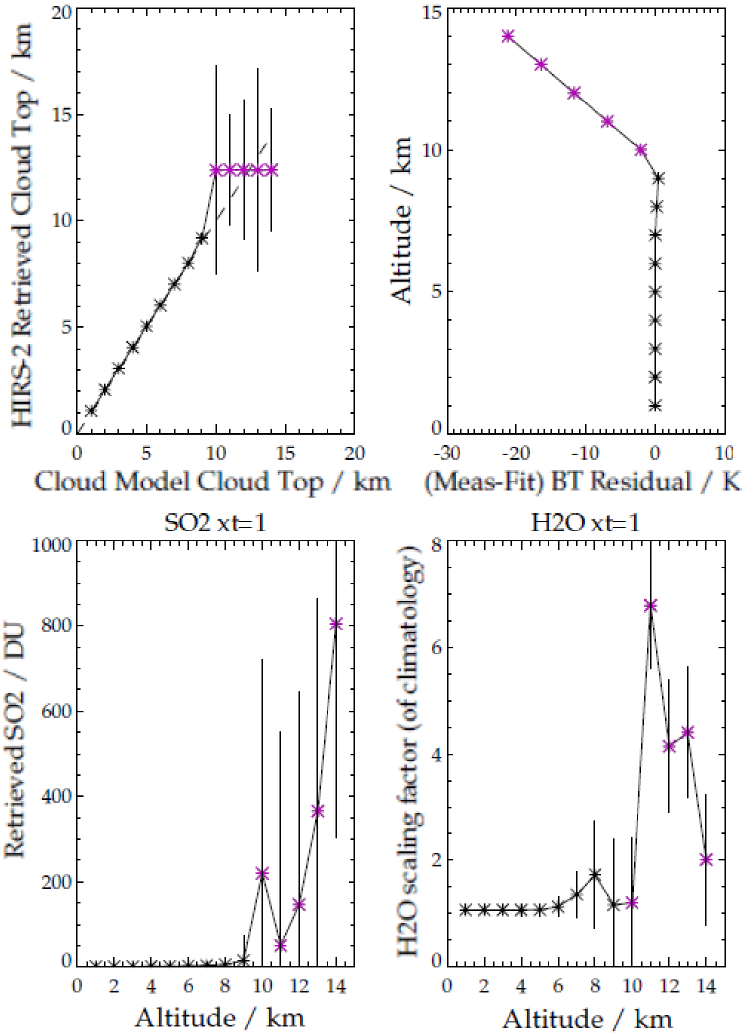

Figure 4.15: The top left plot shows retrieved cloud top height as a function of 'true' cloud top height as simulated by the cloud model. Black symbols indicate that the retrieval converged, and purple indicates that it did not. The top right plot is of the fit residual (measurement minus fit) in the 11.1 μm channel. The bottom left plot shows the retrieved SO_2 as a function of the cloud top height in the cloud model, and the bottom right the equivalent for the water vapour scaling factor.

4.6.5 Sensitivity to plume profile height and shape

The sensitivity of the column retrieval was examined by varying the plume height and thickness in simulations with the forward model. Three plume

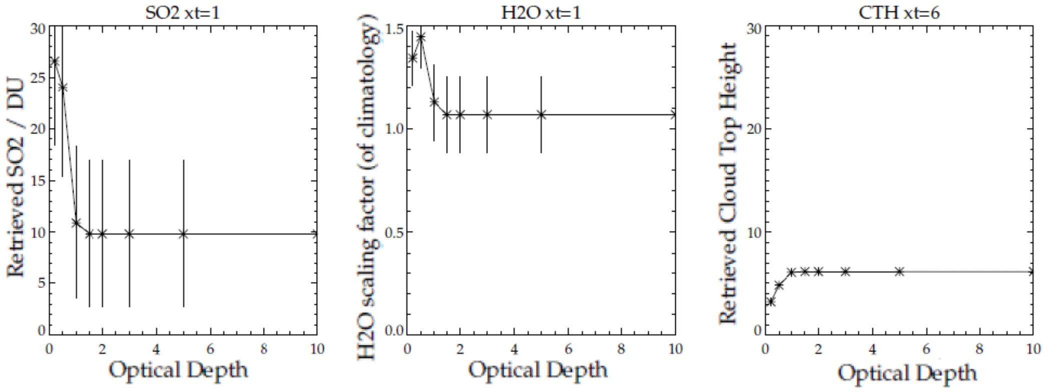

Figure 4.16: The left, centre and right plots show the retrieved values of SO_2, water vapour scaling factor and cloud top height as a function of cloud optical depth in the cloud model used to simulate the measurements, for a liquid cloud at 6km, with droplets with an effective radius of 10 μm. See text for discussion.

thicknesses were selected that were related to the case study triangular profile, with bases of 1 to 4 km, where the 2 km case is that which most closely resembles the eruption profile that will be studied in the next Chapter. Figure 4.17 shows the basic result that was the case for all three plume thicknesses, that the retrieval performs in a linear manner for the range of SO_2 columns tested. In this plot, and in figure 4.18, there is an indication that the modelled error for the retrieved SO_2 column increases with both increasing plume height and marginally cloud height also, showing that there is scope for more investigation of the effect of cloud on retrieved SO_2.

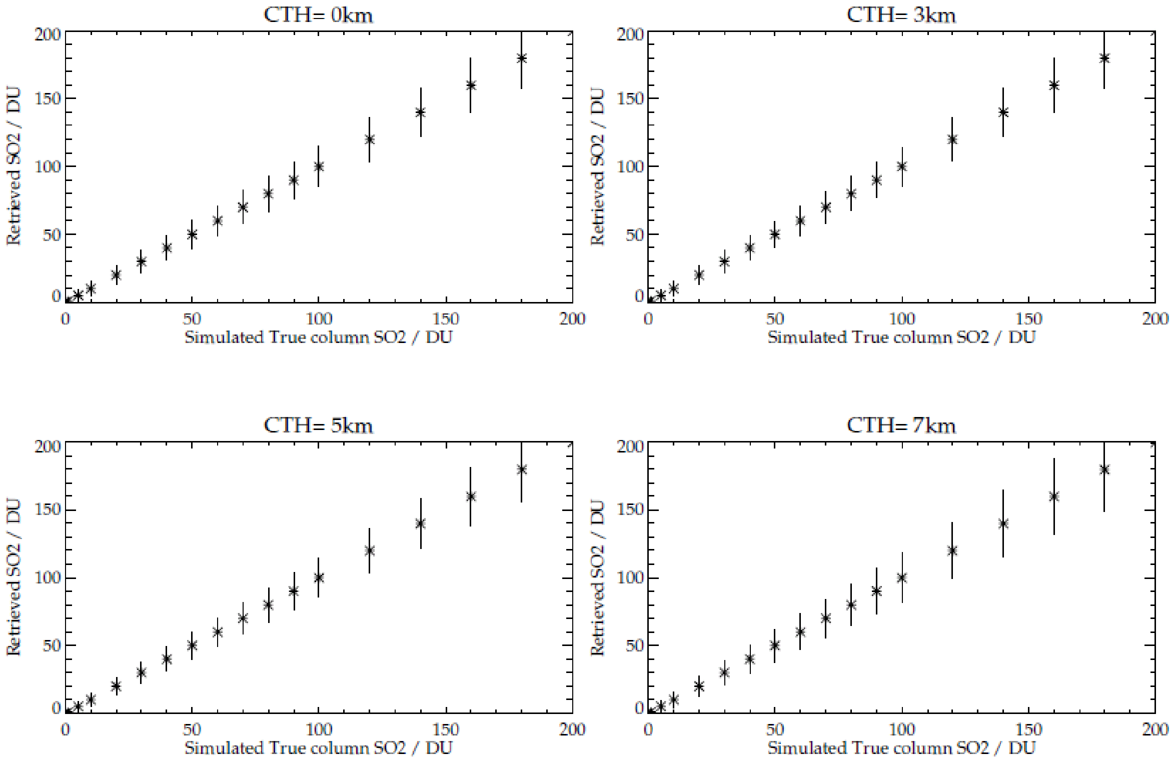

Figure 4.17: All 4 plots show the retrieved SO_2 column verses the 'true' column that was used to simulated the measurements, for an SO_2 plume modelled with a triangular profile from 11 to 13 km, peaking at 12 km. The test was repeated for a 10, 12, 14 km and 11.5, 12, 12.5 km profile, which showed the same results.

Figure 4.18 also shows that the error in the retrieved water vapour scaling factor is nearly 50 % greater for a cloud at 7 km than at 5 km, and that the error in the retrieved cloud top pressure is highest when it is at the surface. This particular case is equivalent in the model to the cloud-free case, in the sense that the cloud is modelled as a grey body, the temperature of which is used to determine whether or not it is beneath or above the surface.

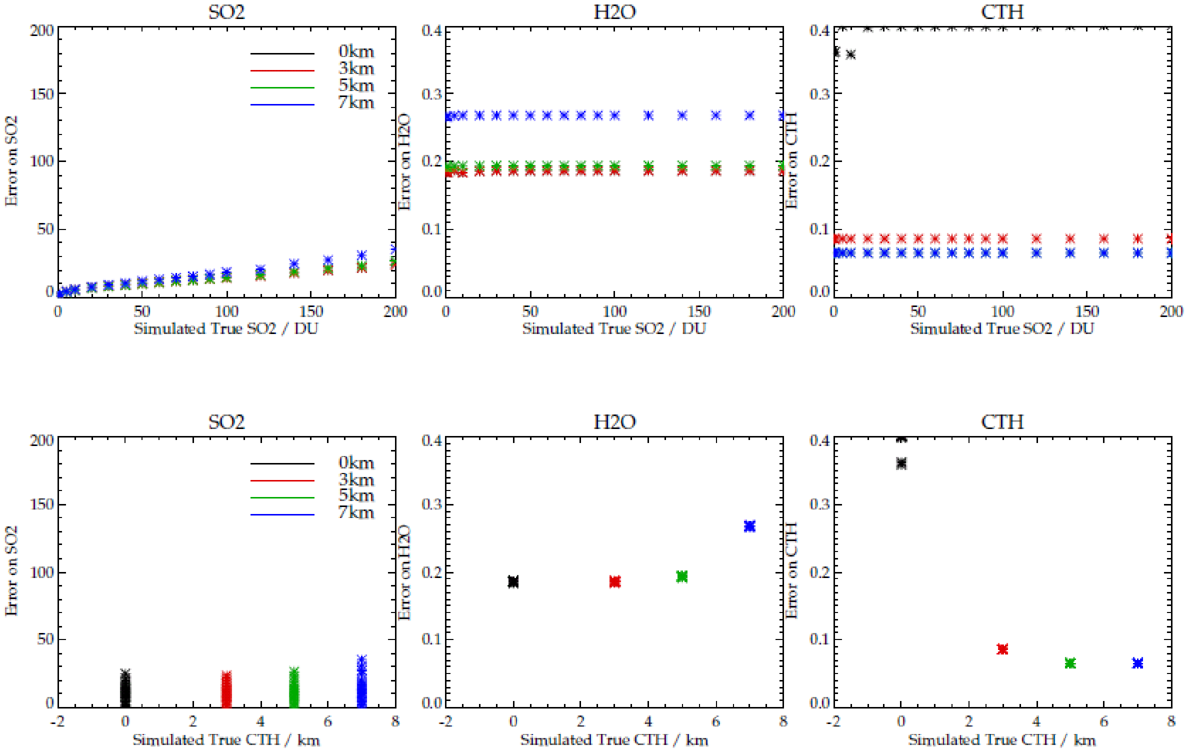

Figure 4.18: The plots in this figure show how cloud modelled at 0, 3, 5 and 7 km altitudes affect the state vector variables in terms of their retrieved error. The 3 plots at the top of the figure left to right are the error on each element of the state vector (SO_2, H_2O scaling factor and cloud top height), for a given 'true' column of SO_2 with cloud modelled at each of the cloud top heights. The bottom row of plots is the same information but viewed as a function of the cloud top height used in the simulation.

Extensive simulations were performed where the plume was simulated at altitudes ranging from 8 km to 18 km, and using plume thicknesses of 1–4 km. The results are shown in figure 4.19. The plots show that there is some suggestion with all plume thicknesses that the retrieval has some difficulty in the case of no cloud and very little SO_2 when the SO_2 plume is above 18 km. This may be a result of poor thermal contrast around the altitude of the SO_2 plume here, as the temperature profile used in these simulations has a deep, more or less isotheral tropopause from 16-19 km. For application of this method to an eruption where the material is expected at 18 km, further simulations and refinement would be necessary.

Given that for many nadir viewing instruments - including TOMS and not least HIRS/2 - there are insufficient pieces of information in the measurements to independently retrieve the height of and SO_2 plume, and their forward modelling requires some *a priori* information from external sources. Nowlan et al. (2011) attempt to retrieve a most probable height of the plume iteratively based on running their GOME-2 SO_2 retrievals and examining which height level achieves the best fit to the measurements. As GOME-2 is a spectrometer there is more information potentially available for such an approach. For interpretation of errors in the retrieval results that can not be represented in the forward model for HIRS/2, it is paramount to assess the sensitivity of the retrieved column SO_2 to inaccuracies in the *a priori* plume height information if it is not included in the retrieval.

Figure 4.20 shows the consequences that can result from retrieving the volcanic plume with a fixed profile shape that represents the thickness of the plume incorrectly. Measurements were simulated using a triangular profile centred at 12 km but with baselines of 1 and 4 km. They were then used in the retrieval with a fixed profile shape with a triangular perturbation also centred at 12 km, but with a baseline of 2 km, thought to be the best representation of the plume used in the case study in the following chapter. The retrieval simulations suggest that errors are larger when the plume thickness is over-estimated, with only small inaccuracies introduced when the plume thickness is under-estimated. The modelled cloud top height was 3 km in all cases.

Figure 4.21 shows the impact on the retrieved SO_2 column as a fraction of the true column, when the true column profile used to simulate the measure-

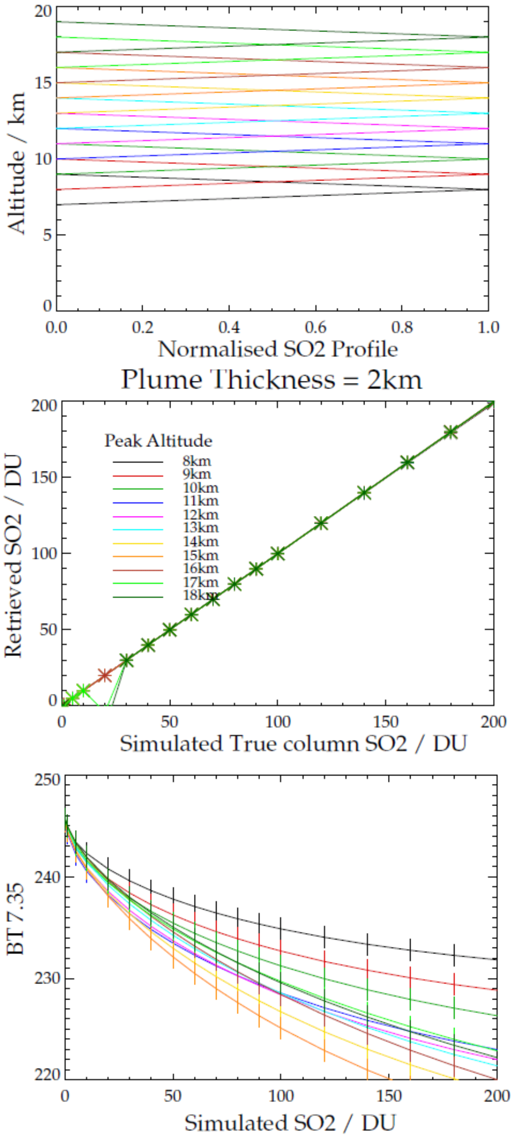

Figure 4.19: The top plot shows the SO_2 perturbation of 2 km baseline height simulated at a range of altitudes. The middle plot shows the relationship between simulated SO_2 in the column, and that retrieved. The bottom plot shows the 7.3 μm channel simulated brightness temperature as a function of simulated SO_2 mass altitude. This was repeated for plume thicknesses of 1 and 4 km, and both showed very similar behaviour.

ments peaked at an altitude different from that which the retrieval used. It is readily apparent that this is potentially the largest source of uncertainty that

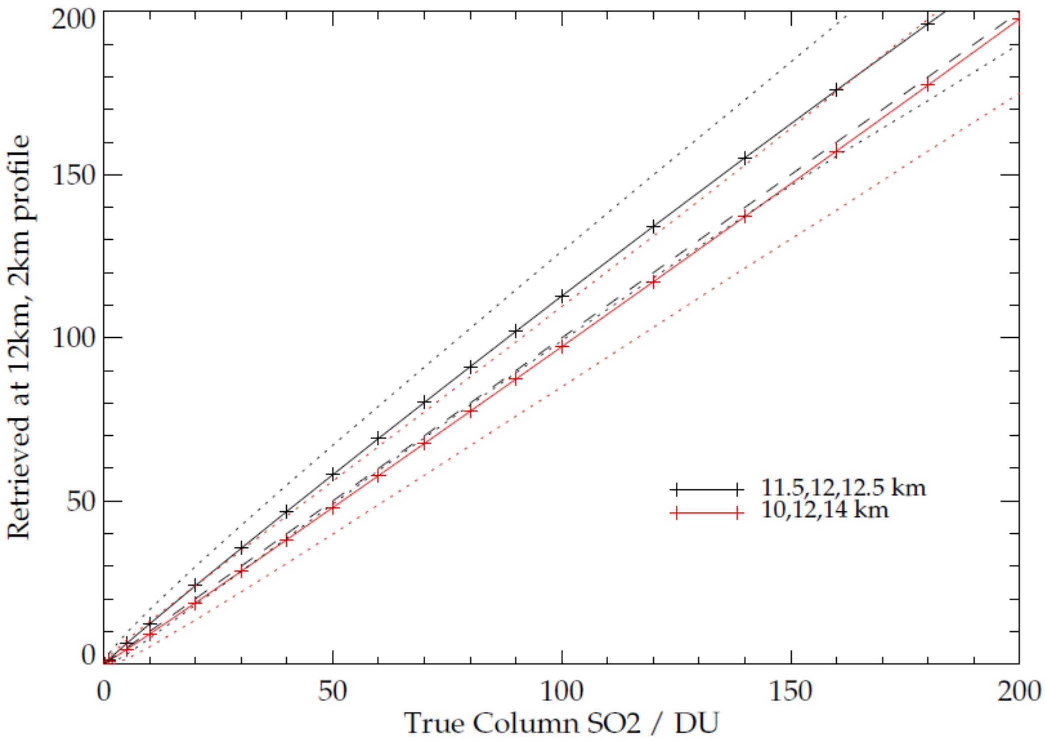

Figure 4.20: The black line indicates how columns from 0.1–200 DU are retrieved on a fixed grid with a scalable triangular profile with base, mid point and top at 11, 12, 13 km respectively, when the true profile shape is given by a triangular profile at 11.5, 12, 13 km, effectively over-estimating the thickness of the plume. The red line shows the equivalent result for an underestimate of the plume thickness, the real profile given by 10, 12, 14 km. The dotted lines show the bounds of retrieved error in each case. The dashed line is x=y shown for clarity.

the retrieval simulations performed here have demonstrated. The modelled cloud top height was 3 km in all cases, and all of the retrievals from simulated measurements converged. They broadly indicate that overestimating the plume height will lead to a systematic underestimate of the SO_2 column amount. This follows the intuitive assumption that as an absorbing gas radiating at a cooler temperature at a given frequency as a function of amount, this might be indistinguishable from a smaller amount located at a higher, colder altitude.

If the specified plume altitude profile peaks within 1-2 km of the actual plume, errors of 10-20 % arise for column amounts of less than 50 DU. Larger underestimates in the case of this atmospheric profile suggest a more complex behaviour. If the true plume height is 14 or 15 km, a fixed retrieval stipulated at 12 km results in an over-estimate of the SO_2 column that in the case of the higher plume can be up to a factor of two for a column of 200 DU. For true plumes above 15 km, the 12 km peaked retrieval underestimated the SO_2 for amounts less than 100 DU, and over-estimated above 100 DU. It is anticipated that this behaviour will be closely tied to the particular temperature profile used in the simulations, to the extent that a full investigation of the sensitivity of the retrieval to errors in the way plume height is represented in the forward model could constitute a significant research study. Whilst it would present an intriguing exercise (perhaps for future work) it is considered that not only is the *a priori* information used to constrain and characterise the profile shape used in the retrieval good and the best available (and therefore there is little that can be done if it is inaccurate), but that the simulations shown here are a fair basis for caution and consideration in the interpretation of the results of the retrieval upon real data.

Analysis of the relative cost of the simulated retrievals that constitute figure 4.21 indicate that irrespective of the plume height the retrieved cost function is highest at around 100 DU with minima either side, indicating that cost alone could not be used to suggest where the plume altitude is incorrect. Equally, the retrieved SO_2 error is only larger than the retrieved SO_2 column for profiles with less than 5 DU, which is in the region of the expected retrieval limit.

Analyses shown in Appendix A demonstrate that equivalent inaccuracies in attribution of plume altitude lead to errors of a similar magnitude. For both methods, it is clear therefore that good prior knowledge of the SO_2 plume altitude is necessary for accurate retrieval or fit of SO_2 column amounts from HIRS/2.

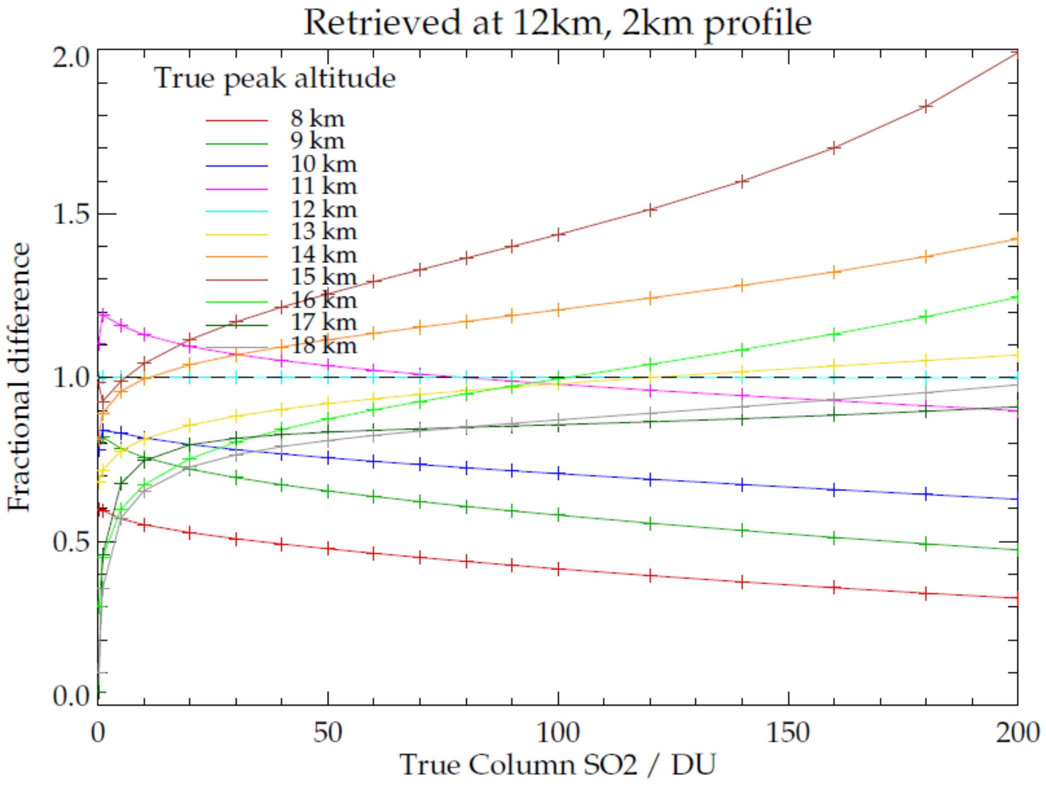

Figure 4.21: A 2 km thick triangular profile centred at 12 km is used to simulate measurements. The profile is then used in a retrieval with the retrieved height assigned to a range of altitudes. The coloured lines indicate the fractional difference to the case when the retrieval used the correct altitude of 12 km.

4.6.6 Summary

The methodology for an optimal estimation HIRS/2 column SO_2 retrieval has been described in detail. Extensive efforts to quantify HIRS/2 forward model error using line-by-line calculations with a range of atmospheric gases has been shown, using the RFM. At this stage there is no estimate of *a priori* error covariance between water vapour and SO_2. Theoretically there is no correlation between the species (above their co-existance in a volcanic plume) on a climatological basis. But as there is more information in the measurements for water vapour and the 7.3 μm channel is sensitive to both, failure to fit water vapour properly will inevitably impact the fitting of SO_2. This will be assessed in the following chapter by utilising real measurements.

The column retrieval forward model was tested with retrievals from measurements simulated by both the forward model itself and that of an accurate line-by-line RTM. They have shown that the retrieval theoretically behaves accurately and robustly for the range of SO_2 column amounts for mid to large sized explosive eruption profiles. Most of these simulations were tailored to the specifics of the case study presented in the following chapter, but not exclusively. Comparative simulations were also performed with the Prata fit method, which revealed that significant errors in the Prata fit could potentially arise due to assumptions made about the atmospheric profile. A cloud model was used to asses the potential impact on the column retrieval of liquid and ice meteorological cloud, and that of ash. It was found that they do affect the retrieval in a manner beyond that of the variability of simply cloud top pressure which is fit by the retrieval. Low optical depth or effective radii for cloud or aerosol can result in poor fitting of the measurements, both resulting in an underestimate of cloud top pressure but false positives of SO_2 and an over-estimation of vater vapour. This yielded a crucial quality control threshold where retrieved cloud top altitudes of greater than 5 km should not be trusted, as they are likely to result in spurious detection of SO_2 and a high retrieval cost. This may imply that very thin cloud beneath 5 km (or incorrectly retrieved to be) could still contribute to poor fitting of the measurements, and the behaviour of the FM with real data can be examined for signs of this.

Simulations also showed that the column retrieval performed well up to plume altitudes of 17 km, after which column amounts of less than 30 DU SO_2 could not be detected. Whilst the Prata fit is thought to become increasingly inaccurate as plume thickness increases (due to the assumption in the band model upon which it is based that the temperature profile within the plume is isothermal), there was no evidence of increased error in the column retrieval due to plume thickness for the range tested of 1.5 and 4 km.

Simulations to test how the retrieval performed when the modelled SO_2 plume perturbation height was not equal to the true plume height suggest that the retrieval (and the Prata fit) are very sensitive to this. They imply that good *a priori* information is a pre-requisite for retrieving a column amount, but also that pixel errors of up to 20 % for column amounts of less than 50 DU and up to 10 % for amounts around 200 DU should be considered applicable above and beyond the indication of retrieved error, if one anticipates a peak plume height error of 1 km. Inaccuracies of 30-40 % can arise for an error in height of up to 2 km, but are smaller for the lower column amounts.

In summary, this chapter has demonstrated a working optimal estimation retrieval for SO_2 with HIRS/2 in theory. It remains to demonstrate this in practice in the following chapter.

Chapter 5

Case Study

This chapter will present the results of the HIRS/2 SO_2 retrieval developed in this work, principally applied to a case study of the sizable Cerro Hudson eruption in 1991. The SO_2 retrieval results for the period of the 1991 eruption of Cerro Hudson will be compared with the Prata fit method and to TOMS SO_2.

5.1 Case study - Cerro Hudson

Cerro Hudson (45.54 °S, 72.58 °W, elevation 1905 m) is a volcano in the south Chilean Andes. A stratovolcano, built up of various layers from successive eruptions, it covers an area of 300 km^2. These types of volcanoes may erupt a variety of magma types, including basalt, andesite and dacite. All are generally highly explosive, with the exception of basalt eruptions (USGS 2002). The tectonic setting of this volcano is extensively described in Naranjo & Stern (1998), and an outline is given here. Hudson is located in a remote region of Patagonia, 280 km east of the Nazca-Antarctic-South American plate intersection. To the west is the Chile trench, where the Nazca is subducted beneath the South American Plate. An oceanic spreading ridge lies perpendicular to the subduction zone, and due west of Hudson. More locally, the volcano and those to the north are associated with a fault system known as Liquiñe-Ofqui. The area is only sparsely populated, and mostly by farming communities. The volcano is capped by a glacier, the melt water of which feeds the river Rio de Los Huemeles through a breach in the caldera (main crater) rim. It was only recognised as an active volcano when it began an eruptive phase in 1971, but there has since been identified at least two major eruptions in the late holocene by Hudson (3600 and 6700 before present)(Naranjo & Stern 1998). Kurbatov et al. (2006) detect a further two thought to be of lesser magnitude in an ice core record taken from the Siple Dome in Western Antarctica. The location of the core and regional flow regimes suggests that the erupted material would have had to circumnavigate the pole before deposition.

Eruptive activity in the region has caused significant damage to crops and the death of people and livestock, and 70 % of the surrounding populated land was buried with ash during the 1971 eruption (Smithsonian 2002). Bad weather and difficult terrain prevented good or frequent observation in 1971, but it is thought that the erupted plume reached no higher than 6 km although tephra deposits covered an area of over 60 km^2. In April 1973 a lava eruption beneath the glacial ice is thought to have occurred, causing what is known as a 'lahar'. This is a highly destructive rapidly flowing mixture of rock fragments, water and mud. An estimated 70 % of the caldera ice cap melted, in a flow that eventually reached the sea 70 km away (Naranjo & Stern 1998). The latest eruptive activity occurred in October 2011, where a small steam and ash cloud reached 1 km and caused an avalanche.

5.2 The 1991 eruption

Hudson's most recent eruption was the second largest in the Andes of the 20th century. The largest was Quizapu (5.65 °S,70.76 °W, elevation 3788 m) in 1932. Hudson began to erupt on 8th August 1991, three months after the equatorial eruption of Pinatubo (15.13 °N, 120.35 °E, 1486 m) and almost precisely 20 years after the initial 1971 occurrence (Smithsonian 1991). The nearest road passes 35 km distant, and little detailed mapping of the volcano exists. The remoteness of the volcano meant that eyewitness accounts are scarce and few photographs or measurements were taken during the eruption. As such, the information is intermittent. Observations again suffered from frequent spells of bad weather (Naranjo 1991). The eruption occurred in three distinct phases: the 8-9th, 12-14th and 15th of August 1991.

5.2.1 8-9th August activity

Eruptive activity was preceeded by earthquakes before a phreato-magmatic explosion (involving both surface water and magma) which produced an ash column 12 km high, and was described as brown/grey in colour (Smithsonian 1991). Intense lightning events were observed within and around the plume, caused by static electricity. The prevailing winds carried the plume North East of the volcano, depositing ash 60 km away. The melt water formed a 'jökullhaup' - a powerful stream that develops beneath the glacier, that can emerge with destructive force. The caldera meltwater caused the river width to swell from 80 m to 170 m (Smithsonian 1991).

Figure 5.1: An eruption of Cerro Hudson on August 8th 1991, during an early paroxysmal phase. Photo: J. Naranjo

5.2.2 12-14th August activity

A large eruption on the 12th deposited ash 80 km SSE of the volcano 55 minutes after the eruption began. This was associated with "intense lightning" and "a sulphurous odour"(Smithsonian 1991). The plume was reported to reach approximately 10 km and was more than 5 km thick. At one point, the plume was observed to rise at a rate of 1.9 km/min (Naranjo & Stern 1998). Activity decreased until the 14th, when a small explosion showered an area 55 km away with lapilli and pumice fragments (Scasso et al. 1994).

5.2.3 15th August activity

The most explosive eruption began and ended on 15th August. It was at this stage of its eruptive phase that the majority of the material was injected into the stratosphere (Constantine et al. 2000). The elongated plume reached 18 km and spanned a horizontal angle of ∼20°. As a result, both the stratospheric plume and fall out deposits were only narrowly dispersed (Scasso et al. 1994, Schoeberl et al. 1993).

The consequences of these eruptions to the local population are as significant as any global atmospheric effects. Ash leachate analysis (where ash deposits are flushed with an ion-rich solution) revealed high levels of fluorine (Decker & Decker 1997). Where the ash falls, this is leached into the soil, where it may eventually be ingested by livestock. Up to 10,000 animal deaths are thought to have occurred from the Hudson eruptions (Smithsonian 2002).

5.3 Observations and modelling

At the time of the 1991 eruption, the only satellite available that could detect SO_2 with any demonstrated precision was TOMS. As discussed in Chapter 1, MLS was launched aboard the Upper Atmosphere Research satellite (UARS) 3 months after the eruption of Pinatubo, and measured SO_2 that was still present above 20 km (Read et al. 1993). There is however no discussion of the Hudson eruption, and no suggestion that measurements of the Hudson plume were made by MLS. The Hudson eruption is thought to have been 10-20 times smaller than that of Pinatubo, and its erupted material placed very much lower in the stratosphere. As such, it is likely that the remnants of the SO_2 would have been tenuous at the time that MLS was able to make observations. There is also no discussion of observations by SBUV-2, other than that reported in relation to the Pinatubo eruption in the months previously (McPeters 1993), but it is not discounted that the measurements may exist. Read et al. (1993) show that SO_2 from the Pinatubo eruption was present in the stratosphere up to relatively high latitudes months after the eruption as it spread poleward at differing rates depending upon the altitude of the SO_2. Strong easterly winds in the tropical stratosphere (related to the phase of the QBO) slowed the poleward progression. When Cerro Hudson erupted it is not readily apparent that SO_2 from Pinatubo over-lay that of Hudson, although the lidar data presented in section 4.4.2 and Read et al. (1993) suggest that it might have been present intermittently, if rather tenuously.

Kratzmann et al. (2009) state that the eruption produced 2.7 km^3 of tephra. Through tephra dispersal simulations they suggest maximum plume heights of 12 km for the 8^{th}-9^{th} activity, and as high as 18 for the paroxysimal phase on 15^{th} among the 3 separate phases of the eruption that occured on that day.

As well as the various ground observations, the Hudson eruption was sensed remotely by TOMS (SO_2 and aerosol), AVHRR (ash), lidar (section 4.4.2) and incidentally by an aircraft (Barton et al. 1992). This allowed daily information about the evolution of the material in the atmosphere. By far the most useful relating to SO_2 was the information from TOMS.

From measurements by ozone sondes, Hofmann et al. (1992) report possible exacerbation of Antarctic ozone depletion due to the presence of Hudson aerosol in the lower stratosphere of 10-15 % in the total column for September 1991. The anomalous depletion occurred within the polar vortex predominantly at 11-13 km and 25-30 km, the respective altitudes of the Hudson and Pinatubo aerosols. The mechanism proposed for this was the liberation of active chlorine by heterogeneous catalysis by the sulphate aerosols.

The transport of the Hudson volcanic cloud was first numerically modelled by Barton et al. (1992), to reasonably good agreement with satellite and lidar observations. The plume was also modelled using an isentropic trajectory model, initiated by TOMS observations of SO_2 (Schoeberl et al. 1993). These models showed good spatial agreement with observations for the first 8 days after the eruption. Numerical modelling provides a test of knowledge of the stratospheric dynamics, although there is scope for more modelling of the chemical evolution of this plume.

5.4 Application of retrieval scheme to real measurements

From TOMS data and elsewhere, it is well understood that the Hudson erupted SO_2 plume encircled the Southern Hemisphere over the 10 days following the paroxysmal eruptive phase, between the latitudes of approximately 40 and 80 °S. The initially elliptical plume remained cohesive but rotated its major axis and also sheered into ribbon-like plumes, which resulted in the wide latitude band. The data analysed in this case study are broadly confined to this latitudinal region.

Initial column retrievals with real measurements from HIRS/2 data from the period of the Cerro Hudson eruption indicated that some further improvements to the scheme were desirable.

5.4.1 Improvements to forward model error

Early results of the retrieval scheme run with real measurements indicated that there were prevalent ‘false positives’ of SO_2 that were retrieved. Their structure indicated that they may be related to either an aspect of cloud or water vapour. The calculation of the forward model error was primarily performed using comparisons of simulations with the RFM, for which many aspects of the real atmosphere and its variability could not be adequately represented. Furthermore, the *a priori* covariance was essentially a variance, and there was no representation of how variability in one component of the state vector was related to any other. As such a new estimate was required of how the limitations of the forward model impact what is retrieved. Particularly, how the fit of water vapour could affect the amount of SO_2 that is retrieved.

As the $7.3\,\mu$m channel is sensitive to both water vapour and SO_2, the error covariance of water vapour and SO_2 must be established. This must be appropriate for the real atmosphere. This is a measure of the error in the retrieved SO_2 that can arise from poor fitting of the water vapour, and from which some level of false positives can arise.

To do this, the retrieval scheme was run for 6^{th} August 1991, a date before the pre-eruptive phase of the volcanic eruption began. As such, it could be expected that little or no SO_2 was present in the atmosphere in the region of interest (beyond the background level). The retrieval was forced not to retrieve SO_2 by artificially constraining the *a priori* variance. The results are shown in Figure 5.2.

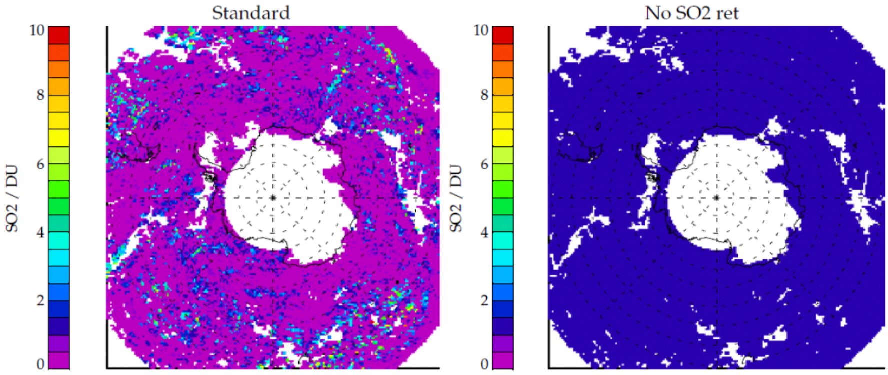

Figure 5.2: The plot on the left shows the retrieved SO_2 for all the orbits on 6^{th} August 1991, before the volcano began to erupt in earnest. The error on the measurements is that prescribed by the forward model error calculated using MIPAS climatological variability, representing the profile on a finite height grid and spectral resolution limitations, all of which were discussed in the previous chapter. The plot on the right hand side is the retrievals for the day where the SO_2 was not retrieved, and as such only the background profile used in the retrieval is returned, which has a nominal value of 1 DU in the expected region of the plume (or more precisely a retrieved scaling factor set to 1).

Figure 5.3 shows the residual of the fit in the 7.3 μm channel for the case where the SO_2 is fit and not. The residual in the case where the SO_2 is fit is very small, but it is expected that nearly all of the SO_2 being retrieved on this day is being falsely attributed, and is actually a result of water vapour variability. Figure 5.3 also shows the fit residual (measurement minus fit) where SO_2 is not retrieved.

Figure 5.4 shows the mean and standard deviation of the column retrieval

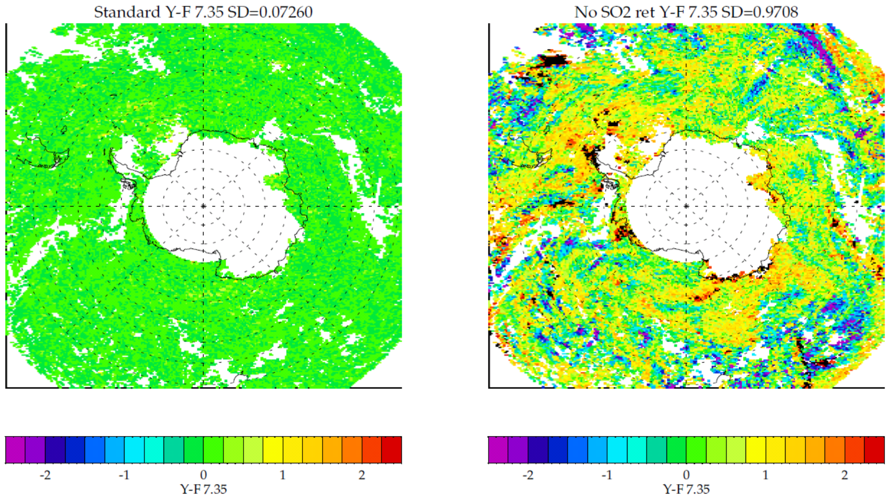

Figure 5.3: The plot on the left shows the fit residual (Y-F) for the case where SO_2 is fit with the retrieval. The fit residual is very small in this case. On the right, the fit residual is shown when SO_2 is not fit.

when no SO_2 is fit, and the synthetic BT difference used in the Prata fit. Since there is not expected to be any volcanic SO_2 present, and functionally the retrieval assumes a very small nominal amount, the residual features show the contribution to SO_2 that is falsely attributed due to the water vapour or other atmospheric features that are not well captured in the forward model. The standard deviation of the fit residual can constitute an estimate of the error covariance of water vapour with SO_2 in the column retrieval (as shown in figure 5.4). The mean values are an indication of the bias in both methods as applied to the 7.3 μm channel. The 'no SO_2' retrieval has a small positive bias, which is partially a result of a default small positive amount of SO_2 that is included in the atmospheric profile.

For reference, figure 5.5 shows the 'synthetic' brightness temperature difference in the 7.3 μm channel. As described in section 4.6.3 and Appendix A, this is the difference between the actual channel brightness temperature, and that which coincides with a straight line made between the 6.8 and 11.1 μm channel. As such, it does not quite represent the brightness temperature difference between the channel and one that definitely does not posses any SO_2,

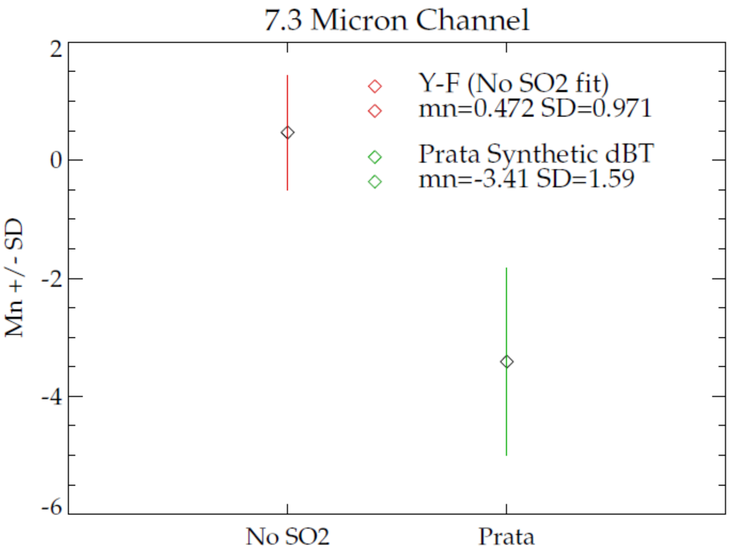

Figure 5.4: The mean (mn) and standard deviation (SD) of the fit residuals for the column retrieval when SO_2 is not fit, and for the synthetic BT difference (dBT) as used in the Prata fit.

but is used as a proxy in the Prata fit method, as discussed in Section 4.6.3 and Figure 4.13. The threshold value of -8 K is used. Figure 5.5 shows that the BT difference alone cannot indicate the presence of SO_2. The method uses differences and ratios of other channel brightness temperatures to reduce the incidences where atmospheric conditions produce a negative BT difference above this threshold but that are not related to the presence of SO_2, namely those associated with temperature and water vapour, but this does not eradicate false positives entirely.

5.4.2 HIRS/2 SO_2 column retrieval results

Quality control

The results of the column retrieval must be subject to some quality control. The criteria that can be used can come mostly from retrieval diagnostics, but as indicated in the previous chapter additional information from the cloud model simulations will be used to indicate conditions where the results from

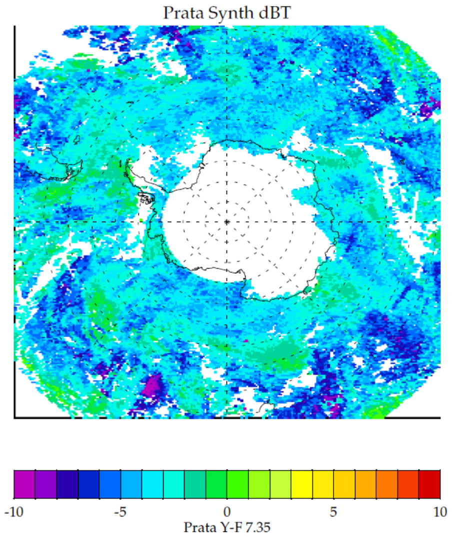

Figure 5.5: This plot shows the brightness temperature difference flag employed by the Prata et al. (2003) HIRS/2 fit.

the retrieval may not be depended upon. To be considered a valid retrieval, a given pixel must converge. The allowable cost, which is a measure of the quality of the retrieval fit to the measurements, must be limited to around the number of elements in the state vector to have confidence in the fit. For the HIRS/2 SO_2 column retrieval, this is frequently the case for converged pixels anyway. Where retrieved error has a large degree of variation, the origin of which can lie outside that which is modelled explicitly in the forward model, it is useful to apply a condition that a pixel will only be considered valid if the retrieved error is less than the absolute value being retrieved. For the purposes of gridding or summing pixels for deriving a global or plume mass estimate, a minimum retrieved SO_2 threshold may be applied in deference to the lower detection limit of the retrieval, in order to avoid spurious low values that the retrieval should not be sensitive to, such as those relating to water vapour or cloud that are not accounted for in either the error covariance or the forward model. An effective way of obtaining this in a quantitative way is to apply a 2 or 3 sigma test, where the sigma is the standard deviation of the retrieved SO_2 on a day when no volcanic perturbation is expected. This threshold gives statistical confidence that a value above it is significantly distinct from the noise above the 95 or 97 percentile. The sigma threshold for 6^{th} August 1991 was 2.7 DU, and is probably a lower estimate of the detection limit of the HIRS/2 SO_2 column retrieval. Multiples of this value indicate confidence that a retrieval result is dominated by signal rather than noise.

External quality control information can be obtained from the other HIRS/2 channels, particularly to identify cases where atmospheric conditions might lead one to expect the retrieval to perform poorly, but in the case of detecting the presence of ash for example, the cloud model simulations are expected to prove more reliable. As shown in figures 5.6 and 5.7, the presence of ash can be indicated for a variety of ratios from channel measurements frequently used in remote sensing from satellites. But as these figures show, without either some tailoring or some relatively sophisticated investigation into their specific use for this instrument, the information requires careful interpretation for an unambiguous result. An optimised retrieval of SO_2 with HIRS/2 would make use of the available AVHRR data that are on the same platform. Constantine et al. (2000) use an AVHRR ash retrieval and report it with their TOMS SO_2 algorithm results (discussed in section 1.4.1). It is sufficient to say that such criteria can always be improved upon, and any total mass estimates will depend in a great part upon the quality control criteria used. Too harsh and sampling is reduced, too lenient and spurious values begin to make an increasing contribution.

5.4.3 Results - 1991 Cerro Hudson eruption

Figures 5.8, 5.9 and 5.11 shows results from the column retrieval for one day in August 1991. The results were filtered for cost, convergence, a retrieved SO_2 to SO_2 error ratio of greater than 1, and with a retrieved cloud top height limit of 5 km, as derived from simulations with the cloud model for the column SO_2 retrieval in the previous chapter that indicated above this the retrieved SO_2 unreliable. A minimum threshold of 3-sigma is applied throughout, except where specified differently.

Figure 5.9 shows the results for both the column retrieval and the corresponding SO_2 from the Prata fit method. It is apparent on this day that in

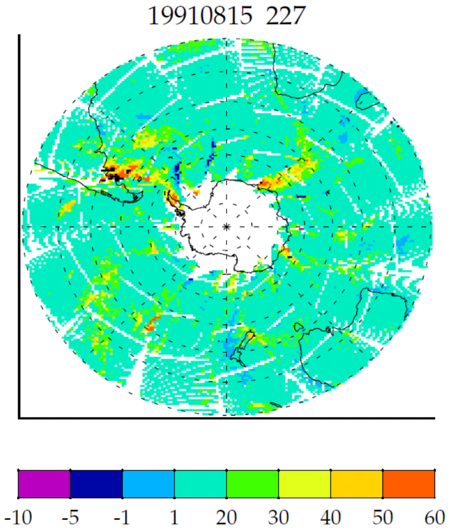

Figure 5.6: 3.75-11.1 μm brightness temperature difference, on 15th August 1991, using day only measurements. There is a strong suggestion of the presence of ash in the region of the Hudson eruption, but it is unclear using just these simple differences whether other features in that latitude are previously erupted ash, cloud artifacts or something else entirely.

the centre of the main SO_2 plume, the Prata fit predicts less SO_2 than the column retrieval. This is a tendency that the simulations with the RFM in the previous chapter suggested would be the case.

Figure 5.10 shows retrieved water vapour scaling factor and cloud top height (with their associated retrieved errors) when no cloud top height limit is used (and the 2-sigma threshold is not applied). This is shown to demonstrate how the retrieval behaves in the presence of cloud higher than 5 km. The cloud model simulations suggested that the retrieval struggles in the presence of high cloud and can on occasion fit spuriously enhanced SO_2, potentially because it results in a poor estimate of water vapour in the correspondingly colder scene. As suggested by the high retrieved water vapour scaling factor error in the presence of high cloud shown in figure 5.10, that is vastly reduced in figure 5.11 when the limit is imposed.

Figures 5.12, 5.14, 5.16 and 5.18 each show 6 days of the column retrieved SO_2, and are followed on their subsequent page by the retrieved error for those

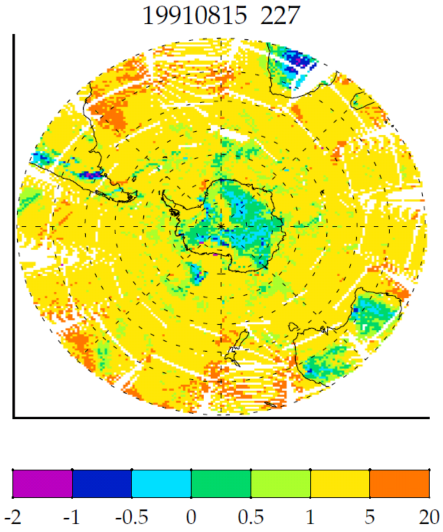

Figure 5.7: 11.1 - 12.6 μm BT difference, on 15th August 1991. A negative BT difference is indicative of ash. The feature emanating from Cerro Hudson (45 °S, on the South American Continent) is almost certainly a good indication of ash being erupted from the volcano. The signal is somewhat more discernable in the night than in the day (not shown). This does demonstrate however, that a simplistic brightness temperature difference with these channels is insufficient to robustly indicate the presence of ash globally.

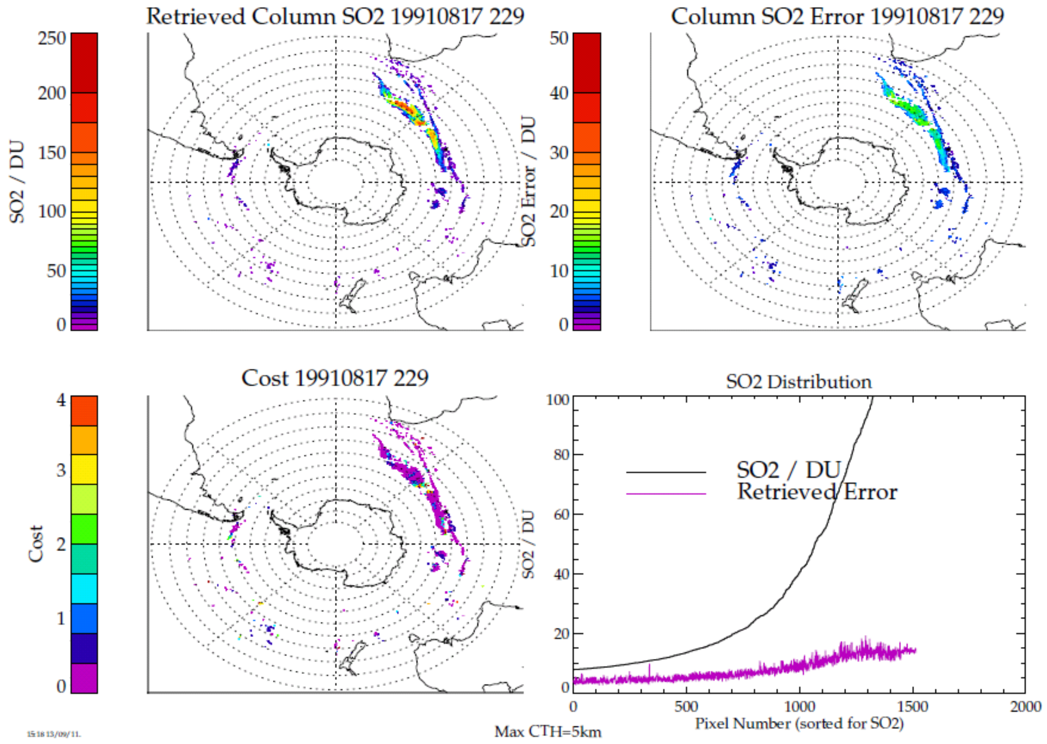

Figure 5.8: The top left plot shows the column retrieved SO_2 on 17th August 1991, with the plot on the top right the corresponding retrieved error. The plot on the bottom left shows the cost, and the bottom right demonstrates how the retrieved error behaves as a function of retrieved SO_2. The quality control criteria are discussed in the main text.

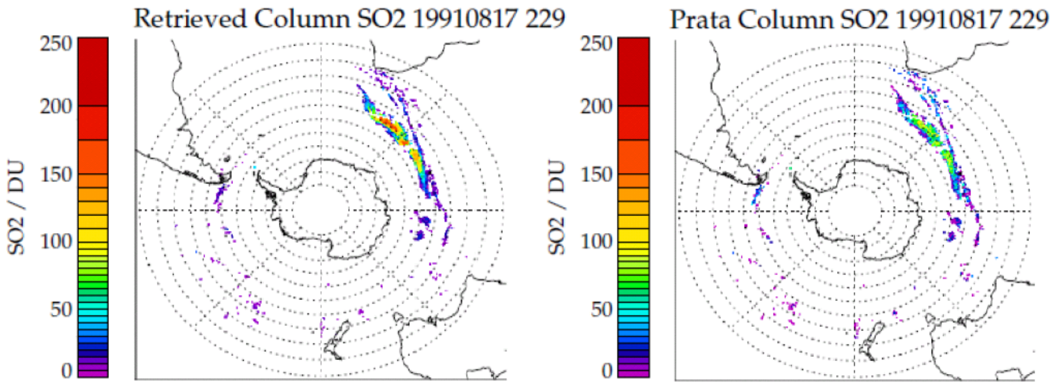

Figure 5.9: The plot on the right shows the corresponding SO_2 as calculated using the Prata fit. For ease of comparison the equivalent plot from Figure 5.8 is shown on the left.

dates. The data have been screened for noise at the 2-sigma level. Namely, cost, convergence, 2-sigma and retrieved cloud top of less than 5 km.

5.4.4 Plume mass estimates

A principal part of the conclusion reached in the second chapter of this work (comprising Miles et al. (2004)), was that the primary uncertainty relating to assessing the climatic impact of past historical eruptions lies in the uncertainty of the mass estimate of erupted SO_2. But this is not a phenomenon restricted to historical eruptions. As discussed in the first chapter of this work, at present there are a number of satellites capable of measuring atmospheric SO_2, with varying sampling, accuracy and precision. In the context of the post-satellite era, we are presently in an extremely fortunate, data-rich time for observations of volcanic plumes from space. However, there still exists a vast difference between the instruments in the mass estimate for any given eruption. This difference arises (as discussed previously) as a result of a number of factors, including sampling, resolution, accuracy, sensitivity (dependence upon the height of the plume, as well as to other atmospheric factors such as cloud), and interpretation. As pointed out in Chapter 1, some instruments

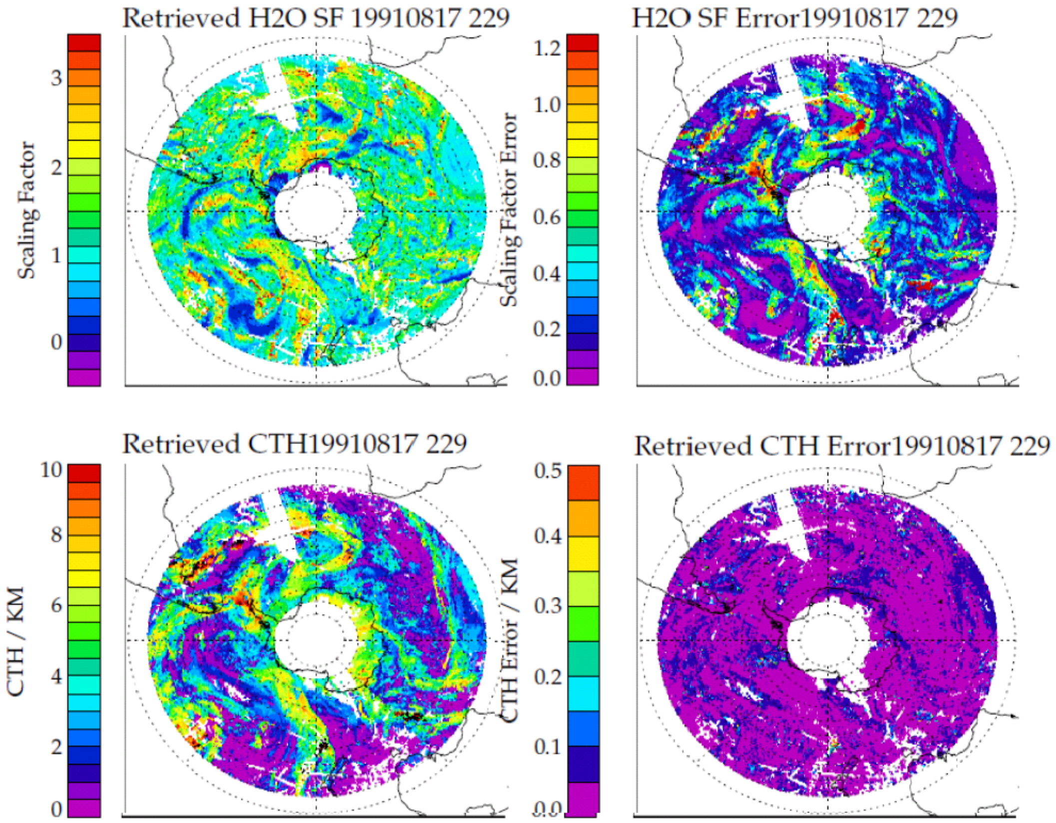

Figure 5.10: The top left and top right show the retrieved water vapour scaling factor and its error from the column retrieval. The bottom left and right the equivalent for the retrieved cloud top height. No cloud top height limit was imposed for these data, but they were filtered for the other quality control criteria listed at the start of this section with the exception of the 2-sigma threshold for verbosity.

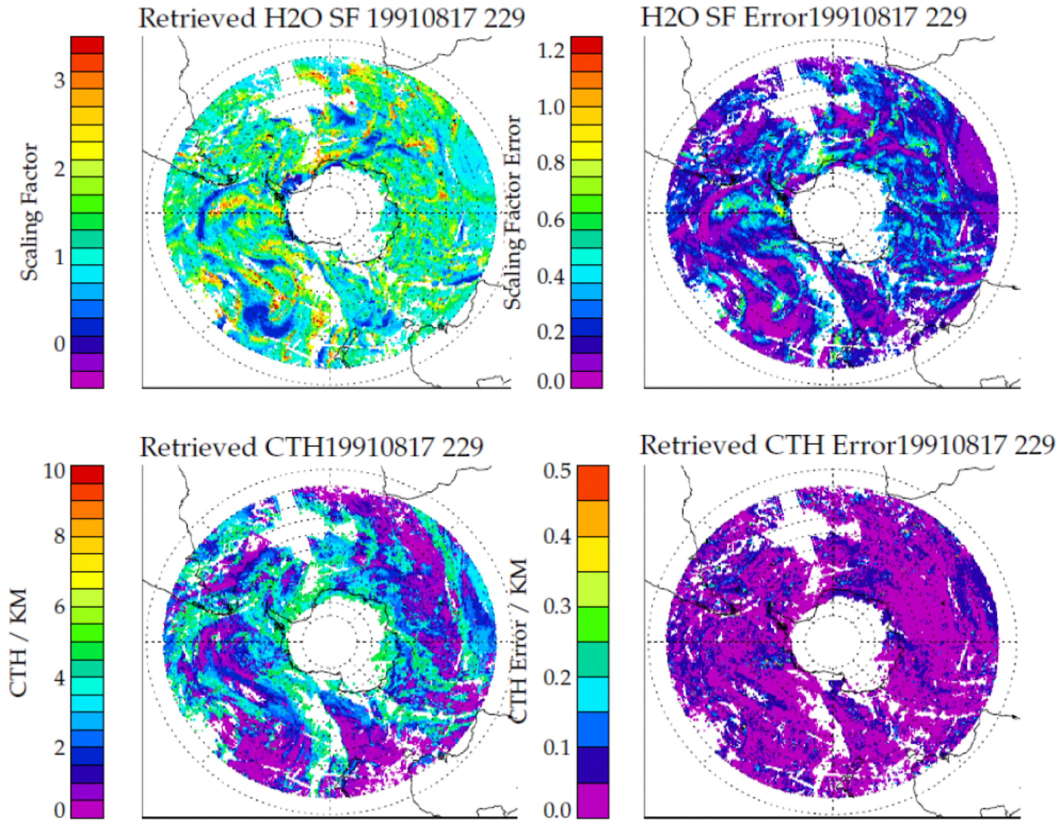

Figure 5.11: These plots are as figure 5.10, but with a 5 km cloud top height limit imposed upon the data filtering.

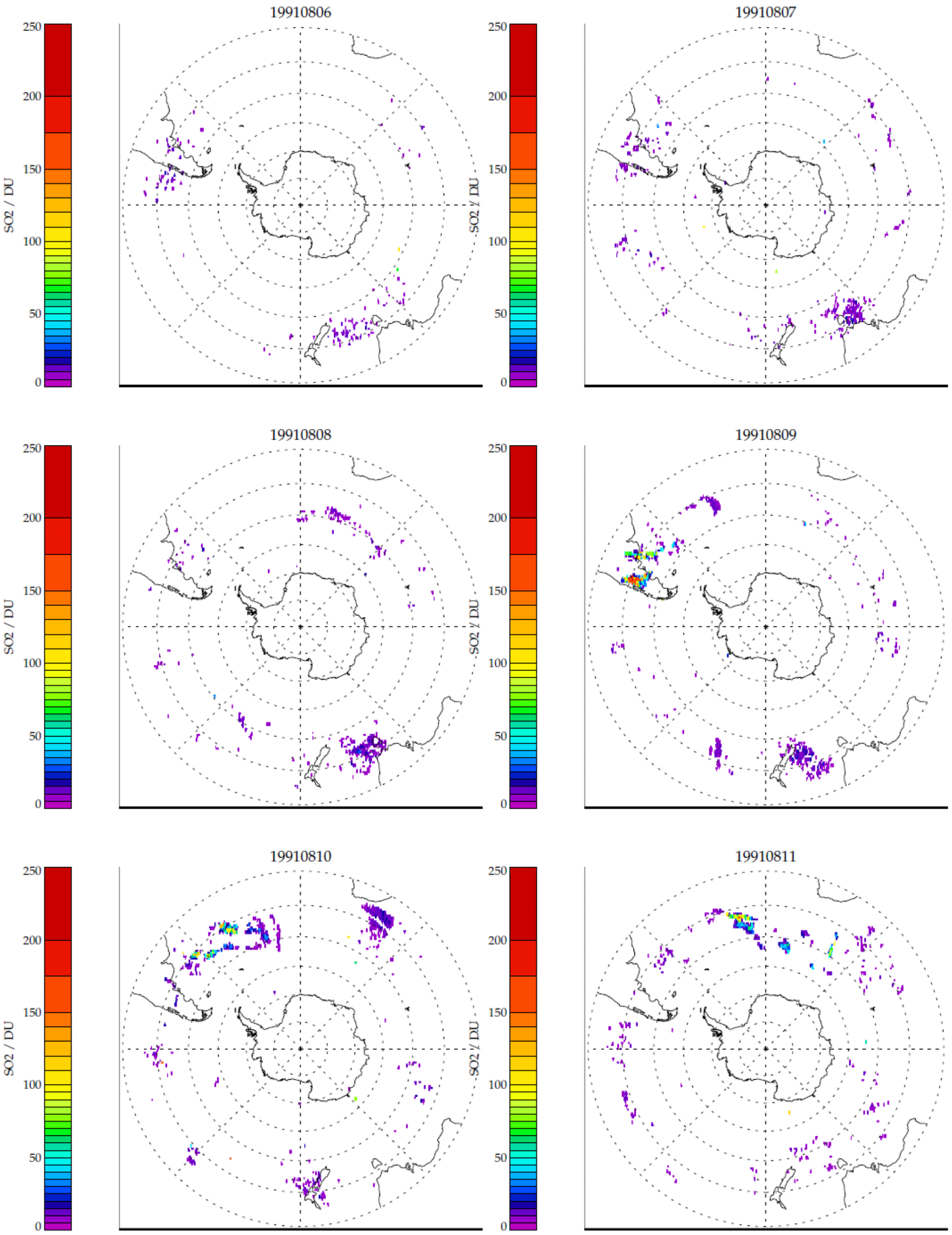

Figure 5.12: 6th-11th August 1991 retrieved SO_2.

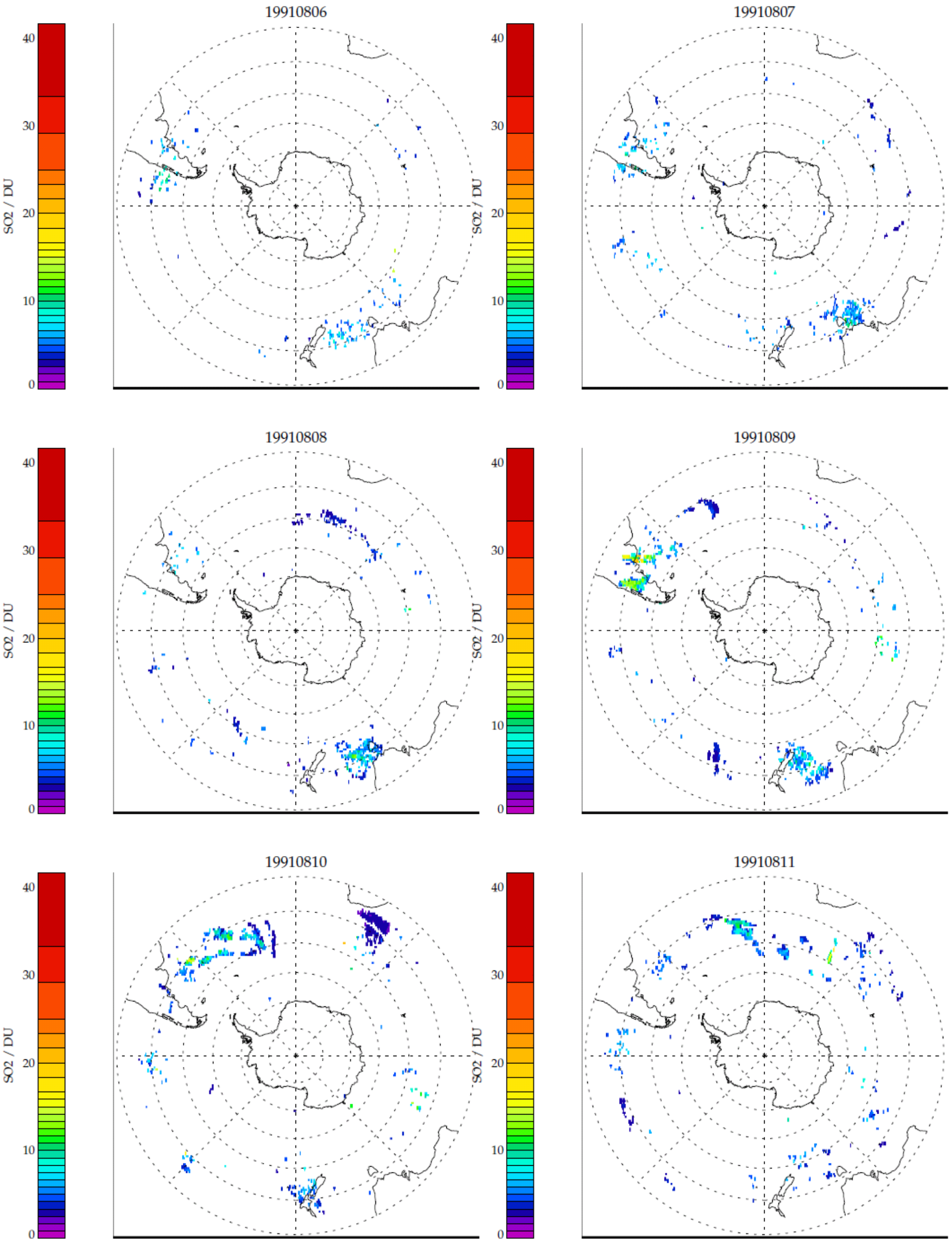
19910806

19910807

19910808

19910809

19910810

19910811

Figure 5.13: 6^{th}-11^{th} August 1991 SO_2 retrieved error.

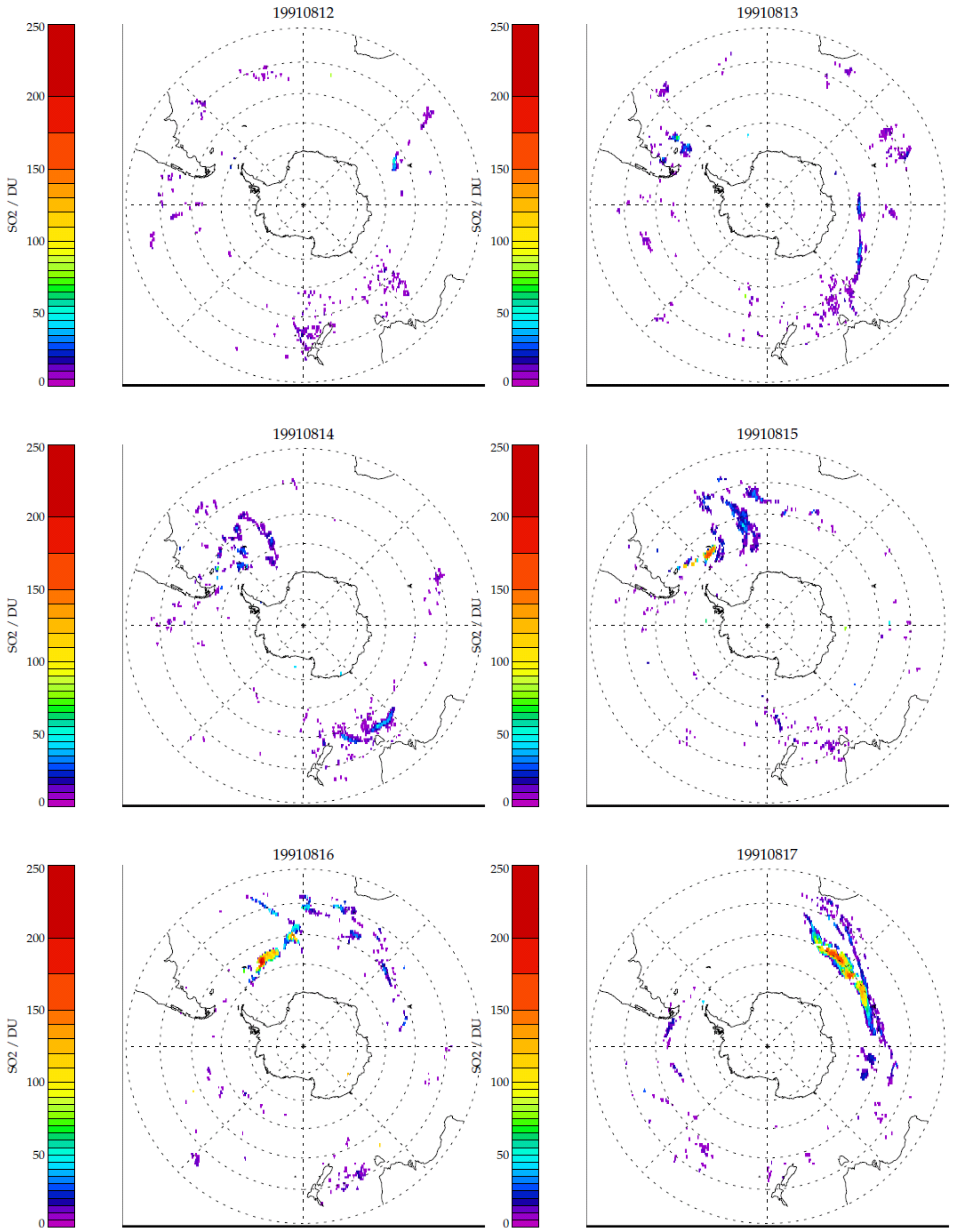

Figure 5.14: 12^{th}-17^{th} August 1991 retrieved SO_2.

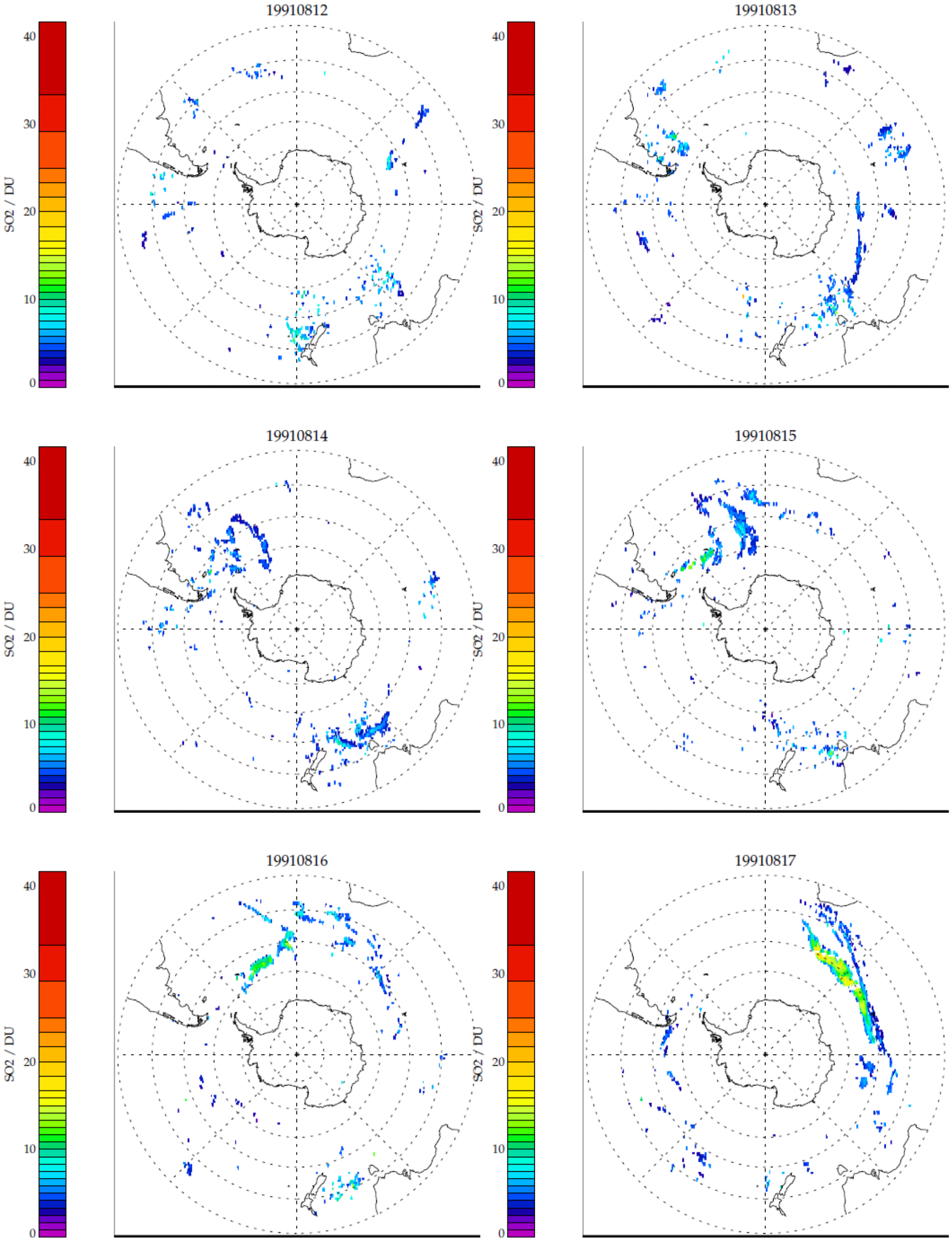

Figure 5.15: 12^{th}-17^{th} August 1991 SO_2 retrieved error.

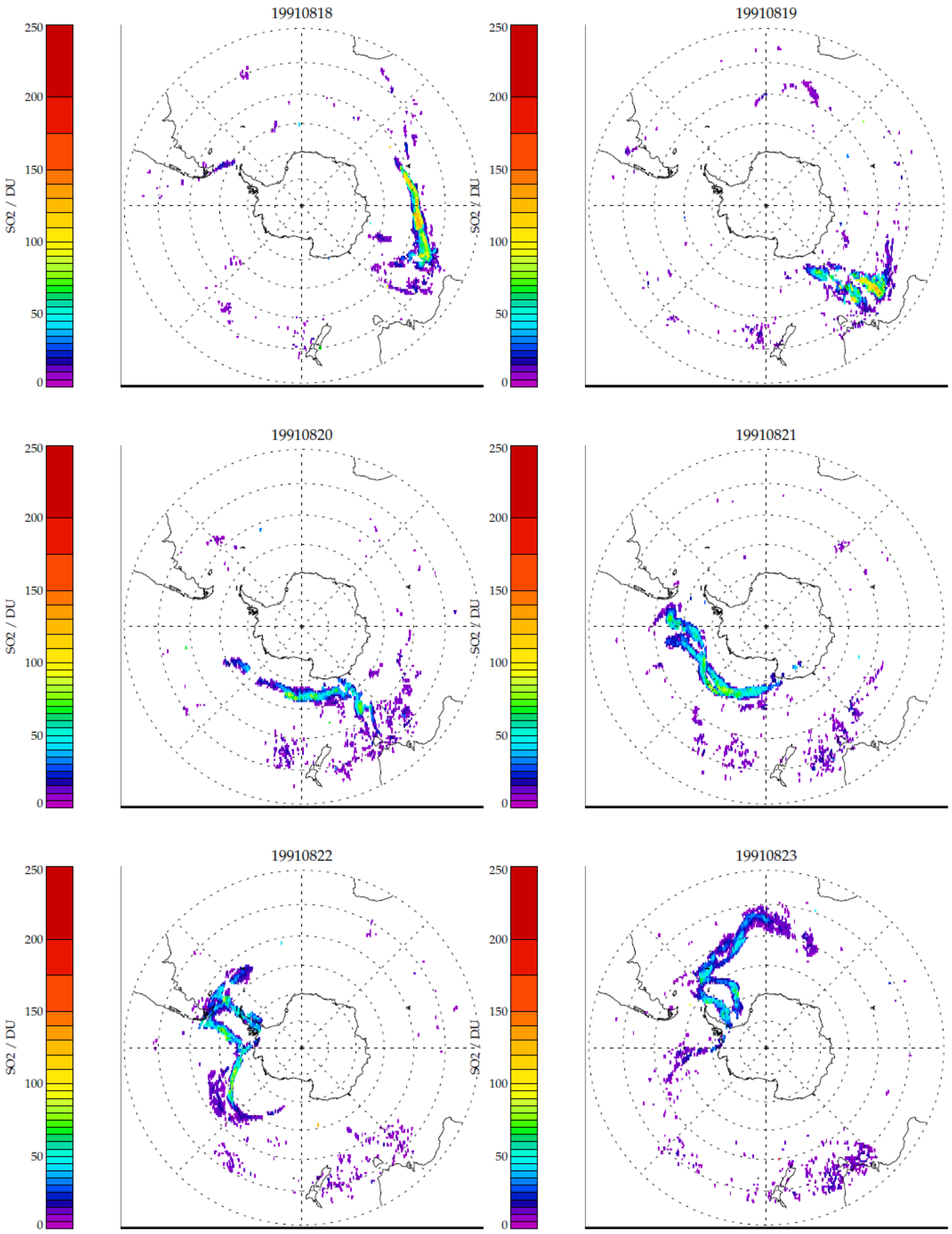

Figure 5.16: 18^{th}-23^{rd} August 1991 retrieved SO_2.

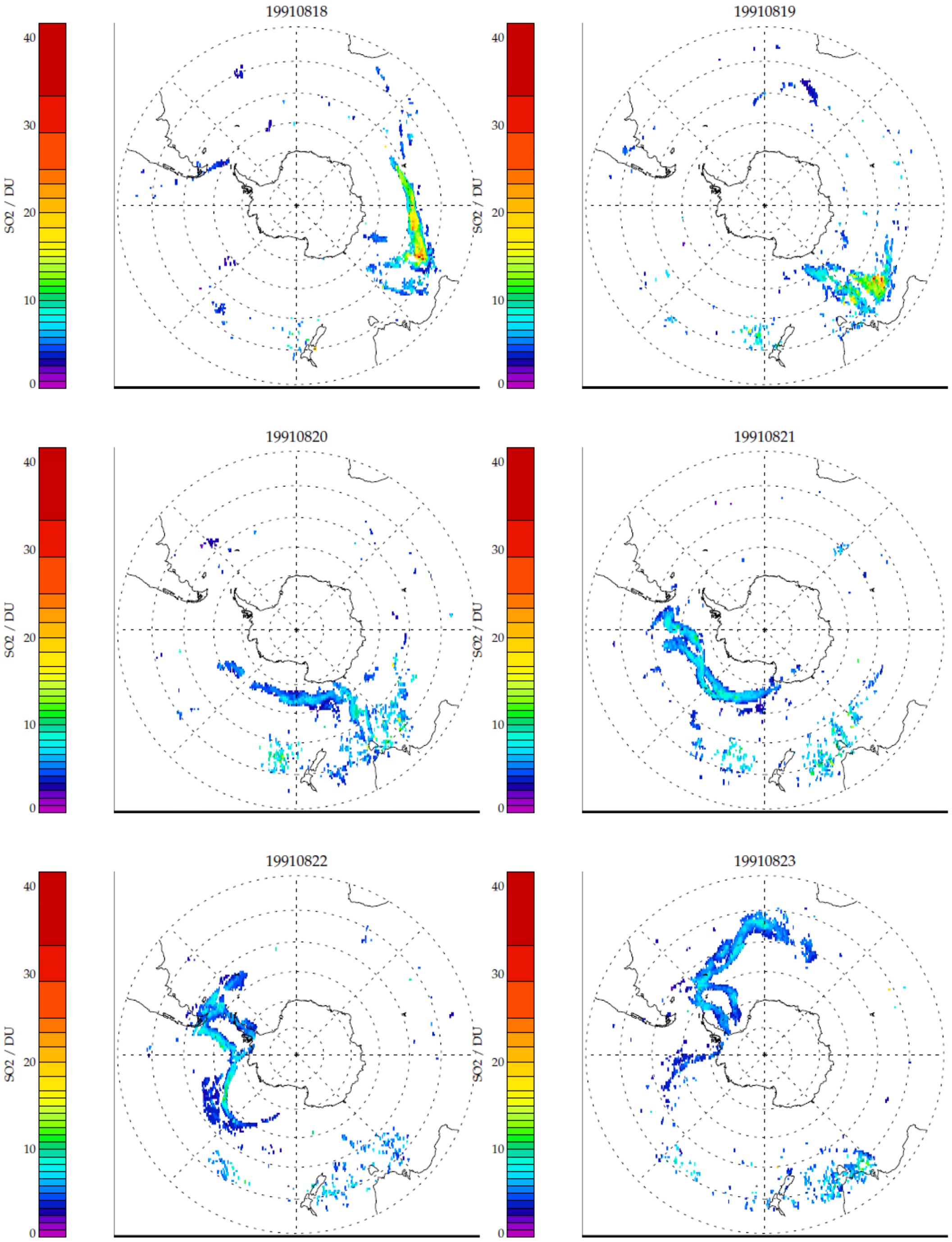

Figure 5.17: 18^{th}-23^{rd} August 1991 SO_2 retrieved error.

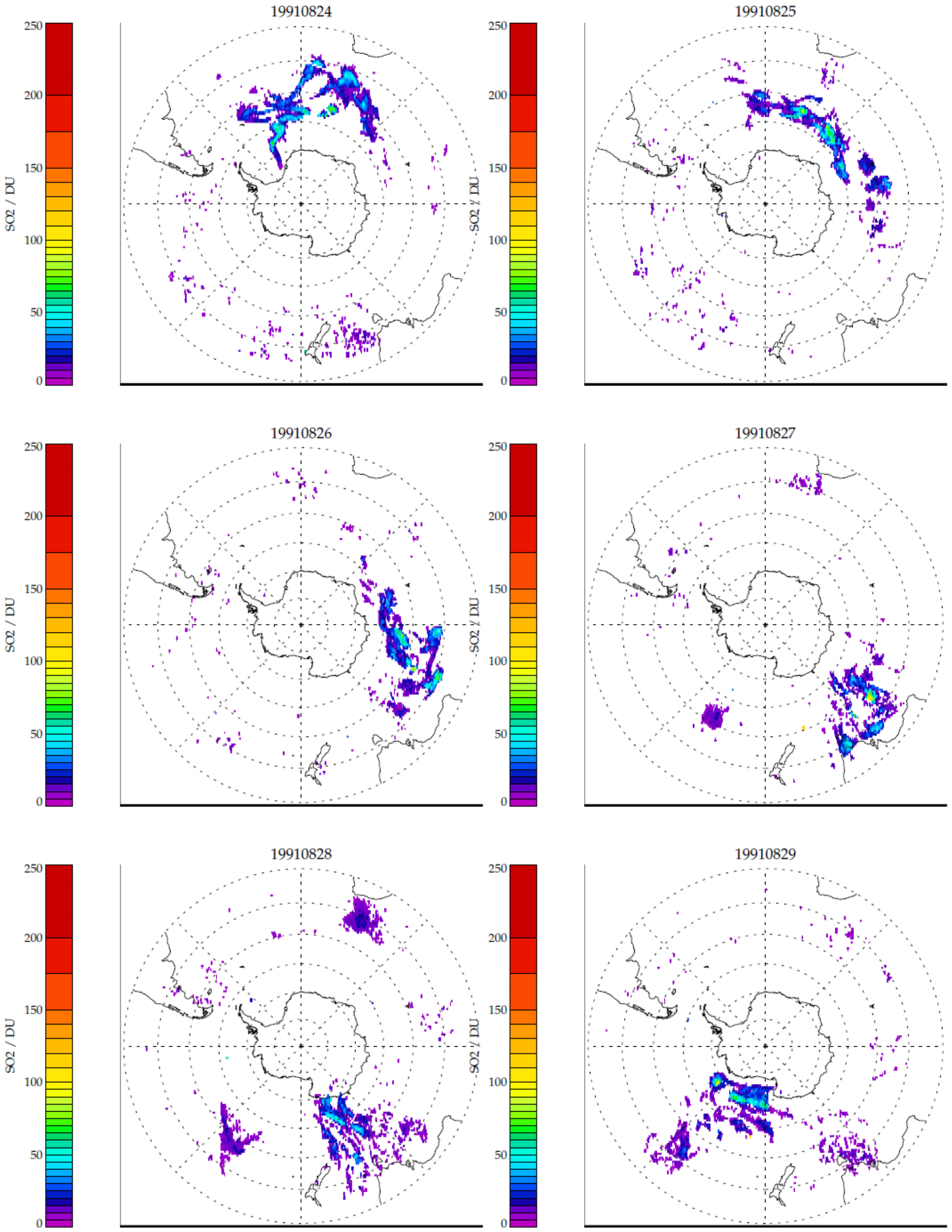

Figure 5.18: 24th-29th August 1991 retrieved SO_2.

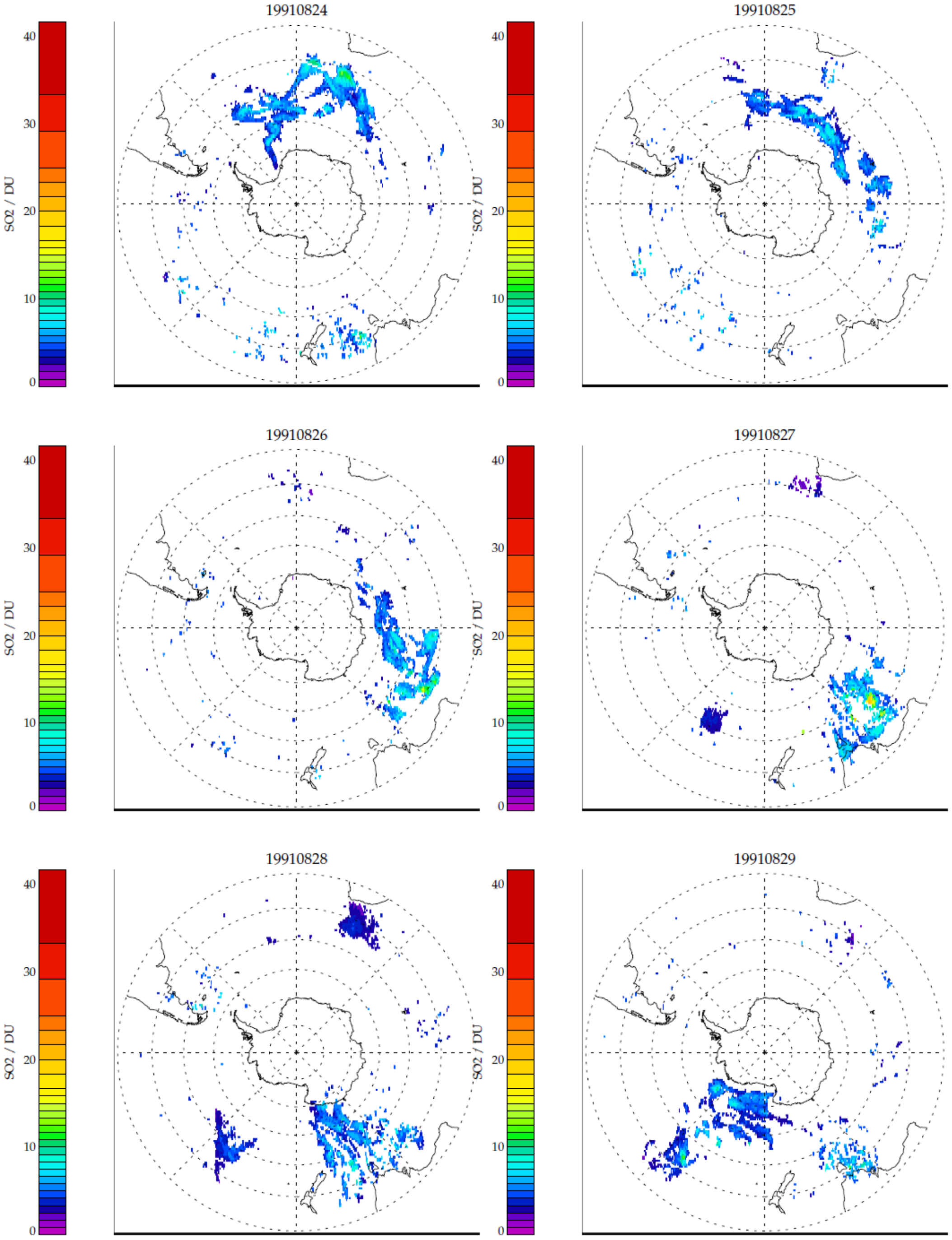

19910824

19910825

19910826

19910827

19910828

19910829

Figure 5.19: 24th-29th August 1991 SO_2 retrieved error.

have both minimum detection limits because of limited spectral information, and high detection limits due to saturation, or differing vertical sensitivity.

For any given accuracy in the retrieval of the column amount for a given instrument pixel, there arises a level of uncertainty surrounding the way in which the total mass in a plume is calculated from them, and it is this value in particular that is one of the most useful for putting an eruption into historical context, and for assessing its relative climatic impact.

The simplest method to estimate the total erupted mass or mass present in a volcanic plume is to take the sum of the representative footprint areas of the satellite that measured SO_2. The HIRS/2 FOV information is shown in Table 4.2, and the ellipses range in diameter from 17.4 km at nadir to 58.5 km at the edge of the swath. Taking into account the curvature of the Earth, equation 5.1 gives the arc length from the nadir point of the satellite to a point along the scan line, where a is the height of the satellite, R the radius of the Earth, θ the scan angle or angle at the edge of the considered rectangle for each FOV. By taking the difference of these arc lengths at the mid point between FOVs, the long length of the equivalent rectangle is given. The short length is assumed constant and is given by the stated distance between the centre of the scan lines (42 km).

$$S = R[\arcsin\left(\frac{(a+R)\tan\theta\sin(\frac{\pi}{2}-\theta)}{R}\right) - \theta] \tag{5.1}$$

An alternative method is to grid the SO_2 values. This averages the data into grid boxes on a latitude and longitude grid. Some care must be taken to account for whether or not the gridded data are representative of the data resolution, and keeping track of bins with no data can be a way to estimate under-sampling. Guo et al. (2004) use two methods of gridding data, that of kriging for TOMS data and nearest neighbour interpolation for HIRS/2 to account for larger spatial gaps between points. These methods either impose statistical methods or manually introduce information. While both can be utilised in such a way as to indicate an estimate of the error or uncertainty that this introduces, the gridding method used here uses only the measurements available.

In order to ensure that the data are sampled fairly, the orbits are first split into ascending and descending nodes. This is in an effort to minimise the recording of the same data point twice when the passage of the cloud has moved it by the time the region is sampled again. The time range over which it is sampled is also split into two, as on occasion the SO_2 plume will pass either the date line or the Greenwich meridian and may be only partially sampled. They are deemed to be 1200 UT of the day in question, plus or minus 12 hours, and 2400 UT plus or minus 12 hours. As such, there are four maps produced each day that each capture the plume slightly differently.

For the purposes of gridding, rather than use a uniform latitude longitude grid, it is desirable (to optimise sampling) to use a grid with boxes of equal area. For a uniform grid the grid box areas decrease the higher the latitude. Weighting the grid box area by the cosine of the latitude effectively yields a more uniform area sampling.

Even accounting for all of the above, the equivalent footprint method may be prone to overestimating the total mass present due to the fact that at the latitude of the plume, consecutive orbits partially overlap. In the gridded case, it is as likely to cause an underestimate as an overestimate in a particular grid box when a non-SO_2 pixel is averaged with an SO_2 filled pixel from a neighbouring orbit if the plume has perceptibly shifted. These caveats serve to highlight that these are only two, relatively straightforward methods of estimating total erupted SO_2 after an eruption.

Figure 5.20 demonstrates how observations around the time of a specific eruption event can identify different temporal stages of the plume, an advantage specific to infrared measurements, which effectively have twice the temporal sampling of UV instruments. Both plots show gridded retrieval results for the 15^{th} August 1991 that have been divided into node maps classed as descending day and descending night, using the system specified above. They distinguish SO_2 erupted shortly before and after the main explosive eruption event. The total erupted mass present in the daytime descending node is around 500 kt ± 200 kt. In the night time descending node, this rises to 1600 kt ± 300 kt, but as discussed later the peak loading is not attained until a couple of days later. The other nodes (day and night ascending) do not capture the plume at all.

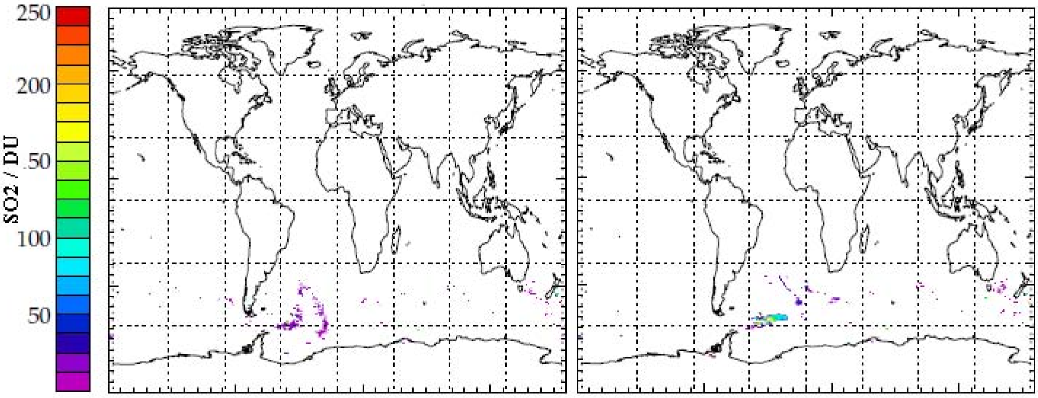

Figure 5.20: The plot on the left is a map of the gridded descending node daytime observations (1200 UT ± 12 hours) for 15 th August 1991. The plot on the right shows the descending node night time observations for the same date (2400 UT ± 12 hours). Both plots have been filtered to the 3-sigma level.

Figure 5.21 shows the mass estimates selected to represent a 'best estimate', with regard to the spatial distribution, that has been screened for noise at the 3-sigma level. Whilst this is a somewhat subjective approach, even taking the steps of gridding and splitting the data into ascending and descending nodes, and shifting the selection time by 12 hours to accommodate the motion of the plume across the date line, there were still occasions where the plume was sampled twice or only partially. As such, a mass estimate that was geographically limited to the region of the plume using a more sophisticated localisation would be an improvement upon this, but would constitute a detailed study in itself that is beyond the scope of this work. The same data are shown in Figure 5.22 where the data have been screened at the slightly more generous level of 2-sigma. Most mass estimates are increased, which alludes to the impact of establishing a detection limit. The mass estimates that are dominated by significant amounts are largely similar, but the higher noise threshold decreases the retrieved error estimate on the mass derived by summing the equivalent footprint, and decreases the background value.

Without screening for noise at the 2 or 3 sigma level, the mass estimates for 17^{th} and 18^{th} of August 1991 were greater than the previous few days, despite the most explosive phase of the erupting occurred on 15^{th} August. Whilst it is apparent in the retrieved data that some of the plume on 15^{th} and 16^{th} August does not pass the standards of quality control that give sufficient confidence that the retrieval is performing well, the majority does. As the cloud model simulations demonstrate, the retrieval is very sensitive to the presence of ash, and has a tendency to confuse ash with very high cloud. The pixels which failed the quality control criteria did so upon either retrieved cloud height or convergence. Constantine et al. (2000) report that using an AVHRR ash algorithm, they were able to show that the ash reduced by 90 % in the 3 days after the main eruption, and for this reason, it might not have been expected to detect a maximum plume mass until the 17^{th} and 18^{th} August.

Constantine et al. (2000) also found that TOMS SO_2 estimates increased by 300 % on 16^{th}. They discuss several reasons why this might be the case, and equally discount most of them, including the notion that the plume is too optically dense to observe all of the SO_2 due to saturation. They suggest that the most likely explanation for their result is oxidation of H_2S in the plume, which occurs an order of magnitude faster than that of SO_2.

By no measure does the SO_2 increase in the two days following the main eruption, but due to how the data are separated for the nighttime gridded descending node, it includes observations made on the morning of 16^{th}, and the plume is not captured so well by the nodes in the following time step. As such, it does not contradict the findings of Constantine et al. (2000), but it does suggest that the time of observation is crucial in the region of a recent post-eruptive plume. From 19-26^{th} August the plume becomes highly striated and it becomes more difficult to ascertain whether parts of the plume are sampled more than once. To distinguish them the node maps would have to be separated into smaller time steps (12 hours) but this would lead to an increased incidence of fractional sampling or non-sampling of the plume on other days. It may suffice to leave mass estimates from this period out of any estimate of the plume's decay rate. After 26^{th} August the plume rotates about its long axis (as shown in Figures 5.14, 5.16 and 5.18), and the mass estimates after this point become more modest.

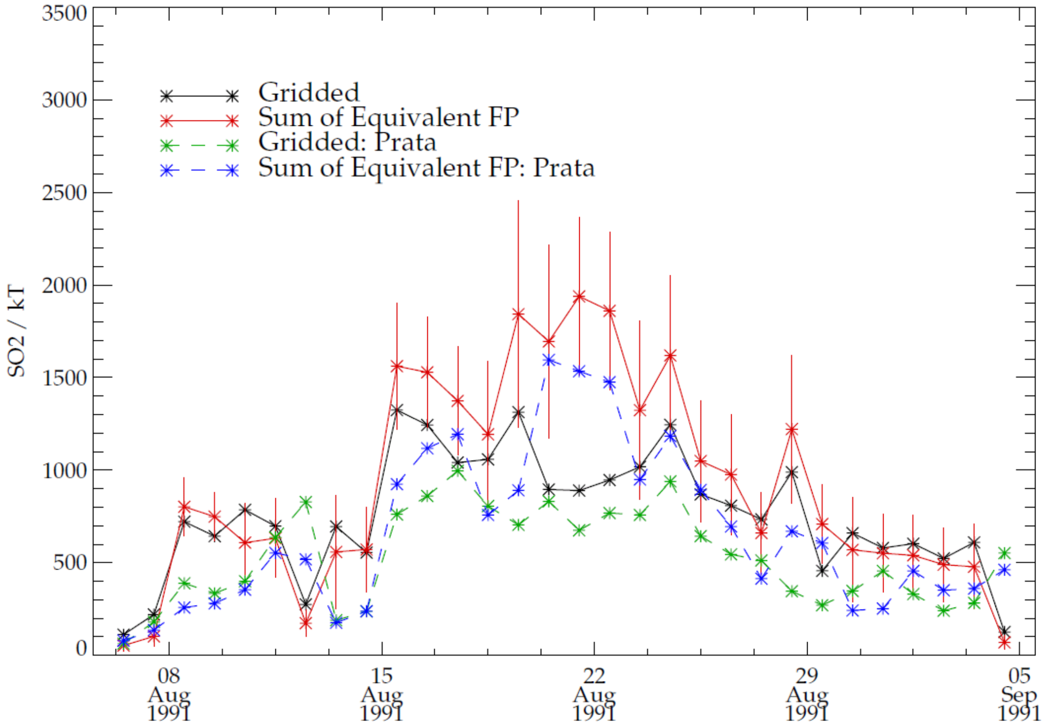

Figure 5.21: Total SO_2 present as retrieved by the column retrieval (solid lines), and by the Prata fit (dashed), for both gridded and the sum of equivalent rectangular footprint. Data have been screened for noise at the 3-sigma level.

5.4.5 HIRS/2 comparative SO_2

The comparative mass estimates from the Prata et al. (2003) fit algorithm are also plotted in figures 5.21 and 5.22. The plot represents the gridded orbits sample selected in which the column retrieval is considered to capture the plume well, which are not necessarily the best representations as found by the fit method. In terms of total mass present in the pixels selected, the Prata fit tends to predict a lower total mass when 2-sigma filtering is used to select

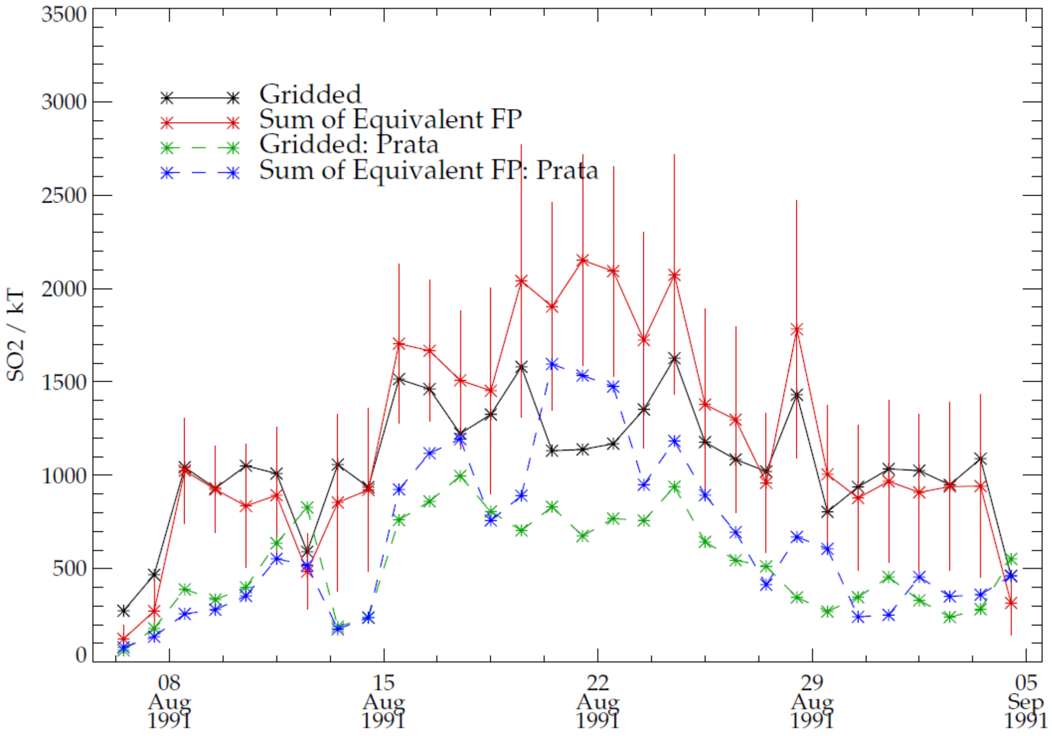

Figure 5.22: Total SO_2 present as retrieved by the column retrieval (solid lines), and by the Prata fit (dashed), for both gridded and the sum of equivalent rectangular footprint. Data have been screened for noise at the 2-sigma level.

the column retrieved pixels, but is comparable with the more robust 3-sigma threshold. It is visually apparent from figure 5.9 and the full series (not shown) that in the centre of the plume where the column retrieved particularly high SO_2 column amounts (greater than 80 DU) the Prata fit predicts lower values.

Figures 5.23 to 5.26 show the correlation of SO_2 from the column retrieval and the Prata fit method, the pixels of which were selected to match those that pass the cost, convergence, maximum cloud threshold and retrieval error fraction quality control criteria, in addition to the 3-sigma threshold. The results shown are from 6^{th} until the end of August 1991.

From the date of the main eruption (15^{th} August 1991) the number of pixels begins to increase for which the Prata fit predicts column amounts of up to 40 DU and the column retrieval predicts very little, indicating a slight high bias of the Prata fit at low values.

For high SO_2 column amounts, either closely following the eruptive events or for pixels above 60 DU, the Prata fit tends to predict lower values than the column retrieval, particularly on 15–19^{th} August. The overall bias of the Prata retrieval is negative, and is strongly so (typically 5–10 DU) until after 19^{th}, when it becomes more modest.

For the more mature plume, from 23^{rd} and beyond, the Prata fit appears to have a small positive bias with respect to the column retrieval for column amounts above 30 DU but below 80 DU.

In general, both methods are positively well correlated, particularly after the main and smaller eruptions, but the bias signified in the different phases of the plume reflect that which was predicted with simulations for this latitude with the RFM in the previous chapter (figure 4.11).

5.4.6 Qualitative comparisons with TOMS SO_2 observations

As discussed in Chapter 1, TOMS was the instrument that initiated the measurement and tracking of volcanic plumes from space, which started with the observations of the 1983 eruption of El Chichón (Krueger et al. 2007). The same TOMS instrument (aboard Nimbus 7) was still operational at the time

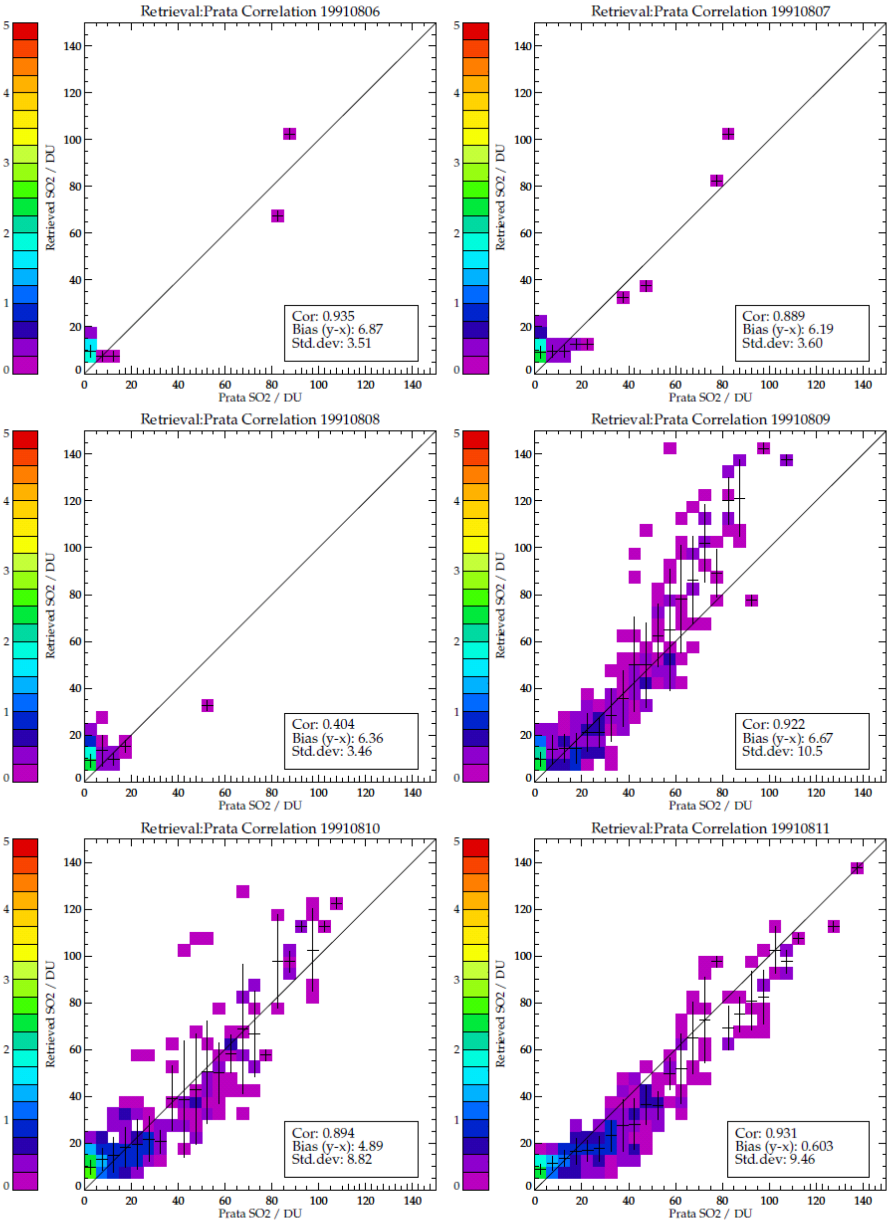

Figure 5.23: Column retrieved and Prata fit SO_2, 6^{th}-11^{th} August 1991, date title format is ‘yyyymmdd’. In the legend, cor denotes correlation coefficient, followed by bias and standard deviation.

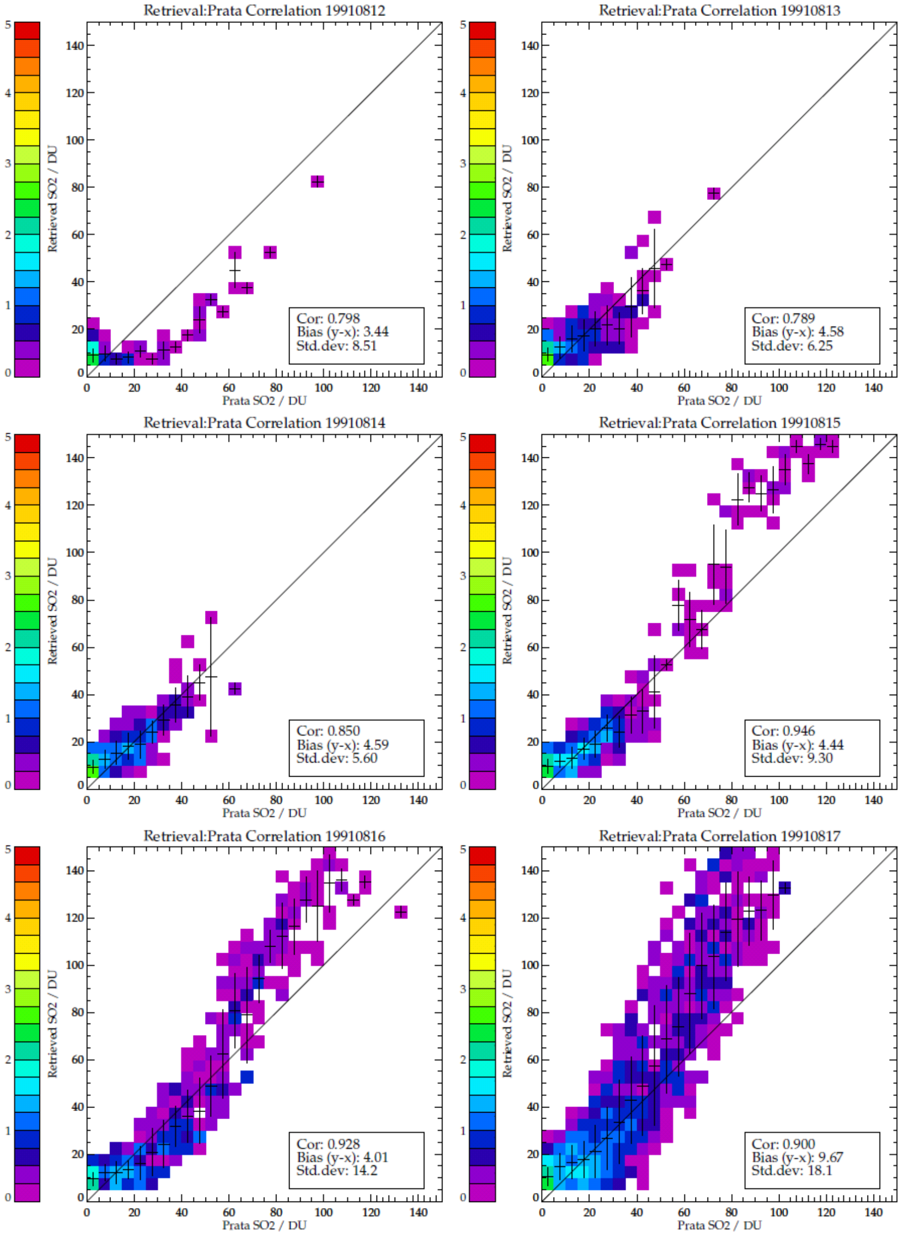

Figure 5.24: Column retrieved and Prata fit SO_2, 12^{th}-17^{th} August 1991, date title format is ‘yyyymmdd’. In the legend, cor denotes correlation coefficient, followed by bias and standard deviation.

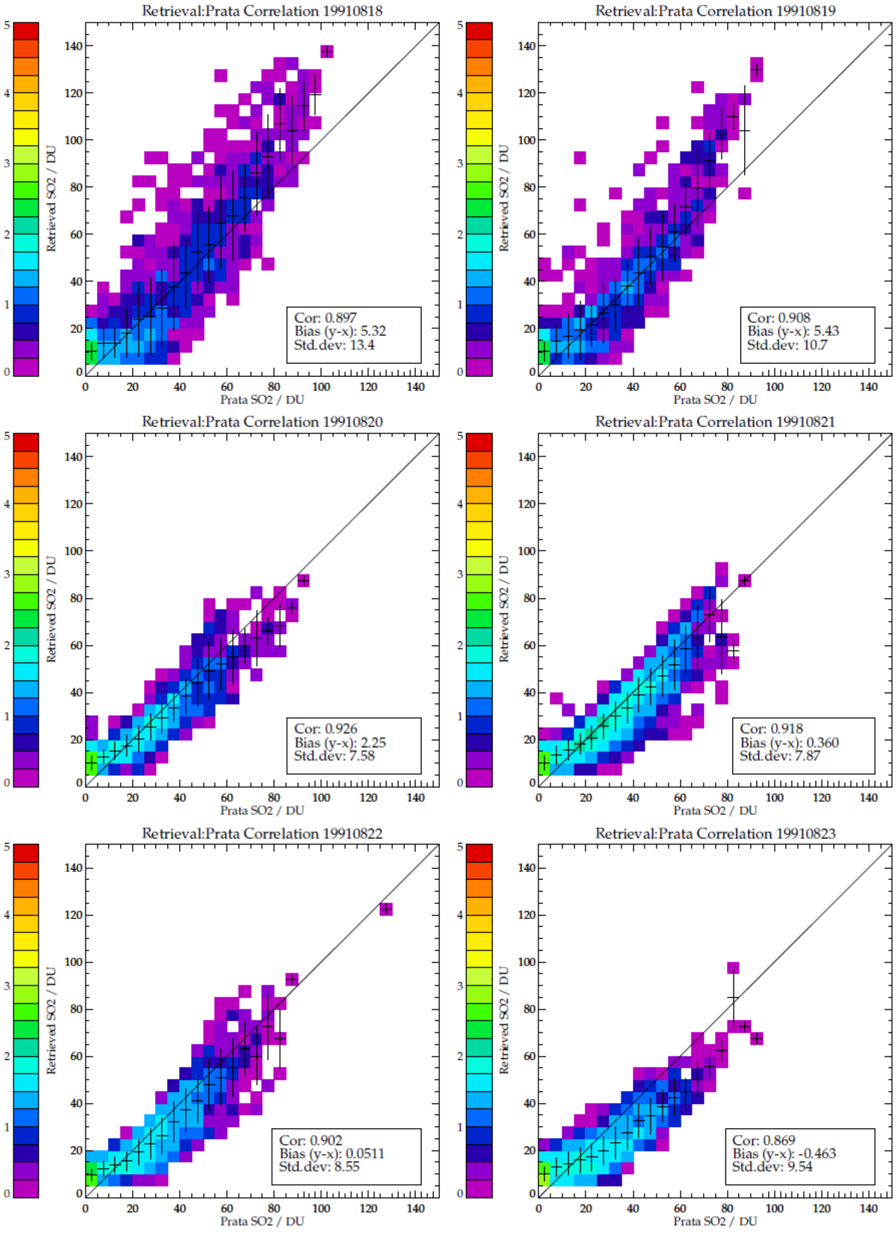

Figure 5.25: Column retrieved and Prata fit SO_2, 18th-23th August 1991, date title format is ‘yyyymmdd’. In the legend, cor denotes correlation coefficient, followed by bias and standard deviation.

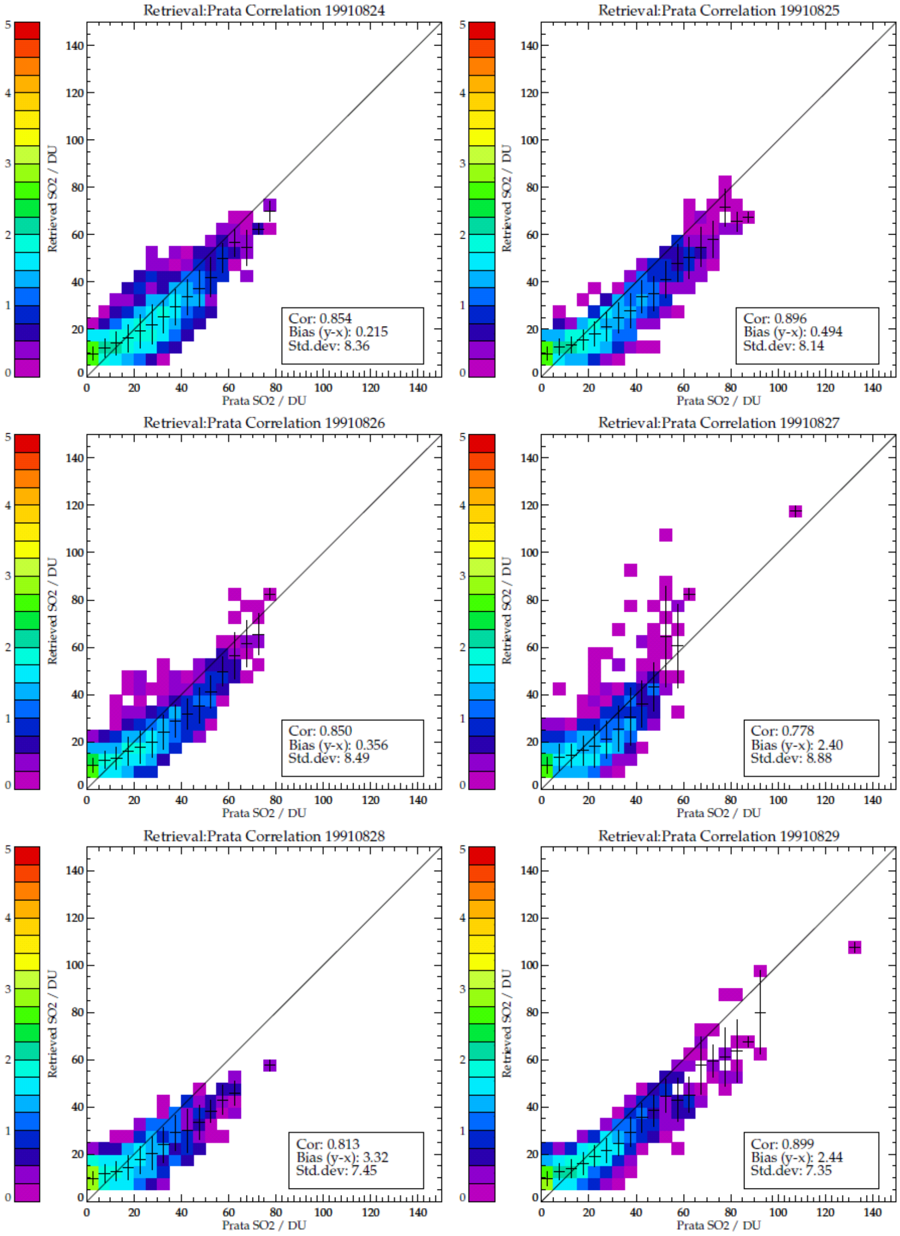

Figure 5.26: Column retrieved and Prata fit SO_2, 24th-29th August 1991, date title format is 'yyyymmdd'. In the legend, cor denotes correlation coefficient, followed by bias and standard deviation.

of that Cerro Hudson erupted.

Constantine et al. (2000) analysed TOMS data specifically for the Cerro Hudson eruption, from 9 - 21st August 1991. Two retrieval algorithms were used for SO_2, as one (version 6) could not measure an Aerosol Index, and the other (version 7) saturated at SO_2 column amounts greater than 200 DU. These were used in a complementary manner, and were considered updates of the estimates made by Doiron et al. (1991) of 500 kt in total. Problems encountered were difficulties with using two algorithms, poorly constrained eruption times and overlapping orbits leading to uncertainties in mass estimates. As such, peak estimates of the SO_2 signal were used to constrain a maximum mass. For the three phases of eruption, the main results are given in Table 5.1 in terms of total cloud mass. The sensitivity of the instrument is in the range 5-20 kt (Schoeberl et al. 1993). Also given in Table 5.1 are conservative mass estimates from the HIRS/2 column retrieval, and the fit after (Prata et al. 2003). The estimates relating to HIRS/2 are taken from figure 5.21 with consideration for the bounds of uncertainty that arise from the differing summing methods and pre-existing levels of SO_2 and representing a mid point value. For the total eruptive period, this method has yielded a total erupted SO_2 mass estimate of 2200 kt with an averaged retrieved error of 27 %. This error does not incorporate error that arises from uncertainty in the height of the SO_2 in the forward model plume (as demonstrated in figure 4.21). As previously discussed, a good estimate of plume height is an unavoidable requirement in SO_2 detection with an instrument with only one channel sensitive to SO_2 in the atmosphere. In the case of this work, height assignment error of ± 1 km introduces a mass dependent bias of between 5 and 20 % for a given pixel.

Eruptive Phase	**TOMS SO_2**	**HIRS/2 Prata fit**	**HIRS/2 Col Ret**
8-9 August	700 kt	300 kt	700 ±150 kt
12 August	600 kt	400 kt	400 ±250 kt
15 August	2700 kt	1000 kt	1100 ±300 kt

Table 5.1: TOMS and HIRS/2 SO_2 mass estimates for the 1991 Cerro Hudson eruption

Ash was monitored by AVHRR, a radiometer, sensitive to particles of 1–15 μm. The Hudson ash cloud from 15^{th} was observed just above the tropopause (beneath the SO_2) and lost 90 % of its mass in the first few days. The SO_2 plume lost two thirds of its mass within the first week (Constantine et al. 2000).

Advances in the interpretation of the TOMS data has led to an adaptive algorithm (Rose 2002). However, this update is unlikely to improve the mass estimates by Constantine et al. (2000) by over 30 %, which is the approximate error on retrieved TOMS SO_2 values (Krueger et al. 1995).

Development of the most recent version of the TOMS SO_2 algorithm is currently in progress, and is as yet unavailable. The data that contributed to Constantine et al. (2000) are also unavailable, preventing a fully quantitative comparison.

A qualitatitive comparison between HIRS/2 and TOMS may be drawn from figures 5.27 and 5.28. They show the published TOMS daily SO_2 column (Constantine et al. 2000) beside the values for similar geographical region as derived by the HIRS/2 column retrieval. Temporally, HIRS/2 has the advantage of being able to make measurements at night and it is not limited by solar zenith angle, particularly important at this latitude. The TOMS SOI, the publicly available SO_2 product described in section 1.4.1 (and explicitly not the same quantity as retrieved SO_2) only captures part of the SO_2 plume on a handful of days for this eruption due to the high solar zenith angle.

Spatially, HIRS/2 has the advantage of smaller footprint than that of TOMS, (IFOV 1.25°×1.25°, 17.4 km×17.4 km versus 3°×3°, 50 km×50 km), but the TOMS swath is 50 % wider at 3000 km. For a case such as the Hudson plume, TOMS is more likely to capture the entire plume in one orbit swath and sample it only once, which on one hand greatly reduces ambiguity in deriving total plume mass but on the other the frequency of observation is reduced. However as reported by Constantine et al. (2000), this was not always the case, and a ‘best’ estimate of the TOMS data was used to contribute to the values in figures 5.27 and 5.28.

The TOMS SO_2 values in the mass estimates given in Table 5.1 are consistently higher than those from either of the HIRS/2 products. This was

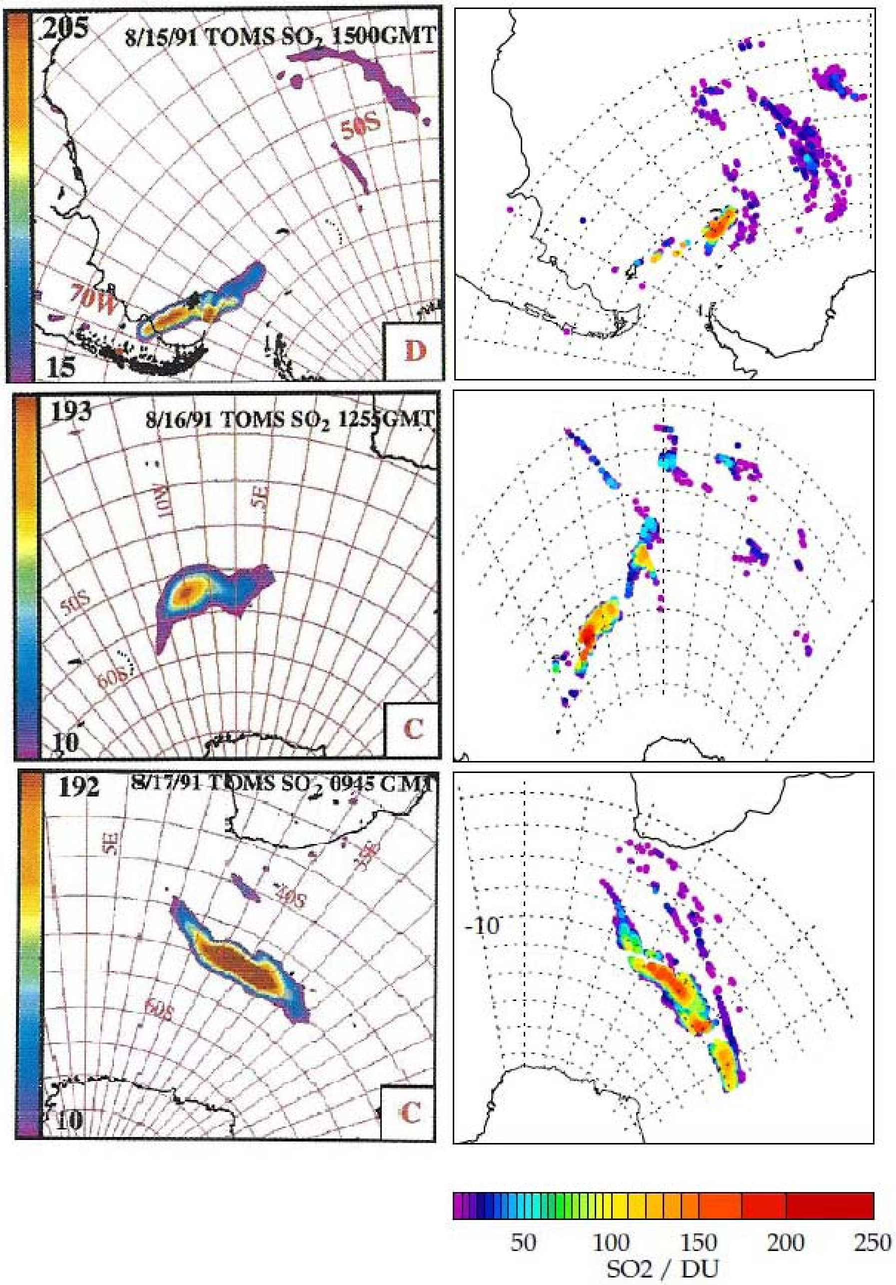

Figure 5.27: The left hand column shows figures taken from Constantine et al. (2000) for TOMS-retrieved SO_2 for the Hudson eruption, for 15-17th August. Note that the TOMS colour scale changes. Version 6 of the TOMS algorithm was used. The right hand column shows the composite results of the HIRS/2 column retrieval for all orbits on each day in similar geographical regions to that observed by TOMS.

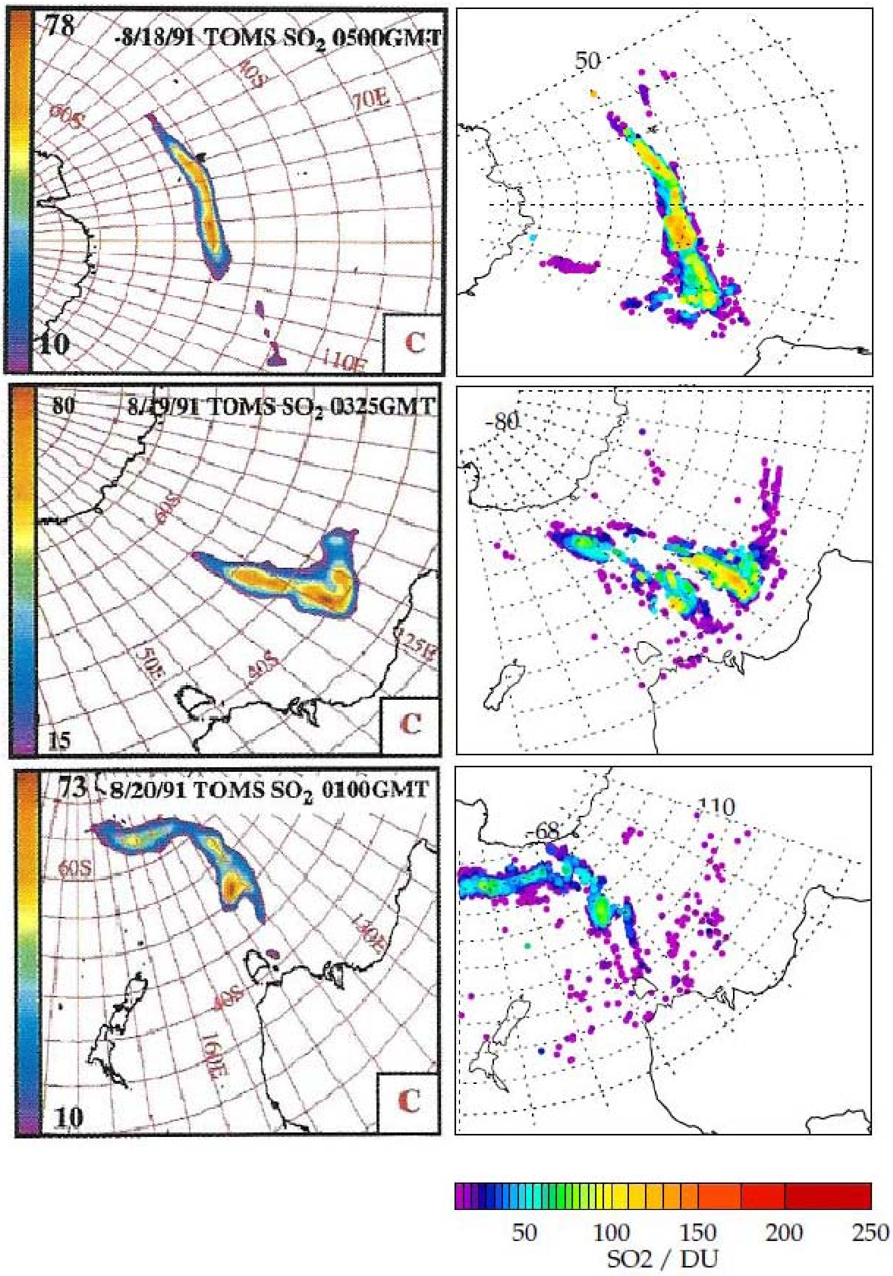

Figure 5.28: The left hand column shows figures taken from Constantine et al. (2000) for TOMS-retrieved SO_2 for the Hudson eruption, for 18-20th August. Note that the TOMS colour scale changes. Version 6 of the TOMS algorithm was used for day 18, and version 7 thereafter. The right hand column shows the composite results of the HIRS/2 column retrieval for all orbits on each day in similar geographical regions to that observed by TOMS.

intuitively unexpected given the comparisons in Figures 5.27 and 5.28 which indicate that the HIRS/2 column retrieval predicts higher SO_2 at the centre of the plume than the TOMS algorithm, and appears to demonstrate greater sensitivity to smaller values of SO_2 surrounding the plume. This may be partly explained by the fact that peak values were used to constrain the TOMS mass estimate, as noted by Constantine et al. (2000), and because it is not explicitly stated how the total masses are calculated, although a total plume area is given. It is inferred from Krueger et al. (1995) that a tonnage multiplicative factor is directly applied to the SO_2 amount for a given pixel that varies as a function of scan angle to account for the air mass slant column factor. There is also some moderate under-sampling of the plume in the HIRS/2 column retrieval, due to some pixels failing to converge in the case of ash or being precluded from summing due to the presence of high cloud. This effect is mollified by gridding, but as figures 5.21 and 5.22 show the estimates from gridding and summing equivalent rectangular footprints of the pixels are broadly similar.

SO_2 e-folding time estimate

As discussed in Chapter 2, the e-folding time for erupted SO_2 is a measure of the residency of the material in the atmosphere, and is affected by the height the material reaches and in the case of very large eruptions, the amount itself. It is also affected by wind sheer (horizontal and vertical) and humidity, which affects the rate at which the SO_2 is oxidised and sulphate aerosols grow. The measure is more suited to large eruptions, of the order of El Chichón or Pinatubo, in terms of inferring effects upon radiative forcing, about which Miles et al. (2004) and other works are concerned. This is because the amount and height that such eruptions reach in the stratosphere gives the SO_2 sufficient time to become globally mixed, and as such affect the radiative forcing globally. In the case of Cerro Hudson, it is unlikely that there were any 0^{th} order (direct) global impacts in terms of radiative forcing, although it is not discounted that in the narrow latitude band in which the erupted plume was confined it had its local radiative balance perturbed. Models or assimilation calculations without inclusion of the erupted plume would have been subject to some degree of error, although in terms of perturbations to the column the presence of Pinatubo aerosol above 20 km is expected to have been more significant.

Equation 5.2 describes the process of exponential decay, where *N(t)* is a quantity at time *t*, N_0 is the initial quantity at time *t=0* and λ is the decay constant.

$$N(t) = N_0 e^{\lambda t} \tag{5.2}$$

The e-folding time, the time in which the initial quantity is reduced to 1/e of its initial value, is given by the reciprocal of the decay constant. Using approximate values from the mass estimates shown in figure 5.21, where the total SO_2 can be said to drop from around 1600 kT to 500 kT 19 days later, this yields an e-folding time of around 16 days. The variability of the mass estimates and the associated retrieval error make only an estimate appropriate for this approach, but it is not considered to be an unreasonable one. If the e-folding time is calculated for the extremes of the retrieved error bounds of the mass estimates, the e-folding time is 10 days at a minimum, and 35 days at its shallowest descent. The e-folding time for this SO_2 plume as estimated by Constantine et al. (2000) is around 15 days, but they state that this is algorithm dependent.

As Miles et al. (2004) discussed, the e-folding time estimates for the Pinatubo plume are around 30–35 days (Bluth et al. (1997),Read et al. (1993)). Reanalysis of the erupted plume by Guo et al. (2004) found lower estimates of 23 and 25 days for TOMS and TOVS respectively, with some margin of error. The Hudson plume, located in the region of 10–14 km is likely to be oxidised more quickly and the aerosols grow due to higher moisture availability at this altitude. Plumes comfortably in the stratosphere benefit from a drier, stably stratified environment, but plumes located in the upper troposphere/lower stratosphere (UTLS) region, which the Hudson can be said to inhabit, are more likely to be affected by dynamic or convective mixing.

5.4.7 Errors

The reported precision (and accuracy) of the Prata fit is 3-5 DU, although from simulations with the RFM (figures 4.11 and 4.12) it is clear that it is subject to sources of error that cannot be quantified by the fit in its current form, and could be shown to exceed 50 % depending on atmospheric conditions. It is formulated to have a lowest detection limit of 5 DU, but this quantity is better interpreted as a minimum brightness temperature difference threshold in a channel, which in reality can mean that SO_2 columns of up to 10 DU can be missed. Quantified in the terms that the column retrieval is screened for noise, the standard deviation of retrieved SO_2 on 6^{th} August (when there should be little SO_2 beyond that of the background) is 6.9, compared to 2.6 for the column retrieval developed here. As such, if the Prata fit data were to be screened for the same confidence interval as that which the column retrieval has been presented here (3-sigma, or 21 DU compared to 7.3 DU), the comparisons might look quite different, but it would result in much less data for the Prata fit. It perhaps goes some way towards explaining the fact that the Prata fit has a high bias with respect to the column fit for low to moderate column amounts. This is contrasted with the behaviour at high SO_2 loadings (above 80 DU), where both simulations and the results for this case study show that the Prata method underestimates the column by up to 50 % at times (as shown in figures 5.24 and 5.25) as compared to the column fit.

Figures 5.13 to 5.19 show that the retrieved error for the column retrieval generally lies between 5 and 10 DU, only rising to 20 DU for retrieved column amounts greater than about 200 DU. It would be fair to surmise that a conservative estimate of the retrieved error is of the order of 10 %, arrived at after screening the data for noise to the 3-sigma level, but is not much changed by relaxing this to two. Average errors on total erupted material are found to vary between 25 and 60 %, but this is quite a different quantity and is heavily influenced by the way in which the plume mass and its error are calculated.

The reported errors on plume mass from the TOMS algorithms featured in this case study are between 15 and 30 %, and TOMS is considered to have sensitivity down to 5-20 kt (Schoeberl et al. 1993). It remains to see whether or not the new algorithm in development will improve upon this, given the progressed methodologies of retrieving SO_2 from UV instruments in recent years. The equivalent sensitivity for the column retrieval expressed in the same terms is difficult to quantify simply, as it is a function of the atmospheric profile in any given pixel and if scaled to an entire plume would depend upon the area considered. The error bounds suggested by the day estimates are expectedly larger.

These results are concluded and discussed in the following chapter.

Chapter 6

Discussion and Future Work

6.1 SO_2 column retrieval scheme for HIRS/2: Conclusions

The HIRS/2 SO_2 column retrieval scheme was applied to real measurements to detect and quantify erupted SO_2 for the Cerro Hudson eruption in 1991. It was immediately found that it lacked a fully defined *a priori* covariance between water vapour and SO_2. The *a priori* error was estimated using a day of measurements where SO_2 was not present, and forcibly not fit, and calculating the standard deviation in the fit in the 7.3 μm channel. Using this estimate of *a priori* error vastly improved the incidence of false detection. Application of a 3-sigma filter, which identified SO_2 column amounts that were statistically above the noise to over the 97 % level, proved a very effective method of quality control, in addition to the usual cost, convergence and fraction error terms that were employed as a matter of course.

It was shown that using simple brightness temperature differences of a variety of channels can suggest the presence of ash, and it is apparent that to do this well they must be treated in a more subtle way, and this presents scope for further work. It is not expected to impact the SO_2 results presented here other than the fact that where ash is present and above 5 km, the retrieved SO_2 cannot be trusted, even though it may not be entirely inaccurate. Improving the functionality of the scheme in the presence of ash could however also constitute further work.

The results of the column retrieval were presented for the eruption of Cerro Hudson, and compared to the Prata fit method. The results accord with line-by-line simulations, in that there are suggestiong of a slight high bias of the Prata fit with respect to the column retrieval for low to moderate SO_2 column amounts, and a stronger low bias (up to 50 %) with respect to SO_2 loading greater than about 80 DU. It is apparent from simulations in Chapter 4 that this behaviour may be latitude dependent.

This column retrieval finds a new total erupted mass estimate for the 1991 eruption of Cerro Hudson of 2200 kT ± 600 kT. This does not incorporate any error from plume altitude estimation but the potential impact has been quantified by forward model simulations. This total mass estimate is lower than that of TOMS (Constantine et al. 2000) but higher than that derived in a similar way using the methodology of Prata et al. (2003). Reasons for this include (but are not limited to) differences in sampling, height sensitivity, instrument differences and attributes or accuracies of the forward model or fit employed in SO_2 detection. From the qualitative comparison with TOMS, the HIRS/2 results presented here are not inconsistent, and a future quantitative comparison is desirable.

The retrieval precision demonstrated in this case study is comparable to that proposed for the TOMS instrument, of around 3 DU. As such, with the increased sampling of the IR instrument it is apparent that HIRS/2 can offer a positive contribution to the atmospheric SO_2 emission record from explosive volcanic eruptions up to and beyond the launch of GOME and other satellites that followed. Moreover, benefits of the optimal estimation approach over and above the more rapid but limited brightness temperature difference method are significant. They include a quantified error on individual pixel measurements, diagnostic indicators of the retrieval performance and goodness-of-fit and treatment of cloud and water vapour consistent to the retrieval of SO_2. When summing mass over a large number of pixels, the precision that these afford becomes increasingly important.

6.2 Summary and discussion of thesis results

This thesis can be considered to comprise two parts. The first relates to the atmospheric effects of explosive volcanic eruptions. The second, to a novel way to accurately detect the volcanic emission into the stratosphere of SO_2, which is the predominant element in determining the subsequent radiative forcing that arises from the eruption.

Chapter 2 developed a box model for relating SO_2 erupted in the tropical stratosphere to global average temperature change, and used it to model the radiative impact of past eruptions in order to quantify their climatic significance. It found that eruptions of about 1 Mt, such as that featuring in the case study, have perhaps the most climatic significance because during the Holocene they occurred more often than very large or super-eruptions. In order to understand the atmospheric response to such volcanic eruptions, their SO_2 emission history must be accurately known, and any improvement upon satellite measurement record of SO_2 would contribute to this. HIRS/2 presented this opportunity. Previous methods based on brightness temperature difference fitting with HIRS/2 measurements presented scope for the optimal estimation approach that was developed in this thesis.

Chapter 3 outlined some of the retrieval theory and forward model concepts that are required for an optimal estimation approach.

Chapter 4 developed the HIRS/2 SO_2 column retrieval algorithm. This required a number of retrieval and model simulations to verify that the retrieval was sufficiently accurate and behaved in an expected way. It was also necessary to use a cloud and aerosol model to identify whether there were atmospheric phenomena not explicitly part of the retrieval forward model for the sake of simplicity, but that the measurements were none the less sensitive to. The most important aspect to arise from that exercise is that in the presence of ash or meteorological cloud above 5 km, the forward model misinterprets the measurements to result in false detection or enhancement of SO_2. This results from a poor fitting of the water vapour column because most of it is masked, and the channel sensitive to SO_2 is also sensitive to water vapour.

It was demonstrated in Chapter 5 that SO_2 column amounts can be derived from real HIRS/2 measurements. The optimal estimation column retrieval developed here presents a significant advancement above the Prata fit method, which showed some skill in fitting an SO_2 column to HIRS/2 measurements but is unable as it stands to quantify any estimate of uncertainty, or to adequately detect when atmospheric conditions relating to water vapour make application of the Prata fit more prone to sizable error. The obvious advantage of the fit method is speed, where processing a day of data might take a matter of minutes, but despite a minimum 8 K brightness temperature difference used as an effective detection limit, the relatively high standard deviation of SO_2 'noise' that is falsely fit is over 3 times that of the column retrieval. It is considered a significant advantage that the column retrieval developed here can be tightly screened to a high statistical confidence above the noise, which is not possible with the Prata fit. The column retrieval is based on a fast forward model, and having been optimised with a good prior estimate of the cloud top height it is considered that with parallel processing capability its speed is certainly within the bounds of acceptability. To take advantage of both, it is noted that using the Prata fit results or the brightness temperature difference in the $7.3\,\mu$m channel as an indicator of where SO_2 is likely to be present for subsequent processing with the column retrieval would be an optimal use of both methods. The application of the column retrieval has produced a new SO_2 eruption mass estimate for the event of 2200 kT ± 600 kT. This confirms it as one of the largest since the 1991 eruption of Pinatubo, and of comparable scale to the Northern Hemisphere eruption of Kasatochi in 2008.

This study presents opportunities and avenues for further work, which are outlined here.

6.3 Optimisation of the case study - multi-satellite retrievals

At the time of the Cerro Hudson eruption (and Pinatubo), there were 3 NOAA satellites in orbit each carrying a HIRS/2 instrument. NOAA 10 and 12 HIRS/2 had a slightly different channel configuration to NOAA 11 used for the case study of Cerro Hudson (Table 4.2). Notably, they have a channel at 8.6 μm rather than a channel at 12.5 μm. Some use could be made of this SO_2 sensitive channel, with accommodation of the fact that the 8.6 μm is also sensitive to ash. Three satellites would vastly increase the sampling of the volcanic plume, potentially providing more accurate total mass estimates since a significant amount of uncertainty arises because of incomplete sampling. It would also provide more detailed information about the evolution of the plume.

6.4 A complete eruption emission characterisation

Modelling tools (which could include both chemistry and trajectory analysis) in addition to HIRS SO_2 could be combined to try to understand fully the atmospheric impact from one or more specific eruptions, as was attempted by Schoeberl et al. (1993) and Doiron et al. (1991) for Hudson with TOMS and the number of other case studies for more recent instruments (Section 1.4.2). Backwards and forward trajectory modelling is also now a frequently used tool for establishing with reduced uncertainty the emission height achieved by erupted SO_2. The frequency and magnitude study (Chapter 2) suggested that the most significant eruptions for climate are the small to middle sized eruptions which just reach the stratosphere. The Cerro Hudson eruption in 1991 was in this class of eruption, and the SO_2 emission is examined in the case study in a previous chapter. The eruption occurred in the Southern Hemisphere midlatitudes two months after the substantially more explosive Pinatubo eruption in the tropics. The signal of Hudson in the atmosphere was considerably overshadowed by the earlier eruption, and extracting information about it presents a non-trivial challenge. A chemistry transport model (CTM) would present a flexible environment to understand different aspects of an eruption. These could include a direct simulation of the 1991 eruption to look at lifetimes of the products in the atmosphere or a passive tracer simulation to look at mixing timescales of the erupted material. Since the model is driven by analysed wind fields which may have been affected by the Pinatubo eruption in the stratosphere, the eruption could also be modelled in a year when there was no significant volcanism. This would identify the eruption specific chemical perturbation that resulted from Cerro Hudson, including implications for Antarctic ozone concentration.

6.5 Further development of RTTOV/cloud model to include SO_2

Work by Dr R.Siddans at the Rutherford Appleton Laboratory has shown that RTTOV coefficients can be derived for gaseous species and for instruments that RTTOV was not designed to handle. It is apparent in simulations both by R.Siddans and by the author, that there may be scope for improvements to how the coefficients are calculated to help improve their accuracy, particularly in relation to the shape of the profile of an explosive volcanic plume perturbation. The coefficients were not ‘trained’ with the particular profile shape selected for use in the column retrieval presented here which (from lidar measurements and CTM modelling of the TOMS-observed plume) is probably a fair physical representation of the real plume profile shape and height. Matricardi (2008) strongly argued the importance of using representative profiles for water vapour and temperature in particular, in order to achieve accurate regression coefficients for IASI and AIRS, although the dependence on this for trace gases was considered to be less severe, or at least more uncertain. It is reasonable to surmise though that the inclusion of more physically representative volcanic SO_2 profiles would improve the accuracy of SO_2 coefficients for HIRS/2.

The cloud model, used in Chapter 4, could be further utilised to try to ascertain how certain types of clouds or ash lead to spurious SO_2 being retrieved by the column retrieval, in order to reduce the number of discarded retrievals because of ash. If more accurate modelling of cloud were to significantly improve the retrieval of SO_2, the cloud model could be modified to be able to include SO_2 as a variable for volcanically perturbed profiles. As presented here, the cloud model can make use of many of the HIRS/2 channels to fully characterise the scene. It could additionally be developed to include the fitting of other selected trace gases, and be combined with measurements from NOAA 11 AVHRR imager data for a fully joint scheme.

6.6 A HIRS/2 sulphur dioxide dataset

Over three decades of HIRS observations could be processed to calculate SO_2 to create a consistent dataset comparative to TOMS SO_2, and the subsequent IR and UV instruments that have emerged in the last decade. This could also be used to calculate any observed trends in SO_2 flux for explosive volcanism. It is envisaged that in order to complete the processing on a realistic or useful time frame, some sort of brightness temperature difference flag would be utilised, similar to that used by Dr Prata's fit method, but potentially using additional channel information for quality control, or with a more forgiving range to capture lower amounts of SO_2 that would otherwise be missed. The Prata fit method is less sensitive to ash as the SO_2 fit is largely dependent upon only the the 7.3 μm channel, whereas the previous chapters have shown that because the full retrieval is sensitive to both the fit of water vapour and ash/water cloud height it is less applicable in the presence of ash. In all other circumstances it is considered more accurate.

The first HIRS instrument was flown aboard TIROS-N in 1978, and there are more or less continual data available to the present, and for the foreseeable future of the Met-Op series of satellites, enabling a potential dataset spanning over 40 years. Generating an SO_2 dataset for the duration would be an opportunity to maximise the value and legacy of the satellite data. For much of the latter half of that period, there are (and will be) other satellites instruments capable of measuring SO_2 in the limb and the nadir, particularly spectrometers with very much enhanced accuracy and precision, that will provide correlative information about the quality of the HIRS/2 SO_2 column retrievals. It would be the author's desire to first apply the methodology presented in this work to data from the HIRS/4 instrument currently aboard MetOp/A. Not only are there other instruments capable of measuring SO_2 aboard that would be able to view the same scenes as HIRS/4 (notably GOME-2 and IASI), but for the period it has been in orbit there are other instruments to which it can be compared, including MIPAS, OMI and AIRS (Section 1.4.2).

6.7 A satellite atmospheric sulphur dioxide inventory

Given the absolute variability of volcanic SO_2 detected by the range of different satellites, it is conceivable that a data assimilation-type process dedicated to SO_2 would be able to combine the information from all observations (and advection models) in an optimal and fair way. Without such an approach, different satellite mass estimates will always disagree with the combined uncertainties introduced by differing spatial, temporal and spectral sampling, and relative sensitivities depending upon the part of the spectrum measured. Whilst this would represent a significant undertaking, and not be without other contributing sources of error, it none the less represents a panacea to the challenges defining a volcanic SO_2 eruption inventory for the satellite era.

Appendix A

Prata Fit Method

A.1 Methodology

A technique for identifying the presence of SO_2 in volcanic plumes is presented in Prata et al. (2003), from which most of the theory below is gleaned. In principle, the transmittance of an SO_2 layer is calculated from the brightness temperature difference from a measured radiance and theoretical clear-sky radiance. The method is based around the SO_2 absorption feature around 7.35 μm, which coincides with the HIRS/2 channel 11 centered at 7.3 μm. The SO_2 feature is modelled using an exponential sum-fitting procedure to model the band transmittance, which was shown to give good agreement with line-by-line calculations below a threshold of 200 DU of SO_2. The forward model uses a set of pre-calculated look-up tables with absorber amounts calculated for 26 atmospheric layers in transmittance steps of 0.001. Prata et al. (2003) use a simplified radiative transfer model to derive the SO_2 transmittance from HIRS/2 measurements. It is based on a three layered structure of the atmosphere, representing the (clear) regions below, above the erupted SO_2 layer, and the layer itself, which is assumed to have an unvarying absorber density between heights $z=a$ and $z=b$. The optical thickness in the three layers is given by

$$l(z) = \begin{cases} l_a(z) & b \leq z \\ l_a(z) + \alpha_s(b - z) & a \leq z \leq b \\ l_a(z) + \alpha_s(b - a) & z \leq a \end{cases} \tag{A.1}$$

$l(z)$ is the optical path from height z to space devoid of SO_2. α_s is the volume absorption coefficient of SO_2. As such, the transmittance to space is given by:

$$t(z) = \begin{cases} t_a(z) & b \leq z \\ t_a(z)e^{(-\alpha_s(b-z))} & a \leq z \leq b \\ t_a(z)e^{(-\alpha_s(b-a))} & z \leq a \end{cases} \tag{A.2}$$

The subscript a indicates a path free of SO_2. τ_s and t_s are the optical depth and transmittance of the SO_2 column, given by:

$$\tau_s = \alpha_s(b - a)t_s = e^{-\tau_s} \tag{A.3}$$

The SO_2 layer itself attenuates the radiation passing through it from below. Within the layer, the presence of SO_2 and the atmosphere mutually affect the absorption by each other. Taking into account all of these factors, the radiance emitted to space is made up of four terms:

$$I = t_s I_a + (1 - t_s)I_{as}^{+} + I_{sa} \tag{A.4}$$

The subscripts a and s refer to the clear atmosphere and SO_2 respectively. The first term represents the emission from the atmosphere alone, attenuated by the presence of SO_2, where

$$\mathrm{I_a} = B_0 t_{a(0)} + \int_0^\infty \alpha_{a(z)b(z)} t_{a(z)} dz \tag{A.5}$$

$\alpha_a(z)$ is the volume absorption coefficient of the atmosphere at height z, B_0 is the Planck emission at the surface, and $B(z)$ the Planck emission from the atmosphere at temperature $T(z)$. The second term in equation A.4 is the radiance emitted by the atmosphere above the SO_2 layer modified by $(1 - t_s)$, where

$$\mathrm{I}_{\mathrm{a}}^{+} = \int\limits_{b}^{\infty} \alpha_{a(z)} B(z) t_{a(z)} dz \tag{A.6}$$

The third term describes the emission by the atmosphere within the SO_2 layer and modified by the presence of SO_2 absorbing in that layer,

$$I_{as} = \int_{a}^{b} \alpha_a B(z) t_a(z) t_s [\exp \tau_s (z-a)/(b-a) - 1] dz \tag{A.7}$$

The fourth term represents the emission by the SO_2 layer attenuated by the atmosphere above.

$$I_{sa} = \int_{a}^{b} \alpha_s B(z) t_a(z) \exp -\tau_s (b-z)/(b-a) dz \tag{A.8}$$

Furthermore, two assumptions about the nature of the SO_2 layer may be used to simplify these equations. Firstly, it is vital to assume that the layer exists above the peak of the weighting function for primary absorber water vapour in the 7.3 μm channel so it will not contribute significantly to the perturbation by SO_2 (i.e. $\alpha_a(z)$ is approximately zero). The second assumption is that the SO_2 layer is isothermal, so that its Planck emission can be characterised at a single temperature. This assumption becomes weaker as the SO_2 layer is very deep. One must also consider the fact that along with volcanic SO_2 emissions there is the presence of both volcanic water vapour and that entrained from the troposphere, in concentrations an order of magnitude greater than the SO_2. It is likely that much of this water vapour freezes in the stratosphere or else is scavenged by ash particles in the plume. Thus, with the assuption that $\alpha_a(z)$ is zero for $z > a$, and the second and third terms of equation A.4 are zero. The assumption of an isothermal SO_2 layer reduces the fourth term to

$$I_{sa} = \alpha_s B_s \int_{a}^{b} \exp -\tau_s (b-z)/(b-a) dz = (1-t_s) B_s \tag{A.9}$$

The radiance emitted to space can therefore be approximated by

$$I = t_s I_a + (1 - t_s) B_s \tag{A.10}$$

This can be re-arranged in the form of

$$I - I_a = (1 - t_s)(B_s - I_a) \tag{A.11}$$

and

$$\exp(-\tau_s) = \frac{B_s - I}{B_s - I_a} \tag{A.12}$$

where τ_s is the quantity to be found. Equation A.11 suggests that the change in radiance between an atmosphere free of SO_2 and one with a layer of SO_2, is a linear function of t_s. In terms of brightness temperature differences equivalent to a change in radiance, this has the form

$$\Delta T = \alpha + \beta(1 - t_s) \tag{A.13}$$

α and β can be modelled to an approximate value, but are in practice dependant upon the state of the atmosphere and temperature of the SO_2 in the plume. This method uses modelled values of α and β, but an independent estimate of the height of the plume is required to generate look-up tables of transmittance.

A.2 Implementation

The brightness temperature difference is calculated using a theoretical clear-sky BT in the effected channel plus an offset, at 7.3 μm. This is found by a linear interpolation of the radiance measured at 6.7 and 11.1 μm, the central channel wavelengths. This linear interpolation estimate has been verified here by the analysis of 'large' amounts of SO_2 free profiles, and is found to be accurate to within 2 K in 95 % of cases. In cases where there was poor agreement, this is thought to be due to partial cloud cover in the instrument field of view.

A.3 Characteristics and sensitivity

The algorithm (Version 1.0) underwent minor modifications for use here. The module for reading and converting the satellite data was adapted to increase the speed of operation. An associated procedure was originally implemented to fill in the data gaps caused by the instrument in callibration mode (three swaths wide), using an interpolation between good data points. It is considered that this adds false information unnecessarily so has been eliminated. Thus data gaps will exist in the final product, and will contribute towards the uncertainty of any estimates made from the information as a whole.

A.3.1 Plume height and thickness

As discussed above, this fit method assumes a 'thin' SO_2 plume, or at least it is desirable in terms of accuracy for there to be a minimal temperature gradient with height within the plume. It is also accepted to be sensitive to the assumed plume height. As such, it is worth assessing the performance of the fit when a plume height is assumed for measurements simulated where this is not the true height, and the thickness of the plume is varied. Figure A.1 shows how the Prata fit SO_2 varies as a function of true SO_2 amount, and plume thickness.

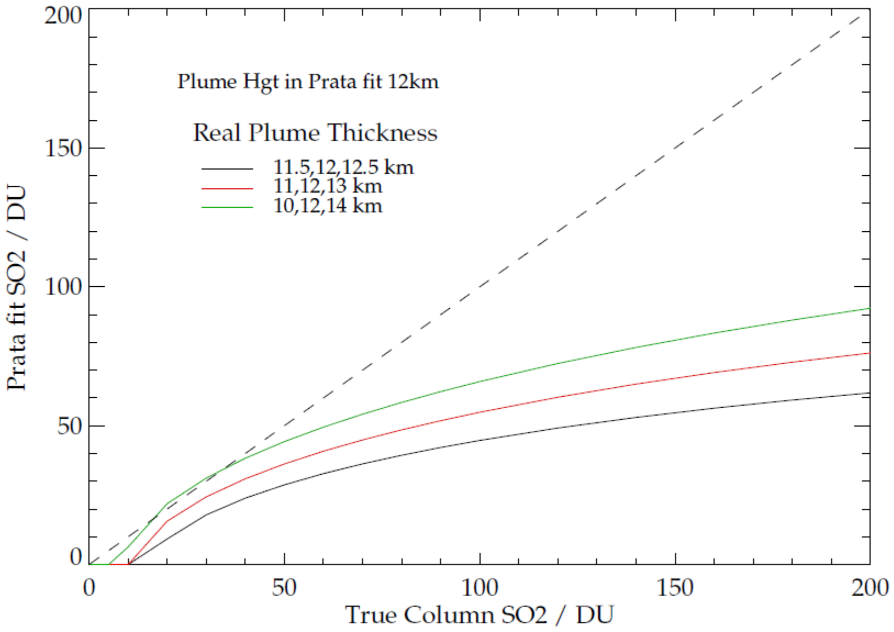

Figure A.1: Variation of Prata fit SO_2 from simulated measurements using ERA-Interim profiles at 60 °S on 6^{th} August 1991. The assumed altitude is 12 km, and the true plume profile also peaks at 12 km, but is varied between 1 and 4 km in thickness.

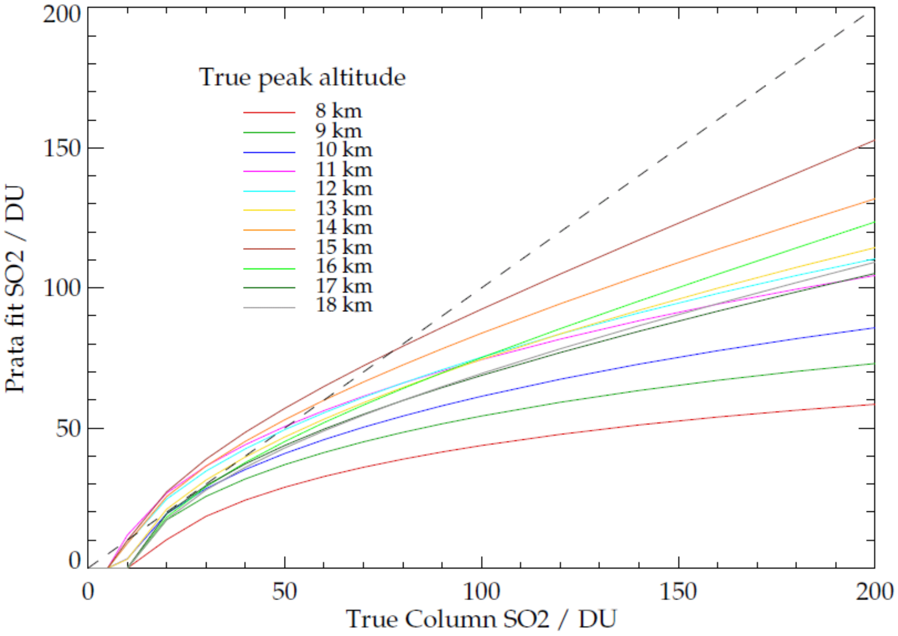

Figure A.2: Variation of Prata fit SO_2 from simulated measurements using ERA-Interim profiles at 60 °S on 6^{th} August 1991. The assumed altitude is 12 km, and the true plume profile peak is varied from 8 to 18 km, with a thickness of 2 km

Bibliography

Ackerman, S. A. (1996), 'Global satellite observations of negative brightness temperature differences between 11 and 6.7 microns', *J. Atmos. Sci.* **53**, 2803–2812.

Andres, R. & Kasgnoc, A. D. (1998), 'A time-averaged inventory of subaerial volcanic sulfur emissions', *J. Geophys. Res.,* **103**, 25251–25261.

Andronova, N., Rozanov, E., Yang, F., Schlesinger, M. & Stenchikov, G. (1999), 'Radiative forcing by volcanic aerosols from 1850 through 1994', *J. Geophys. Res.,* **104**, 16807–16826.

Barton, I., Prata, A., Watterson, I. & Young, S. (1992), 'Identification of the Mount Hudson volcanic cloud over SE Australia', *Geophys. Res. Lett.* **19**, 1211–1214.

Bekki, S. (1995), 'Oxidation of volcanic SO_2: A sink for stratospheric OH and H_2O', *Geophys. Res. Lett.* **22**, 913–916.

Bekki, S., Pyle, J., Zhong, W., Toumi, R., Haigh, J. & Pyle, D. (1996), 'The role of microphysical and chemical processes in prolonging the climate forcing of the Toba eruption', *Geophys. Res. Lett.* **23**, 2669–2672.

Bhartia, P. & Wellemeyer, C. (2002), TOMS-V8 total O3 algorithm, Algorithm Theoretical Basis Document, OMI ozone products,ATBD-OMI-02, version 2.0, vol. ii, Technical report, NASA Goddard Space Flight Cent., Greenbelt, Md. Available at http://eospso.gsfc.nasa.gov/eos_homepage/for_scientists/atbd/docs/OMI/ATBD-OMI-02.pdf.

Bluth, G., Doiron, S., Schnetzler, C., Krueger, A. & Walter, L. (1992), 'Global tracking of the SO_2 cloud from the June, 1991 Mount Pinatubo eruptions', *Geophys. Res. Lett.* **19**, 151–154.

Bluth, G., Rose, W., Sprod, I. & Krueger, A. (1997), 'Stratospheric loading of sulphur from explosive volcanic eruptions', *J. Geol.* **105**, 671–683.

Bollasina, M. A., Ming, Y. & Ramaswamy, V. (2011), ‘Anthropogenic aerosols and the weakening of the South Asian Summer Monsoon’, *Science* **344**, 502–505.

Bovensmann, H., Burrows, J. P., Buchwitz, M., Frerick, J., Noel, S., Rozanov, V. V., Chance, K. V. & Goede, A. P. H. (1999), ‘SCIAMACHY: Mission Objectives and Measurement Modes’, *J. Atmos. Sci.* **56**, 127–150.

Buchwitz, M., Rozanov, V. & Burrows, J. (2000), ‘A near-infrared optimized DOAS method for the fast global retrieval of atmospheric CH_4, CO, CO_2, H_2O, and N_2O total column amounts from SCIAMACHY Envisat-1 nadir radiances’, *J. Geophys. Res.* **D105**, 15231–15245.

Campion, R., Salerno, G., Coheur, P.-F., Hurtmans, D., Clarisse, L., Kazahaya, K., Burton, M., Caltabiano, T., Clerbaux, C. & Bernard, A. (2010), ‘Measuring volcanic degassing of SO_2 in the lower troposphere with ASTER band ratios’, *J. Volcanol. Geoth. Res.* **194**, 42–54.

Carn, S., Krueger, A., Krotkov, N., Yang, K. & Evans, K. (2009), ‘Tracking volcanic sulfur dioxide clouds for aviation hazard mitigation’, *Nat. Hazards* **51**, 325–343.

Carn, S., Strow, L., Souza-Machado, S. D., Edmonds, Y. & Hannon, S. (2005), ‘Quantifying tropospheric volcanic emissions with AIRS; the 2002 eruption of Mt. Etna (Italy)’, *Geophys. Res. Lett.* **32**, L02301.

Casadevall, T., Rose, W., Gerlach, T., Greenland, L., Ewert, J., Wunderman, R. & Symonds, R. (1983), ‘Gas emissions and the eruptions of Mount St. Helens through 1982’, *Science* **221**, 1383–1385.

Chahine, M. T., Pagano, T. S., Aumann, H. H. et al. (2006), ‘AIRS: Improving weather forecasting and providing new data on greenhouse gases’, *Bull. Am. Meteorol. Soc* **87(7)**, 911–926.

Clerbaux, C., Coheur, P.-F., Clarisse, L., Hadji-Lazaro, J., Hurtmans, D., Turquety, S., Bowman, K., Worden, H. & Carn, S. A. (2008), ‘Measurements of SO_2 profiles in volcanic plumes from the NASA Tropospheric Emission Spectrometer (TES)’, *Geophys. Res. Lett* **25**, L22807.

Clerbaux, C., Coheur, P.-F., Hurtmans, D., Barret, B., Carleer, M., Colin, R., Semeniuk, K., McConnell, J. C., Boone, C. & Bernath, P. (2005), ‘Carbon monoxide distribution from the ACE-FTS solar occultation measurements’, *Geophys. Res. Lett.* **32**, L16S01.

CMDL (2003), ‘Climate change and greenhouse gases’. http://www.cmdl.noaa.gov/ccgg.

Coffey, M. (1996), ‘Observations of the impact of volcanic activity on stratospheric chemistry’, *J. Geophys. Res.* **101**, 6767–6780.

Coheur, P.-F., Barret, B., Turquety, S., Hurtmans, D., Hadji-Lazaro, J. & Clerbaux, C. (2005), ‘Retrieval and characterization of ozone vertical profiles from a thermal infrared nadir sounder’, *J. Geophys. Res.* **110**, D24303.

Cole-Dai, J., Mosley-Thompson, E. & Thompson, L. (1997), ‘Annually resolved southern hemisphere volcanic history from two antarctic ice cores’, *J. Geophys. Res.* **102**, 16761–16771.

Constantine, E., Bluth, G. & Rose, W. (2000), ‘TOMS and AVHRR observations of drifting volcanic clouds from the August 1991 eruptions of Cerro Hudson’, *Remote Sensing of Active Volcanism, AGU Geophysical monograph* **116**, 45–64.

Corradini, S., Merucci, L. & Prata, A. J. (2009), ‘Retrieval of SO_2 from thermal infrared satellite measurements: correction procedures for the effects of volcanic ash’, *Atmos. Meas. Tech.* **2**, 177–191.

Corradini, S., Piccolo, C., Rodgers, C. D., Dudhia, A., Grainger, R. G. & Pugnaghi, S. (2006), ‘SO_2 volcanic plume retrieval using TES nadir measurements: Feasibility study’, *Geophysical Research Abstracts* **8**, 01117.

Crowley, T. (2004), ‘Discussion’. Personal communication.

Decker, R. & Decker, B. (1997), *Volcanoes*, academic edn, Freeman.

Dee, D. P., Uppala, S. M., Simmons, A. J., Berrisford, P., Poli, P., Kobayashi, S., Andrae, U., Balmaseda, M. A., Balsamo, G., Bauer, P., Bechtold, P., Beljaars, A. C. M., van de Berg, L., Bidlot, J., Bormann, N., Delsol, C., Dragani, R., Fuentes, M., Geer, A. J., Haimberger, L., Healy, S. B., Hersbach, H., Hlm, E. V., Isaksen1, L., Kllberg, P., Khler, M., Matricardi, M., McNally, A. P., Monge-Sanz, B. M., Morcrette, J.-J., Park, B.-K., Peubey, C., de Rosnay, P., Tavolato, C., Thpaut, J.-N. & Vitart, F. (2011), ‘The ERA-Interim reanalysis: configuration and performance of the data assimilation system’, *Quart. J. Roy. Meterol. Soc.* **137**, 553–397.

Deshler, T., Hervig, M., Kröger, C., Hofmann, D., Rosen, J. & Liley, J. (2003), ‘Thirty years of in situ stratospheric aerosol size distribution measurements from Laramie, Wyoming (41° n), using balloon-borne instruments’, *J. Geophys. Res.* **108**, D5,4167.

DLR (2010), Algorithm Theoretical Basis Document for GOME-2 Total Column Products of Ozone, NO2, SO2, BrO, H2O, HCHO, OClO, tropospheric NO2 and Cloud Properties (GDP 4.4 for O3M-SAF OTO and NTO), Technical report, DLR / Ozone SAF. DLR/GOME-2/ATBD/01,Iss./Rev. 2/C.

Doiron, S., Bluth, G., Schnetzler, C., Krueger, A. & Walter, L. (1991), 'Transport of Cerro Hudson SO_2 clouds', *EOS Trans.* **72**, 489,498.

Dudhia, A. (2002), 'RFM Software User's Manual'. Issue 4.2, http://www.atm.ox.ac.uk/RFM/sum.html.

Dyer, A. & Hicks, B. (1968), 'Global spread of volcanic dust from the Bali eruption of 1963', *Q. J. R. Meteorol. Soc.* **94**, 545–554.

ECMWF (2001), 'An improved general fast radiative transfer model for the assimilation of radiance observations.'. ECMWF Technical Memo No. 345.

Edwards, D. (1992), GENLN2. a general line-by-line atmospheric transmittance and radiance model, Technical report, National Center for Atmospheric Research, Boulder,Co. NCAR Technical note NCAR/TN-367+STR.

Eisinger, M. & Burrows, J. (1998), 'Tropospheric sulfur dioxide observed by the ERS-2 GOME instrument', *Geophys. Res. Lett.* **25**, 41774180.

Farman, J. C., Gardiner, B. G. & Shanklin, J. D. (1985), 'Large losses of total ozone in Antarctica reveal seasonal ClOx/NOx interaction', *Nature* **315**, 207–210.

Galle, B., Oppenheimer, C., Geyer, A., McGonigle, A., Edmonds, M. & Horrocks, L. (2002), 'A miniature ultraviolet spectrometer for remote sensing of SO_2 fluxes: a new tool for volcano surveillance', *J. Volcanol. Geoth. Res.* **119**, 241–254.

Garand, L., Turner, D. S., Larocque, M., Bates, J., Boukabara, S., Brunel, P., Chevallier, F., Deblonde, G., Engelen, R., Hollingshead, M., Jackson, D., Jedlovec, G., Joiner, J., Kleespies, T., McKague, D. S., McMillin, L., Moncet, J.-L., Pardo, J. R., Rayer, P. J., Salathe, E., Saunders, R., Scott, N. A., Deist, P. V. & Woolf, H. (2001), 'Radiance and jacobian intercomparison of radiative transfer models applied to HIRS and AMSU channels', *J. Geophys. Res.* **106**, 24017–24031.

Gerlach, T. (2011), 'Volcanic Versus Anthropogenic Carbon Dioxide', *EOS Transactions of the Geophysical Union* **92**, 201–208.

Goody, R. & Yung, Y. (1995), *Atmospheric Radiation: theoretical basis*, academic edn, Oxford University Press.

Gottwald, M., Bovensmann, H., Lichtenberg, G., Noel, S., von Bargen, A., Slijkhuis, A., Piters, A., Hoogeveen, R., von Savigny, C., Buchwitz, M., Kokhanovsky, A., Richter, A., Rozanov, A., Holzer-Popp, T., Bramstedt, K., Lambert, J.-C., Skupin, J., Wittrock, F., Schrijver, H. & Burrows, J. (2006), *SCIAMACHY, Monitoring the Changing Earth's Atmosphere*, DLR.

Graf, H., Hertzog, M., Oberhuber, J. & Textor, C. (1999), 'Effect of environmental conditions on volcanic plume rise', *J. Geophys. Res.* **104**, 24309–24320.

Grainger, R. & Highwood, E. (2003), Atmospheric effects of volcanoes, *in* C. Oppenheimer, ed., 'Volcanic Degassing', Geological Society Special Publication.

Guo, S., Bluth, G., Rose, W., Watson, I. & Prata, A. (2004), 'Re-evaluation of SO_2 release of 15^{th} June 1991 Pinatubo eruption using ultraviolet and infrared satellite sensors', *Geochem Geophys Geosys* **5(4)**, Q04001.

Haken & Wolf (1987), *The physics of atoms and quanta: an introduction to experiment and theory*, 3 edn, Springer-Verlag.

Halmer, M. (2001), Characterization of Aerosol Sources, PhD thesis, University of Kiel.

Halmer, M. (2003), 'The impact of moderate-scale explosive eruptions on stratospheric gas injections', *Bulletin of Volcanology* **65**, 433–440.

Hansen, J., Lacis, A., Ruedy, R. & Sato, M. (1992), 'Potential climate impact of Mount Pinatubo eruption', *Geophys. Res. Lett.* **19**, 215–218.

Hansen, J., Sata, M., Ruedy, R., Nazarenko, L., Lacis, A., Schmidt, G. & Russell, G. (2005), 'Efficacy of climate forcings', *J. Geophys. Res.* **110**, D18104.

Heath, D., Krueger, A., Roeder, H. & Henderson, B. (1975), 'The solar backscatter ultraviolet and total ozone mapping spectrometer (SBUV/TOMS)', *Opt. Eng.* **14**, 323–331.

Highwood, E. & Stevenson, D. (2003), 'Atmospheric impact of the 1783-1784 Laki eruption: Part II climate effect of sulphate aerosol', *Atmos. Chem. Physics* **3**, 1177–1189.

Hofmann, D., Barnes, J., ONeill, M., Trudeau, M. & Neely, R. (2009), 'Increase in background stratospheric aerosol observed with lidar at Mauna Loa Observatory and Boulder, Colorado', *Geophys. Res. Lett.* **36**, L15808.

Hofmann, D., Oltmans, S., Harriss, J., Solomon, S., Dreshler, T. & Johnson, B. (1992), 'Observation and possible causes of new ozone depletion in Antarctica', *Nature* **359**, 283–287.

Holloway, A. & Wayne, R. (2010), *Atmospheric Chemistry*, 1st edition edn, Royal Society of Chemistry Publishing.

Hyde, W. & Crowley, J. (2000), 'Probability of future climatically significant volcanic eruptions', *J. Climate* **13**, 1445–1450.

IPCC (1996), *Climate change 1995: The Science of Climate Change*, Cambridge University Press.

Jay, V. (2000), Remote sounding of the atmosphere by high spectral resolution spectroscopy, PhD thesis, University of Oxford.

Joshi, M. & Jones, G. (2009), 'The climatic effects of the direct injection of water vapour into the stratosphere by large volcanic eruptions', *Atmos. Chem. Phys.* **9**, 6109–6118.

JPL (1997), Chemical kinetics and photochemical data for use in stratospheric modeling, Technical report, Jet Propulsion Laboratory, NASA. Evaluation number 12, Publication 97-4.

JPL (2003), 'Mission and Spacecraft Library (NOAA)'. http://samadhi.jpl.nasa.gov/msl/QuickLooks/tirosnQL.html.

Karagulian, F., Clarisse, L., Clerbaux, C., Prata, A., Hurtmans, D. & Coheur, P. (2010), 'Detection of volcanic SO_2, ash, and H_2SO_4 using the Infrared Atmospheric Sounding Interferometer (IASI)', *J. Geophys. Res.* **115**, D00L02.

Kaufmann, R., Kauppi, H., Mann, M. L. & Stock, J. (2011), 'Reconciling anthropogenic climate change with observed temperature 19982008', *Proc. Natl. Acad. Sci.* **-**, –.

Kearney, C. & Watson, I. (2009), 'Correcting satellite-based infrared sulfur dioxide retrievals for the presence of silicate ash', *J. Geophys. Res.* **114**, D22208.

Kerr, J., McElroy, C. & Olafson, R. (1980), 'Measurements of ozone with the Brewer ozone spectrophotometer', *Proc. Int. Ozone Symp.* **1**, 74–79.

Khokhar, M., Frankenberg, C., Roozendael, M. V., Beirle, S., Kuhl, S., Richter, A., Platt, U. & Wagner, T. (2005), 'Satellite observations of atmospheric SO_2 from volcanic eruptions during the time-period of 1996-2002', *Adv. Space. Res.* **36**, 879–887.

Kinfe, H. (2003), Comparison of simple climate models, Master's thesis, University of Reading.

Kinne, S., Toon, O. B. & Prather, M. J. (1992), 'Buffering of the stratospheric circulation by changing amounts of topical ozone: A Pinatubo case study', *Geophys. Res. Lett.* **19**, 1927–1930.

Kratzmann, D., Carey, S., Fero, J., Scasso, R. & Naranjo, J.-A. (2009), 'Simulations of tephra dispersal from the 1991 explosive eruptions of Hudson volcano, Chile', *J. Volcanol. Geoth. Res.* **190**, 337–382.

Kristiansen, N., Stohl, A., Prata, A., Richter, A., Eckhardt, S., Seibert, P., Hoffmann, A., Ritter, C., Bitar, L. & Stebel, T. D. K. (2010), 'Remote sensing and inverse transport modeling of the kasatochi eruption sulfur dioxide cloud', *J. Geophys. Res.* **115**, D00L16.

Krotkov, N. A., Schoeberl, M. R., Morris, G. A., Carn, S., & Yang, K. (2010), 'Dispersion and lifetime of the SO_2 cloud from the August 2008 Kasatochi eruption', *J. Geophys. Res.* **115**, D00L20.

Krotkov, N., Carn, S. A., Krueger, A. J., Bhartia, P. K. & Yang, K. (2006), 'Band residual difference algorithm for retrieval of SO_2 from the Aura Ozone Monitoring Instrument (OMI)', *IEEE Trans. Geosci. Remote Sens.* **44(5)**, 12591266.

Krotkov, N., McClure, B., Dickerson, R., Carn, S., Li, C., Bhartia, P., Yang, K., Krueger, A., Li, Z., Levelt, P., Chen, H., Wang, P. & Lu, D. (2008), 'Validation of SO_2 retrievals from the Ozone Monitoring Instrument over NE China', *J. Geophys. Res.* **113**, D16S40.

Krueger, A. (1983), 'Sighting of El Chichon sulphur dioxide clouds with the Nimbus 7 Total Ozone Mapping Spectrometer', *Science* **220**, 1377–1378.

Krueger, A., Krotkov, N. & Carn, S. (2007), 'El chichón: The genesis of volcanic sulphur dioxide monitoring from space', *J. Volcanol. Geoth. Res.*

Krueger, A., Walter, L., Bhartia, P., Schnetzler, C., Krotkov, N., I.Sprod & Bluth, G. (1995), 'Volcanic sulphur dioxide measurements from the Total Ozone Mapping Spectrometer (TOMS) instruments', *J. Geophys. Res.* **100**, 14057–14076.

Kurbatov, A. V., Zielinski, G. A., Dunbar, N. W., Mayewski, P. A., Meyerson, E. A., Sneed, S. B. & Taylor, K. C. (2006), ‘A 12,000 year record of explosive volcanism in the Siple Dome Ice Core, West Antarctica’, *J. Geophys. Res.* **111**, D12307.

Lacis, A., Hansen, J. & Sato, M. (1992), ‘Climate forcing by stratospheric aerosols’, *Geophys. Res. Lett.* **19**, 1607–1610.

Lamb, H. (1977), ‘Volcanic dust in the atmosphere; with a chronology and assessment of its meteorological significance’, *Phil. Trans. R. Soc. London* **266**, 425–533.

Lambert, A., Grainger, R., Rodgers, C., Taylor, F., Mergenthaler, J., Kumer, J. & Massie, S. (1997), ‘Global evolution of the Mt Pinatubo volcanic aerosols observed by the infrared limb-sounding instruments CLAES and ISAMS on the Upper Atmosphere Research Satellite’, *J. Geophys. Res.* **102**, 1495–1512.

Lee, C., Richter, A., Weber, M. & Burrows, J. P. (2008), ‘SO_2 retrieval from SCIAMACHY using the weighting function DOAS (WFDOAS) technique: comparison with standard DOAS retrieval’, *Atmos. Chem. Phys.* **8**, 61376145.

Levelt, P., van den Oord, G., Dobber, M., Malkki, A., Visser, H., Vries, J. D., Stammes, P., Lundell, J. & Saari, H. (2006), ‘The Ozone Monitoring Instrument’, *IEEE Trans. Geosci. Remote Sens.* **44(5)**, 1093–1101.

Marks, R. & Rodgers, C. (1993), ‘A retrieval method for atmospheric composition from limb emission measurements’, *J. Geophys. Res.* **98**, 14939–14953.

Marshall, G., Turner, J. & Miners, W. (1998), ‘Interpreting recent accumulation records through an understanding of the regional synoptic climatology: an example from the southern Antarctic Peninsula’, *Ann. Glaciol.* **27**, 610–616.

Matricardi, M. (2008), The generation of RTTOV regression coefficients for IASI and AIRS using a new profile training set and a new line-by-line database, Technical report, ECMWF. Technical Memorandum 564.

Matricardi, M. (2010), ‘A principal component based version of the RTTOV fast radiative transfer model’, *Q. J. R. Meteorol. Soc.* **136 Part A**, 1823–1835.

McCormick, M. & Veiga, R. (1992), ‘SAGE II measurements of early Pinatubo aerosols’, *Geophys. Res. Lett.* **19**, 155–158.

McPeters, R. (1993), ‘The atmospheric SO_2 budget for pinatubo derived from NOAA-11 SBUV/2 spectral data’, *Geophys. Res. Lett* **20**, 1971–1974.

Miles, G., Grainger, R. & Highwood, E. (2004), ‘The significance of volcanic eruption strength and frequency for climate’, *Q. J. Roy. Meteor. Soc.* **130**, 2361–2376.

Miles, G., Marshall, G., McConnell, J. R. & Aristarain, A. (2008), ‘Recent accumulation variability and change on the Antarctic Peninsula from the ERA40 reanalysis’, *Int. J. Climatol.* **28**, 1409–1422.

Molina, M. & Rowland, F. S. (1974), ‘Stratospheric sink for chlorofluoromethanes: chlorine atomc-atalysed destruction of ozone’, *Nature* **249**, 1409–1422.

Munro, R., Siddans, R., Reburn, W. & Kerridge, B. (1998), ‘Direct measurement of tropospheric ozone distributions from space’, *Nature* **392**, 168–171.

Naranjo, J. (1991), ‘Major eruption reported in Chile’, *EOS Trans Am Geophys Union* **72**, 393–394.

Naranjo, J. & Stern, C. (1998), ‘Holocene explosive activity of Hudson Volcano, southern Andes’, *Bull. Volcanol.* **58**, 291–306.

Newhall, C. & Self, S. (1982), ‘The Volcanic Explosivity Index (VEI): An estimate of the explosive magnitude for historical volcanism’, *J. Geophys. Res.* **87**, 1231–1238.

NOAA (1981), NOAA Technical Report NESS 83: Atmospheric Sounding User’s Guide, Technical report, National Oceanic and Atmospheric Administration. NESS 83.

NOAA (2000), ‘NOAA Polar Orbiter Data User’s Guide’. http://www2.ncdc.noaa.gov/docs/podug/.

Nowlan, C., Liu, X., Chance, K., Cai, Z., Kurosu, T., Lee, C. & Martin, R. (2011), ‘Retrievals of sulfur dioxide from GOME-2 using an optimal estimation approach: Algorithm and initial validation’, *J. Geophys. Res.* **-**, In press.

Oman, L., Robock, A., Stenchikov, G., Schmidt, G. & Ruedy, R. (2005), 'Climatic response to high-latitude volcanic eruptions', *J. Geophys. Res.* **110**, D13103.

Pieri, D. & Abrams, M. (2004), 'ASTER watches the world's volcanoes: a new paradigm for volcanological observations from orbit', *J. Volcano. Geothrm Res.* **135**, 13–28.

Pinto, J., Turco, J. & Toon, O. (1989), 'Self limiting physical and chemical effects in volcanic eruption clouds', *J. Geophys. Res.* **94**, 11165–11174.

Pitts, M. & Thomason, L. (1993), 'The impact of the eruptions of Mount Pinatubo and Cerro Hudson on Antarctic aerosol levels during the 1991 austral spring', *Geophys. Res. Lett.* **20**, 2451–2454.

Platt, U. & Stutz, J. (2008), *Differential optical absorption spectroscopy. Principles and Applications*, Vol. 71, Springer-Verlag, Berlin Hidelberg.

Pollack, J., Toon, O., Sagan, C., Summers, A., Baldwin, B. & Camp, W. V. (1976), 'Stratospheric aerosols and climate change', *J. Geophys. Res.* **94**, 11165–11174.

Poulsen, C., Watts, P., Thomas, G., Sayer, A., Siddans, R., Grainger, R., Lawrence, B., Campmany, E., Dean, S. & Arnold, C. (2011), 'Cloud retrievals from satellitedata using optimal estimation, evaluation and application to ATSR', *J. Atmos. Meas. Tech.* **-**, In Press.

Prata, A. (2009), 'Satellite detection of hazardous volcanic clouds and the risk to global air traffic', *Nat. Hazards* **51**, 303–324.

Prata, A. & Bernado, C. (2007), 'Retrieval of volcanic so_2 column abundence from Atmospheric Infrared Sounder data', *J. Geophys. Res.* **112**, D20204.

Prata, A. & Kerkmann, J. (2007), 'Simultaneous retrieval of volcanic ash and so_2 using MSG-SEVIRI measurements', *Geophys. Res. Lett.* **34**, L05813.

Prata, A., Gangale, G., L.Clarisse & Karagulian, F. (2010), 'Ash and sulphur dioxide in the 2008 eruptions of Okmok and Kasatochi: Insights from high spectral resolution satellite measurements', *J. Geophys. Res.* **115**, D00L18.

Prata, A., Rose, W., Self, S. & O'Brien, D. (2003), *Volcanism and the Earth's Atmosphere, Geophysical Monograph Series, ed. A. Robock and C. Oppenheimer*, Vol. 139, American Geophysical Union, Washington, DC, chapter Global, long-term sulphur dioxide measurements from TOVS data: a new tool for studying explosive volcanism and climate, pp. 75–92.

Prata, F. & Corradini, S. (2009), Algorithm theoretical basis document: Infrared sulphur dioxide algorithms, Technical report, Norweigan Air Institute; Istituto Nazionale di Geoysica e Vulcanologia;University of Natural Resources and Applied Life Sciences, Vienna. http://savaa.nilu.no/.

Pruppacher, J. A. & Klett, J. D. (1997), *Microphysics of clouds and precipitation*, 2nd edition edn, Kluwer Academic Publications.

Pugnagni, Gangale, G., Corradini, S. & Buongiorno, M. (2006), 'Mt. Etna sulfur dioxide flux monitoring using ASTER-TIR data and atmospheric observations', . *Volcanol. Geoth. Res.* **152**, 74–90.

Pyle, D., Beattie, P. & Bluth, G. (1996), 'Sulphur emissions to the stratosphere from explosive volcanic eruptions', *Bull. Volcanol.* **57**, 663–671.

Read, W., Froidevaux, L. & Waters, J. W. (1993), 'Microwave limb sounder measurement of stratospheric SO_2 from the Mt. Pinatubo volcano', *Geophys. Res. Lett.* **20**, 12991302.

Read, W., Froidvaux, L., Santee, M. & Livesey, N. (2009), 'Observations of volcanic SO_2 and HCl from Aura MLS'. American Geophysical Union, Fall Meeting 2009, abstract number V24B-03.

Realmuto, V., Abrams, M., Buongiorno, M. & Pieri, D. (1994), 'The use of multispectral thermal infrared image data to estimate the sulfur-dioxide flux from volcanoes - a case-study from mount etna, sicily, july 29, 1986', *J. Geophys. Res.* **99(B1)**, 481–488.

Rix, M., P.Valks, Loyola, D., van Gent, J., van Roozendael, M., Spurr, R., Hao, N. & Zimmer, W. (2011), 'Monitoring of volcanic eruptions and determination of SO_2 plume height from GOME-2 measurements'. Oral presentation at the 2011 EUMETSAT conference in Oslo, Norway.

Rix, M., Valks, P., Maerker, J. V. G. C., Seidenberger, K., Erbertseder, T., Van Roozendael, M., Hao, N. & Loyola, D. (2009), 'Operational monitoring of SO_2 emissions using the GOME-2 satellite instrument'. Proceedings of the 2009 EUMETSAT Meteorological Satellite Conference,21-25 Sept. 2009, Bath, England, EUMETSAT publication P.55.

Robock, A. (2000), 'Volcanic eruptions and climate', *Reviews of Geophysics* **38**, 191–219.

Robock, A. (2005). Personal communication.

Robock, A. & Mao, J. (1995*a*), 'The volcanic signal in surface temperature observations', *J. Climate* **8**, 1086–1103.

Robock, A. & Mao, J. (1995*b*), 'The volcanic signal in surface temperature observations', *J. Climate* **8**, 1086–1103.

Rodgers, C. (2000), *Inverse methods for atmospheric sounding: theory and practice*, 1 edn, World Scientific.

Roscoe, H. (2001), 'The risk of large volcanic eruptions and the impact of this risk on future ozone depleation', *Natural Hazards* **23**, 231–246.

Rose, W. (2002). Personal communication.

Rose, W., Bluth, G. & Ernst, G. (2000), 'Integrating retrievals of volcanic cloud characteristics from satellite remote sensors: a summary', *Phil. Trans. R. Lond. A* **358**, 1585–1606.

Rose, W., Schneider, D. D. D., Bluth, G., Krueger, A., Sprod, I., McKee, C., Davies, H. & Ernst, G. (1995), 'Ice in Rabaul eruption cloud of 19 21 September 1994', *Nature* **375**, 477 479.

Rozanov, V. V. & Rozanov, A. V. (2010), 'Differential optical absorption spectroscopy (doas) and air mass factor concept for a multiply scattering vertically inhomogeneous medium: theoretical consideration', *Atmos. Meas. Techn.* **3**, 751–780.

Ryan, J. & Mukherjee, N. (1975), 'Sources of stratospheric gaseous chlorine', *Rev. Geophys. Space Phys.* **13**, 650–658.

Sadler, J. & Grattan, J. (1999), 'Volcanoes as agents of past environmental change', *Global and Planetary Change* **21**, 181–196.

Sato, M., Hansen, J., McCormick, M. & Pollack, J. (1993), 'Stratospheric Aerosol Optical Depths, 1850-1990', *J. Geophys. Res.* **98**, 22987–22994.

Saunders, R., Matricardi, M. & Brunel, P. (1999), 'An improved fast radiative transfer model for assimilation of satellite radiance observations', *Q. J. R. Meteorol. Soc.* **125**, 1407–1425.

Scasso, R., Corbella, H. & Tiberi, P. (1994), 'Sedimentological analysis of the tephra from the 12-15 August 1991 eruption of Hudson volcano', *Bull Volcanol* **56**, 121–132.

Schnetzler, C., Bluth, G., Krurger, A. & Walter, L. (1997), 'A proposed volcanic sulphur dioxide index(VSI)', *J. Geophys. Res.* **102**, 20087–20091.

Schoeberl, M., Doiron, S., Lait, L., Newman, P. & Krueger, A. (1993), 'A simulation of the Cerro Hudson so_2 cloud', *J Geophys Res* **98**, 2949–2955.

Self, S. & King, A. (1996), 'Petrology and sulfur and chlorine emissions of the 1963 eruption of Gungung Agung, Bali, Indonesia', *Bull. Volcanol.* **58**, 263–285.

Shine, K. & Highwood, E. (2002), Problems in quantifying natural and anthropogenic perturbations to the Earth's energy balance, *in* E. R. Peace, ed., 'Meteorology at the Millennium', Academic Press.

Siddans, R. (2011), Fast transmittance modelling of the MSG and MTG solar channels for cloud retrievals - Final Report, Technical report, STFC. Delivered in response to EUMETSAT RFQ 10/202521.

Siegrist, M., ed. (1994), *Differential optical absorption spectroscopy (DOAS), Air Monitoring by Spectroscopic Techniques*, Vol. Chemical Analysis Series 127, -.

Sigurdsson, H. & Laj, P. (1992), *Atmospheric Effects of Volcanic Eruptions*, Academic Press.

Smith, C. A., Haigh, J. D. & Toumi, R. (2001), 'Radiative forcing due to trends in stratospheric water vapour', *Geophys. Res. Lett.* **28**, 179–182.

Smithsonian, I. (1991), 'Hudson', *Bulletin of the Global Volcanism Network* **16**, 2–5.

Smithsonian, I. (2002), 'Cerro Hudson'. http://www.volcano.si.edu/gvp/.

Solomon, S., Portmann, R., Garcia, R., Randel, W., Wu, F., Nagatani, R., Gleason, J., Thomason, L., Poole, L. & McCormick, M. (1996), 'The role of aerosol variations in anthropogenic ozone depletion at northern midlatitudes', *J. Geophys. Res.* **101**, 6713–6727.

Solomon, S., Portmann, R., Garcia, R., Randel, W., Wu, F., Nagatani, R., Gleason, J., Thomason, L., Poole, L. & McCormick, M. (1998), 'Ozone depletion at mid-latitudes: Coupling of volcanic aerosols and temperature variability to anthropogenic chlorine', *Geophys. Res. Lett.* **25**, 1871–1874.

Sparks, R. S. J., Bursik, M. I., Carey, S. N., Gilbert, J. S., Glaze, L. S., Sigurdsson, H. & Woods, A. W. (1997), *Volcanic Plumes*, 1st edition edn, Wiley.

Spinei, E., Carn, S., Krotkov, N., Mount, G., Yang, K. & Krueger, A. (2010), 'Validation of the ozone monitoring instrument SO_2 measurements in the okmok volcanic cloud over Pullman, WA, July 2008', *J. Geophys. Res.* **115**, D00L08.

Stenchikov, G., Kirchner, I., Robock, A., Graf, H., Antuna, J., Grainger, R., Lambert, A. & Thomason, L. (1998), 'Radiative forcing from the 1991 mount pinatubo volcanic eruption', *J. Geophys. Res.* **103**, 13837–13857.

Stevenson, D., Johnson, C., Highwood, E., Collins, W. & Derwent, R. (2003), 'Atmospheric impact of the 17831784 Laki eruption: Part i chemistry modelling', *Atmos. Chem. Phys.* **3**, 487507.

Stoiber, R. & Jepsen, A. (1973), 'Sulfur dioxide contributions to the atmosphere by volcanoes', *Science* **182**, 577–578.

Stoiber, R., Williams, S. & Huebert, B. (1986), 'Annual contribution of sulfur dioxide to the atmosphere by volcanoes', *J. Volcanol. Geotherm. Res.* **33**, 1–8.

Stothers, R. (1984), 'The great Tambora eruption in 1815 and its aftermath', *Science* **224**, 1191–1198.

Strow, L., Hannon, S., Machado, S., Motteler, H. & Tobin, D. (2003), 'An overview of the AIRS radiative transfer model', *IEEE Trans. Geosci. Remote Sens.* **41(2)**, 303 313.

Susskind, J., Rosenfield, J. & Reuter, D. (1983), 'An accurate radiative transfer model for use in the direct physical inversion of HIRS2 and MSU temperature sounding data', *J. Geophys. Res.* **88**, 8550–8568.

T. Yu, W. R. & Prata, A. (2002), 'Atmospheric correction for satellite-based volcanic ash mapping and retrievals using "split window" IR data from GOES and AVHRR', *J. Geophys. Res.* **107(D16)**, 4311.

Thomas, H. & Prata, A. (2011), 'Sulphur dioxide as a volcanic ash proxy during the AprilMay 2010 eruption of Eyjafjallajökull Volcano, Iceland', *Atmos. Chem. Phys. Discuss.* **11**, Under review11, 77577780.

Thomas, H., Watson, I., Kearney, C., Carn, S. & Murray, S. (2009), ‘A multi-sensor comparison of sulphur dioxide emissions from the 2005 eruption of Sierra Negra volcano, Galpagos Islands’, *emote Sensing of Environment* **113**, 1331–1342.

Thomas, W., Erbertseder, T., Ruppert, T., van Roozendael, M., Verdebout, J., Balis, D., Meleti, C. & Zerefos, C. (2005), ‘On the retrieval of volcanic sulfur dioxide emissions from the GOME backscatter measurements’, *J. Atmos. Chem.* **50**, 295–320.

Trenberth, K. E. & Hoar, T. (1996), ‘The 19901995 El Niño-Southern Oscillation event: Longest on record’, *Geophys. Res. Lett.* **23**, 57–60.

Trentmann, J., Andreae, M., Graf, H., Hobbs, P., Ottmar, R. & Trautmann, T. (2002), ‘Simulation of a biomass-burning plume: Comparison of model results with observations’, *J. Geophys. Res.* **107**, 110–111.

Trepte, C., Veiga, R. & McCormick, M. (1993), ‘The poleward dispersal of Mount Pinatubo volcanic aerosol’, *J. Geophys. Res.* **98**, 18563–18573.

USGS (2002), ‘Photo glossary of volcano terms’. http://volcanoes.usgs.gov/Products/Pglossary/stratovolcano.html.

Vernier, J.-P., Thomason, L. W., Pommereau, J.-P., Bourassa, A., Pelon, J., Garnier, A., Hauchecorne, A., Blanot, L., Trepte, C., Degenstein, D. & Vargas, F. (2011), ‘Major influence of tropical volcanic eruptions on the stratospheric aerosol layer during the last decade’, *Geophys. Res. Lett.* **38**, L1280.

Wallace, P. (2001), ‘Volcanic SO_2 emissions and the abundence and distribution of exsolved gas in magma bodies’, *J. Volcanol. Geoth. Res.* **108**, 85–106.

Watson, I., Realmuto, V., Rose, W., Prata, A., Bluth, G., Gu, Y., Bader, C. & Yu, T. (2004), ‘Thermal infrared remote sensing of volcanic emissions using the moderate resolution imaging spectroradiometer’, *J. Volcanol. Geoth. Res.* **135**, 75 89.

Weaver, C., Joiner, J. & Ginoux, P. (2003), ‘Mineral contamination of TIROS Operational Vertical Sounder (TOVS) temperature and moisture retrievals’, *J. Geophys Res.* **108**, AAC 5.

Westrich, H. & Gerlach, T. (1992), ‘Magmatic gas source for the stratospheric so_2 cloud from the June 15, 1991, eruption of Mount-Pinatubo’, *Geology* **20**, 867–870.

WMO (1998), WMO Scientific Assessment of Ozone Depletion: 1998, Technical report, World Meteorological Organization. Report No. 44.

Wylie, D. P., Jackson, D., Menzel, W. P. & Bates, J. (2005), 'Global cloud cover trends inferred from two decades of HIRS observations', *J. Climate* **18**, 3021–3031.

Wylie, D. P., Menzel, W. P., Woolf, H. M. & Strabala, K. I. (1994), 'Four years of global cirrus cloud statistics using HIRS', *J. Climate* **7**, 1972–1986.

Yamaguchi, Y., Kahle, A., Tsu, H., Kawakami, T. & Pniel, M. (1998), 'Overview of Advanced Spaceborne Thermal Emission and Reflection Radiometer (aster)', *IEEE Trans. Geosci. Remote Sens.* **36(4)**, 1062–1071.

Yang, K., Krotkov, N., Krueger, A., Carn, S., Bhartia, P. & Levelt, P. (2007), 'Retrieval of large volcanic SO_2 columns from the Aura Ozone Monitoring Instrument: Comparison and limitations', *J. Geophys. Res.* **112**, D24S43.

Young, S., Manson, P. & Patterson, G. (1992), 'Southern hemisphere lidar measurements of the aerosol clouds from Mt Pinatubo and Mt Hudson', *Extended Abstracts: 16th International Laser Radar Conference, Cambridge, Mass. July 20-24th* **1**, 3–6.

Zielinski, G. (1995), 'Stratospheric loading and optical depth estimates of explosive volcanism over the last 2100 years derived from the Greenland Ice Sheet Project 2 ice core', *J. Geophys. Res.* **100**, 20937–20955.

Zielinski, G., Mayewski, L., Meeker, L., Whitlow, S., Twickler, T., Morrison, M., Meese, D., Gow, A. & Alley, R. (1994), 'Record of volcanism since 7000 B.C. from the GISP2 Greenland Ice Core and implications for the volcano-climate system', *Science* **264**, 948–952.